4-6-2022 10:00 AM

Analysis of Standing Seam Metal Roofs Subjected to Extreme Wind Loads

Yuchao Xia, *The University of Western Ontario*

Supervisor: Kopp, Gregory A., *The University of Western Ontario*
Joint Supervisor: Chen, Shuifu, *Zhejiang University*
A thesis submitted in partial fulfillment of the requirements for the Doctor of Philosophy degree in Civil and Environmental Engineering

Abstract

Standing seam metal roof (SSMR) systems are widely used in low-rise buildings. This study aims to understand the behavior of SSMR systems, especially the failure mechanisms, under severe wind loads. Full-scale experiments conducted at Insurance Research Lab for Better Homes make it possible to examine the performance of SSMR systems with realistic dimensions and boundary conditions. The induced loads on the clips could be measured directly. The results show that there is a linear relationship between the wind pressure and clip reaction under low wind pressure (less than 500 Pa). It is found that load sharing among clips changes at higher pressures due to the large deformation of the roof panel. As a result, more loads transfer to the clips and fasteners at the roof edges. Finite element method considers all nonlinearities (e.g., geometric, contact, and material nonlinearities) in the wind-induced response of SSMR systems, which reveal the whole process of failure. The initial location of global buckling, the disengagement failure between panel and clip at seam were simulated, which is consistent with the observation from the experiment. Both the finite element method and experiment show that the roof panel undergoes overall buckling before the roof system reach the ultimate bearing capacity and the initial position of overall buckling is in the middle of the two clips near the seam. Moreover, the results show the boundary conditions have notable effects on load distribution while these were usually ignored by the current standards. An updated analytical model was proposed using the influence function concept. The performance of the standing seam can be considered as a continuous beam with modeling clips and fasteners as vertical springs. Using the Database-assisted design (DAD) method, the clip reactions under spatio-temporal varying pressure were studied, which is also compared with the results from standards. It is found that the estimated clip reactions using GB 50009 (2012) are much smaller than the peaks using the DAD method, which makes the clips more vulnerable under severe wind suction. In contrast, ASCE 7-16 gives a conservative estimation of clip reaction.

Keywords

Standing seam metal roof systems; Low-rise buildings; Wind loads; Full-scale tests; Components and Cladding; Finite element method; Wind-induced response; Failure mode; Influence function; Database-assisted design

Summary for Lay Audience

The roof is one of the most vulnerable parts of low-rise buildings during severe wind storms, which have caused significant losses. Standing seam metal roof (SSMR) systems are widely used in low-rise buildings, while the load paths and failure mechanisms are still not fully understood. The traditional methods of estimating the uplift resistance of roof systems are generally through standardized tests, which do not consider the effects of boundary conditions.

In this thesis, full-scale test and finite element method have been used to improve the understanding of load paths and structural behavior of SSMR systems subjected to wind uplift load up to the limit state. The clip reaction influence functions have been obtained as well. The results indicate that this improved model provides better estimations for the clip reaction of SSMR systems. Theoretically, this model is applicable for roofs that subjected to spatial and time varying wind pressures.

Acknowledgments

First, I would like to thank my supervisor at the University of Western Ontario, Dr. Gregory A. Kopp, for his continual support and patience throughout my work. He gave creative ideas and all the necessary facilities for the research. Outside of his knowledge as a researcher, his guidance on critical thinking and skills of communication has been invaluable in my studies and career.

I also want to express my deepest thanks to my supervisor at Zhejiang University, Dr. Shuifu Chen, for providing me with opportunities to gain knowledge on wind engineering and for all the encouragement, support, and guidance.

Special thanks to Dr. Mahshid Nasiri for sharing her test data, and for all the help during this research project. Without her help, this thesis work would not be possible. Sincere thanks to Dr. Morrison, and Meisenzahl, for providing the data from the IBHS full-scale wind tunnel to validate my analytical model.

Many thanks to Dr. Yitian Guo, Dr. Yi Liu, Dr. Jin Wang, Dr. Chieh-Hsun Wu, Dr. Miller, Jinlin Xia, Shiyu Zhao, and other students in the Wind Engineering group for all the help during my Ph.D. life.

Thanks to my parents, my family members, and all my friends for all the love and support. I would like to give great thanks to my wife Xuewen for her help, love, and support.

Table of Contents

List of Tables

List of Figures

List of Nomenclature

A_e	Effective tributary area of the component.
A_g	Geometric tributary area.
C_P	Pressure coefficients.
$[C]$	Damping matrix.
$\{F\}$	Vector of nodal loads.
F_U	Design loads for a cladding component.
$F(t)$	Wind-induced force/response of the component.
(GCp)	Peak pressure coefficient in ASCE 7-16.
H	Mean roof height of the building.
I	Influence functions.
k	Turbulence kinetic energy.
k_i	Stiffness at clip *i*.
$[K]$	Stiffness matrix.
K_d	Wind directionality factor.
K_e	Ground elevation factor.
K_Z	Velocity pressure exposure factor.
K_{zt}	Topographic factor.
$[M]$	Mass matrix.
P_0	Reference static pressure.
P_{ASCE}	Design pressure in ASCE 7-16.
P_{GB}	Design pressure in GB 50009-2012.
$P(x, y, t)$	Building surface pressures.
R_i	Reaction at support *i*.
V	Magnitude of the velocity vector.
$\{u\}$	Vector of nodal displacements.
$\{\dot{u}\}$	Vector of nodal velocities.

$\{\ddot{u}\}$	Vector of nodal accelerations.
V_*	Friction velocity.
$\bar{V}(z)$	Mean wind speed at height z.
V_0	Basic wind speed in ASCE 7-16.
V_i	mean wind speed at reference height, z_i.
$V(z,t)$	wind speed of height, z, and time, t.
$\overline{V}(z)$	Mean component of the wind speed.
$V'(z,t)$	Fluctuating part of the wind speed.
v_0	Basic wind speed in GB 50009-2012.
w_0	Basic wind pressure.
x	x-coordinate of the space.
y	y-coordinate of the space.
z	z-coordinate of the space.
z_0	Aerodynamic roughness length.
α	Power-law exponent.
β_{gz}	Gust response factor.
ρ	Air density.
μ_{sl}	Local shape factor.
μ_z	Exposure factor.
δ_{ij}	Vertical displacement at point i due to unit load at point j.
δ'_{ij}	Vertical displacement of beam deflection at i due to a unit vertical load at j.
δ''_{ij}	Vertical displacement of support displacement at i due to a unit vertical load at j.
Δ	Support displacement.

1. Introduction

1.1 Wind damage on buildings

Tropical cyclones, tornadoes, and other severe windstorms have been recognized as major causes of damage to buildings, which lead to significant economic losses (Tamura, 2009). Cyclone Tracy in 1975 destroyed much of Darwin, Australia. Walker (1975) reported that the losses from Cyclone Tracy were about $380 million. Hurricane Hugo in 1989 cost the insurance industry about $3 billion and Hurricane Andrew in 1992 cost about $15 billion (Sparks et al., 1994). Losses from selected wind storms in the past few decades are listed in Table 1.1. Based on statistics from 1970 to 2012, around 70% of the insurance losses are caused by wind storms (Holmes, 2018). Furthermore, the occurrence of wind-induced losses is increasing yearly (Yang et al., 2018).

Table 1.1: Wind storms in the past decades

Year	Name	Country or region	Economic losses ($US million)
1990	Gales	Western Europe	15000 (Corbel et al., 2007)
2003	Typhoon Maemi	Japan	6000 (Ishihara et al., 2003)
2005	Hurricane Katrina	United States	150000 (Vigdor et al., 2008)
2011	Cyclone Yasi	Australia	3500 (Asbridge et al., 2018)
2012	Hurricane Sandy	United States	35000 (Kunz et al., 2013)
2014	Super Typhoon Rammasun	China	3800 (An et al., 2019)
2019	Super Typhoon Lekima	China	7600 (Wu et al., 2021)

Historically, the Main Wind Force Resisting System (MWFRS) is the primary focus of the wind-resistant design for engineers. However, damage surveys have emphasized that the roof is one of the most vulnerable components of low-rise buildings in extreme winds

(Sparks et al., 1994). Walker (1975) also pointed out that the most notable type of failure in Cyclone Tracy was the failure of roof cladding, for which more than 90% of houses suffered significant losses. A damage survey (Crandell et al., 1993) following Hurricane Andrew found that the most vulnerable part of wood-frames houses is the roof while the MWFRS is less vulnerable. The result is not surprising because roofs of low-rise buildings are subjected to the most intense fluctuating wind loads during windstorms, which leads to large net uplift loads. Meanwhile, the worst suctions on the roof occur on relatively small areas compared to the total roof and have a relatively small effect on the total structural response of MWFRS. Thus, extreme negative pressures are critically important for roof cladding and components (C&C) (Kind, 1986; Kind and Wardlaw, 1982). Once the roof is breached, rain accompanying the storm can intrude to the building resulting in significant interior damage, which produces large insurance and economic losses (Sparks et al., 1994). Furthermore, when wind-borne debris breeches an opening on a wall, the internal pressure can increase rapidly, which can lead to significant overloading on both the MWFRS and C&C that they are often not designed to handle (FEMA 2005). This may lead to the collapse of the building. Repairs of buildings often take several months to years to be finished (Henderson and Ginger, 2008). Therefore, it is crucial to ensure the resistance of roof cladding to severe wind loads, which can minimize losses and enhance disaster recovery.

1.2 Metal roof systems

Standing seam metal roof (SSMR) systems are widely used on metal buildings in the United States and Canada because they are watertight, economic, and high-performance roof systems compared with through-fastened roof systems. The typical structures of through-fastened roof systems and SSMR systems are shown in Figure 1.1(a) and Figure 1.1(b), respectively. Through-fastened roof systems that pierce metal panels with screws can lead to water ingress around the screw heads. In contrast, SSMR systems use clips to

fit over the seams of adjacent panels to form watertight joints and can avoid water leakage because this type of metal roof system does not have screw holes drilled through panels. In addition, the sliding clips allow the movement of panels in the longitudinal direction, which can eliminate the effect of thermal expansion and contraction. This feature allows SSMR systems to perform better during extreme temperature variations compared with through-fastened roof systems (Griffin and Fricklas, 2006). Furthermore, errors in the manufacturing process and during installation are reduced since roof panels are prefabricated in factories and then assembled with electric seaming machines. (Song et al., 2015). There are two common profiles of SSMR systems, trapezoidal roof, and vertical-leg roof, which are shown in Figures 2.1(a) and 2.2(b), respectively. The span is defined as the space between adjacent seams.

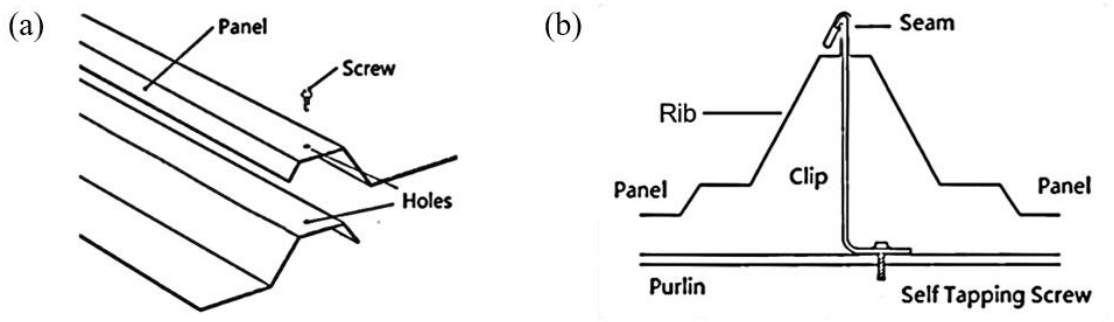

Figure 1.1: Profile of roof systems: (a) through-fastened roof systems, and (b) SSMR systems (Rosenfield et al., 1986).

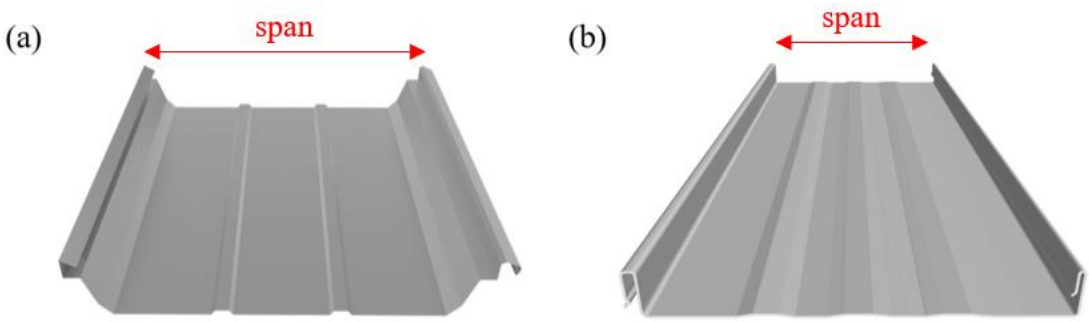

Figure 1.2: Common profiles of panel (a) trapezoidal roof and, (b) vertical-leg roof (Habte et al., 2015).

Although SSMR systems have the above-mentioned advantages, it still should be noted that the sliding clips may weaken the connection between panels and purlins (El Damatty et al., 2003). Besides, the panels of SSMR systems are lightweight and have notable geometric deformation even under relatively small wind loads.

The failure modes of SSMR systems are different from through-fastened roof systems (Baskaran et al., 2011). Based on the horizontal stiffness of clips and the flexural stiffness of panels, there are two typical failure modes (Dixon et al., 2010): seam opening and horizontal movement of the seam, which are shown in Figure 1.3. The most common failure that happens in SSMR systems is clip separation from the seam (Dixon et al., 2010). Once a seam joint is broken, it creates a breach on the roof and the strong wind can blow the panels from the building. Figure 1.4 depicts a typical failure of SSMR systems observed after damage surveys. It can be observed that the clips were still attached to the purlins and the MWFRS did not sustain any obvious damage. In other words, only the roof cladding suffered significant damage. On the other hand, it is difficult to evaluate the strength of seam joints through pullout tests because no single mechanism controls the failure of seam joints (Dixon et al., 2011). Different roof components work together to resist wind loads.

Other interfering factors also affect the performance of SSMR systems. A study to assess the performance of structures during Hurricane Katrina and Hurricane Rita showed that inadequate installation and design caused the failures of metal roofs. For example, insufficient perimeter metal flashings led to damage near the windward edge of roofs and insufficient clips at the eave edge caused metal panels to peel off (Cauffman, 2006).

Therefore, it is important to understand the failure modes and load-bearing capacity of SSMR systems when subjected to high wind loads, especially the failure mechanism near the seam joints.

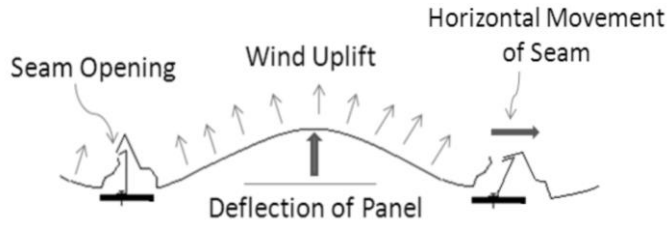

Figure 1.3: Failure modes of SSMR systems (Dixon et al., 2010).

Figure 1.4: Roof failure during extreme wind events (Dixon and Prevatt, 2010).

1.3 The relation between wind loads and response of SSMR systems

As wind flow approaches a building, it flows over and around the building. The separation of flow at the windward edge of the roof gives rise to negative (uplift) pressure on the roof. The wind field and the loads acting on building cladding are connected via the building aerodynamics. The turbulence in the atmospheric boundary layer, turbulence generated by buildings, and the interaction of these generate spatially and temporally varying pressures on building cladding. The high suction forces happen near the roof corners and edges. Roof components close to the edges of the roof are subjected to the highest local negative pressures.

Previous structural research has mainly focused on gravity loads and lateral (e.g., seismic) load resistance (Wolfe and McCarthy 1989; Cramer et al., 2000; Paevere et al., 2003; Collins et al., 2005a; Collins et al., 2005b) on MWFRS. Relatively limited research has been conducted on the actual structural performance of the roof components subjected to extreme wind loads, with the primary focus on the load paths. The wind loads act on the roof cladding first, then transfer the load to clips. After that, the loads go through the clips to the purlins, and finally, the loads transfer to the MWFRS. When determining the load transfer pathways from the cladding to the structural components, the complexity of the cladding details leads to complex and redundant load paths. Moreover, the panels of SSMR systems are lightweight and flexible, which results in significant deformation under wind load. Load redistribution among clips has been observed due to the deformation of the panel (Morrison et al., 2015). Consequently, local damage to the roof components changes the load paths to the MWFRS. Thus, except for the strength of each structural component, the integrity of the entire building relies heavily on the adequacy of the connections between components to properly transfer the forces. The clips are perhaps the most

important part of the load path, and clip reactions must be fully investigated, including load distribution and load redistribution among clips.

In summary, these mechanisms described above should be fully understood to mitigate wind damage. The current approach to evaluating the performance of the roof under wind loads includes two steps (Habte et al., 2015):

1. Determining the design load for roof components using different provisions,

2. Conducting physical tests on the roof system to assess its capability to withstand the design loads.

However, it is difficult to assess the actual response of SSMR systems due to several reasons, which include:

1. Wind loads on low-rise buildings are complex due to significant spatial and temporal variations,

2. Structural analysis is challenging because of the complexity of load paths.

1.4 Current approaches to determine the design wind loads for roof components

The current procedure to determine design loads for roof components is based on wind tunnel data. Boundary layer wind tunnel testing has been recognized as a well-established tool to determine the wind loads on buildings (Cermak, 1975). In boundary layer wind tunnel testing, the properties (mean wind profile, turbulence spectrum, turbulence intensity, and integral length scale) of the simulated wind flows are intended to be the same as those of atmospheric boundary layer (ABL) flows. Using the simulated wind flows around the building, data of wind pressure distribution on the building can be obtained. Davenport (1961) investigated the characteristics of the loads on structures with fluctuating wind and

suggested that the response of a structure to wind forces can be summarized using the wind loading chain, which provides the foundation for the analysis of structural systems of high-rise buildings. Stathopoulos (1979) went a further step and his work became the foundation of design standards of low-rise buildings for Canada and the United States. Since it is not feasible and necessary to conduct wind tunnel testing on every low-rise building, especially those that are regularly shaped, there is a need for codification of wind loads on buildings. To reduce the complexity of pressure variations, the building surfaces are typically divided into several zones, each zone having a uniform load. However, the zones and corresponding loads on each zone are different from standard to standard around the world. The ASCE 7-16 (2017) and GB 5009-2012 (2012) standards are summarized below.

1.4.1 American Society of Civil Engineers (ASCE 7-16)

ASCE 7-16 (2017) depicts all significant types of loads such as dead loads, live loads, snow loads, wind loads, and so on. The wind load provisions for roof components and cladding in ASCE 7-16 for low-rise buildings are largely based on the study by Kopp and Morrison (2018), building on the early study of Stathopoulos (1979). Through the long period of revisions, ASCE 7-16 covers various kinds of roofs including singe-span, multi-span, mono-sloped, gable roof, hip roof, stepped roofs, and domed roofs with different roof slopes. Roof zones and corresponding design wind load coefficients for a low-sloped gable roof are presented in Figure 1.5.

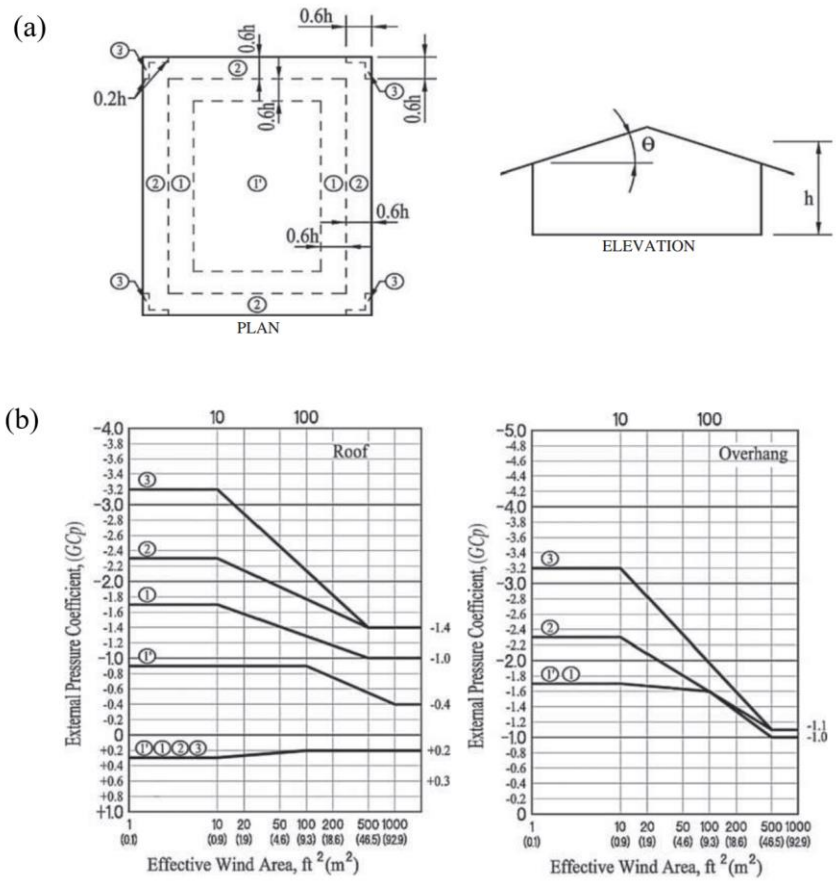

Figure 1.5: Wind pressure coefficients for enclosed and partially enclosed gable-roof low-rise buildings with roof slope less than 7° (a) roof zones, (b) wind pressure coefficients (ASCE 7, 2016).

The design loads on a specific roof component are based on statistical average values of pressure distributions weighted by factors related to the location and terrain. The design loads for a cladding component can be calculated as:

$$F_U = P_{ASCE}A_e = GC_p(0.613\,K_eK_{zt}K_dK_zV^2)A_e \qquad (1.1)$$

where GC_p, is the peak pressure coefficient, K_e is the ground elevation factor, K_{zt} is the topographic factor, K_d is the wind directionality factor, K_z is velocity pressure exposure factor, V is the basic wind speed in m/s, and A_e is the tributary area of the component. ASCE generally assumes the use of the geometric tributary area, A_g, which is typically

defined by using half of the distance to an adjacent fixing for a given component, except for long, thin components. In general, A_e is not equal to A_g for statically-indeterminant systems such as SSMR systems. The basic wind speed is defined as a 3-second gust wind speed at 10 m above the ground in open terrain.

1.4.2 Chinese Load Code for the Design of Building Structures (GB 50009-2012)

The wind loading provisions in China were started from the 1950s in Shanghai and north-east regions of China (Zhang, 1988). The first national load provision was established in 1955 and had several revisions after that. The current load provision used in China is GB 50009-2012 (2012). The design loads for a cladding component can be calculated as:

$$F_U = P_{GB}A_e = \beta_{gz}\mu_{sl}\mu_z w_0 A_e = \mu_{sl}(\frac{1}{2}\rho\beta_{gz}\mu_z v_0^2)A_e \tag{1.2}$$

where β_{gz} is the gust response factor, μ_{sl} is the local shape factor, μ_z is the exposure factor, w_0 is the basic wind pressure, which is equal to $\frac{1}{2}\rho v_0^2$, v_0 is the basic wind speed in m/s, ρ is the air density, which is taken as 1.25kg/m^3, and A_e is the tributary area of the component. The definition of the tributary area in GB 50009-2012 is the same as that in ASCE 7-16. It should be noted that the value of $\frac{1}{2}\rho$ is 0.625, which is close to 0.613 in equation (1.1). The time duration of the basic wind speed is defined as 10 minutes at a height of 10 m in open terrain. Roof zones and corresponding shape factors for a low-sloped gable roof are presented in Figure 1.6.

(a)

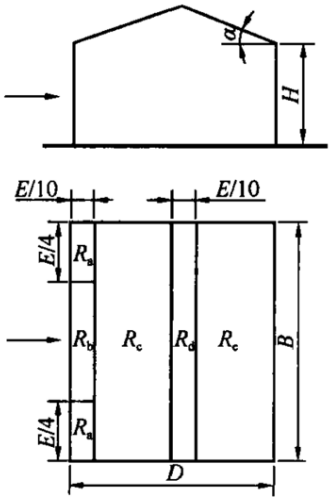

(b)

R_a		R_b	R_c	R_d	R_e
H/D<0.5	H/D>1.0				
-1.8	-2.0	-1.8	-1.2	-0.6	-0.6

Figure 1.6: Shape factors for enclosed and partially enclosed gable-roof low-rise buildings with roof slope less than 5° (a) roof zones, (b) Shape factors (GB 50009, 2012).

Both ASCE 7-16 and GB 50009-2012 assumed the geometric tributary area method to develop the pressure coefficients in Figure1.5 and 1.6. Users of the geometric tributary area method assign the geometric area to a clip and then use the pressure coefficient associated with it. Once the geometric area of the clip is decided, the uniform pressure is assumed to act on the entire geometric area and provides the design pressure for that clip. The geometric tributary area method is easy to use in design, but its validity to actual spatio-temporal wind loads acting on the structure is questionable since it does not account for the true load distribution. As a result, the loads on components with the same geometric tributary area are the same even for different roof systems. While some improvements to hurricane resistance have been made in the recent codes (Gurley et al., 2006), extensive damage still happens even for wind speeds that do not exceed the design wind speed (van de Lindt et al., 2007). This is at least partially due to an inadequate understanding of

structural load paths and the behavior of these systems. However, there could be situations where this approach is extremely conservative (Surry et al., 2007). Thus, the need to understand the load paths of roof systems is necessary to propose improved mitigation approaches.

1.5 Standardized wind load pressure tests

In North America, there are several standard test procedures used to determine the wind-induced uplift performance of metal roofs, which are:

1. FM 4474 (2014)
2. ASTM E1592 (2017)
3. UL 580 (2019)
4. UL 1897 (2020)
5. CSA A123.21 (2020)

FM 4474, ASTM E1592, UL 580, and UL 1897 are laboratory uplift tests that apply static pressures to cladding systems. CSA A123.21 is the only laboratory test method among these that applies oscillating wind loads. The test set-ups of these laboratory uplift tests are similar, consisting of a pressure and/or a vacuum chamber and a frame to support the test specimen. A typical test set up is shown in Figure 1.7.

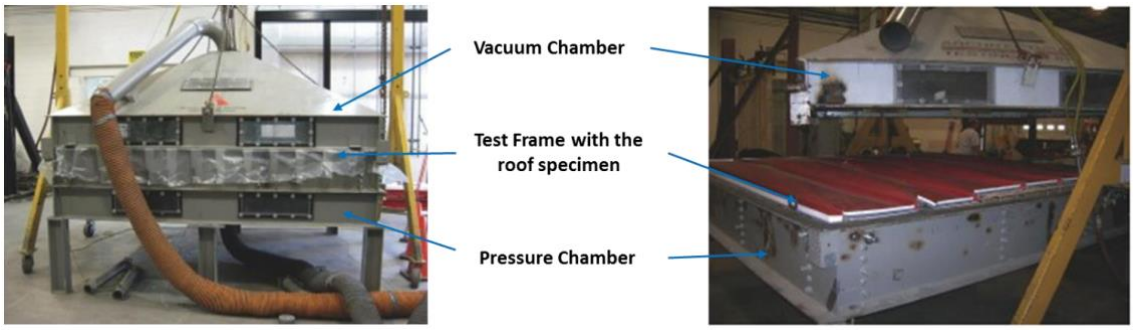

Figure 1.7: A typical wind uplift test setup used for the evaluation of flat roof assemblies (Construction Magnet Contributors, 2010).

1.5.1 FM 4474

FM 4474 was first proposed by FM Approvals, which is an American National Standards Institute (ANSI) accredited standards developer (ASD). A 12 ft × 24 ft frame is used to evaluate roof specimens by applying pressure using the pressure chamber. The specimen meets the manufacturer specifications and is mounted on the steel frame. The boundary of the specimen is clamped to the steel frame, and a gasket is used between the specimen and the pressure chamber. According to FM 4474, an initial uplift pressure of 15 psf is applied to the specimen and maintained for 60 seconds. During this process, the specimen is visually examined to ensure it meets the specification in FM 4474. After that, the uplift pressure is applied successively in 15 psf increments. The loading rate is 1.5 psf/sec. At each increment, the pressure is maintained for 60 seconds, and the specimen is visually examined. This process is continued until failure. Figure 1.8 shows a typical test set-up of FM 4474.

Figure 1.8: Test setup of FM 4474 (Sika, 2015).

1.5.2 ASTM E1592

ASTM E1592, originally proposed in 1995 and most recently revised in 2017, depicts a test procedure to evaluate the uplift resistance of sheet metal roof systems, which is applicable to standing seam, trapezoidal, ribbed or corrugated metal panels with single skin construction or one sheet metal layer of multiple skin construction. As illustrated in Figure 1.9, the specimen is placed on the test frame, and the test frame is fixed to a 12 ft × 24 ft pressure chamber. Displacement measuring equipment is mounted at the mid-span of the specimen to measure the maximum deflection. The size requirement of the specimen is specified in the standard.

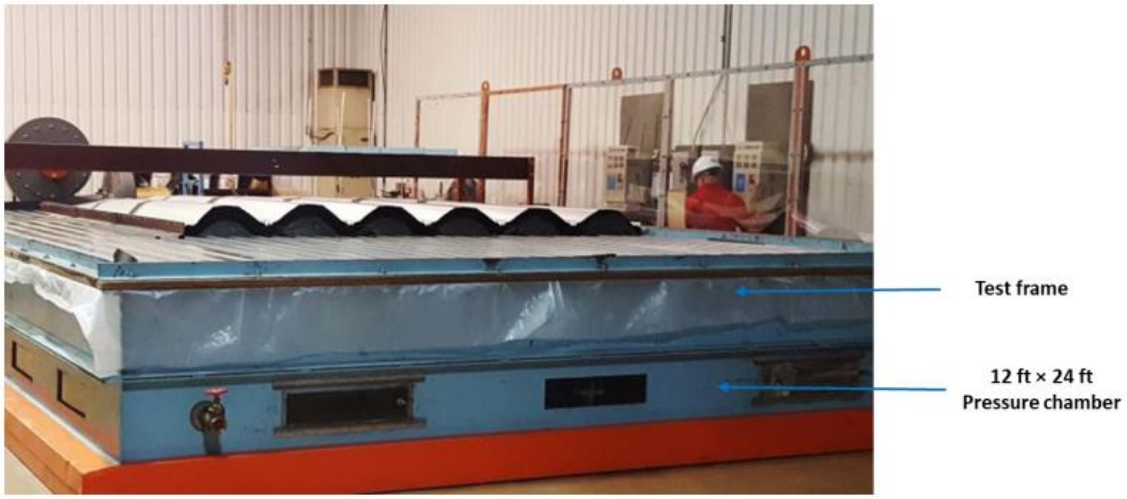

Figure 1.9: Test setup of ASTM E1592 (Allen, 2016).

The initial pressure applied on the specimen is equal to at least four times but not more than ten times the dead weight of the specimen (reference value). Then the pressure is increased to one-third of the anticipated failure pressure (first increment of pressure). This pressure is held constant for 60 seconds and then is dropped to zero. The pressure is increased to the reference value again after a while. Then the increment of pressure is set to the previous increment of pressure plus one-sixth of the anticipated failure pressure. This procedure is repeated until failure is observed. The load-deflection curves for the roof panels are obtained based on this procedure.

1.5.3 UL 580

UL 580 evaluates the uplift resistance of roof systems. The test apparatus has three parts: a vacuum chamber, a 10 ft × 10 ft test frame, and a pressure chamber (as illustrated in Figure 1.10). The vacuum chamber is used to apply steady and oscillating negative pressure and the test chamber is used to apply steady positive pressure. Unlike other test procedures, UL 580 is not a pass or fail test but a rating test. As listed in Table 1.2, in UL 580, there are four rating classes specified for the roof systems, which are UL 15, UL 30, UL 60, and UL 90. In each rating class, there are five phases. During each phase, the pressure is applied

on the specimen for a given duration. It allows fluctuating pressure in test phase 3. The roof system is classified as a particular rating class if the specimen can undergo the corresponding loading sequence, which consists of five phases. A shortcoming of UL 580 is that it does not determine the ultimate load-bearing capacity of the roof system.

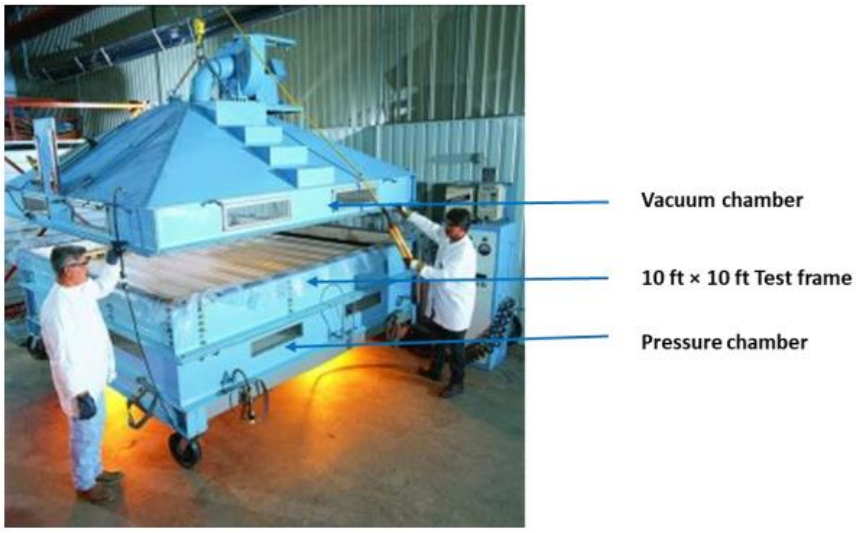

Figure 1.10: Test apparatus of UL 580 (Allen, 2016).

Table 1.2: UL 580 Loading Sequence (UL 580, 2019).

Rating (a)	Test Phase (b)	Duration, min (c)	Negative Pressure, psf (kPa) (d)	Positive Pressure, psf (kPa) (e)
UL 15	1	5	9.4 (0.45)	0.0 (0.0)
	2	5	9.4 (0.45)	5.2 (0.25)
	3	60	5.7 – 16.2 (0.27 – 0.78)	5.2 (0.25)
	4	5	14.6 (0.7)	0.0 (0.0)
	5	5	14.6 (0.7)	8.3 (0.4)
UL 30	1	5	16.2 (0.79)	0.0 (0.0)
	2	5	16.2 (0.79)	13.8 (0.66)
	3	60	8.1 – 27.7 (0.39 – 1.33)	13.8 (0.66)
	4	5	24.2 (1.16)	0.0 (0.0)
	5	5	24.2 (1.16)	20.8 (1.0)
UL 60	1	5	32.3 (1.55)	0.0 (0.0)
	2	5	32.3 (1.55)	27.7 (1.33)
	3	60	16.2 – 55.4 (0.79 – 2.66)	27.7 (1.33)
	4	5	40.4 (1.94)	0.0 (0.0)
	5	5	40.4 (1.94)	34.6 (1.66)
UL 90	1	5	48.5 (2.33)	0.0 (0.0)
	2	5	48.5 (2.33)	41.5 (1.99)
	3	60	24.2 – 48.5 (1.16 – 2.33)	41.5 (1.99)
	4	5	56.5 (2.71)	0.0 (0.0)
	5	5	56.5 (2.71)	48.5 (2.33)

1.5.4 UL 1897

The test apparatus of UL 1897 is similar to the one of UL 580. The specimen is subjected to uplift pressure. The increment of the applied pressure is 15 psf and the pressure is held constant for 60 seconds. This process is repeated until the failure is observed. Unlike UL 580, UL 1897 is a failure test.

1.5.5 CSA A123.21

CSA A123.21 was proposed by a Special Interest Group for Dynamic Evaluation of Roofing Systems (SIGDERS) formed by the National Research Council, Canada. This test protocol aims to provide more reliable uplift resistance and failure modes of roof systems in the laboratory using a dynamic load cycle. The dynamic load cycle is used to simulate

the actual wind conditions, which are based on wind tunnel tests (Baskaran et al., 1999). The test apparatus consists of a 240 in. × 86 in. × 32 in. adjustable bottom frame over which the test specimen is installed. A vacuum chamber containing the gust simulator, fan chamber, and the observation windows is placed over the test specimen as illustrated in Figure 1.11. The dynamic loading cycles of CSA A123.21 are illustrated in Figure 1.12.

The loading cycles consist of five load levels (From A to E) and each load level has eight phases with different numbers of gusts, pressure magnitudes, and durations. The pressure corresponding to a load level is a factored value (e.g., 1 at Level 1 and 2 at Level 5) of the design pressure (P). The design pressure is specified by the design building codes (Baskaran et al., 2003). To evaluate the ultimate load-bearing capacity of the roof system, the specimen is initiated with the pressure of Level A and tested with the pressure of the sequential load level until failure. The maximum pressure is assigned based on the pressure magnitude of the last completed phase.

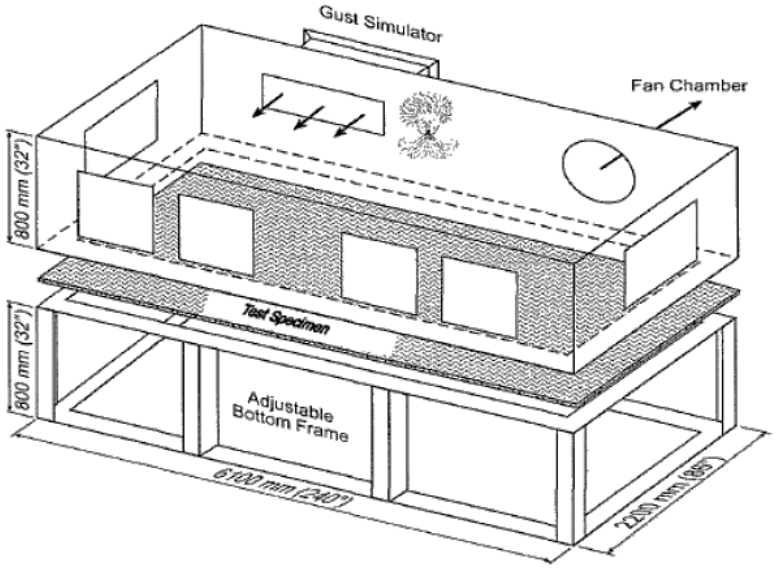

Figure 1.11: Test apparatus of CSA A123.21 (CSA, 2020).

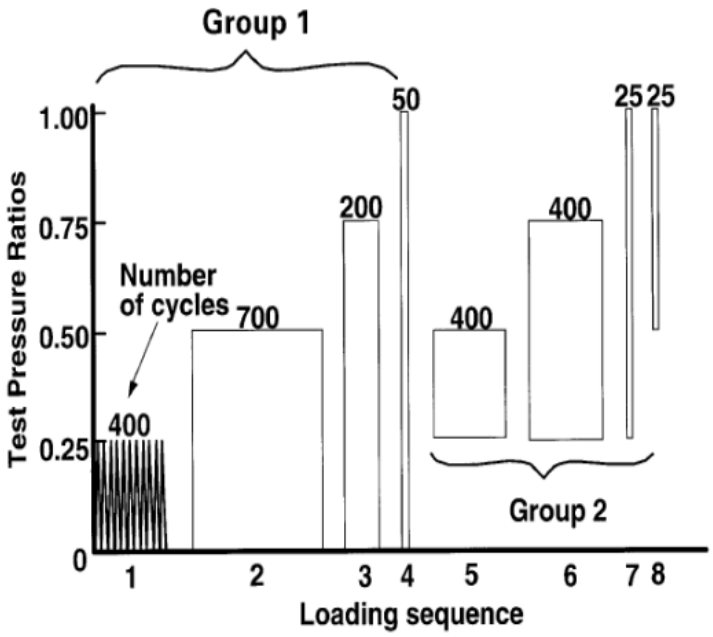

Figure 1.12: Dynamic wind load cycles of CSA A123.21 (CSA, 2020).

1.5.6 Discussion of test standards

The fundamental difference between these test protocols is the way they apply wind loads to SSMR systems and the size of the specimen. FM 4474, ASTM E1592, UL 580, and UL 1897 are all static uplift tests. For FM 4474 and UL 1897, an initial pressure is applied on the specimen and is held constantly for 60 seconds. Subsequently, the pressure is continuously increased from one load level to the next with equal increments while maintaining the pressure at the end of each load level for 60 seconds. For ASTM E1592, the pressure is reduced to a reference pressure at the end of a loading interval before proceeding to the next load level. UL 580 is the only static test incorporating cyclic loading. CSA 123.21 is the only dynamic test procedure of all the tests discussed herein, which requires a relatively longer duration to complete. Kirby et al (2003) tested SSMR systems by using UL580 and UL1897 protocols. These authors found that increased durations significantly increase the probability of roof failure.

Farquhar et al. (2005) tested a scale model of the SSMR system to investigate the failure loads under uniform and wind tunnel pressures. The wind tunnel model was designed to fail at the clips. The relation between uniform pressures used in standard test procedures and dynamic pressures that occurred during real wind loading was quantified. It was found ASCE 7-02 overestimates the design clip load by about 30%. However, the structural dynamics were not fully replicated due to the simplifications of roof components. Morrison and Kopp (2010) extended the work of Farquhar et al. (2005) and concluded the reason for this overestimation is that clips were not located in the worse aerodynamic region of the roof. Baskaran et al. (2011) evaluated the wind-uplift performance of SSMR systems by using CSA A123.21 dynamic test protocol. The results of CSA A123.21 protocol are different from ASTM E1592, UL 580, and UL 1897 because CSA A123.21 is the only North American test standard using dynamic wind load cycles. Habte et al. (2015) conducted a full-scale test of SSMR systems under simulated wind loading at the Wall of Wind (WOW) facility at Florida International University and found that deflections and failure modes were different from those in uniform loading tests. Thus, these results all suggest fluctuating and spatially-varying loads significantly affect the roof performance.

On the other hand, the current standardized tests do not consider the effect of the boundary conditions. Schroter (1985) showed end conditions would influence crosswise distortion of panels and the end effect would affect results as much as 12 feet away from the ends of panels. It was found UL 580 protocol used a specimen with insufficient size for SSMR systems. As a result, it leads to un-conservative results because the deflections of panels are reduced by an overly restrained specimen caused by the edge condition. Dixon et al. (2011) investigated the influence of boundary conditions on load paths of SSMR systems. They concluded that the measured loads of clips on the edges of cladding were about 40% lower than loads of interior clips. The results explain why clip failures seldom happen at the edge of the roof and other failure mechanisms (i.e., sheet tearing or boundary anchor failure) control the roof edge failures. Most of the tests are based on the artificial edge

conditions and the influence of edge conditions could not be investigated. Besides, few standard test protocols record fastener load when evaluating the wind uplift performance of roofing systems, and so the spatial distribution of loads within a specimen at failure remains a mystery (Dixon and Prevatt., 2010).

To evaluate the effects of applied wind loads as well as the size and edge conditions of the specimen, full-scale tests are essential to improve understanding of the response of SSMR systems. Meanwhile, the finite element method (FEM) provides the opportunity to investigate the performance of the roof systems with the least amount of approximation regarding the boundary conditions and can be used to assess the failure mechanisms of roof components. The combination of full-scale tests and FEM would lead to a more reliable standardized test protocol.

1.6 Objectives

As discussed in the previous section, the load-bearing capacity of SSMR systems is affected by the boundary conditions of the roof systems and the current standardized tests only focus on the uplift resistance of roof systems without considering the performance of the clips at the boundaries of the tested specimen. On the other hand, the load paths of SSMR systems are complex and there is a limited understanding of how the entire system works together especially up to the limit state. Thus, the objectives of this study are:

1. To develop a fundamental understanding of the load paths and structural behavior of SSMR cladding systems subjected to wind uplift loads using full-scale tests;

2. To develop numerical models that can accurately simulate the available full-scale scenarios;

3. To examine the load distribution and determine the effective tributary areas and influence functions of clips using the analytical model and FEM;

4. To investigate the influence of panel deformation, load-level, and boundary conditions on the performance of the SSMR system.

1.7 Overview

The dissertation is organized in the following chapters. Figure 1.13 gives the roadmap of this thesis.

Chapter 1 presents background information on the structure and wind-induced damage of SSMR systems. Design codes from America and China (ASCE 7-16 and GB 50009-2012) are also included, which is the current approach to determine the design load for roof systems. The current standardized pressure tests for evaluating the uplift resistance of roof systems are discussed.

Chapter 2 is a literature review of the previous investigations of the performance of roof systems under more realistic conditions.

Chapter 3 describes the experimental approach and equipment used for applying static and dynamic wind pressure on SSMR systems. The measuring equipment is also introduced.

Chapter 4 describes the results of full-scale experiments. The performance of SSMR systems under wind pressures is discussed, which includes roof deformation, clip reactions, and several failure modes.

Chapter 5 presents the explicit FEM, as well as the basic data checks, and comparison with full-scale experiment data. Load transfer and failure mechanisms are investigated.

Chapter 6 presents the implicit FEM, as well as the basic data checks, and comparison with full-scale experiment data. Load sharing among clips is investigated. Also, the wind loading transfer to the gable and eave edge of the roof is given, which provides a design requirement for SSMR roof edges.

Chapter 7 examines the influence function of clips determined using FEM. Also, the effects of boundary conditions and load levels on the influence function are investigated.

Chapter 8 puts forward an analytical model of the clip reaction influence functions. The influence functions of clip reactions with different methods are discussed. The Database-Assisted Design (DAD) method is used to calculate the clip reaction of SSMR systems subjected to spatial and temporal varying pressures. The results are compared with the loads determined from the American and Chinese design standards.

Chapter 9 summarizes the major findings and contributions of this study, and recommendations for future research.

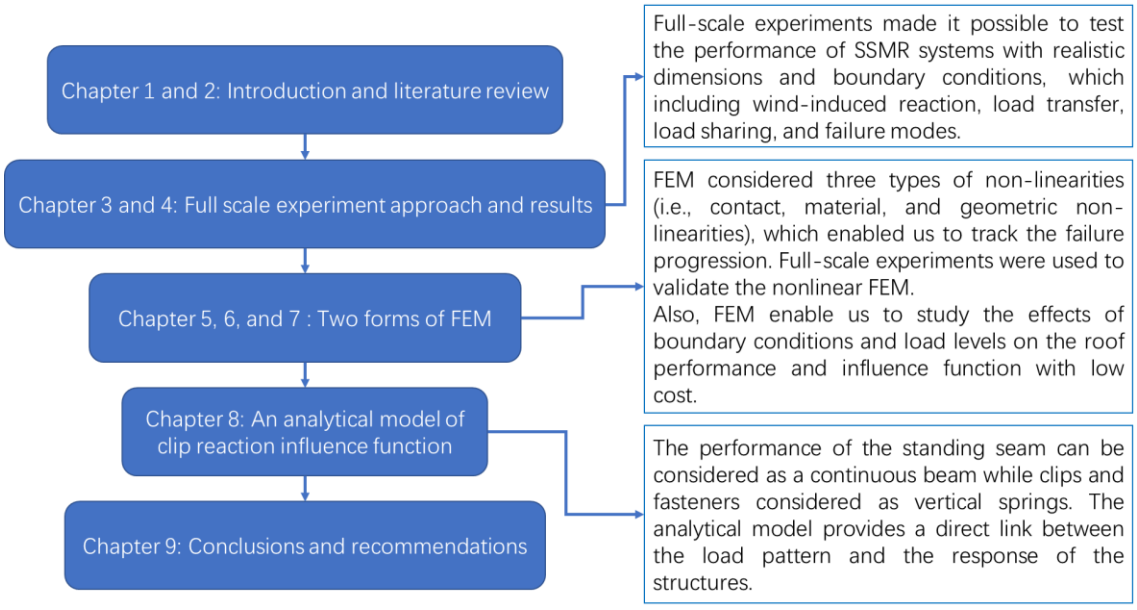

Figure 1.13: Roadmap of this study.

2. Literature review

2.1 Wind loads on low-rise buildings

Wind engineers are mainly interested in the atmospheric boundary layer (ABL) since large-scale synoptic storms tend to govern wind design in many parts of the world. The ABL details depend on the terrain characteristics. The wind speed increases with respect to height in the ABL. As illustrated in Figure 2.1, the wind speed at the ground height is zero and increases as a function of height and ground roughness. At the top of the ABL, the wind speed reaches the maximum value, which is referred as the gradient wind speed (V_g). Above the ABL, the wind speed has much less variation.

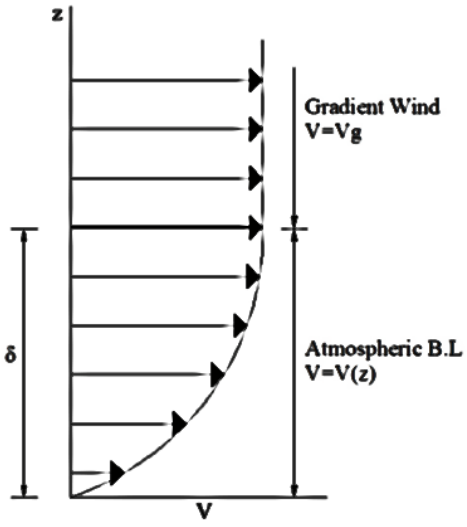

Figure 2.1: Wind speed profile of ABL (Zisis, 2011).

There are two main models of the wind speed profiles, which are the logarithmic law (Equation 2.1) and the power law (Equation 2.2).

$$\bar{V}(z) = \frac{1}{k} V_* In \frac{z}{z_0} \tag{2.1}$$

$$\bar{V}(z) = V_i \left(\frac{z}{z_i}\right)^{\alpha} \tag{2.2}$$

where $\bar{V}(z)$ is the mean wind speed at height z, k is the Von Karman constant (approximately equal to 0.4), V_* is the friction velocity, z_0 is the aerodynamic roughness length, V_i is the mean wind speed at reference height, z_i, and α is the power-law exponent. Theoretically, the logarithmic law is more precise to describe the wind speed profile near the surface. However, the power law is selected for most of the national load provisions due to its simplicity. The usual form of the power law is given as;

$$\bar{V}(z) = V_{10}\left(\frac{z}{10}\right)^{\alpha} \tag{2.3}$$

where V_{10} is the reference wind speed at 10 m elevation.

The wind is turbulent in nature, especially near the ground. The fluctuating flow can be described using the Reynolds decomposition, presuming the flow is statistically stationary, as:

$$V(z,t) = \overline{V}(z) + V'(z,t) \tag{2.4}$$

where $V(z,t)$ is the wind speed of height, z, and time, t, $\overline{V}(z)$ is the mean component of the wind speed and $V'(z,t)$ is the fluctuating part.

The mean component is the average value over a certain duration of a wind speed record. The mean wind speed in large-scale synoptic storms tends to remain relatively steady over a period of time from about 10 minutes to an hour (Van der Hoven, 1957).

The fluctuating wind speed for durations of less than 10 min to an hour is usually assumed to be a result of turbulence, which can be thought of as a superposition of vortices (eddies). The amplitudes and frequencies of vortices vary over a wide range, from millimeters to kilometers. These vortices all together contribute to the fluctuation of wind. Turbulence is described by the intensity, the integral scales, and the power spectrum of the wind speed fluctuations.

When wind acts on a building, it creates pressure over the building surfaces. Buildings are generally described as bluff bodies in the language of aerodynamics because of the non-streamlined shape. Thus, the scope of wind engineering on buildings is to study the aerodynamics of bluff bodies and investigate the wind field around these bodies theoretically and experimentally. The characteristics and properties of the wind flows are crucial and closely related to the wind-induced pressure on building surfaces. For low-rise buildings with flat roofs, the flow phenomenon usually can be divided into two important cases:

1. Flow separation at roof edges, for wind approximately normal to walls,

2. Conical vortices forming along roof edges, for oblique wind.

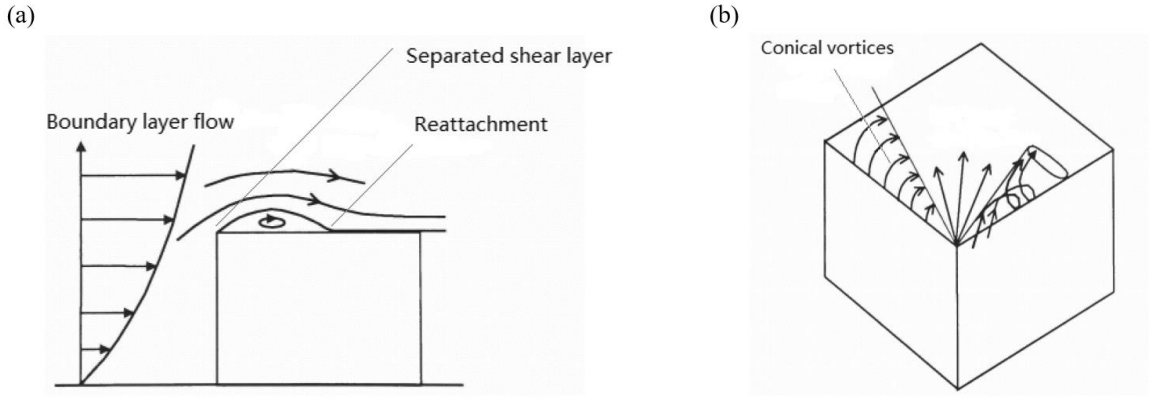

Figure 2.2: Flow over flat roofs with (a) normal-to-wall wind and (b) oblique wind.

As shown in Figure 2.2(a), when the normal-to-wall wind approaches a flat-roof low-rise building, the flow separates at the roof edge to form a separated shear layer. Then it usually reattaches to the roof to form a separation bubble. The flow structure with separation and reattachment is called a “separation bubble”. Large peak suctions are found to be associated with the presence of the separation bubble. In contrast, when the wind is skewed at an angle to the walls, the oblique flow separating along the wall edge entrains into a circulation, which increases as it moves downstream to create a pair of conical vortices. This is

illustrated in Figure 2.2(b). These vortices are the cause of high uplift loads near roof corners (Tieleman, 2003).

Over the past 60 years, following the attempts of Davenport (1961) and Jensen and Franck (1965), boundary layer wind tunnel testing has been recognized as the most effective tool for investigating the wind flows and wind loads on low rise buildings, which contributes to the development and continuous revision of wind-related building standards. Pressure taps installed on the building surfaces provide the spatio-temporal distribution of wind pressure on the envelope of buildings for various directions and terrain conditions. Wind pressures on buildings are typically presented in non-dimensional form as:

$$C_p(x,y,t) = \frac{P(x,y,t) - P_0}{\frac{1}{2}\rho V^2} \tag{2.5}$$

where $C_p(x,y,t)$ is the pressure coefficients at a point (x,y) in time, t, $P(x,y,t)$ is the pressure measured on the building, P_0 is the reference static pressure, ρ denotes the air density, and V represents a reference wind velocity averaged over a particular time duration at the reference location.

2.2 Response of roofs to wind loads

Much of the early wind engineering research was focused on the response of high-rise structures. However, low-rise buildings such as residences, commercial and industrial structures constitute over 70 percent of all buildings (Mooneghi, 2014). (According to ASCE 7-16, the term “low-rise” is used to describe a building whose mean roof heights: (i) are less than 60 ft, and (ii) do not exceed the building’s least horizontal dimension.) As discussed in the previous section, low-rise buildings are often the most vulnerable structures subjected to severe wind loads because many are not engineered. The significant losses incurred during wind disasters highlight the need for continued research on low-rise buildings.

The regions of the worst suction on the roof comprise only a small fraction of the total roof and have relatively small effects on the total structural response for large buildings, but are critically important for roof cladding (Kind, 1986; Kind and Wardlaw, 1982). Cladding receives the wind loads directly and transfers these loads to the MWFRS (Jungmann, 2007). However, there is relatively little knowledge available on how loads are actually transferred through the complex 3D cladding systems to the MWFRS, as discussed in chapter 1 and below.

2.2.1 Influence functions and load sharing

Since there are multiple load paths within low-rise buildings, the redundancy of load paths makes it hard to know which are the most critical and important load paths. The lack of understanding of load paths has often contributed to inadequate design. For example, FEMA (1999) concluded that the major structural failures in residences during wind storms were due to the lack of a continuous vertical load path.

Influence functions, or influence coefficients, provide a quantitative measure of a specific reaction (e.g., bending moment, vertical reaction, torsion, etc.) due to an applied load at a certain point on the structure (Datin, 2010). Influence coefficients can be thought of as the proportion of the applied load that is transferred through the given support. They provide a direct link between the load pattern and the response of the structures. As a result, influence coefficients are widely used in structural analysis (Hibbeler 2015). This concept has also been used in wind engineering to calculate the dynamic response due to spatial-temporal wind loads (Davenport, 1995).

Wind-induced forces on cladding and components are induced by surface pressures, which can be calculated by the integration of influence coefficients and aerodynamic pressure over the area where $I \neq 0$. The equation can be written as;

$$F(t) = \int_{A_{tot}} \frac{1}{2} \rho V^2 \, C_p(x, y, t) I(x, y) dA \tag{2.6}$$

where $F(t)$ is wind-induced force/response of the component; $I(x, y)$ denotes the influence functions (influence coefficients) over the geometric area, and A_{tot} denotes the geometric area that the pressure acts on.

The effective area when the pressure is spatially uniform is:

$$A_e = \int_{A_{tot}} I(x, y) dA \tag{2.7}$$

For a clip, the influence function, $I(A, B)$, represents the reaction at clip A when a concentrated unit load is applied at point B. Figure 2.3 depicts the location of clips and applied concentrated load on the SSMR system. For example, Nasiri (2019) obtained the influence functions of clip A, the unit point load was applied on point B_i $(i = 1 - 20)$. Thus, the influence functions $I(A, B_i)$ $(i = 1 - 20)$ represents reactions associated with the applied concentrated unit load, at each location. The total load is formed through summation, i.e., $R_A = \sum_{i=1}^{20} P_i \cdot I(A, B_i)$. For continuous loads, this can be extended to $R_A = \iint_{A_{tot}} P(x, y) \cdot I(x, y) dx dy$ through continuously-varying influence functions $I(x, \mathrm{y})$. Thus, the influence function of clip A at any point within this area could be obtained through interpolation of discrete influence functions.

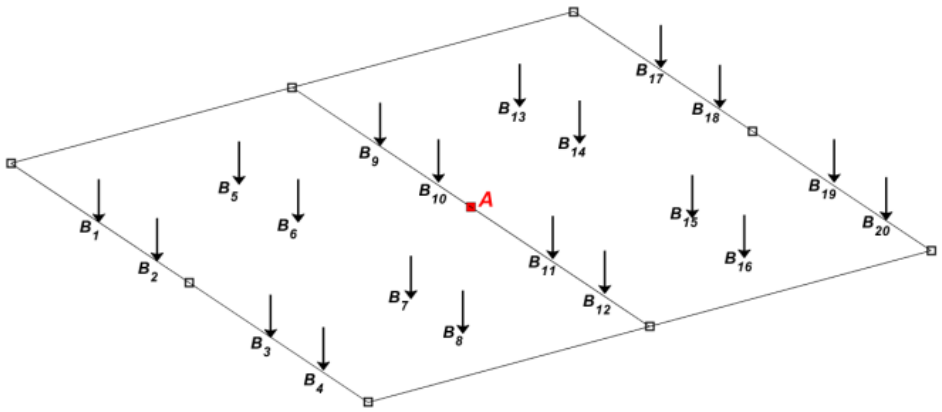

Figure 2.3: Schematic plot of clips (squares), and point load application locations (Nasiri, 2019).

Prevatt et al. (1995) used influence coefficients for evaluating clip reactions of a SSMR system subjected to uplift pressure. The influence coefficients (influence surface) were acquired by applying a series of point loads with a magnitude of 100 lbs along with a backing pressure at different locations successively, which is shown in Figure 2.4. Figure 2.5 shows the measured influence surface of the tested specimen at two backing pressures. When the applied pressure equals 0 kPa (i.e., the panel is in its flat state), the load effect contributing to the clip reaction comes at least a complete purlin span away from the clip, and influence coefficients range from 0.4 to 0.8. However, when the panels deform to a barrel-shaped configuration using a higher backing pressure, the influence coefficients decrease while the dimensions of the clip effective tributary area (i.e., the surface with nonzero influence coefficients) increase longitudinally (along seams) and decrease in the transverse (perpendicular to seams) direction (Prevatt et al., 1995). Thus, the load level has a significant effect on the effective tributary area.

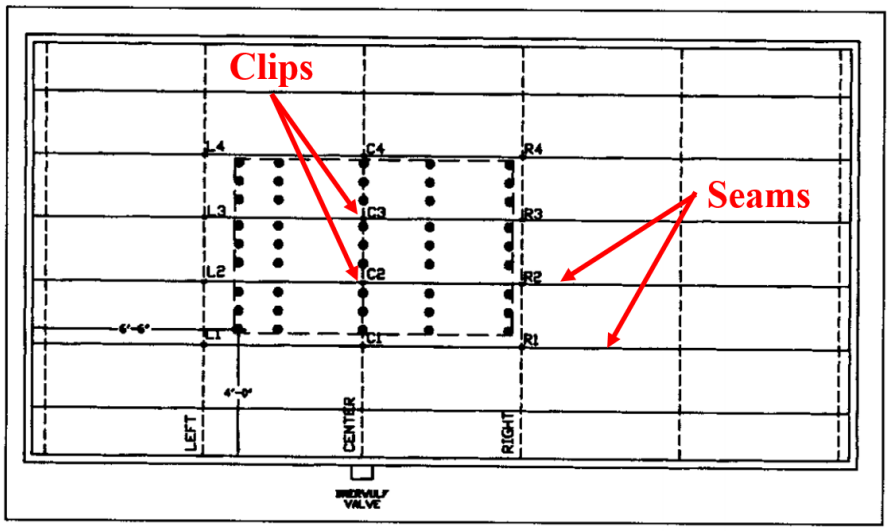

Figure 2.4: Locations of grid points for influence surface determination around clips C2 and C3 (Prevatt et al., 1995).

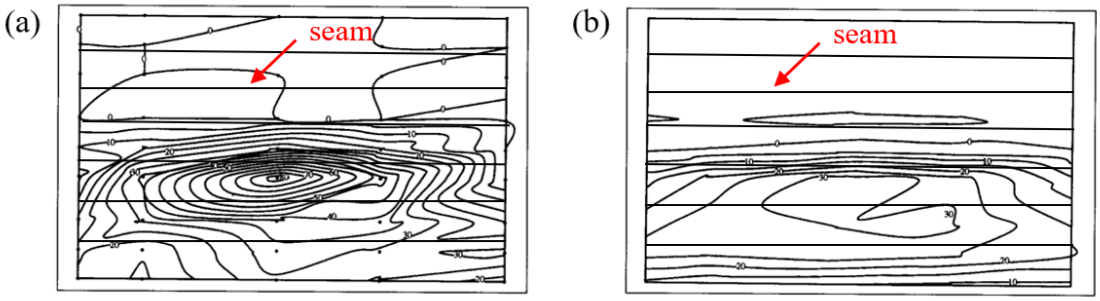

Figure 2.5: Influence surfaces for clip fasteners at C2 location with the base pressure of (a) 0 kPa (0 psf) and (b) 0.48 kPa (10 psf) (Prevatt et al., 1995).

Ho et al. (1995) used a continuous beam with simple supports to model the theoretical influence coefficients along the seam with influence coefficients decreasing linearly perpendicular to the seam. Figure 2.6 depicts the clip reaction influence surface at the first interior support (Ho et al., 1995). The clips are assumed as simple supports and the clip reaction is equal to -1 when the unit uplift load moves to that clip. For the locations on the panels away from the seam, the influence coefficients change linearly from the calculated influence coefficients on the primary seam to zero on the adjacent seam.

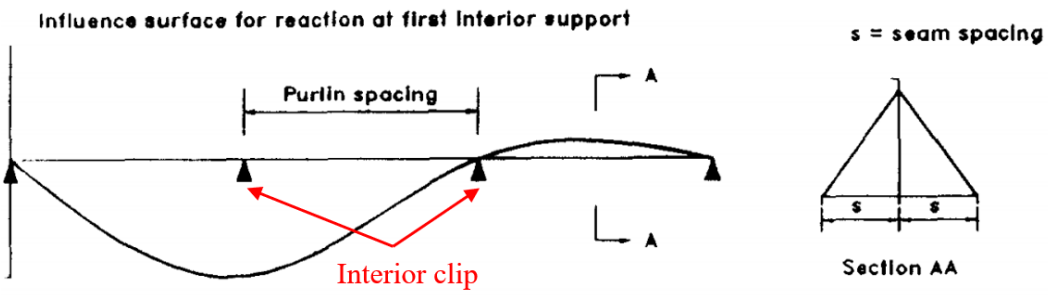

Figure 2.6: Clip reaction influence surface at interior clips used by Ho et al. (Ho et al., 1995).

Farquhar (2003) examined the influence functions of clip reactions using a simplified scale model of the SSMR system. In his model, the influence coefficients in the transfer direction are equal to the deflection of a beam due to a point load at mid-span, with the values of influence coefficients for points away from the seam decreasing linearly from the influence coefficients on the seam to zero at the adjacent seam. Figure 2.7 shows the influence coefficients for the end clips and interior clips. It is known that the constraints at clips affect the deflected beam shape. The beam deflection shapes with pinned and fixed constraints at the clips are given in the Figure as well. Farquhar concluded that the restraint provided by the clips could be assumed to be between those for pinned supports and fixed supports.

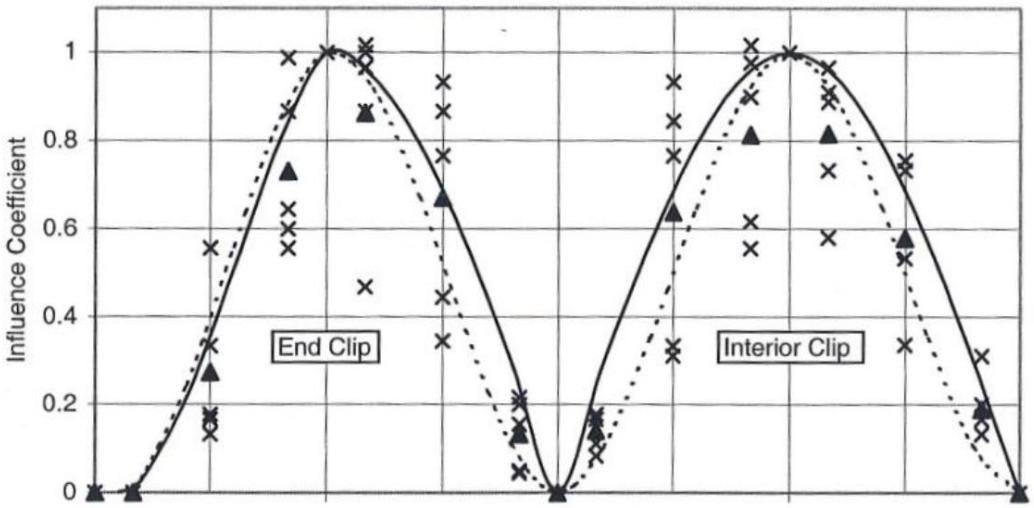

Figure 2.7: Influence coefficients for clip reactions, beam deflection shapes using pinned (-) and fixed (--) connections, individual experimental measurements (x), and the average of experimental measurements at each point (▲) (Farquhar, 2003).

Dixon et al. (2011) investigated the effect of boundary conditions on load distribution among clips. It was found that the cross restraints at the panel-end reduced clip loads in locations up to two spans or 3.0 m away from the restrained boundary. These authors determined that the geometric tributary area method for predicting the clip loads is not suitable if the clip is within two span distances from a restrained boundary.

Nasiri (2019) measured clip reaction influence functions by applying a concentrated load at 576 locations of a full-scale SSMR system, which are illustrated in Figure 2.8. Figure 2.9 depicts the measured clip reaction influence function of a type I clip. (The definitions of clip types are illustrated in Figure 2.10.) Also, by assuming the standing seam as a continuous beam supported by vertical springs, a linear analytical model was developed, as shown in Figure 2.10. A linear relationship between pressure distributions and structural responses can be considered under low wind pressures (less than 500 Pa). However, a change in the load sharing was found among the clips under higher uplift loads. Nasiri found that as pressure increases, more load transfers to the gable and eave edges of the roof.

It is believed that the restraints at the ridge and eave edge of the panel are one of the main reasons for load redistribution among clips. The geometric tributary area method underestimates the loads transfer to the edges of the roof, and more severely underestimates those to the eave edge, at the corner of the roof by around 50% (Nasiri, 2019).

To sum up, these influence function models reveal the influence coefficients on the surface of SSMR systems, which provide a direct link between the applied loads and the response at the clips. However, the load transfer through the roof edges under different load levels is still largely unknown.

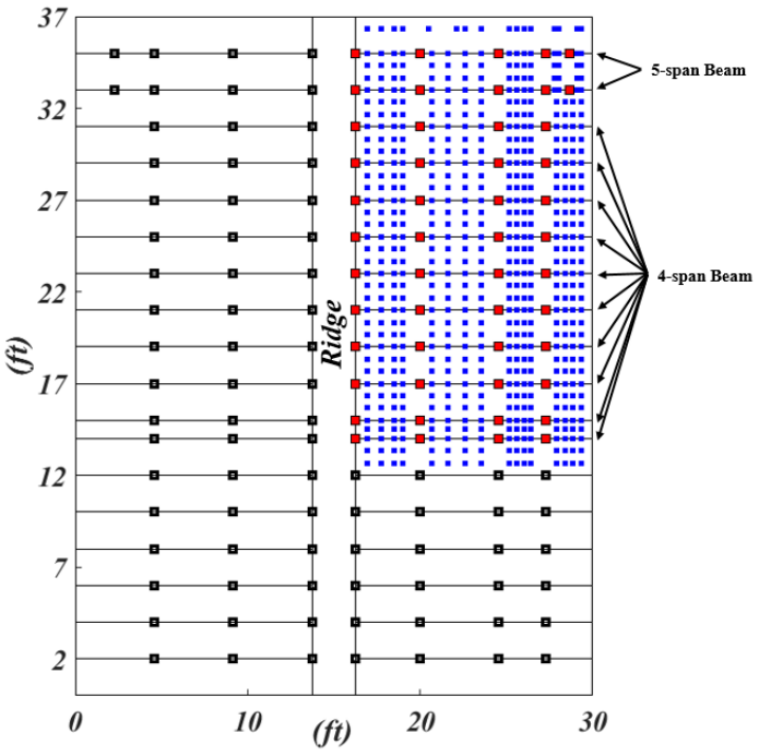

Figure 2.8: Locations of clips (black square), clip locations with installed load cells (red square) and applied point load (blue square) (Nasiri, 2019).

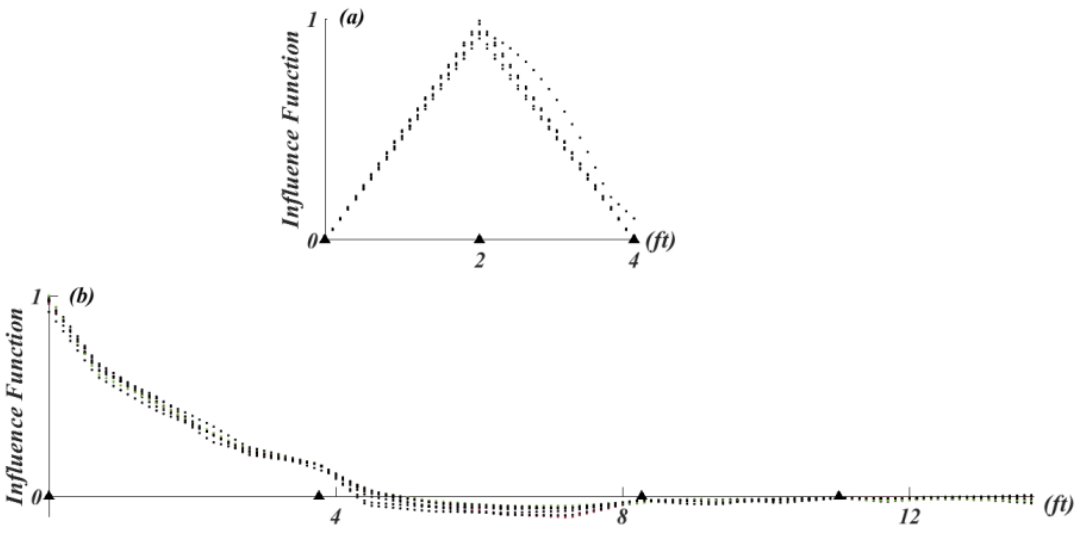

Figure 2.9: Clip reaction influence function of type I clip (a) perpendicular to the seam (b) along the seam (Nasiri, 2019).

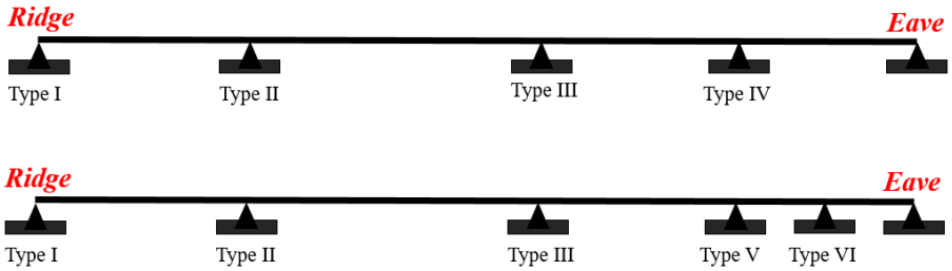

Figure 2.10: Definition of clip types and equivalent beam models of standing seams (Nasiri, 2019).

2.2.2 Limit states

Currently, the limit states of SSMR systems under severe wind loads have been mostly obtained from field survey observations and experiments. There are few analytical simulation results on the limit states of SSMR systems due to the significant non-linearities.

Scholar (1985) identified the failure mechanisms and limit states of SSMR systems, as presented in Figure 2.11. There are four distinct, discontinuous curves which represent the possible failure modes. The clip strength, clip engagement, flexural bending strength of panels, and standing seam strength are the factors that affect the load-bearing capacity and limit states of the system. It illustrates the complexity of limit states of SSMR systems due to the diversity of these failure mechanisms (Perry et al., 1990; Smith, 1995).

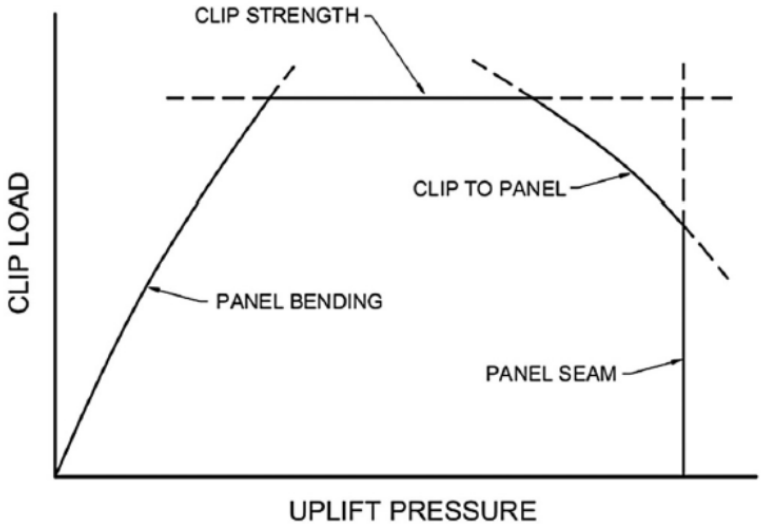

Figure 2.11: Possible limit states of uplift capacity (Scholar, 1985).

Figure 2.12 illustrates the test conducted at the Missouri Institute of Technology. The tests were conducted until failure. Figure 2.11(b) shows the seam line failure, which results from the excessive deformation of roof panels (Sinno, 2008).

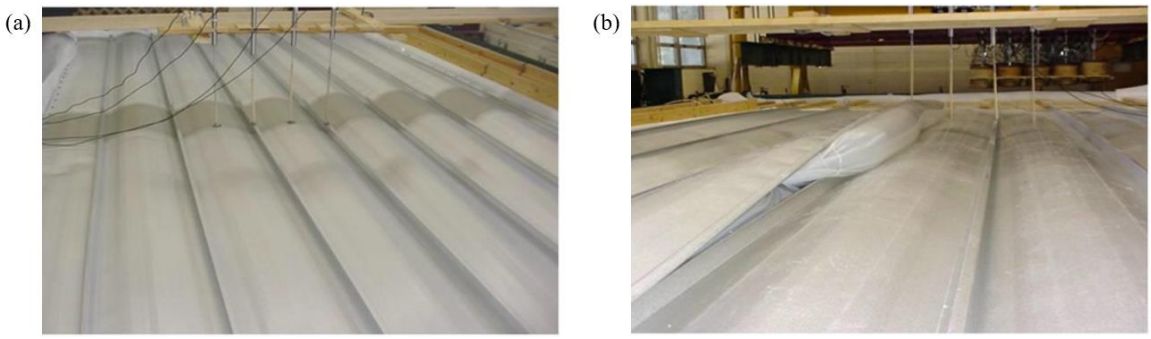

Figure 2.12: SSMR system subjected to uplift pressure: (a) roof panel during loading and (b) failure at seam lines (Sinno, 2008).

Habte et al. (2015) investigated the wind-induced roof surface pressure and roof panel deflection under realistic wind loading on a very small building in the Wall of Wind (WoW) facility at Florida International University (FIU). The failure mode observed from these experiments was seam to clip separation (Figure 2.12), which is due to excessive deflection at the seam to clip connection. The separation weakened the rigidity of the seam and led to progressive failure along the seam. As a result, seam disengagement at the clips adjacent to the separated clip was observed (Figure 2.13).

Nasiri (2019) presents the deformation of panels and clips under applied uniform pressure in Figures 2.14 and 2.15, respectively. It can be observed that the roof panels underwent considerable deformation under wind pressure. However, clips remain attached to the purlins despite seam opening at clips. Eventually, the seams buckled.

Figure 2.13: Seam to clip separation (Habte et al., 2015).

Figure 2.14: Initiation of seam disengagement (Habte et al., 2015).

Figure 2.15: Deformation of panels subjected to uplift wind loads (Nasiri, 2019).

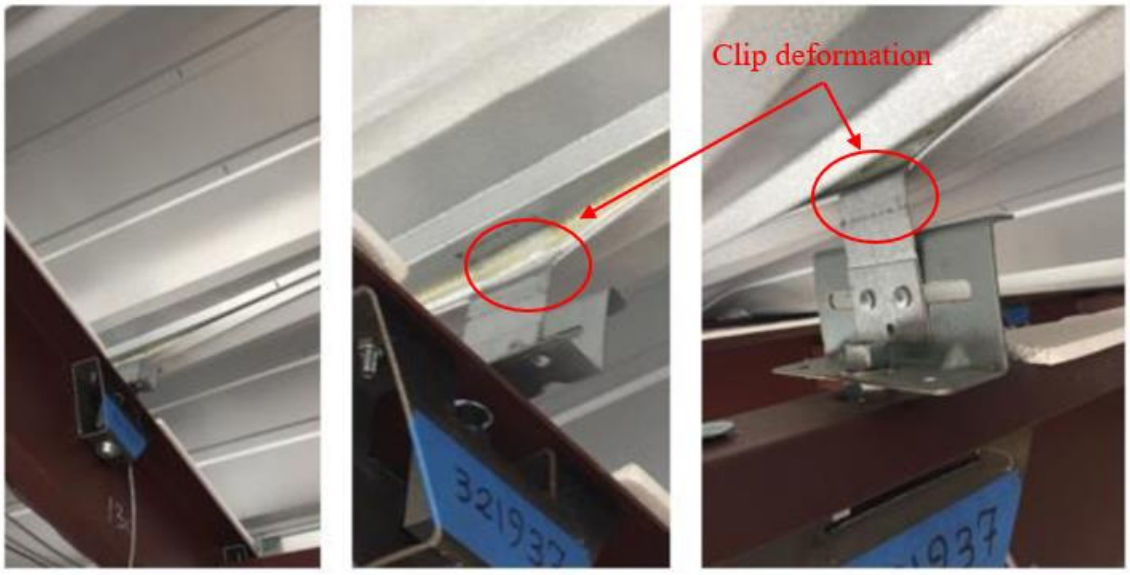

Figure 2.16: Deformation of clips (Nasiri, 2019).

2.3 Modeling approaches

As mentioned in the previous section, the panel size and boundary conditions in different standardized protocols are not consistent, which leads to the difference in structural behavior and failure modes (Kopp et al., 2010). To overcome the limitations of standardized tests, there have been some efforts to investigate the response of SSMR systems in more realistic test conditions.

2.3.1 Full-scale tests on SSMR systems

Full-scale tests are one of the most reliable methods for evaluating the performance and structural response of roof systems. Since roof components work together to resist wind loads, the structural behavior of the complete roof system is influenced by the stiffness, strength, and failure mode of each component, and the interactions between components. Full-scale tests allow one to study the global structural behavior and complex load paths of roof systems. Several loading systems have been developed to simulate the dynamic

pressure characteristics of wind loads, and thus, to investigate structural response under such simulated wind loads.

2.3.1.1 Static air pressure loading system

Schroter (1985) conducted static air pressure tests to measure the resistance of a 5-panel-wide roof sample subject to uplift wind pressure, which provides a more reliable result than mechanical pull-out tests. It was observed that the ultimate strength of SSMR systems was buckling of ribs or separation of panel seams. It was also found that the panel size plays a critical role in the performance of SSMR systems and test specimens of insufficient size would cause unconservative results (i.e., failure pressures higher than reality).

2.3.1.2 Fluctuating pressure-based loading system

The BRE Real-time Wind Uniform Load Follower (BRERWULF) test chamber was developed at the British Research Establishment (BRE) as a research tool to reconstruct the wind loading events in the laboratory (Cook et al., 1988). Its dimension is approximately 5 m x 5 m. It can be mounted to the surface of SSMR systems and enabled the application of uniform pressures or suctions in the range of up to ± 8.5 kPa. It utilized a closed-loop control system that changed the pressure in a test chamber to follow a predefined pressure sequence. Although the BRERWULF approach can only produce uniform, time-varying pressure and cannot duplicate the spatial variation of actual wind loading, it is regarded as one of the earliest efforts to evaluate the performance of SSMR systems to non-static simulated uplift pressures. Prevatt et al. (1995) investigated the roof performance and load distribution among the clips by using the BRERWULF test chamber. They used the influence surface method to investigate the load transfer mechanisms. It was found that the non-linear structural response and larger displacement of SSMR panels under uplift loads cause variation in load distribution among clips.

2.3.1.3 Electromagnetic loading system

Sinno et al. (2003) developed a loading system at Mississippi State University, as shown in Figure 2.16. They used electromagnets to apply spatially and temporally varying loads on SSMR systems. An array of electromagnets were mounted on a metal roof to reproduce the uplift pressure. The pressure trace applied on the metal roof was obtained from model-scale measurements in the wind tunnel.

However, this novel idea was an extraordinary challenge that took many years to develop. The primary problems were developing magnets with large loads, and control systems with high accuracy to apply loads equivalent to target pressures. Surry et al. (2007) conducted an experiment to match the time-history load traces from UWO wind tunnel. However, the limited resolution of applied force caused by electromagnets and unrealistic boundary conditions result in somewhat unrealistic structural dynamics.

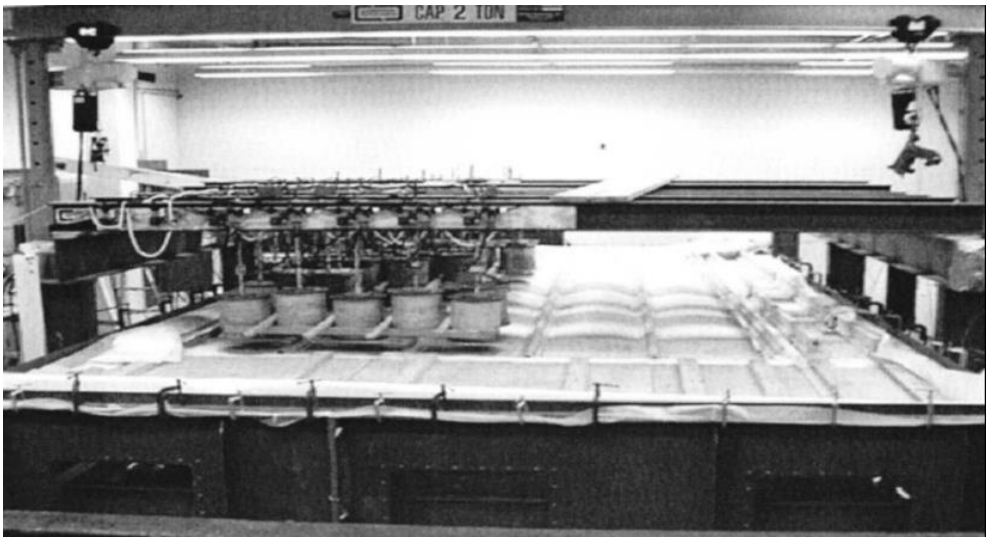

Figure 2.17: Loading system using electromagnets at Mississippi State University (Sinno et al, 2003).

2.3.1.4 Large-scale wind tunnel

The 12-fan Wall of Wind (WOW) open jet facility at Florida International University (FIU) is used to generate full-scale wind loads on small structures. Habte et al. (2015) tested two types of SSMR panels (vertical-leg and trapezoidal) with dimensions of 3.1 m by 4.6 m. The roof height was 1.5m. The profiles of these two types of SSMR panels are given in Figure 2.17. It was found that the profiles of roof panels could affect the load distribution. In addition, failure modes under uniform pressures were different from those under dynamic pressures. Since the eave height of this SSMR system was only 1.5 m, the applied wind loads did not fully replicate the true wind field on real SSMR systems (e.g., the size of the separation bubble is proportional to the building height, so it was very small in these experiments).

The Insurance Institute for Business & Home Safety (IBHS) developed an open-jet wind tunnel, which is large enough to subject one or two-story residential structures and commercial buildings with more realistic full-scale dimensions to a variety of wind conditions. As shown in Figure 2.18, 105 vane-axial fans with a diameter of 1.68 m are used to simulate the large-scale flow characteristics of the atmospheric boundary layer (Morrison et al., 2013). Morrison et al. (2015) tested the performance of a SSMR system with dimensions of 9.1 m by 13.7 m and boundary conditions under realistic wind pressures. The external wind loads on the roof and the reaction loads at clips were obtained when the roof was subjected to different wind profiles over an entire 360° wind swath at different wind speeds (25.8, 31.9, 37.8, and 44.0 m/s). They found that the deflection of the panels led to load redistribution along the length of the panel and a significant portion of the loads were transferred to the edge of the roof. The data from the IBHS full-scale wind tunnel is the most realistic data that are available for now. However, the wind speed is not high enough to observe failures of the SSMR system.

Figure 2.18: Photograph of the full-scale wind tunnel at IBHS (Morrison et al., 2013).

2.3.1.5 Pressure loading actuators

Previous pressure-based loading systems (e.g., BRERWULF) need to be applied to nominally airtight building components or segments of cladding that did not allow leakage through the components or cladding. They also could not produce pressures with high frequency. Kopp et al. (2010, 2012) developed a loading system based on "pressure loading actuators" (PLAs) at Insurance Research Lab for Better Homes (IRLBH) at University of Western Ontario (UWO). Figure 2.19 shows the components of a PLA unit. It has a blower (fan) to produce pressures, a valve to regulate the applied pressures, and a feedback control system to monitor the applied pressures (Kopp et al., 2012). Figure 2.19 also depicts the structure of the air-box which consists of a steel-framed, plywood lid, and a flexible vinyl membrane. The vinyl membrane is glued to both the lid and the surface of the specimen. The steel frame is mounted away from the surface of the specimen and attached to a steel reaction frame. The vinyl membrane allows the unobstructed movement of the structure. Each PLA unit is attached to an air-box and can apply the area-averaged, time-varying

pressure for its location on the building. Thus, the whole system can produce non-uniform fluctuating loads on the surfaces of the building.

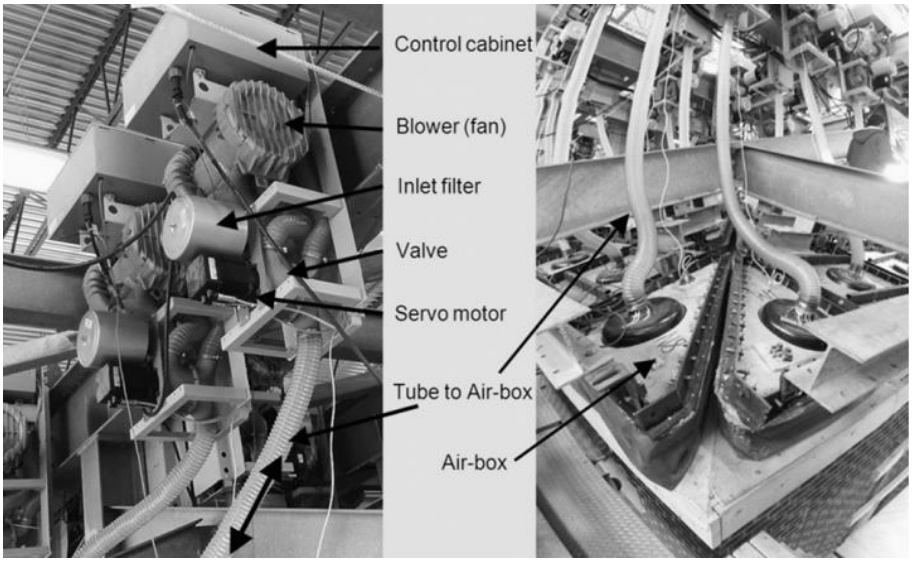

Figure 2.19: Components of a PLA unit (Kopp et al., 2012).

This system consists of up to 100 PLAs, which can apply temporally and spatially varying pressures on full-scale buildings or building components. It can simulate pressure fluctuations up to 10 Hz with the peak pressure up to 23 kPa and peak suction up to -20 kPa. It overcomes the disadvantage of the previous pressure-based systems by allowing varying amounts of leakage so that it can be applied to SSMR systems which may have leakage due to seam opening during the loading process.

Nasiri (2019) investigated the load paths among the clips of the SSMR system at IRLBH. The tested standing seam metal roof is a replica of the tested SSMR system at IBHS. However, the dimensions of the tested specimen at IBHS were 9.1 m by 13.7 m and the size of the tested specimen at IRLBH was 9.1 m by 11.3 m, which is due to the limited lab space. The findings of her study can be summarized as:

1. About 25% of the wind load transfers to the edge of the roof and only 1% of the wind load was transferred to the other side of the roof, which implies the performance of each side of the roof can be investigated separately.

2. A linear relationship between pressure distribution and structural responses was observed under low wind pressures, which is in agreement with the study of Sinno(2008). Load sharing among the clips changes with greater load transfer to the eaves of the roof due to the large deflection of panels caused by the increment of wind loads. Thus, failures at the edge of the roof should also be considered. However, industry standard test protocols only focus on the performance of the clips.

2.3.2 Computational analysis of SSMR systems

Full-scale experiments have some disadvantages, which are summarized by Gulavani (2011):

1. Cost of the test set-up, skilled technicians, and data measuring equipment is quite high.

2. Physical experiments are destructive and irreversible. However, it is hard to have an initial estimation of the results, especially for complex structures, and unnecessary experiments are inevitable. Hence, physical experiments are expensive and time-consuming.

3. The effects of variable parameters, i.e., clip spacing or panel thickness, are hard to analyze through full-scale experiments. There are limited publications that provide parametric analysis of the SSMR systems.

Due to these disadvantages of experiments, some researchers tried to model the behavior of SSMR systems using the FEM, which has produced some preliminary results of this topic. Serrette et al. (1997) put forward a simplified design method for the inelastic

behavior of SSMR systems. The effect of clip support stiffness was not considered in their work. El Damatty et al. (2003) adopted a finite element model by considering the interaction between seams and clips as equivalent springs to simplify the complexity of these components. The equivalent spring system is illustrated in Figure 2.20. The stiffness of springs was measured by component tests. The authors found that the excessive seam opening caused the failure of the connection between seam and clip.

Ali et al. (2003) conducted a three-dimensional static and dynamic finite element analysis by modeling the geometry and boundary conditions of a SSMR system. Figure 2.21 depicts the mesh of a SSMR system. Contact elements were used to simulate the interaction between seams and clips. But the type of contact was tied, which did not allow contact surfaces to separate. The experiment conducted at Mississippi State University was used to verify this model. Comparison between experiment and numerical simulation indicates that the boundary conditions, the contact between roof components, and geometric and material nonlinearities are needed in numerical simulations to improve the computed deflections of roof panels. Mahaarachchi et al. (2009) proposed a model to study the crest-fixed trapezoidal steel cladding, which included the new splitting criterion, geometric imperfections, buckling effects, and contact modeling. The design strength was obtained.

Liu et al. (2014) investigated the total torsional rigidity provided by the panel, clip, and purlin using experiment and numerical simulation separately. The factors that affect the total torsional rigidity were obtained. Song (2017) proposed a finite element model to simulate the failure modes and load-bearing capacity of full-scale SSMR systems under uniform loading. It was assumed that the relative sliding between adjacent roof panels or between roof panels and clips was small and the nodes between adjacent roof panels and between roof panels and clips were coupled.

To sum up, previous researchers usually simplified the structure near the seams by replacing clips with equivalent springs or coupling the nodes near the seams. While much

has been learned from these studies, these kinds of simplifications cannot model the exact deflection near the seams and may result in unrealistic failure modes.

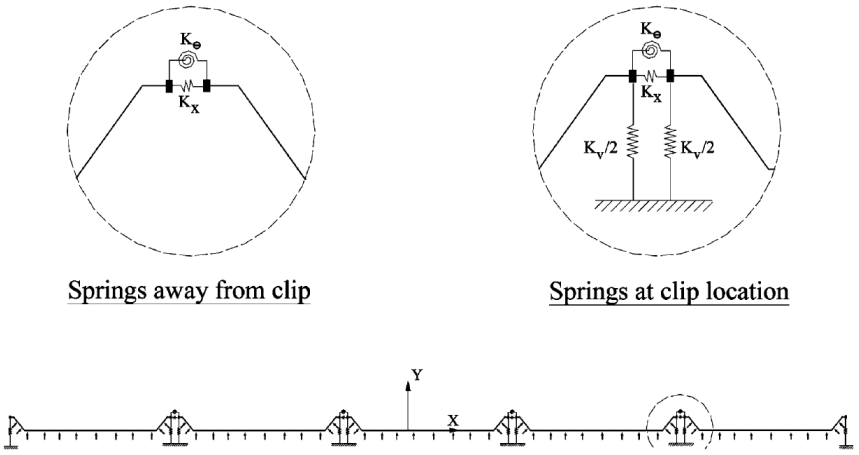

Figure 2.20: Equivalent spring system (El Damatty et al., 2003).

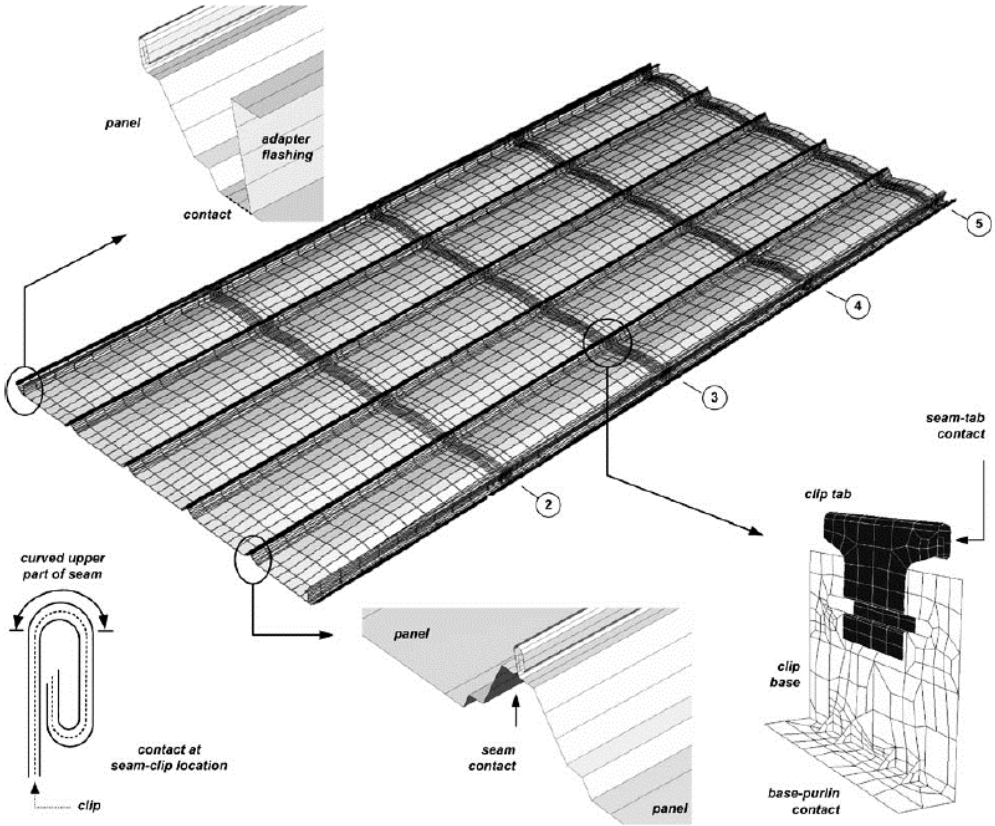

Figure 2.21: Finite element mesh (Ali et al., 2003).

2.3.2.1 The major steps in FEM

The principle of the FEM is to replace a continuous region with several subdomains in order to calculate the forces and displacement in the domain. Each subdomain has a finite number of unknowns and interpolation functions are used to represent the unknowns within the subdomains. Thus, the original problem, with an infinite number of degrees of freedom, can be modeled as a problem with a finite number of degrees of freedom (Prathap, 2013).

Finite element analysis of a problem includes the following basic steps:

1. Discretization the continuous domain;

2. Selection of the interpolation functions to provide an approximation of the unknown within subdomains;

3. Formulation of the equilibrium equation of static analysis, which can be written as;

$$[K] \times \{u\} = \{F\} \tag{2.8}$$

where $\{F\}$ is the vector of nodal loads, $[K]$ is the stiffness matrix, and $\{u\}$ is the vector of nodal displacements. For dynamic analysis, the governing equation is written as;

$$[M]\{\ddot{u}\} + [C]\{\dot{u}\} + [K] \times \{u\} = \{F\} \tag{2.9}$$

where $[M]$ is the mass matrix, $[C]$ is the damping matrix, $\{\ddot{u}\}$ is the vector of nodal accelerations, and $\{\dot{u}\}$ is the vector of nodal velocities.

4. The solution of the equilibrium equation.

Implicit analyses solve the nodal displacements, $\{u\}$, through matric inversion. In the nonlinear implicit analyses, the solution of each step requires a series of iterations to achieve equilibrium within a certain tolerance. The implicit analyses are unconditionally stable and facilitate larger time steps.

In contrast, in explicit analyses, the nodal accelerations $\{\ddot{u}\}$ are solved directly and no iteration is required. Once the accelerations are calculated at a certain step, the displacements at the next step can be calculated accordingly. The explicit analyses are not unconditionally stable and, thus, tiny time steps are required (Ortiz et al., 1986). Explicit analyses, in general, are time-consuming due to the smaller time steps. However, explicit analyses handle nonlinearities (e.g., geometric, contact, and material nonlinearities) with relative ease when compared to implicit analyses (Rust et al., 2003).

In the nonlinear analyses, the stiffness matrix, $[K]$, depends on the geometry, material properties, and contact. When a structure deforms under a load, its stiffness changes. For linear analysis, it can be assumed the stiffness of the structure remains constant throughout the entire process of loading. This assumption greatly simplifies the problem since the equation will be solved only once. However, for non-linear analysis, the stiffness of the structure changes due to the large deformations or plastic strain of the material. The stiffness matrix must be updated during the iterative solution process, which increases the computational time. Modeling the response of SSMR systems is quite complex since it is a highly non-linear problem. All three types of non-linearities, i.e., contact, material, and geometric non-linearities, should be considered during the analysis. The description of three different non-linearities is given below (Belytschko et al.,2013).

Geometric non-linearity

Geometric non-linearity is related to the change of the stiffness matrix and arises from changes in the shape of the structure under loading. The geometric non-linear analysis will update the stiffness matrix based on the nodal displacement at each equilibrium iteration. In addition, if the changes in stiffness are sufficient to cause the structure's stiffness to drop to zero, buckling occurs and the structure experiences a rapid deformation. It then either falls apart or acquires a new stiffness in its post-buckling state.

Material non-linearity

A linear material model assumes stress to be proportional to strain and no permanent deformation occurs. For non-linear material, the relationship between stress and strain is no longer linear. There are various types of non-linear material models. The elasto-plastic material is commonly used for engineering materials. A typical stress-strain curve of elastoplastic material is illustrated in Figure 2.22. The material behaves elastically below the yield point and strain below the yield point is reversible. When the load is further increased, the material will undergo plastic deformation.

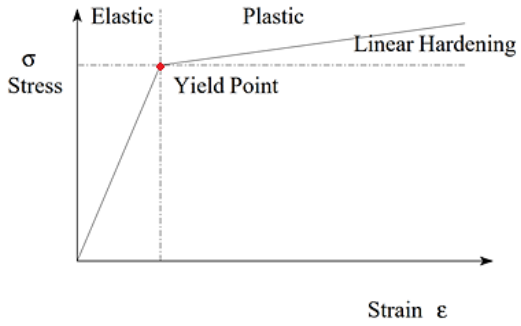

Figure 2.22: The stress-strain curve of elatoplastic material (Roylance, 2001).

Contact nonlinearity

Contact nonlinearity occurs between two contacting surfaces. The status, normal contact forces, and sliding friction between two contacting parts changes throughout the process of contact. Figure 2.23 shows the schematic of a contact problem. There are two individual parts: master and slave surfaces. As two surfaces are in contact, the displacements on the contact boundary are limited such that they cannot penetrate each other. At the same time, it is usually unknown which part of the surface will be in contact. As the contact boundary varies, the contact force on the boundary also varies. Thus, in the contact problem, both the contact boundary and contact forces are unknown.

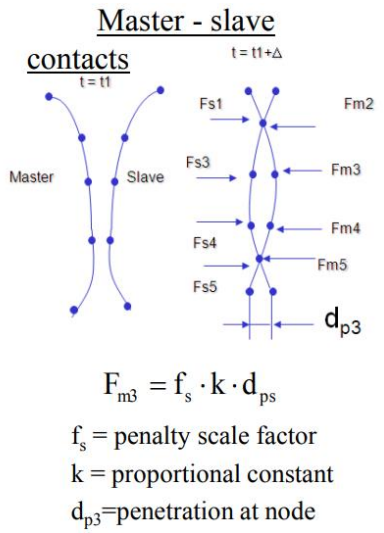

Figure 2.23: schematic of a contact problem (Belytschko et al.,2013).

2.3.3 Database-Assisted Design (DAD)

Database-assisted design (DAD) is a time-domain technique for estimating structural reactions due to spatio-temporal varying wind loads on structures, which integrates wind tunnel data with structural analysis. There are two inputs needed for DAD: (1) aerodynamic information and (2) structural information. Aerodynamic information is typically provided by an aerodynamic database (e.g., NIST database) containing wind tunnel pressure time histories for various building types and geometries (Main and Fritz, 2006). Structural information generally requires influence coefficients. Using these inputs, the DAD methodology can produce time histories of reaction loads (Simiu et al. 2003). For each wind direction and specified wind speed, internal forces induced in members are calculated using the influence coefficients multiplied by the effective wind loads.

The calculations of DAD are performed in the time domain, the superposition of wind loads acting on different locations of the building could be considered directly, which is not performed in the frequency domain (Simiu, 2011).

DAD methodology for the design of low-rise buildings was first proposed by Simiu and Stathopoulos (1997). The first DAD software was developed by the National Institute of Standards and Technology (NIST) (Whalen et al., 1998). Gupta and Limkatanyoo (2008) conclude that the DAD approach would provide risk consist design, meaning the level of risk or probability of failure are consistent for different building types, building materials, or loading conditions.

2.3.3.1 NIST Aerodynamic Database

The NIST aerodynamic database was a part of the "NIST/TTU Cooperative Agreement—Windstorm Mitigation Initiative", which was used to create a database providing time series of wind load data on low rise buildings (Ho et al., 2005). Wind tunnel tests were conducted in the UWO Boundary Layer Wind Tunnel in the early 2000s. The cross-section of the UWO wind tunnel is 11 ft wide and the height varies between 6 ft and 9 ft. Two prototype roughness lengths z_0 = 0.03 m and z_0 = 0. 29 m were adopted to simulate open and suburban exposures, respectively. The turbulence intensities at 10 m (in prototype) were 0.18 and 0.25 corresponding to the open and suburban exposures, respectively. The NIST aerodynamic database includes a series of rectangular-shaped, low-rise buildings with various eave heights, plan dimensions, and roof slopes. The geometric scale of the tested models was 1:100, and the time scale was approximately 3:100. A tested model with pressure taps on the surface is shown in Figure 2.24. Each of the models was tested in both open terrain and suburban exposures for 37 wind directions in 5° increments. The sampling frequency of pressure data was 500 Hz and the test duration was 100 s. More information regarding the NIST aerodynamic database can be acquired from Ho et al. (2003a; 2003b), and Ho et al. (2005). Detailed analyses of these data can be found in St. Pierre et al. (2005), Simiu et al. (2003), Kopp and Morrison (2018), Wang and Kopp (2020), amongst others.

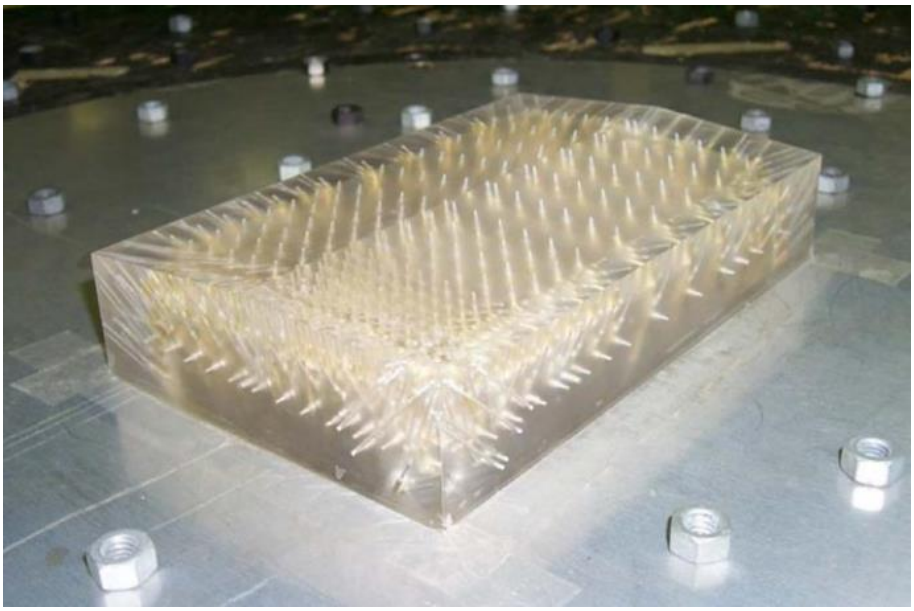

Figure 2.24: UWO Boundary Layer Wind Tunnel Building Model (Ho et al. 2003a).

2.4 Summary

The performance of SSMR systems has been studied over the past few decades by several different methods. Wind tunnel testing can provide detailed information about the wind loads on the roof but it prevents consideration of the performance of all the details of roof systems. Damage surveys can give us valuable information of failure modes of SSMR systems during severe wind events but cannot tell us how the failures initiated and progressed, or what the failure loads were. Standardized tests have provided the failure loads, but the results are difficult to interpret due to the unrealistic wind loads, boundary conditions, and dimensions of the specimen.

Full-scale experiments offer the opportunity to better understand the load transfer mechanisms on SSMR systems. The influence functions of clip reactions provide an approach to estimating the wind-induced loads on roof components. The influence of boundary conditions on load sharing and induced loads on clips is still not clear.

Computational analysis can be used to examine the behavior of roof components and the performance of SSMR systems at a relatively low cost. However, there is limited research on the limit states of SSMR systems due to the complexity.

This SSMR system was previously utilized and built by Nasiri (2019) to investigate the response of the SSMR system under temporally and spatially varying pressures. The work of the thesis is based on her experiment and goes a step further. The failure modes of SSMR systems subjected to uplift wind loads were obtained. The influence of the boundary conditions on the performance and load sharing of roof systems, especially near the limit state was investigated.

For the current study, replicating the same SSMR system as IBHS experiments at Insurance Research Lab for Better Homes (IRLBH), provided the opportunity to investigate the performance of the roof components, load sharing among them, and the influence of panel deformation on load sharing. On the other hand, FEM is adopted by considering different non-linearities to study the wind-resistant performance of the roof systems, especially the wind-induced failure modes and ultimate bearing capacity.

3. Full-scale experimental approach

A full-scale SSMR system was built in the Insurance Research Lab for Better Homes (IRLBH) of the University of Western Ontario. This roof is a full-scale replica of the one used in the Insurance Institute for Business and Home Safety (IBHS) experiments (Morrison et al., 2015). The loading approach used in this study is to apply the pressure field directly to the full-scale building surface. In other words, it is the wind effects that are replicated. The pressure field can be applied directly to building surfaced through the use of pressure chambers with pressure loading actuators.

3.1 Details of SSMR system tested at IRLBH

The tested SSMR system has plan dimensions of 9.1 m (30 ft) by 11.3 m (37 ft), and a roof slope of 1/4 on 12. The metal panels have a width of 0.61 m (2 ft), while a single panel in the middle of the roof had a width of 0.3 m (1 ft). Figure 3.1 illustrates a schematic of the purlin layout and clip locations, as well as the arrangement of pressure chambers. On the left side of the ridge in the Figure, there are 3 purlins evenly spaced at 1.4 m (4 ft 7 in) intervals. On the right side of the ridge, there are 4 purlins with spacing ranging from 0.83 m (2 ft 9 in) to 1.4 m (4 ft 6 in). In addition, a structural enhancement was installed in the corner, which consists of a 1.5 m (5 ft) long purlin to provide additional clip locations to strengthen the roof.

The details of the roof panel and clips are given in Figures 3.2 and 3.3, respectively. Due to the smaller available lab space, the roof size of experiments at IRLBH is 9.1 m (30 ft) by 11.3 m (37 ft), while the tested SSMR system at IBHS had dimensions of 9.1 m (30 ft) by 13.7 m (45 ft). The arrangement of panels and clips remained the same as in the IBHS experiment despite the smaller size. Also, the clips are numbered based on those used for the IBHS tests. There were 130 clips on the tested SSMR system in IRLBH.

The tested roof system was designed and provided by NCI Building Systems. All the details of the installation requirements of the SSMR system can be found in MBCI (2021). The installation of edge restraints is shown in Figure 3.4. Figure 3.4(a) depicts the attachment of the panel at the gable edge. Fasteners are screwed to the rib of the panel and top flange of the rake support. Then, the rack support is fixed to the purlin with fasteners. For the restraints at the eave edge, as shown in Figure 3.4(b), fasteners are used to attach each panel to the top of the eave plate and several fasteners are used to attach the eave plate to the purlin. At the ridge edge of the roof system, a back-up plate beneath the ridge cap is attached to the panel through fasteners, as shown in Figure 3.4(c).

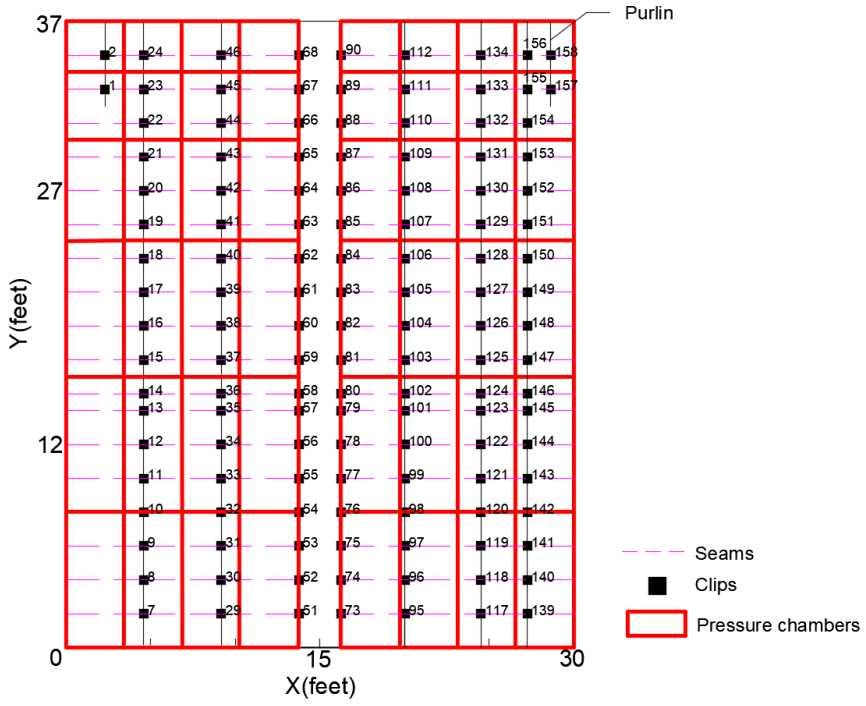

Figure 3.1: Plan view of the locations for purlins (black lines), clips (black squares), and arrangement of pressure chambers (red lines) on the test SSMR system.

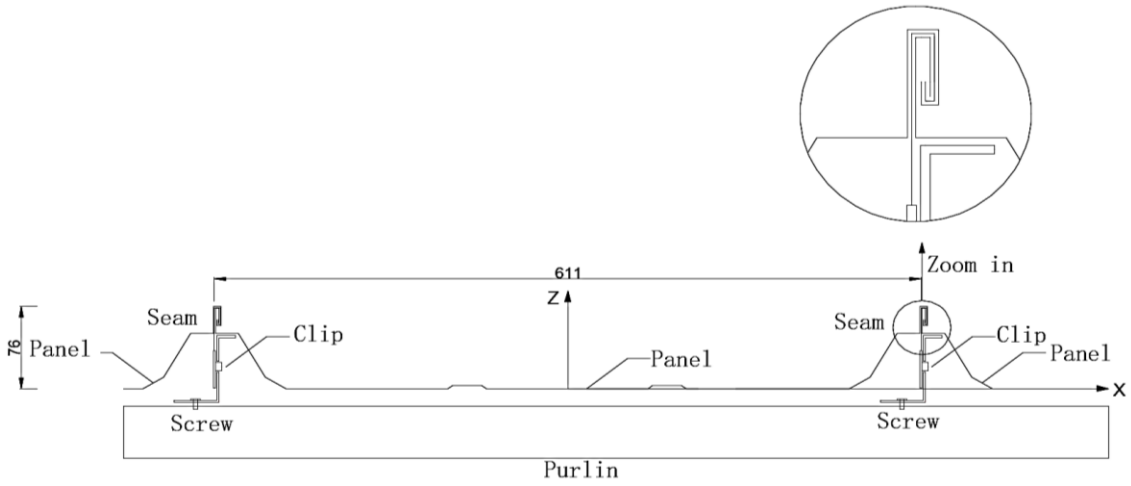

Figure 3.2: Cross-section of roof panel (Unit: mm)

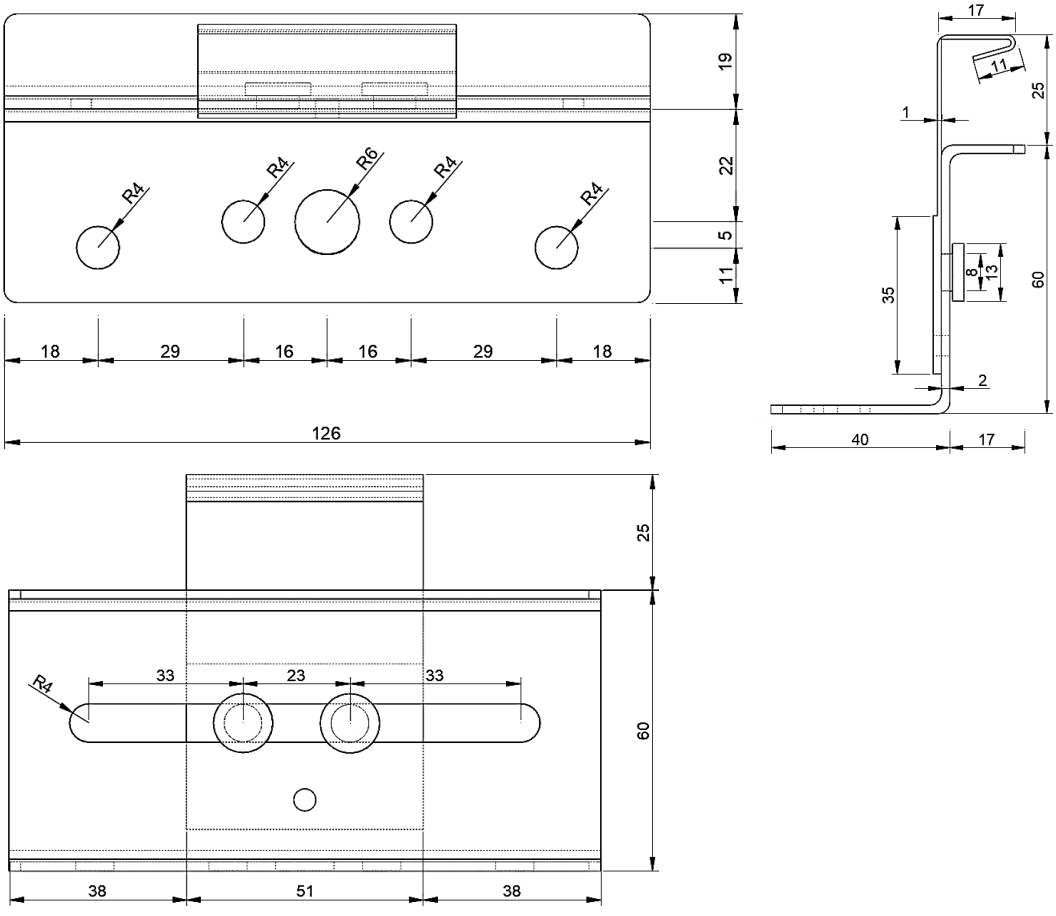

Figure 3.3: Dimension of standing seam clips (Unit: mm).

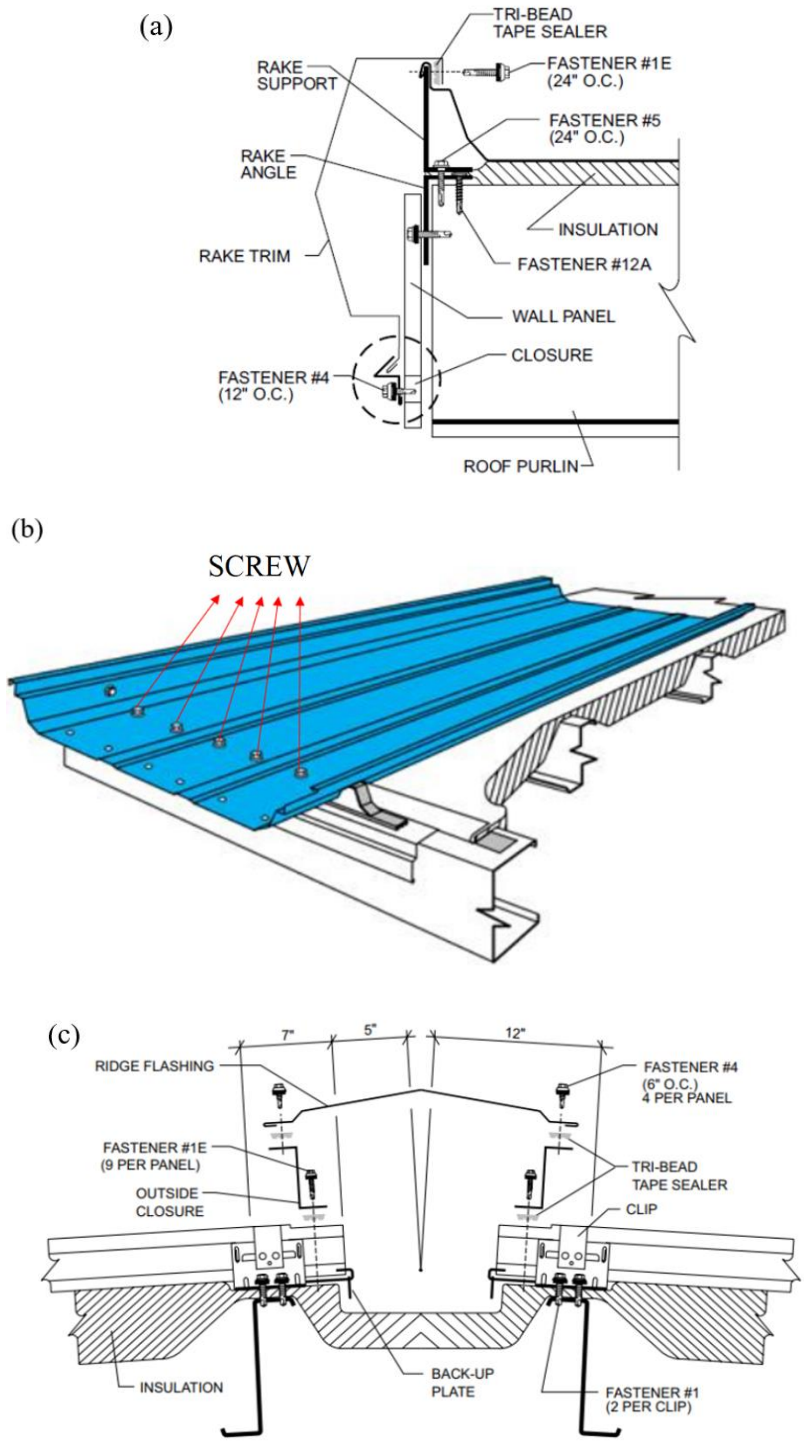

Figure 3.4: Edge restraints of the roof at (a) gable edge, (b) eave edge, and (c) ridge edge (Nasiri, 2019).

3.2 Pressure loading system

The pressure loading actuators (PLA) were used as the loading system for the current experiments at IRLBH. These were designed by Cambridge Consultants Ltd, Cambridge, U.K., under the supervision of UWO (Miller et al., 2017). A three-dimensional drawing of a pressure loading actuator (PLA) unit is provided in Figure 3.5. The blower (fan) is used to generate the required pressure rise and flow rates while a rotating disk inside the valve assembly together with the servo motor could regulate the applied pressure. Details can be found in Miller et al. (2017).

Figure 3.6 depicts the set-up of pressure loading actuators. A hose was used to transmit the pressure from the PLA to the pressure chamber. Figure 3.7 shows the installation of the pressure chambers on the roof. The structure of the pressure chamber consists of a steel-framed, plywood lid, and flexible vinyl membrane side walls. A steel frame is mounted away from the surface of the specimen and attached to a steel reaction frame. The vinyl membrane is glued to both the lid and the surface of the specimen. The vinyl membrane allows the unobstructed movement of the roof system. The vinyl was taped around the attachment with the roof to prevent leakage. A pressure transducer is placed in each pressure chamber and is used for monitoring and controlling the pressure inside each chamber. This ensured that the applied load traces match the predefined load traces. For these experiments, 48 pressure chambers, of four different sizes, were installed on the roof, as depicted in Figure 3.1. Figure 3.8 also shows a sketch of the layout of the pressure chambers on the roof, while the dimensions of the pressure chambers are provided in Table 3.1. Each PLA unit can supply an area-averaged pressure trace for its location. Thus, the whole system can produce non-uniform fluctuating loads on the roof.

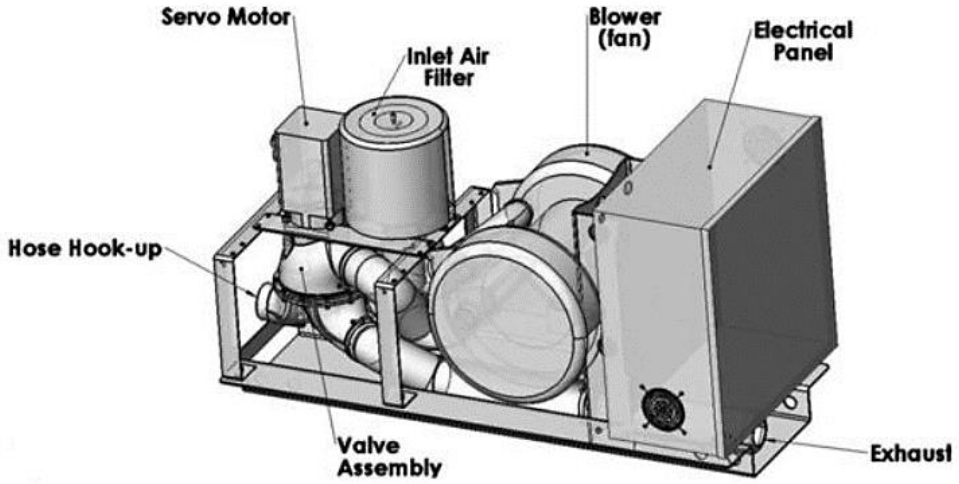

Figure 3.5: Three-dimensional drawing of pressure loading actuator (Kopp et al., 2010).

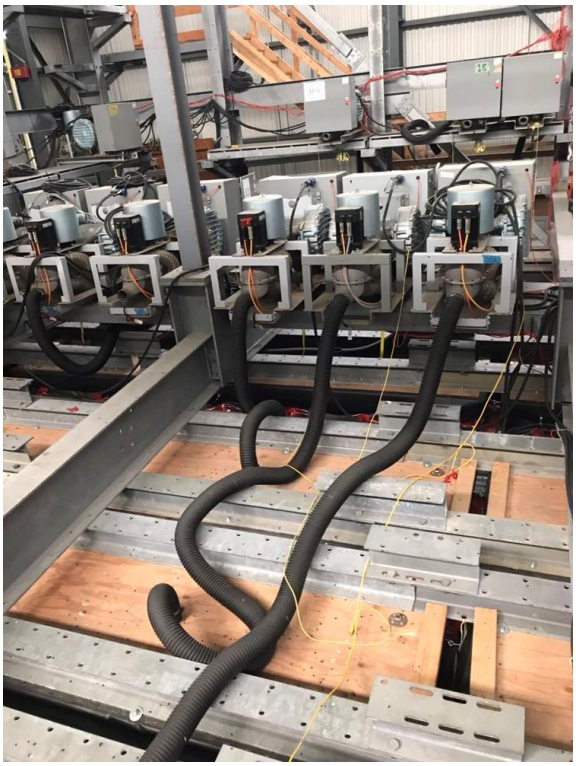

Figure 3.6: Setting up the Pressure Loading Actuators (PLA).

Figure 3.7: Installing pressure chambers.

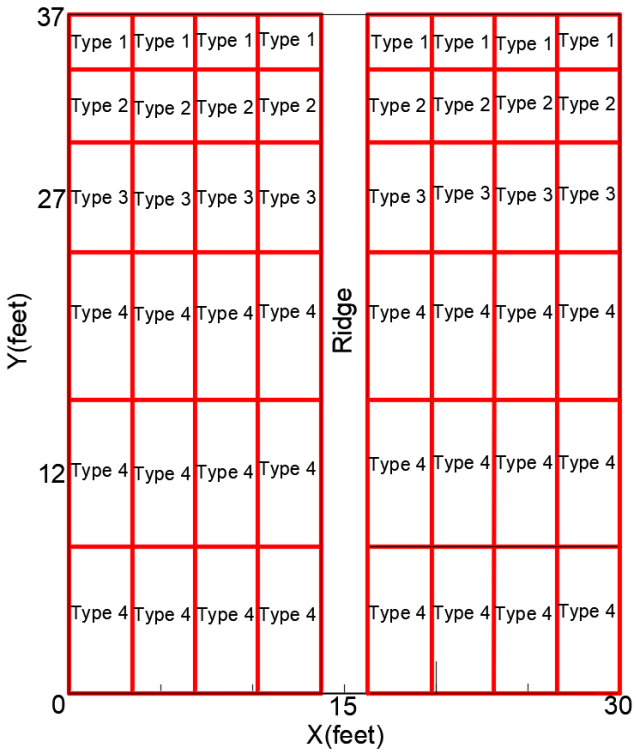

Figure 3.8: Locations of 48 pressure chambers with different sizes on the tested roof.

Table 3.1: Dimensions of the installed pressure chambers

Pressure Chamber Type	Dimensions
1	1.05 m x 0.92 m (3.44 ft x 3 ft)
2	1.05 m x 1.22 m (3.44 ft x 4 ft)
3	1.05 m x 1.83 m (3.44 ft x 6 ft)
4	1.05 m x 2.44 m (3.44 ft x 8 ft)

3.3 Measurement equipment

Loads at the clip locations are measured using load cells. A strain gauge sensor within the load cell measures the strain change, which is proportional to the load. The load is converted into an electrical signal that was recorded for further processing by MATLAB. Similar to the IBHS experiments, clip reaction measurements at IRLBH adopted S-shaped load cells (LC), which only measure forces in the vertical direction. Both compression and tension could be measured by S-shape load cells. A photo of an S-shaped load cell is provided in Figure 3.9.

For a typical installation, the clip is screwed to the purlin. However, the installation of the clips was changed to install the load cells, which was developed by IBHS. The detailed installation of a clip with a load cell is illustrated in Figure 3.10. The clip was bolted to the load cell with a space between the clip and the purlin, which can measure the loads from clip to purlin directly.

As shown in Figure 3.11, the displacements of the panels are measured using linear variable differential transformers (LVDTs). Both the LCs and LVDTs were measured at a sampling

rate of 100Hz. The maximum measuring range of LCs is 10000 N with an accuracy of ± 10 N. The maximum measuring range of LVDTs is 100 mm with an accuracy of ±0.75 mm.

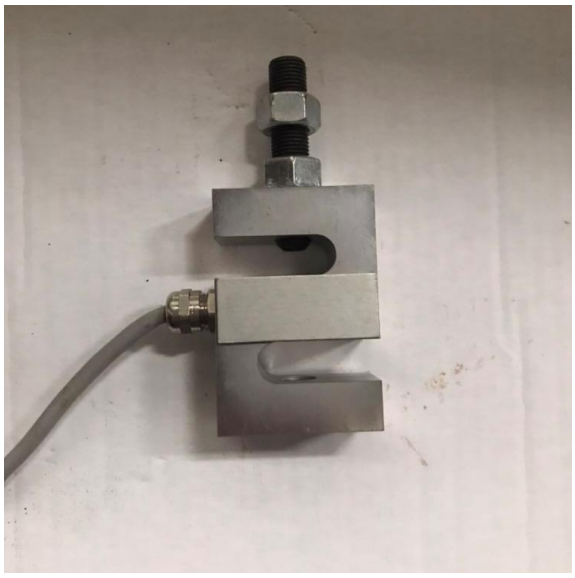

Figure 3.9: Photo of the S-shape load cell.

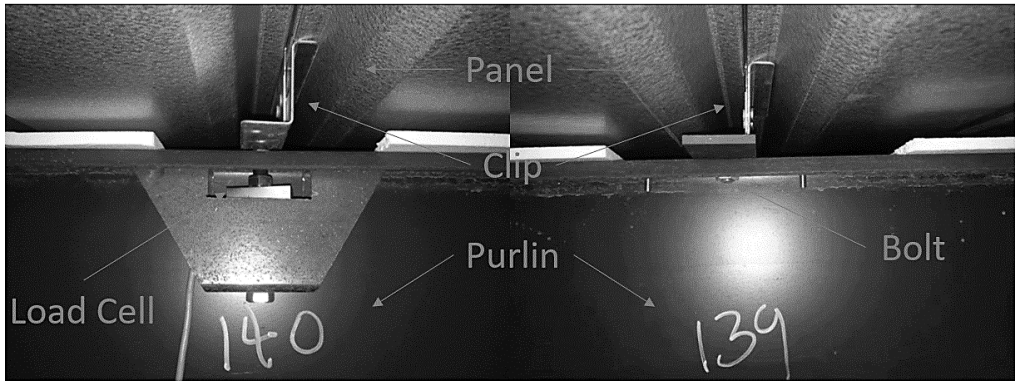

Figure 3.10: (Left) Clip installation with a load cell. (Right) Clip installation without the load cell.

Figure 3.11: Photo of the LVDT.

3.4 Validation of pressure loading and response measurement of the SSMR system

When the roof is subjected to pressure, load transfers to the clips and the edges of the roof. The total applied loads on the tested roof can be calculated by multiplying the applied pressure by the tributary area of the pressure chamber. In addition, loads transferred to the clips could be measured by the load cells. Nasiri (2019) showed that when there are no pressure chambers on the edges, all of the applied load could be measured. However, when there are pressure chambers on the edges, a portion of the load transfers to the roof edge, which is not instrumented. Thus, to validate load measurements using installed load cells, only the pressure chambers away from the edges can be used for applying pressure. The reader is referred to Nasiri (2019) for details.

Nasiri (2019) also showed that very little load was transferred across the ridge. Here, we examine the proportion of load taken by screw fasteners at the ridge. Figure 3.12 depicts the locations of the pressure chamber while induced loads are measured using the installed

load cells. A uniform pressure with a magnitude of 300 Pa was applied to the area of the specific pressure chamber. The comparison between the total applied loads and the total measured loads are given in Figure 3.13. The ratio of the measured load to total applied loads shows how much of the applied load is measured by installed load cells. It can be seen that 97.96% ± 0.33% of the total loads were measured by load cells. In other words, almost all the applied loads were measured by the installed load cells. Thus, the screws at the ridge take very little of the load, roughly 2% of that taken by the adjacent clips.

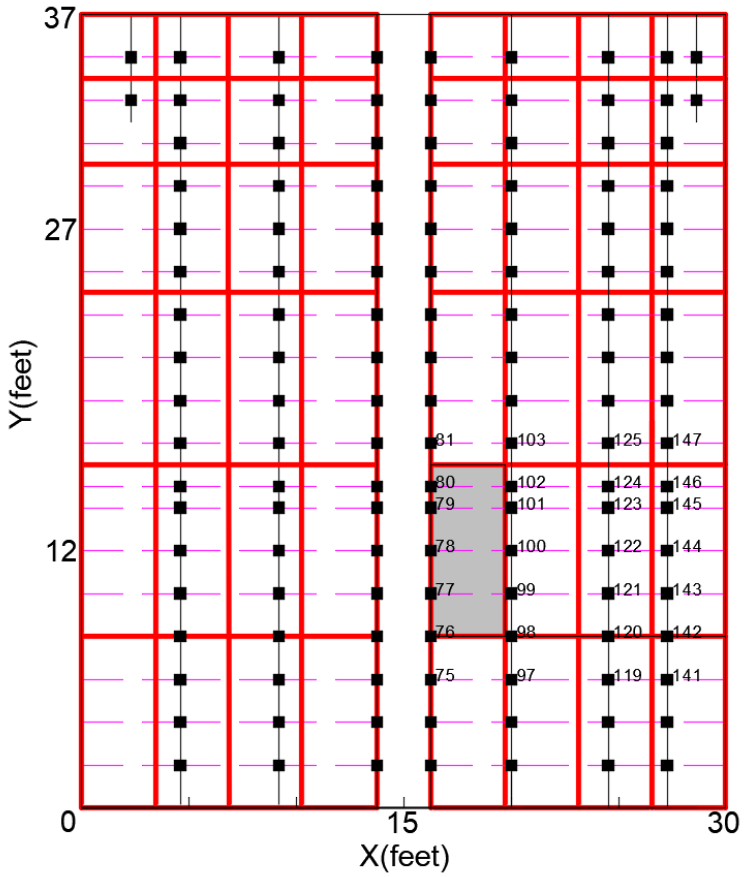

Figure 3.12: Locations of the pressure chamber used to apply uniform wind load.

The ratio of the measured loads on each clip to the total applied loads is calculated and provided in Table 3.2. It is noted that clip76 to clip80, clip98 to clip102, and clip120 to clip124 took most of the applied loads. Even though clip120 to clip124 are away from the

pressure chamber, the loads transferring to these clips cannot be ignored, as discussed in chapters 1 and 2.

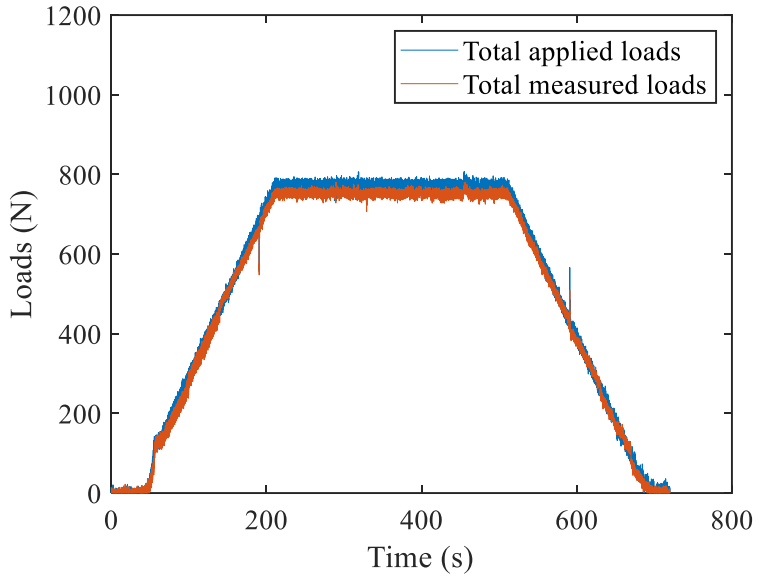

Figure 3.13: Comparison between total applied load and total measured load.

Table 3.2: Mean values of clip load ratios

Clip #	Ratio %	Clip #	Ratio %	Clip #	Ratio %	Clip #	Ratio %
81	0.94	103	0.24	125	0.12	147	-0.03
80	9.44	102	4.95	124	1.91	146	-0.32
79	10.08	101	5.45	123	1.73	145	-0.39
78	12.82	100	7.59	122	3.23	144	-1.25
77	14.34	99	8.87	121	3.57	143	-0.81
76	7.77	98	4.91	120	1.61	142	-0.33
75	0.85	97	0.41	119	0.23	141	0.03

3.5 Loading cases

Nasiri (2019) measured clip reaction influence functions by applying a concentrated load at 576 locations and using load cells at 50 clips. As shown in Figure 3.14, it can be observed that the influence functions on locations away from two adjacent panels are about zero. The result showed that the majority of the load at a clip comes from the two panels directly connected to that clip. In other words, loads only affect clips at adjacent seams. Thus, only partial roof areas were used in this study, which could save time and cost.

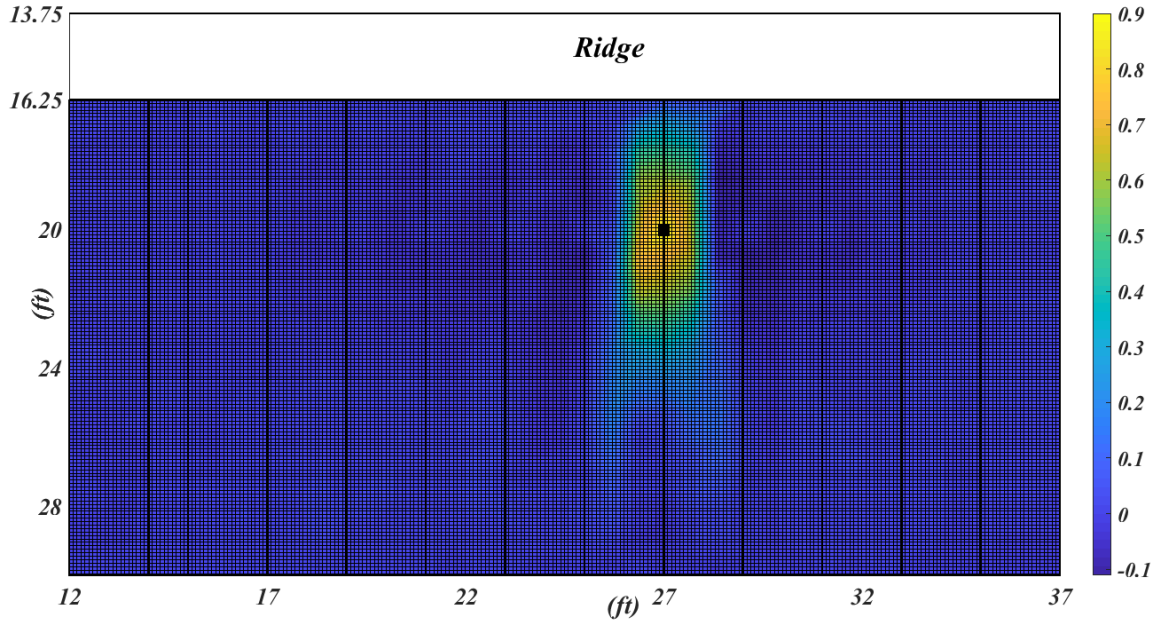

Figure 3.14: Measured influence function of a type II clip (black square) over the area subjected to the concentrated load (Nasiri, 2019).

As mentioned, these experiments are concentrated on understanding the load sharing among the components of SSMR systems. These experiments are based on the experiments of Nasiri (2019) and take a step further, which gives a fundamental understanding of the load paths and structural behavior of SSMR systems up to the limit state.

As shown in Figure 3.15, uniform pressure was applied on four pressure chambers and increased linearly until the permanent deformation of panels. To avoid the effect of the damaged roof, the following experiments should keep at least one panel wide away from the damaged roof panel. Three experiments were carried out with uniform pressures applied on the roofs. The pressure chambers and corresponding loading trace of each experiment are given in Figure 3.16, Figure 3.17, and Figure 3.18, respectively. The pressure chambers in each experiment are filled with grey in these Figures.

In order to investigate how load sharing on SSMR changes under high pressure and due to the panel deformation, applied pressure increases linearly until the failure of the SSMR for experiment 1, as shown in Figure 3.16. A loading rate of 0.5 kPa/min was chosen, which could be regarded as a static loading process.

In order to investigate how load sharing on SSMR near gable end changes under varying pressure, the pressure is applied on the tested roof successively in 0.25 kPa increments and the loading rate is 0.5 kPa/min for experiment 2, as shown in Figure 3.17. The pressure is maintained for 30 seconds at each increment. This process is continued until failure.

To investigate the effect of dynamic pressure on failure modes of SSMR, dynamic pressure was applied on SSMR using 4 pressure chambers for experiment 3, as shown in Figure 3.18. Time histories of applied load contain several segments and the duration of each segment is 60 seconds. The first 60-second segment of time-history pressure trace comes from IBHS data with a mean value of 0.5 kPa. The following segments were obtained by multiplying the first segment by 2, 3, 4, 5, and so on. This process was continued until failure.

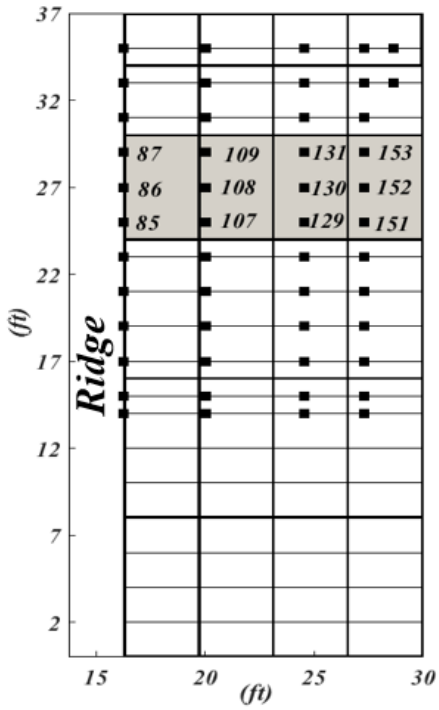

Figure 3.15: Locations of clips with installed load cells (black square) and used pressure chambers.

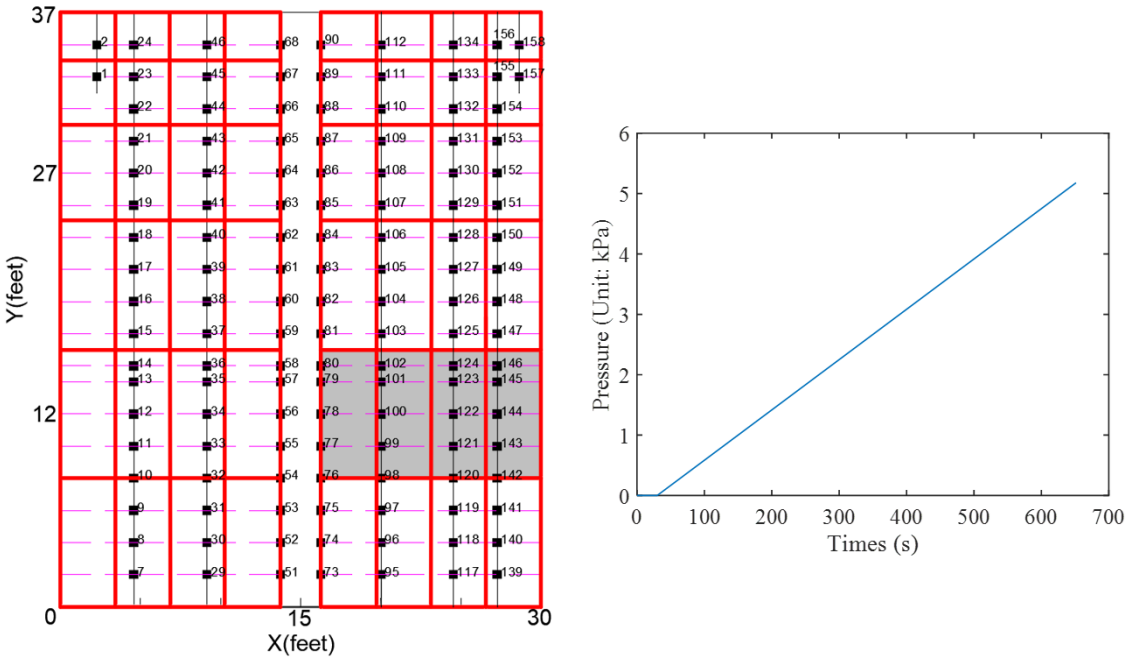

Figure 3.16: Used pressure chambers and corresponding load trace of experiment 1.

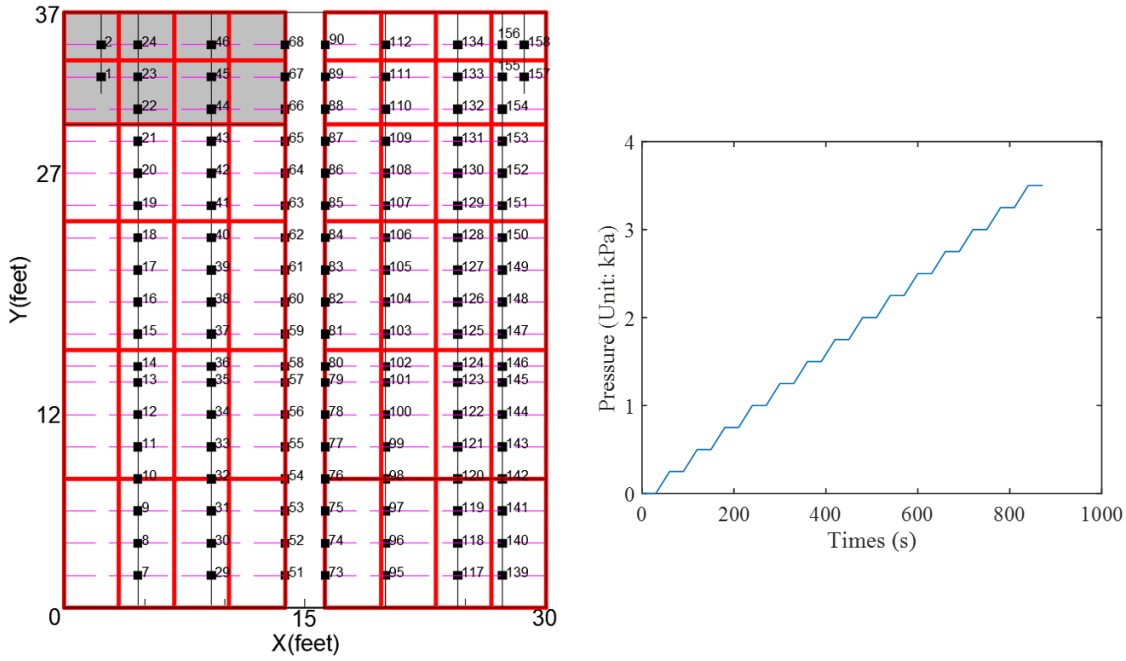

Figure 3.17: Used pressure chambers and corresponding load trace of experiment 2.

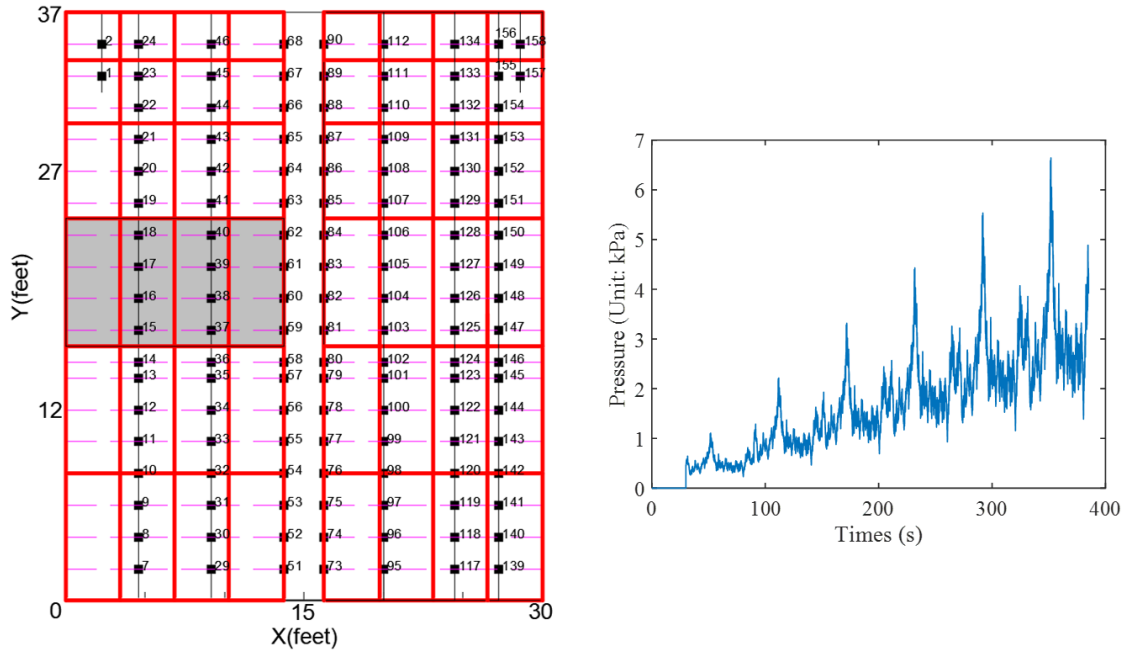

Figure 3.18: Used pressure chambers and corresponding load trace of experiment 3.

The work of this thesis builds on the experiments conducted by Nasiri, but go a step further. The major differences between are shown in Figure 3.19.

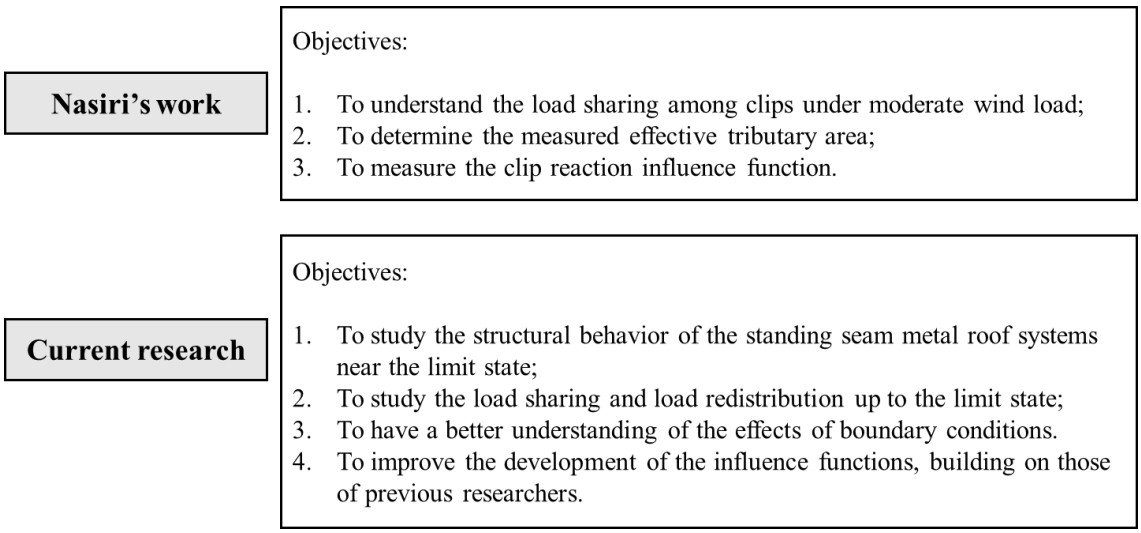

Figure 3.19: The major differences between Nasiri's experiments and the current research.

4. Experimental results

Wind-induced deformations and clip reactions were measured using displacement transducers and load cells on the full-scale roof. These experiments were conducted to investigate the load path and load sharing among clips as well as the failure modes of the SSMR system.

4.1 Failure sequence and loads in Experiment 1

LVDTs and LCs were used to obtain the roof deformation and clip reactions under uplift wind pressures. The arrangement of LVDTs and LCs is given in Figure 4.1 for Experiment 1 (see Figure 3.16). The displacement-pressure curves at points a, b, c, and d, at the mid-span between two seams shown in Figure 4.1, are plotted in Figure 4.2. Since the maximum measuring range of LVDTs used in the experiments is 100 mm, only displacements below 100 mm are given. It can be seen there are significant nonlinear relationships between displacements and pressures, with the slope of the curves reduced at higher pressures and large displacements. These large displacements are caused by the pans “popping” upwards between seams as sketched in Figure 1.3.

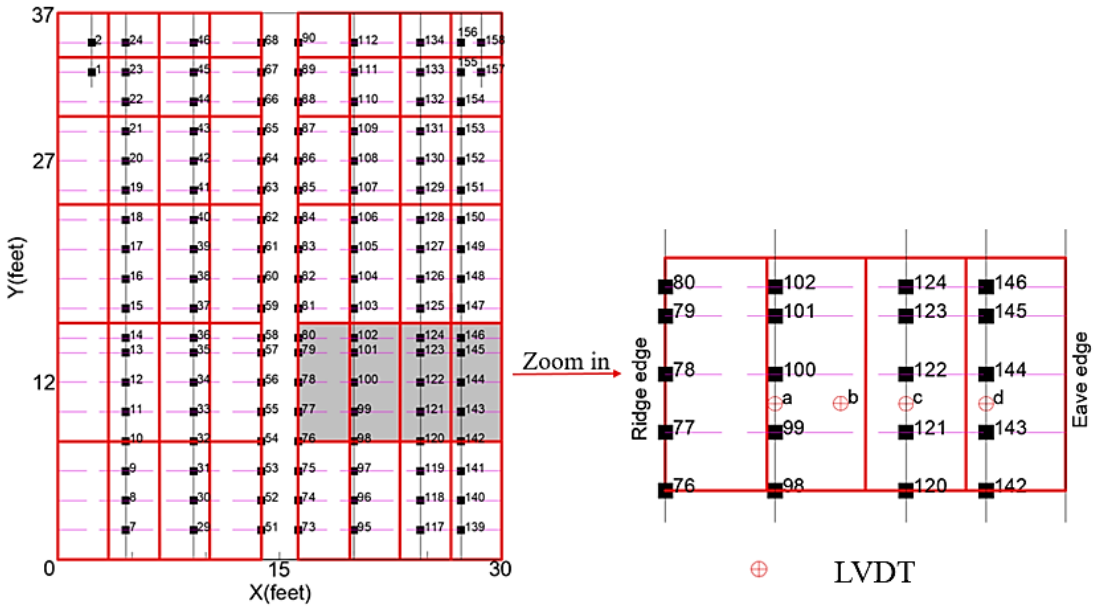

Figure 4.1: Arrangement of LVDTs and LCs for Experiment 1.

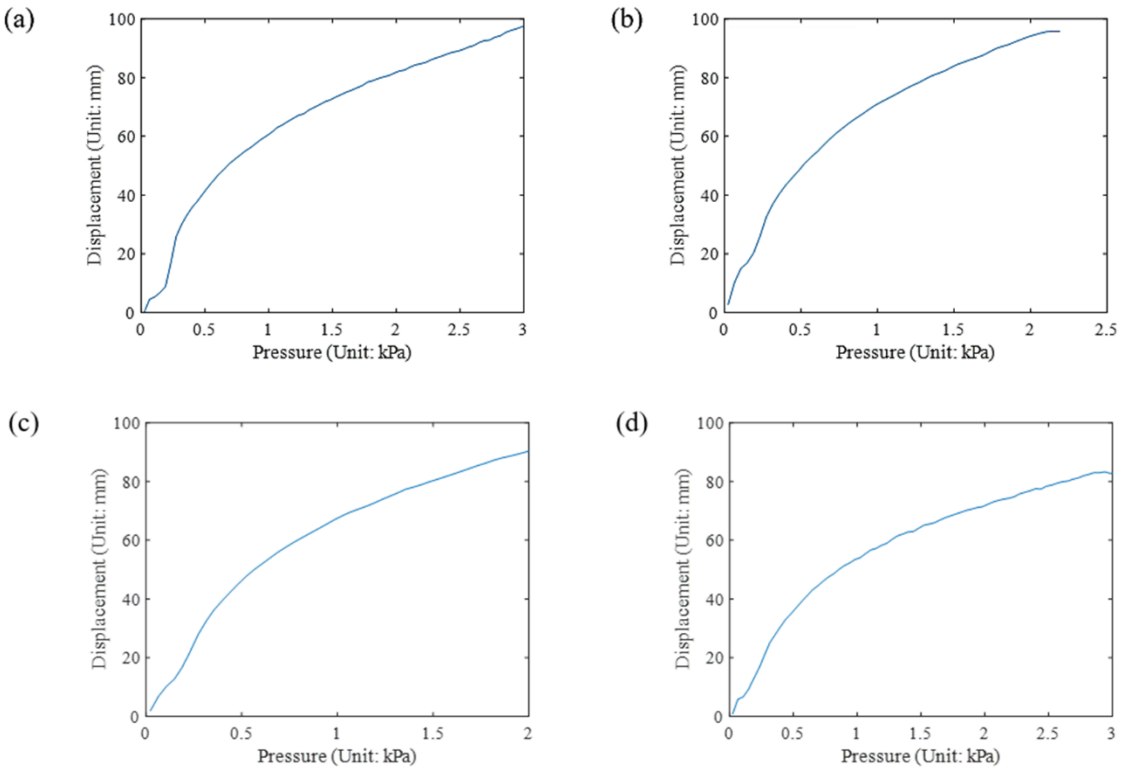

Figure 4.2: Displacement vs pressure at (a) point a, (b) point b, (c) point c, and (d) point d for Experiment 1 (see Figures 3.15 and 4.1).

Load-pressure curves for the clips are shown in Figure 4.3. These curves also show significant nonlinear relationships between clip reactions and pressures. In addition, when the pressure reaches 3.7 kPa, the clip reactions undergo a significant offset, accompanied by the roof buckling. The loads on clip100 and clip122 increase sharply, while loads on clip78 and clip144 decrease rapidly. For clip 122, the induced loads jumped from 922 N to 2427 N. The upward and downward spikes in the plots reflect the load redistribution among clips. Also, roof buckling was noticed, which can be concluded that the offset is due to the roof buckling. When the pressure was about 5.8 kPa, clip loads reached the peak value, which was 3682 N.

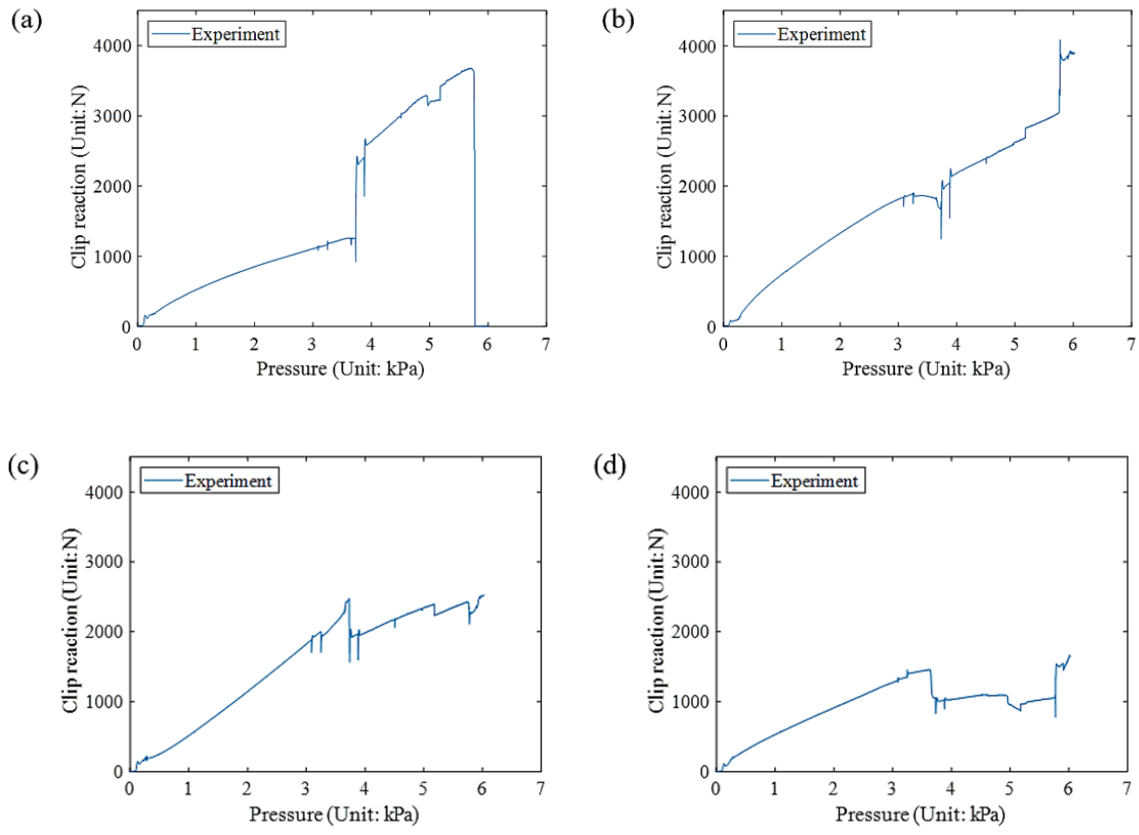

Figure 4.3: Load-pressure curves of (a) clip122, (b) clip100, (c) clip78, and (d) clip144 for Experiment 1 (see Figures 3.16 and 4.1).

The failure modes in each of the different experiments varied. In experiment 1, there are several stages of the response, which are described here. First, the SSMR panel billowed up and the maximum deflection occurred along the panel centerline, i.e., midway between two adjacent seams as shown in Figure 4.2. Rotation of ribs around the clips and panel-clip separation occurred successively, which is described by Schroter (1985) and shown in Figure 4.4. Coburn et al. (2014) pointed out there are two types of panel buckling modes, as shown in Figure 4.5. Local buckling is characterized by the skin buckling between stiffening elements while global buckling is the preferred first failure mode due to its higher post-buckling stiffness and lower out-of-plane deflection. For larger pressure, local buckling occurred on the panel near the seam, which can be seen in Figure 4.6. At still higher loads, buckling of the panel happened near the seam and midway between the two clips, which is shown in Figure 4.7. This buckling caused the global deflection of the roof, as illustrated in Figure 4.8. For still higher pressures, a seam opened near the location of the clip (clip 122), which is shown in Figure 4.9. Finally, the slippage between the clip and seam occurred, as shown in Figure 4.10, with the clip still attached to the purlin. As depicted in Figure 4.3, there was a jump of the measured load at clip 122 when the pressure reached 3.7 kPa, which corresponds to the moment of global buckling of the roof.

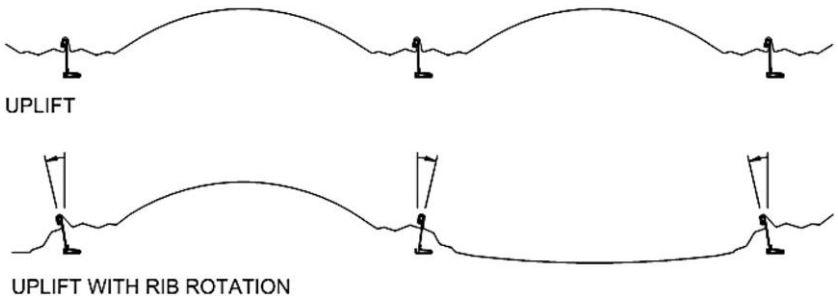

Figure 4.4: States of standing seam metal panel deflections (Schroter, 1985).

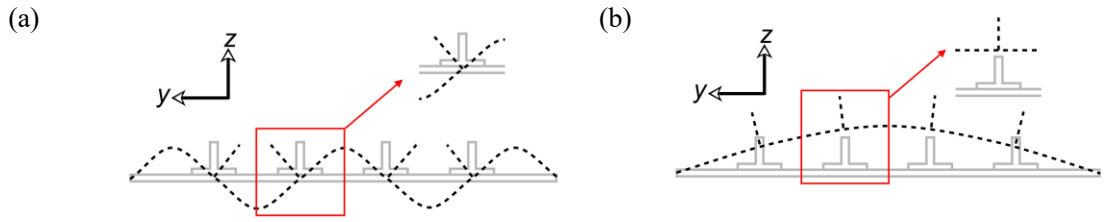

Figure 4.5: Panel buckling modes: (a) Local buckling mode and (b) Global buckling mode (Coburn et al., 2014).

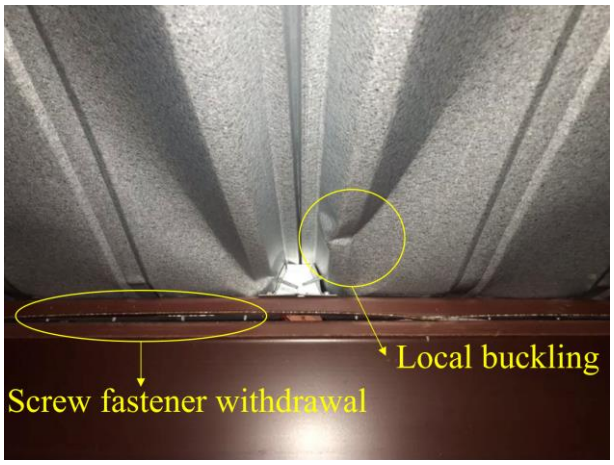

Figure 4.6: Local buckling of panels and screw fastener withdrawal near the eave edge under high uniform pressure.

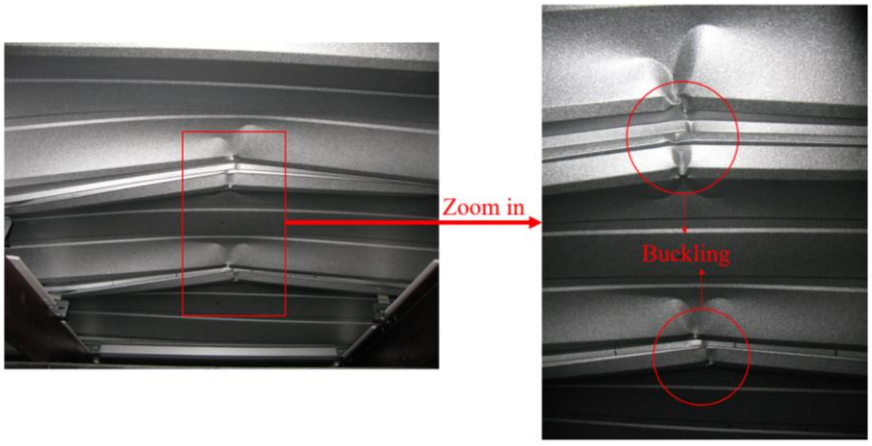

Figure 4.7: Global buckling of panels under high uniform pressure.

Figure 4.8: Deformation of panels under high uniform pressure.

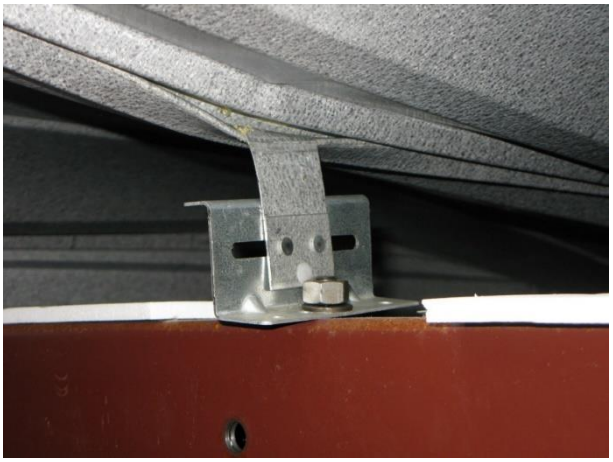

Figure 4.9: Seam opening affected by deformation of panels.

Figure 4.10: Slippage between seam and clip (clip 122).

In addition to the failure sequence that led to the buckling failure of the panel, the deformation and slippage of the clip, and the eave edge also had a significant failure, as can be seen in Figure 4.5. Figure 4.11 shows another view of this failure, which shows both withdrawal of the screw fasteners and a tearing failure of the eave plate. Thus, substantial load is going through the screw fasteners at the eaves. To examine this, the ratios of total induced loads on clips to total applied loads for Experiment 1 were calculated and listed in Table 4.1. Several observations can be made. First, between 17 and 23% of the load is not captured by the clips. As shown in chapter 3, very little load goes through the ridge (about 2%), so most of this is going to the eaves through the screw fasteners. Second, it is observed that the value of the ratio decreases under higher pressure. Thus, as the panels deform under higher pressures, it appears that more load transfers to the roof edge. As a result, the roof edge could be more vulnerable under higher pressures, which may not be captured because of the effects of boundary conditions in standardized tests. This point merits further investigation, which is done later in the thesis.

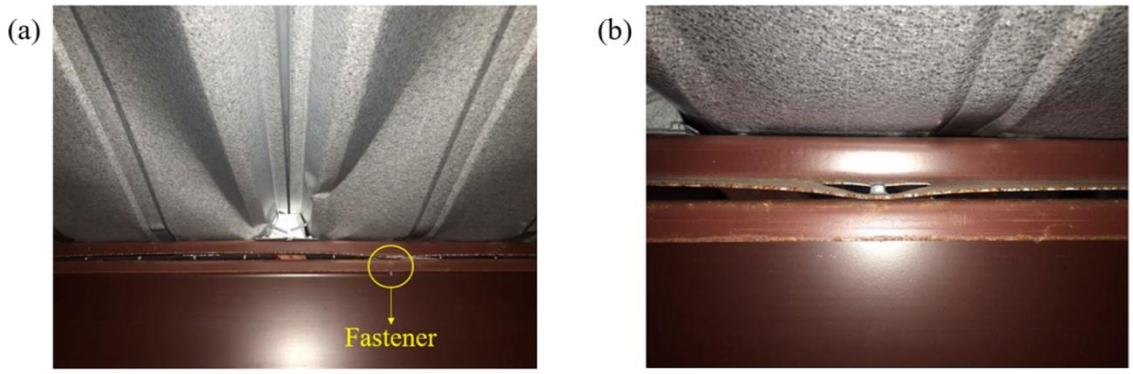

Figure 4.11: Deformation of SSMR at: (a) eave plate and (b) fasteners.

Table 4.1: Ratio of the induced load to the total applied load for Experiment 1

	Pressure (kPa)						
	0.5	1	1.5	2	2.5	3	3.5
Ratio %	83.42	87.10	84.32	81.64	80.48	79.12	77.30

4.2 Failure sequence and loads in Experiment 2

The arrangement of LVDTs and LCs is given in Figure 4.12 for Experiment 2 (see Figure 3.17). The displacement-pressure curves at points a, b, c, and d as shown in Figure 4.12, are plotted in Figure 4.13.

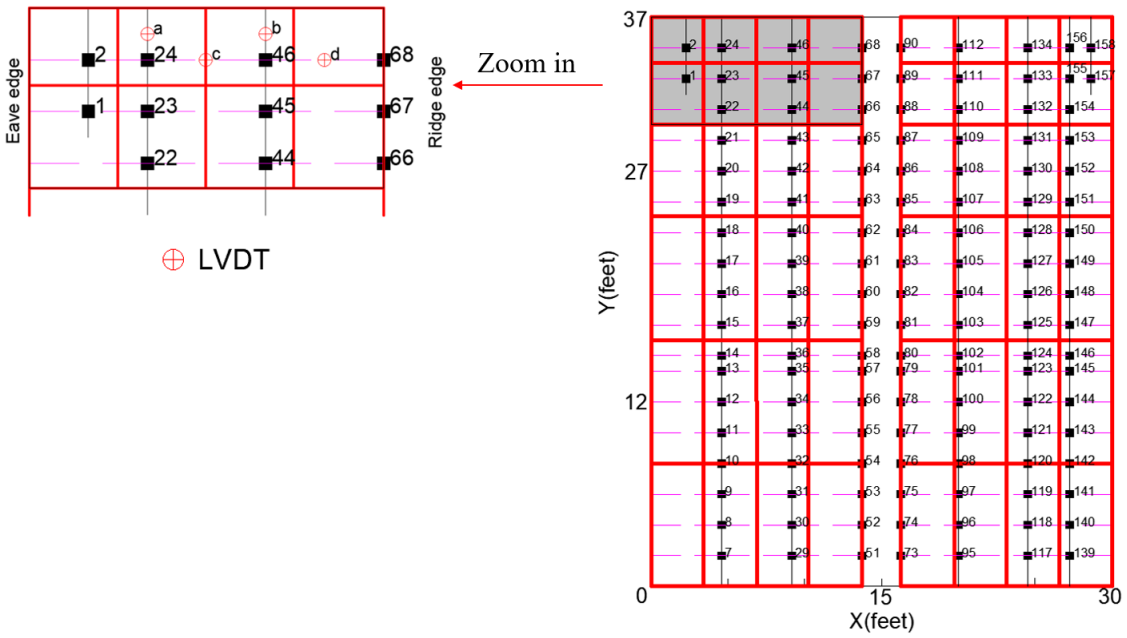

Figure 4.12: Arrangement of LVDTs and LCs for Experiment 2.

In Figures 4.13(a) and 4.13(b), the curves show nonlinear relationships between displacements and pressures, which were also observed in experiment 1. However, the results in Figures 4.13(c) and 4.13(d) are quite different since these two LVDTs were installed along the seam (see Figure 4.11). It can be seen when pressure is under 2.5 kPa, the displacements at the seams are proportional to pressures. Then, these two curves undergo significant offsets, accompanied by the roof buckling. Moreover, it can be seen that the displacements at seams are much smaller than the values at mid-span between two seams. Since the vertical stiffness at mid-span is relatively small, even low wind pressure could cause notable displacements. As pressure increases, the pans pop upwards, and the

stiffness increases. As a result, the growth of displacement slowdown. In contrast, the stiffness at the seams is relatively large and keeps constant until the roof buckling.

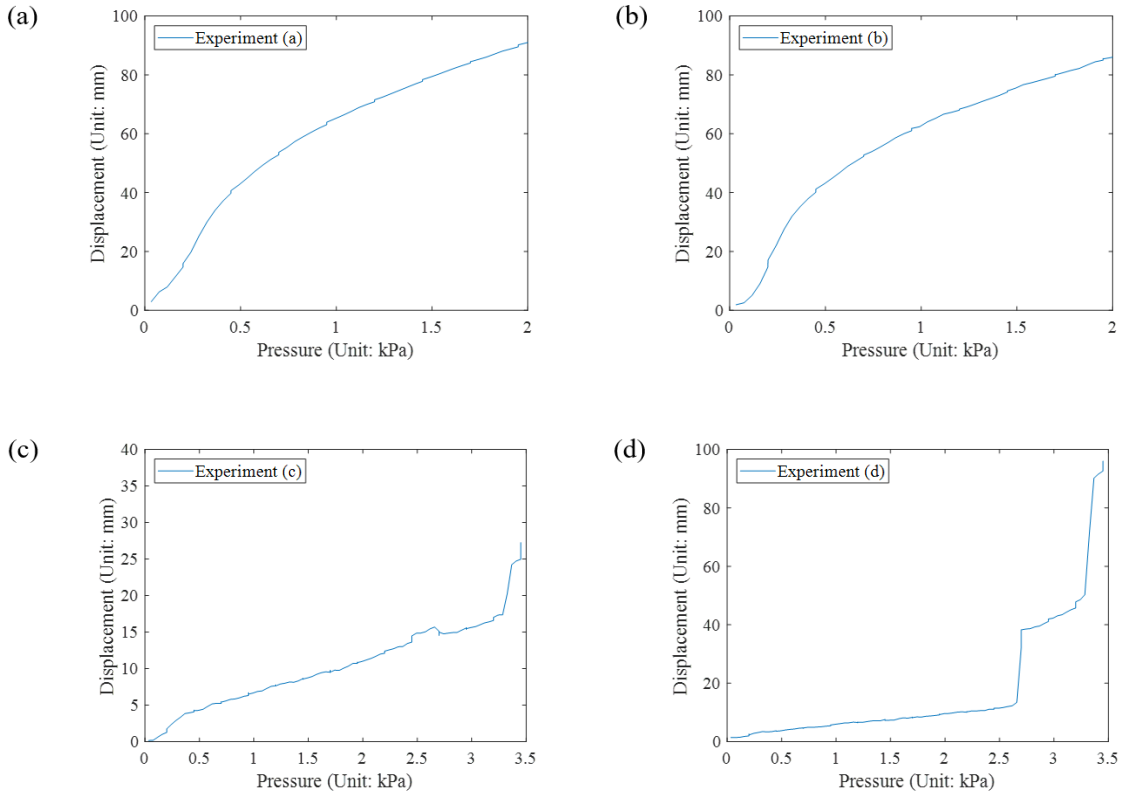

Figure 4.13: Displacement vs pressure at (a) point a, (b) point b, (c) point c, and (d) point d for Experiment 2 (see Figures 3.17 and 4.11).

Load-pressure curves for the clips are shown in Figure 4.14. These curves also show significant nonlinear relationships between clip reactions and pressures. The clip reactions undergo several significant offsets when the pressures reach 2.75 kPa, 3.5 kPa, 4.5 kPa, 5 kPa, 5.3 kPa, and 6 kPa. Roof buckling happened at these pressures, accompanied by loud sounds. When the pressure reaches 2.75 kPa, local buckling occurred on the panel near clip 68. As a result, the load on clip 68 has a shape increase, while loads on clip 24 and clip 46 have an obvious decrease. When the pressure was about 5.35 kPa, the induced loads on clip 46 decreased from 3623 N to 0 N. Meanwhile, the loads on clip 24 increased from 472 N to 1930 N. When the pressure reaches 6.0 kPa, the loads on clip 2 and clip 24 reached

the peak value (4525 N and 3236 N), then drop to 0 N. Since the load offset is accompanied by roof buckling, it can be concluded that the roof buckling leads to the redistribution of loads among clips.

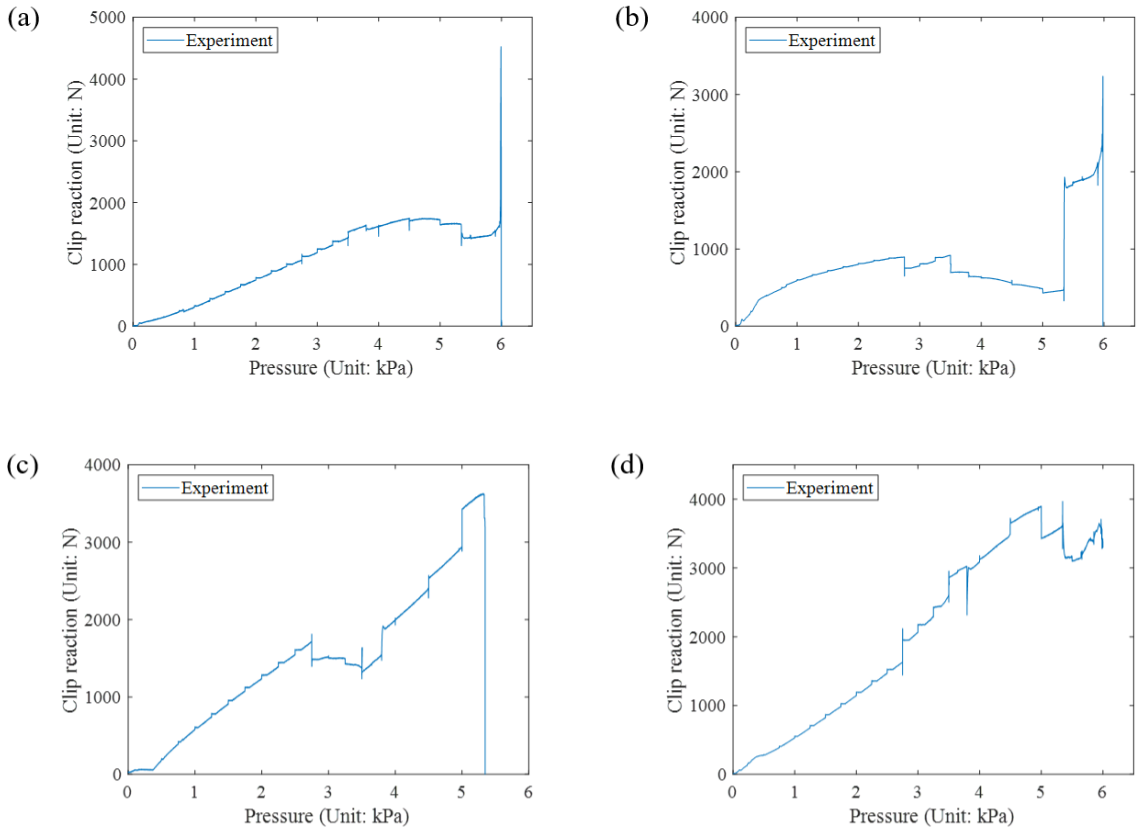

Figure 4.14: Load-pressure curves of (a) clip2, (b) clip24, (c) clip46, and (d) clip68 for Experiment 2 (see Figures 3.17 and 4.11).

In addition to the panel buckling and clip slippage (in order: clip 46, clip 24, and clip 2), fastener failure was observed, which is shown in Figures 4.15, 4.16, and 4.17. It can be seen that the fastener failure occurred both at the ridge edge and eave edge. The fastener failure results in the detachment between the roof panel and purlin. Similar to Experiment 1, the ratios of total induced loads on clips to total applied loads for Experiment 2 were calculated and listed in Table 4.2. Between 27 and 47% of the load is not captured by the

clips, which shows a significant effect with two edges (eave and gable end). Most of this is going to the eaves and gable end through the screw fasteners.

Figure 4.15: Edge failure as the SSMR was subjected to pressure.

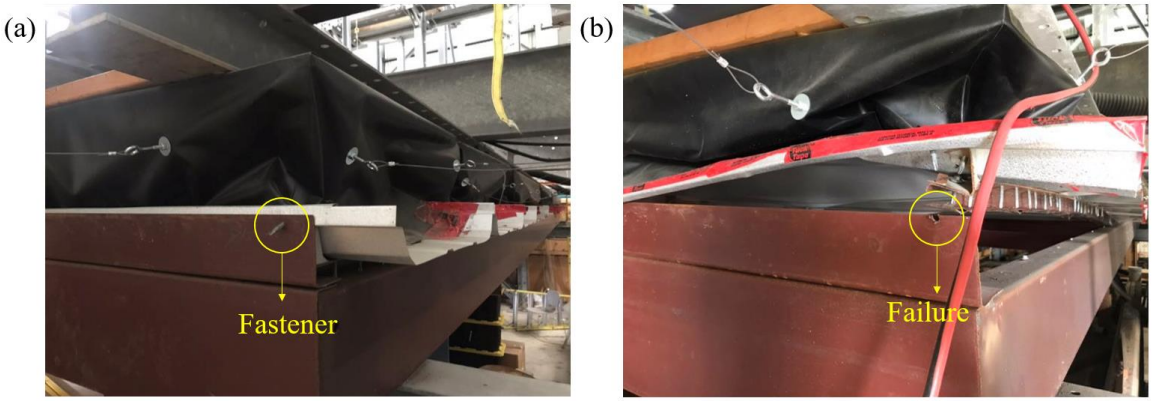

Figure 4.16: Fastener failure at the gable edge (a) before the test (b) after the test.

(a)

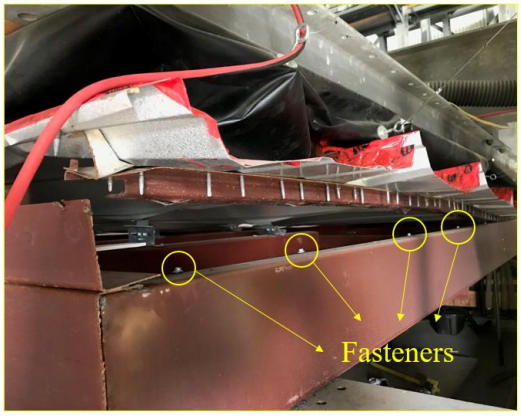

(b)

Figure 4.17: Fastener failure at the eave edge (experiment 2).

Table 4.2: Ratio of the induced load to the total applied load for Experiment 2

	Pressure (kPa)						
	0.5	1	1.5	2	2.5	3	3.5
Ratio %	73.32	70.88	67.99	65.59	63.68	61.15	53.50

4.3 Failure sequence and loads in Experiment 3

The arrangement of LVDTs and LCs is given in Figure 4.18 for Experiment 3 (see Figure 3.18). LVDT a and b were used to measure the displacement at LC 17 and 39, respectively. The loading trace for Experiment 3 is shown in Figure 4.19. As depicted in Figure 3.18, the loading trace can be divided into several segments, which are named segments#1, 2, 3, 4, and 5. The displacement time series at points a, b, c, and d as shown in Figure 4.18, are plotted in Figure 4.20. For Figure 4.20(b), only the data within 150 s is plotted since the following displacements are over the measuring range of LVDT.

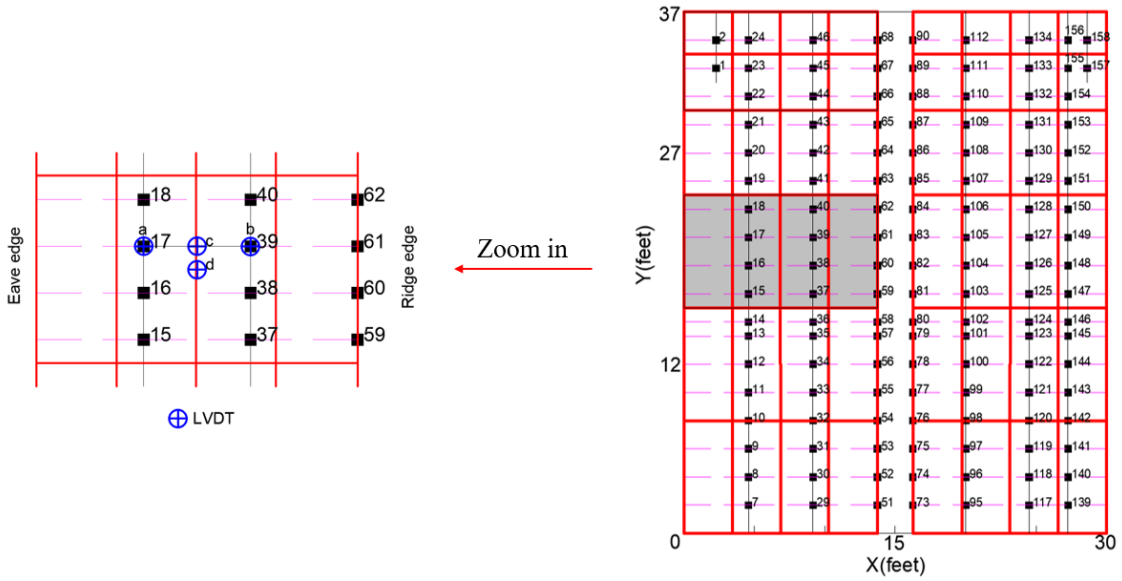

Figure 4.18: Arrangement of LVDTs and LCs for Experiment 3.

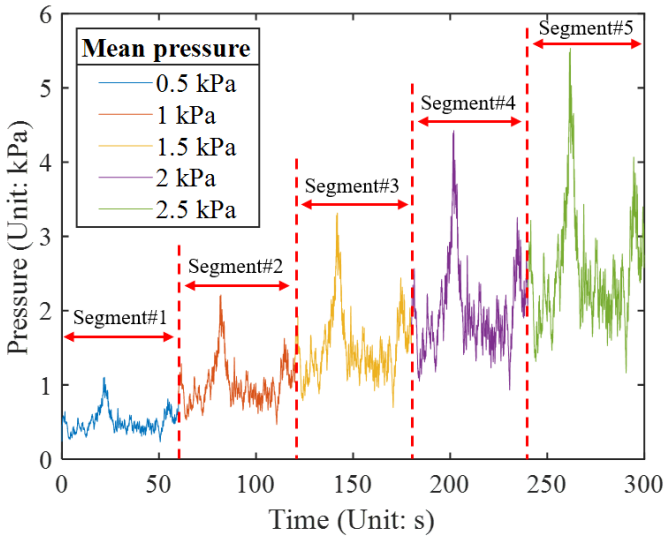

Figure 4.19: Loading trace for Experiment 3.

Rather than the displacements gradually increasing as in Experiments 1 and 2, the displacement time series in Experiment 3 are fluctuating. Moreover, when times are 203 s and 261 s, there are two significant offsets as indicated in Figure 4.20(a). Meanwhile, roof buckling was observed. By comparing the loading trace in Figure 4.19, these time points

are corresponding to the local peaks (4.4 kPa and 5.5 kPa) in segments 4 and 5, respectively. The peak loads that cause this incremental deformation of SSMR systems will be referred to as “damaging peaks”. It can be seen that the majority of the permanent damage occurs at a series of damaging peak loads.

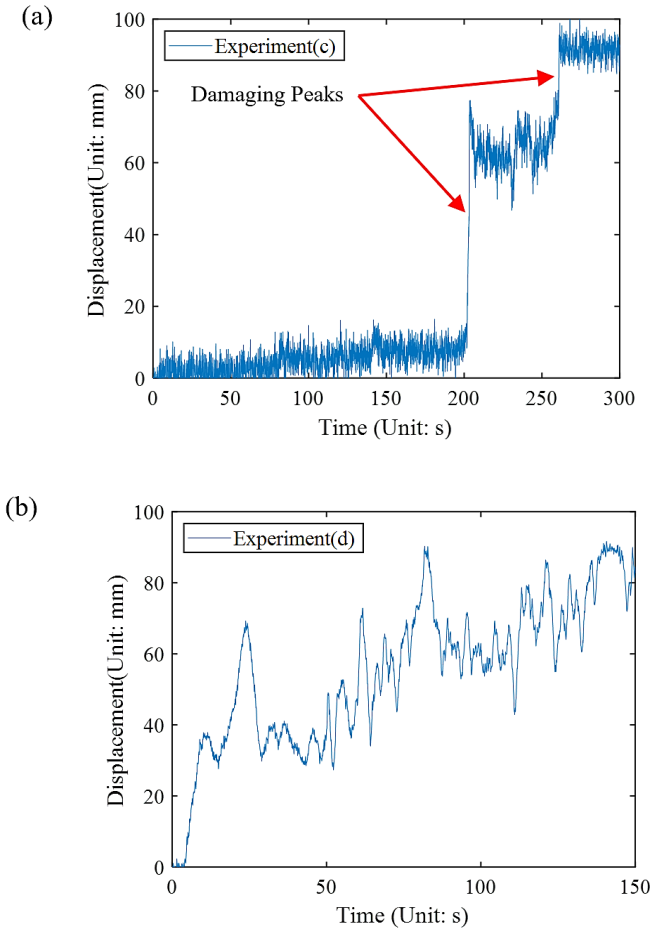

Figure 4.20: Displacement time series at (a) point c, and (b) point d for Experiment 3 (see Figures 3.18 and 4.18).

Figure 4.21 shows the load vs. displacement relationship of clips. Over the first three segments when the applied loads are relatively small, the load-displacement behavior is nearly linear; however, following the first damaging peak (as indicated in the figure), the load-displacement curve shifts to the right. The second damaging peak continues to increase the permanent displacement. Surprisingly, between these damaging peaks, the

slope of the load-displacement curve remains similar to the undamaged case. This indicates that the stiffness of the connection between clips and seams remains unchanged despite having notable deformation.

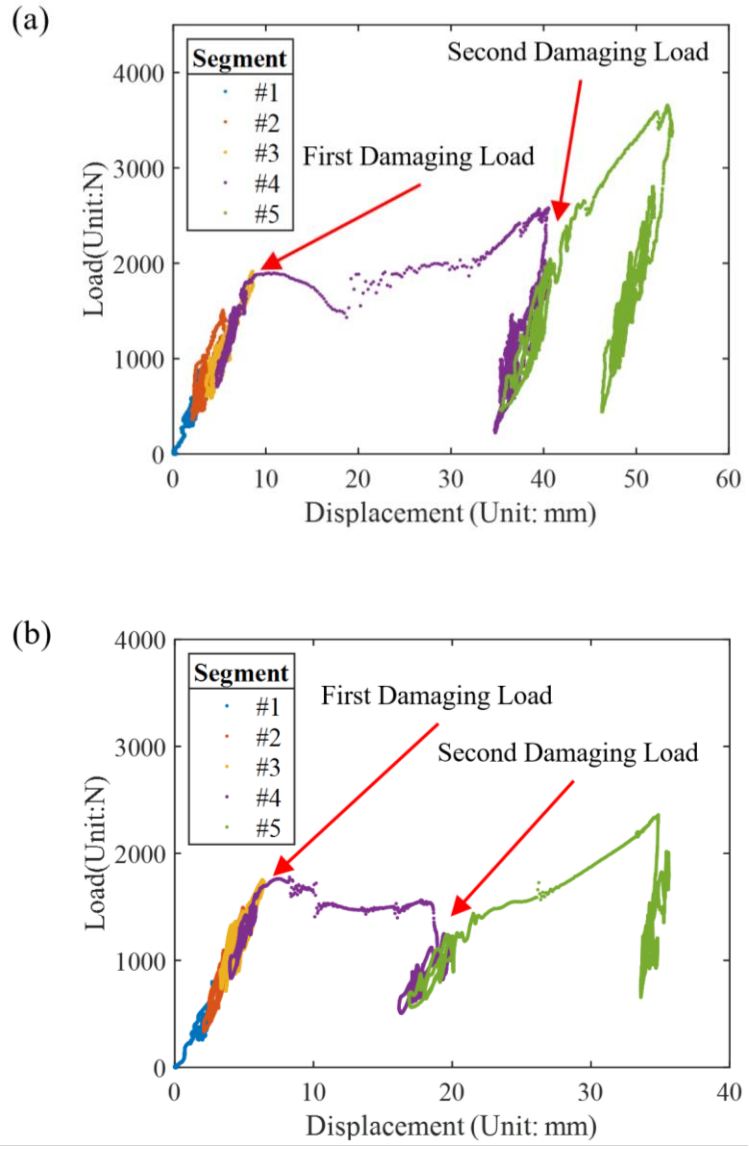

Figure 4.21: Load vs. Displacement of (a) clip17, and (b) clip39 for Experiment 3 (see Figures 3.18 and 4.18).

Since the failure pressure was 5.3 kPa and there is corner enhancement in Experiment 2, it is reasonable to infer the failure pressure should be lower than 5.3 kPa if ramp loads were

applied in Experiment 3. However, the clip slippage did not happen in Experiment 3 when peak pressure reached to 5.5 kPa, which is slightly higher than that of the ramp loading test. The fastener failure was observed in Experiment 3 as shown in Figure 4.22. By comparing the fastener failures in experiment 2 and experiment 3, it could be found that the fastener head in experiment 2 did not have obvious damage while the fastener head is fractured in experiment 3. The different failure modes may be due to the effect of dynamic wind pressure.

Figure 4.22: Fastener failure at the eave edge (experiment 3).

The initial locations of global buckling in these tests are illustrated in Figure 4.23. In Experiments 1 and 3, global buckling was initiated in the middle of the roof panel. However, global buckling was initiated close to the ridge edge in Experiment 2. Only clip slippage occurred in Experiment 1, and only fastener failure occurred in Experiment 3. Both clip slippage and fastener failure occurred in Experiment 2. It is assumed that the initial locations of global buckling and failure modes vary with boundary conditions and clip arrangement. It is noted that the induced load of clips near the initial location of global buckling has a sudden jump (see Figures 4.3(a) and 4.14(d)). The roof buckling has a critical effect on load redistribution.

Fastener failure was observed during the tests, which emphasizes the importance of boundary conditions. However, this is usually ignored by the current standardized protocols. It is not an easy task to model the performance of the details at the boundaries of the roof. But it is important to be able to consider the influence of these boundary conditions on the performance of the clips and load sharing on the roof, especially near the limit state. This will be discussed in the following sections.

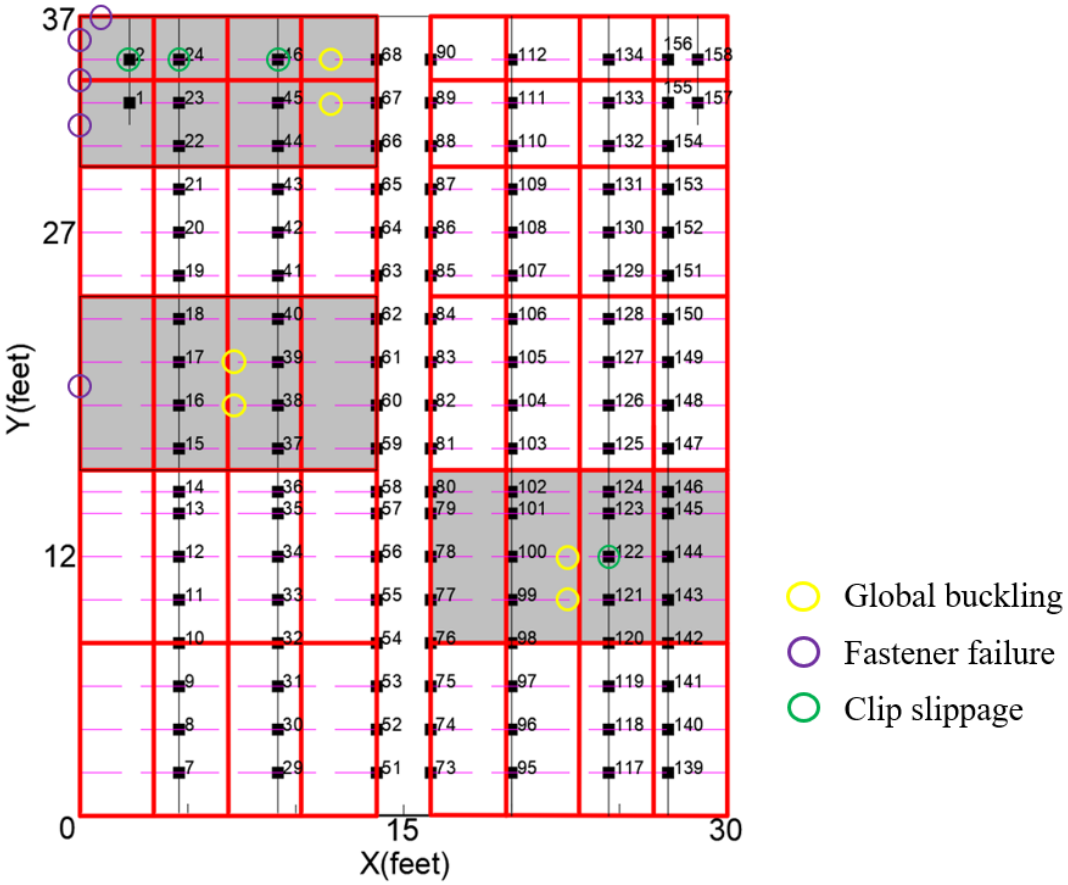

Figure 4.23: Location and types of failures observed in Experiments 1, 2, and 3.

4.4 Summary

The tested SSMR system at IRLBH has realistic dimensions and boundary conditions, which provides the opportunity to test the performance of the SSMR system under more

realistic conditions. Load path and load sharing among clips were investigated using installed load cells on clips. Although the induced load of the fasteners at the roof edge could not be measured directly, the influence of boundary restraints on the load sharing among clips could be investigated.

Two failure modes of connections, clip slippage and fastener failure, were observed during the tests. However, the failure modes vary with the clip arrangement and boundary conditions. Global buckling of panels occurred before connection failures and the initial location of global buckling was near the seam and in the middle of two adjacent clips. Fastener failure occurred at the roof edges. For the roof near the corner, between 27 to 47% of the applied load transferred to the edges of the eave and gable end. For the roof away from the corner, between 17 to 23% of the applied load transferred to the eave edge.

The failure load during the dynamic wind load experiment was found to be slightly higher than that obtained from the ramp load experiment. This indicates that the ramp load experiment is slightly conservative compared to the dynamic wind load test. The fastener head experienced fatigue failure under dynamic wind load while the fastener head under static wind load was still in contact. However, fastener failure under dynamic loads has focused on low cycle fatigue, which is beyond the scope of this thesis. Therefore, more dynamic pressure tests are needed for future work. Additionally, different failure modes occurring for each specimen ask for the necessity to define the failures of the SSMR system, especially fastener failure at the roof edge.

5. Numerical simulation

Since only a limited number of experiments could be conducted due to the cost and time of full-scale tests, other methods (e.g., FEM) were adopted to develop a more detailed understanding of the response and failure mechanisms of the SSMR system subject to uplift loads. These full-scale tests provide the data for validation of FEM, which will be discussed below.

As shown in chapter 4, there is a nonlinear relationship between pressure distributions and structural responses. The numerical simulation aims to create a three-dimensional finite element model that can simulate the response of the full-scale SSMR system under uplift wind loads. The state of the roof system up to the limit state was investigated, giving insight into the load paths and failure mechanisms that could not be obtained via the measurement tools.

5.1 Description of the finite element model (explicit analysis)

It is impractical to model every component of the roof structure using FEM due to the complexity of SSMR systems. Therefore, the following assumptions and simplifications were made to create the finite element model:

1. Fasteners and screws were not physically modeled; only their constraining effects were simulated by coupling the nodes at panels and purlins. Roof panels, clips, and purlins were created with dimensions that were the same as the test specimens.

2. Part of the roof system, rather than the whole roof system, was created since it is found the loads applied on the roof only affect the adjacent panels.

3. Only the effects of gravity and wind loads were considered, other effects such as temperature and installation errors were not considered in the simulation.

The commercial software, ANSYS/LS-DYNA, was used in the simulation. Ansys/LS-DYNA is a commonly used explicit simulation program. A refined 3D model of the roof system, which considers the three kinds of nonlinearities, enabled the author to track the failure progression since interactions and load transfers could be modeled accurately. Experiment 1 is chosen as the basis for simulation. As shown in Figure 5.1, only the roof components within the blue dashed lines were considered due to the symmetry. A series of displacement transducers (DTs) were placed along the centerline to measure the displacement of the roof subjected to uplift loads.

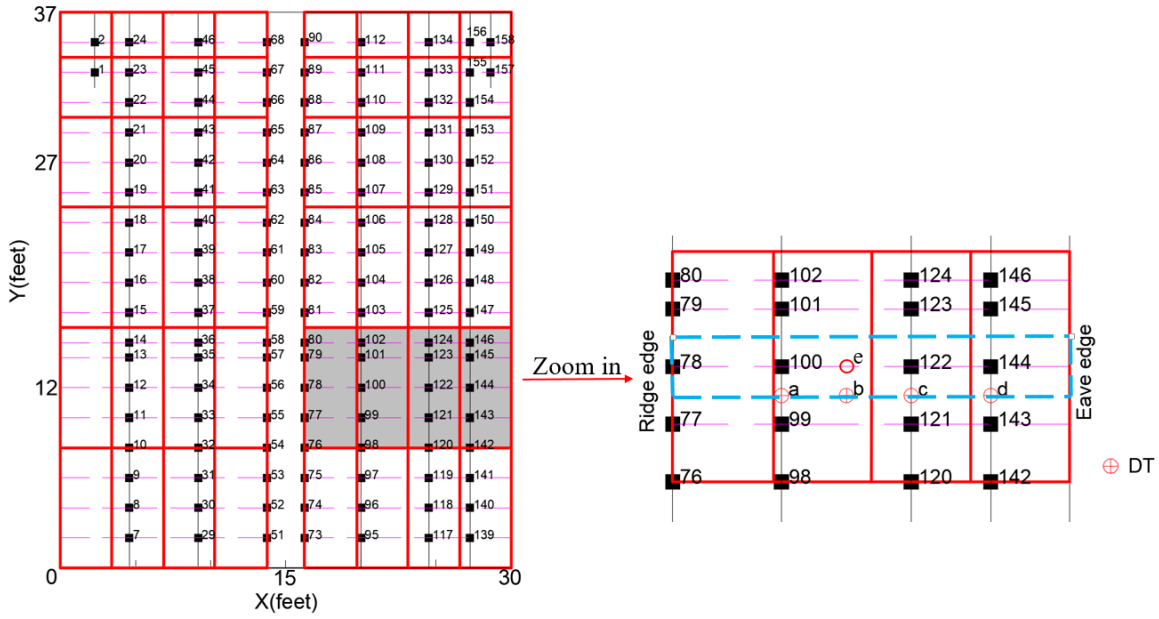

Figure 5.1: Modeling area of FEM (filled with grey).

Since the thickness of the roof panels is 0.5 mm and the ratio of length and thickness of the panels is relatively large, the panel is a typical thin plate/shell structure. Thus, it is appropriate to use shell elements to simulate the roof panels. Similarly, the clips and purlins were also simulated using shell elements. The 4-node shell element SHELL163 was adopted. This element has 12 degrees of freedom at each node. The mapping method was used to generate a high-quality mesh. The mesh was refined at locations expecting contact

and stress concentrations. Therefore, as shown in Figure 5.2, the mesh size of the clip and the seam in contact with the clips is 10 mm while the mesh size is 20 mm for other locations.

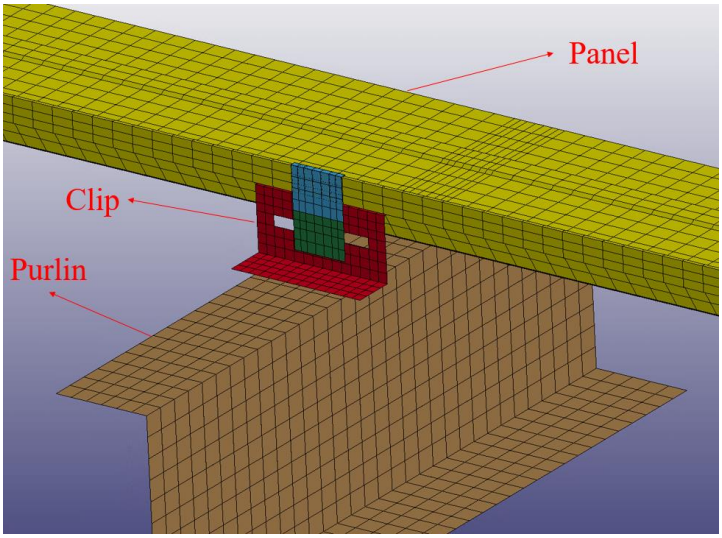

Figure 5.2: Mesh of roof components.

The difficulties in modeling the roof system are the simulation of edge restraints and the interaction between roof components. The roof panel near the eave edge is fixed to the purlin through the eave plate. Because no obvious damage was observed at this location during experiment 1, the connection between the roof panel and purlin can be reasonably assumed to be rigid, therefore node coupling was used to connect the roof panel to the purlin. Thus, the roof panel and purlin at the eave edge can move together when the roof system deforms under wind load.

As for the restraints at the ridge of the roof, a back-up plate was attached to the panel along the roof ridge, which was used to increase the stiffness at the ridge. The loads still transferred through clips to purlins directly and the back-up plate did not carry loads to the purlins. Thus, the back-up plate was created and attached to the panel in the numerical simulation. Furthermore, clips were fastened to purlins with screws. Based on the observation during the experiments, there was no notable relative movement between clips and purlins. Thus, the clip and purlin work together by coupling the nodes at the interface

of the clip base and purlin flange. The finite element model of the SSMR system is illustrated in Figure 5.3.

One of the difficulties in numerical simulation is how to deal with the contact problem appropriately. Since the deformation of the roof can be large, the contact between roof components is complex. The predetermination of where and how contact occurs would be difficult or even impossible to set. Thus, automatic general contact is adopted, which can detect penetration coming from either side of a shell element. Once two shell elements are contacted or the shell element is self-contacted, the contact force is automatically calculated. Another issue is to consider the material nonlinearity. The bi-linear elastoplastic constitutive relations are considered in this analysis; details of the material property are listed in Table 5.1. To simulate the experiment, the load applied in experiment 1 was used in the FE model, i.e., a linearly increasing load until failure.

A mesh sensitivity study was performed by changing the mesh size and maintaining other parameters constant. For this verification, the mesh size was changed to 0.5, 2, and 4 times from the optimized mesh size. Figure 5.4 shows the displacement-pressure curves at point b using different mesh sizes. It illustrates that the deflections depend on mesh size when the mesh size was changed to 2 and 4 times from the original mesh size. Further reduction in mesh size was not significantly influencing the deflections. Based on this mesh sensitivity verification, it can be concluded that further FEM can use this mesh size.

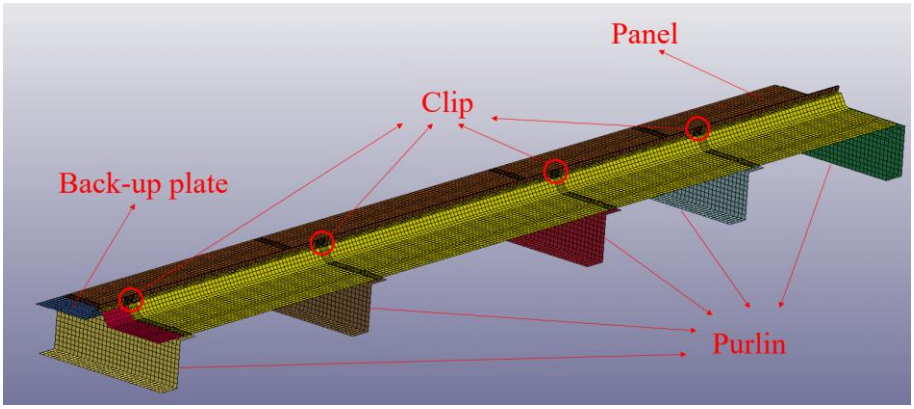

Figure 5.3: The finite element model of the SSMR system.

Table 5.1: Material property

Thickness of panel	Yield strength	Elastic modulus
0.5 mm	345 MPa	2.06×10^5 MPa
Poisson's ratio	Tensile strength	Tangent modulus
0.3	450 MPa	6.7×10^3 MPa

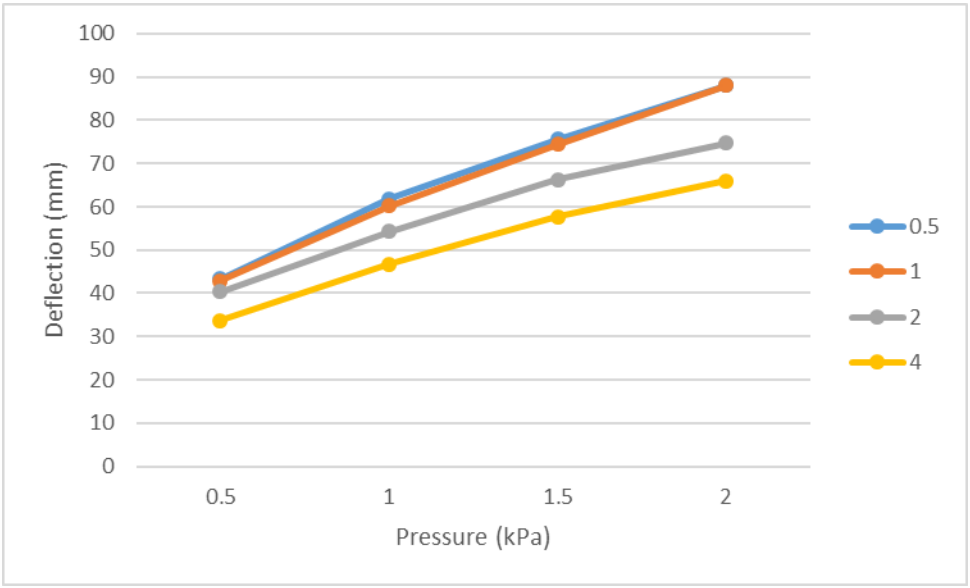

Figure 5.4: Displacement-pressure curves at point b using different mesh sizes.

5.2 Validation of FEM using the data from full-scale tests

The comparison of displacements between FEM and experiment under different pressures at points a, b, c, and d (shown in Figure 5.1) are plotted in Figure 5.5. Since the maximum measuring range of displacement transducers used in the experiments is 100 mm, only displacements below 100 mm are provided. It can be seen that the curves from FEM capture the trend of the data from the experiment, with differences up to about 10 mm.

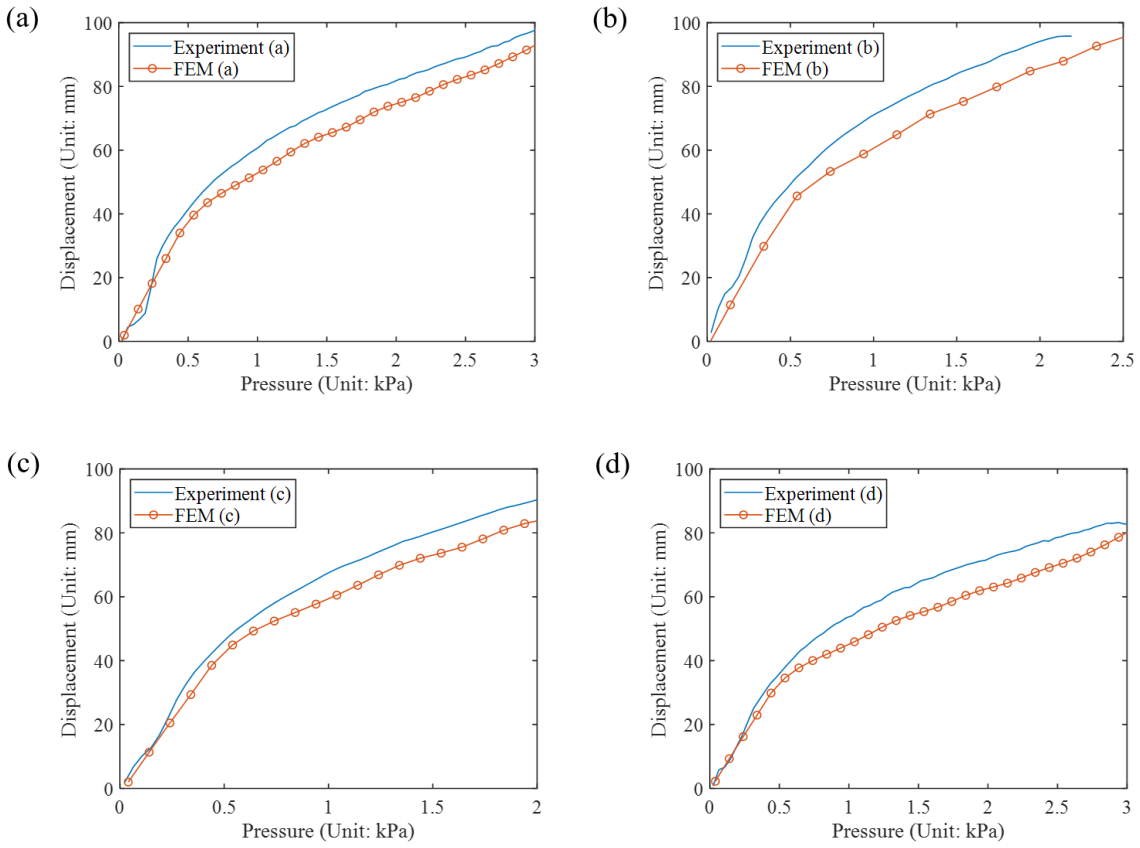

Figure 5.5: Displacement vs pressure at (a) point a, (b) point b, (c) point c, and (d) point d for explicit analysis (see Figure 5.1).

Since deflection was validated only at the linear stage, the comparison of clip reaction between FEM and experiment is given in Figure 5.6. It can be seen that the curves from FEM fit well with the curves from the experiment, which gives confidence in the accuracy

of the simulation. It can be concluded that the FEM is suitable to describe the deformation of the SSMR system, which will be examined in detail below. Figure 5.6 shows that there is a drastic change of load for all clips when the pressure reaches 3.7 kPa, which implies a load redistribution. It can be seen that loads at clip 122 and clip 100 jump at this moment. In contrast, the loads at clips 78 and clip 144 have a notable decrease. From the observation from the experiment, the initial location of global buckling happens in the middle of clip 122 and clip 100. It can be concluded that the global buckling leads to the increment of loads of clips located near the initial location of global buckling. More loads transfer to these two clips and less load transfer to other clips.

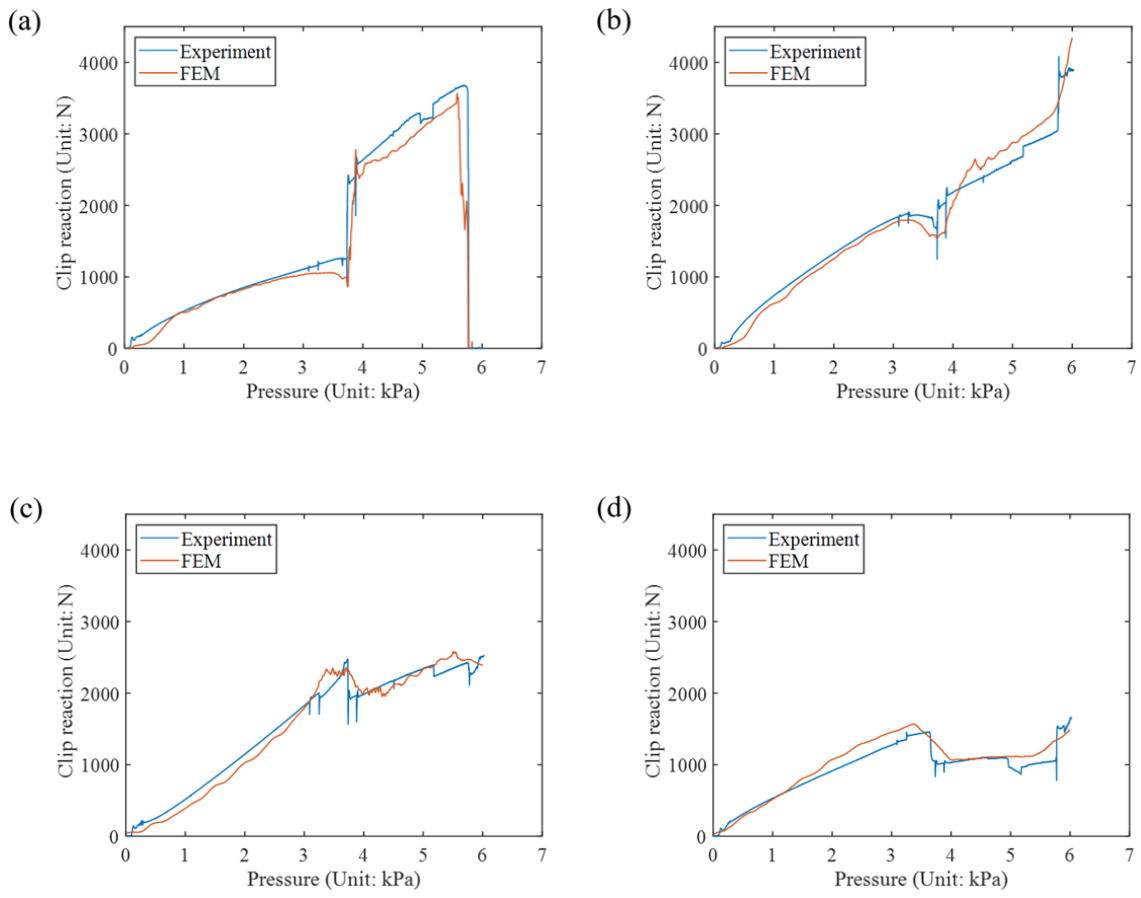

Figure 5.6: Load-pressure curve of (a) clip122, (b) clip100, (c) clip78, and (d) clip144 for explicit analysis (see Figure 5.1).

5.3 Simulation of failure progression

Figure 5.5 only gives the displacement-pressure curves within the measurement range; Figures 5.7 and 5.8 depict the displacement-pressure curves through the entire failure sequence. From Figure 5.7, it can be seen the slope of the curve is steep initially since the deformation of the roof panel could be notable even at low pressure due to the flexibility of the roof panel. In particular, the deflection at point b in the middle of the panel is over 60 mm when the pressure is 1 kPa. At higher pressures, between 1 and 3.4 kPa, the curve flattens because the increment of panel flexural stiffness and the edge restraints on the roof restrict the deflection. There is a drastic change in the slope when the pressure is between 3.4 kPa and 3.9 kPa, which corresponds to the global buckling of the panel. The deflection increases from 112 mm to 251 mm in this interval. When the pressure is over 3.9 kPa, the slope flattens again. At last, the slippage of the clip results in a steep slope of the curve when the pressure reaches 5.8 kPa. Similar results can be found in Figure 5.8 for point e. However, the deflection at point e, on the seam is relatively small even at high pressure (e.g., the deflection is only 32 mm when the pressure is 3.6 kPa) because of the higher stiffness of the seam compared to the panel. The deflection increases rapidly from 32 mm to 158 mm when the pressure increases from 3.6 kPa to 4 kPa.

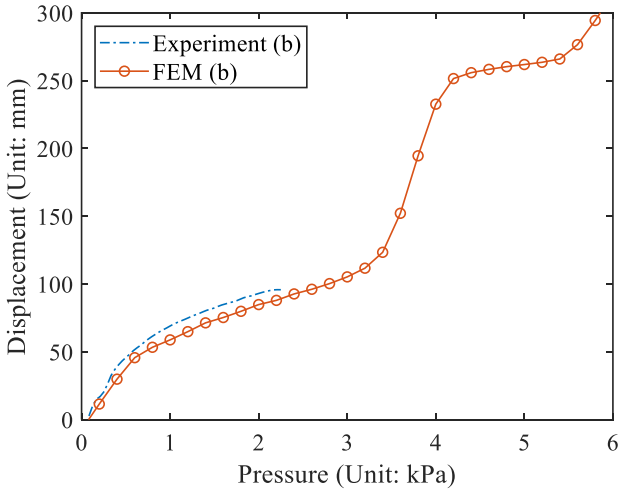

Figure 5.7: Displacement-pressure curve at point b for explicit analysis.

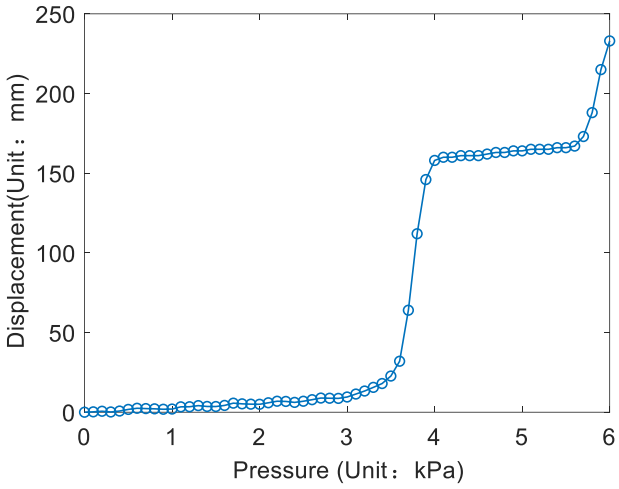

Figure 5.8: Displacement-pressure curve at point e for explicit analysis.

Seam opening was observed in both the experiment and the FEM analysis, as shown in Figure 5.9. It is seen that the intense wind pressures result in the permanent deformation of the roof panel while the clip tab, initially sealed in the seam, was gradually exposed. Figure 5.10 depicts the deformation of the roof system after the pull-out failure. The failure modes obtained from FEM and experiment are quite similar, which implies FEM is a suitable tool to simulate the failure progression of the SSMR system subjected to uplift wind pressure.

Figure 5.11 provides a section view of the failure progression of the roof components at the seam under increasing wind pressures using FEM. As shown in Figure 5.11 (a), the roof panel is flat before applying wind pressure. The horizontal portion of the roof panel has a distinct deflection at low pressure (i.e., 0.3 kPa). The pitched part of the roof panel starts to rotate about the seam joint when pressure is higher than 1 kPa. The components of the seam joint are in close contact, there is no significant gap between the interface even when the pressure reaches 3 kPa. The structure of the seam joint drastically deforms under the pressure with a magnitude of 3.7 kPa. Seam opening happens at this stage. The deformation of the roof panel is roughly constant when the pressure is in the range of 3.8 kPa to 5.7 kPa. This is consistent with the findings from Figure 5.7 and Figure 5.8. The

deflections at point b and point e increase slowly at this interval. The seam joint finally fails at 5.8 kPa due to the slippage of the clip.

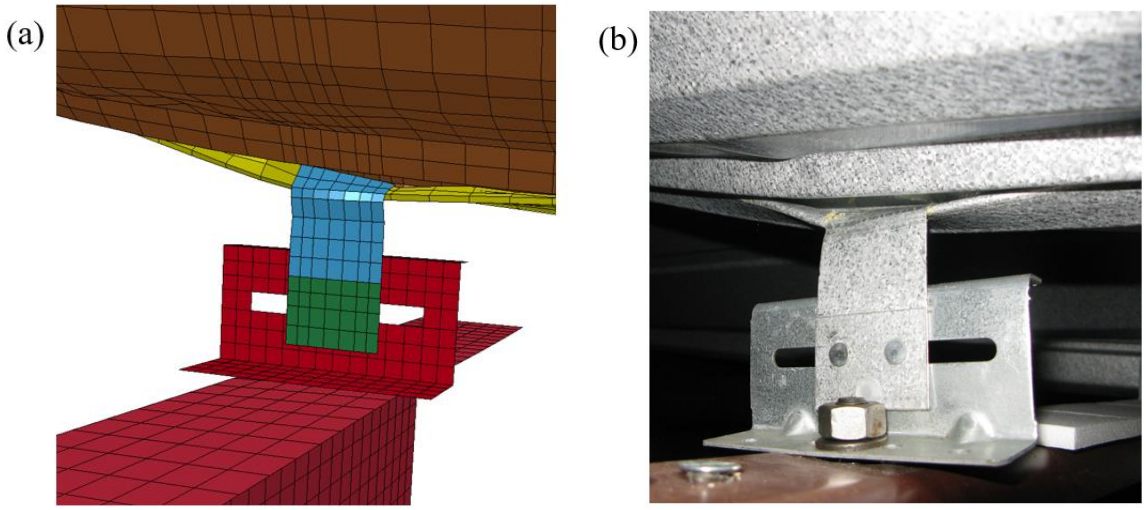

Figure 5.9: Seam opening from (a) FEM and (b) experiment.

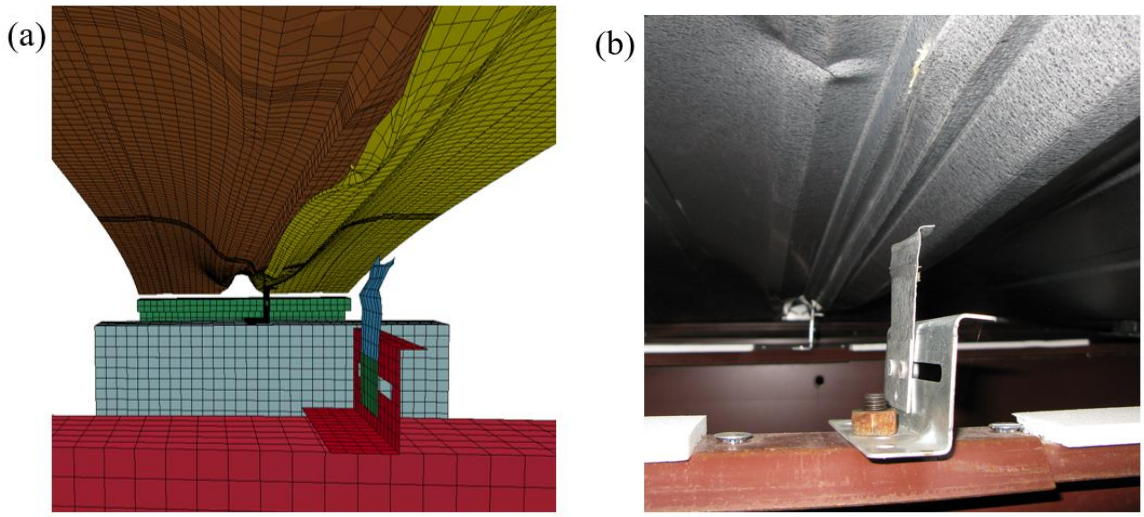

Figure 5.10: Pull-out failure from (a) FEM and (b) experiment.

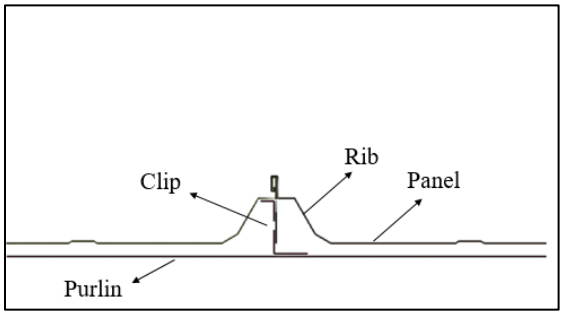

(a) 0 kPa

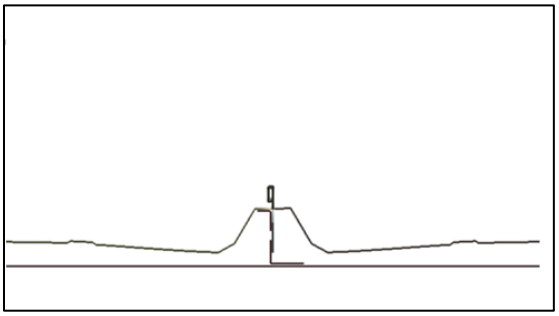

(b) 0.3 kPa

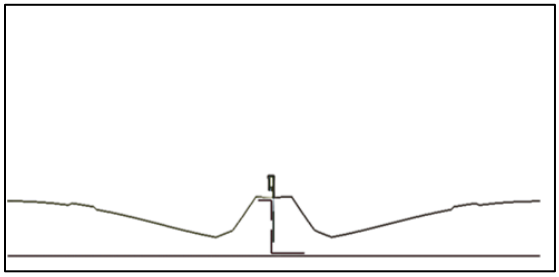

(c) 0.5 kPa

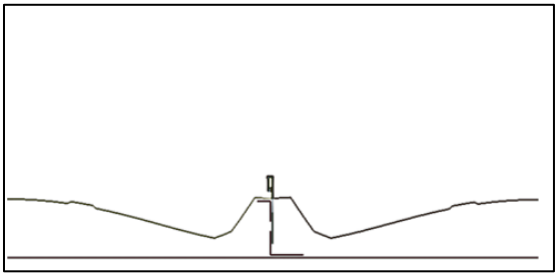

(d) 1 kPa

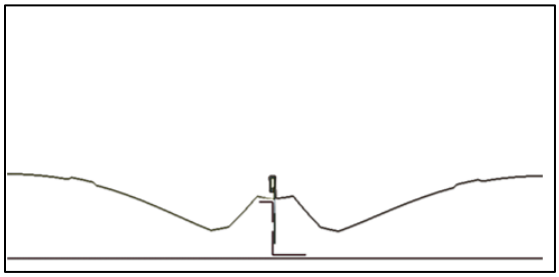

(e) 2 kPa

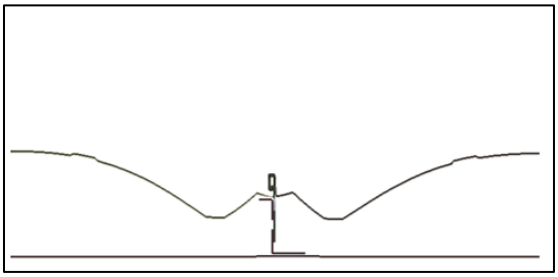

(f) 3 kPa

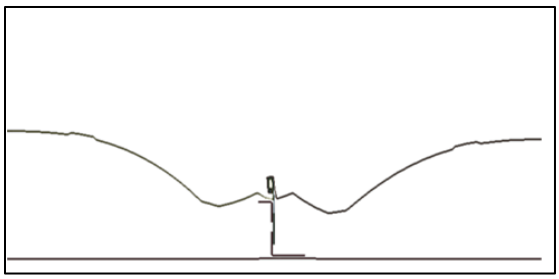

(g) 3.5 kPa

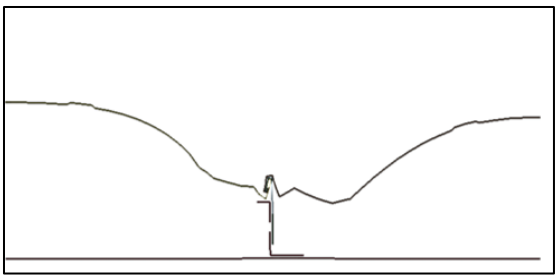

(h) 3.7 kPa

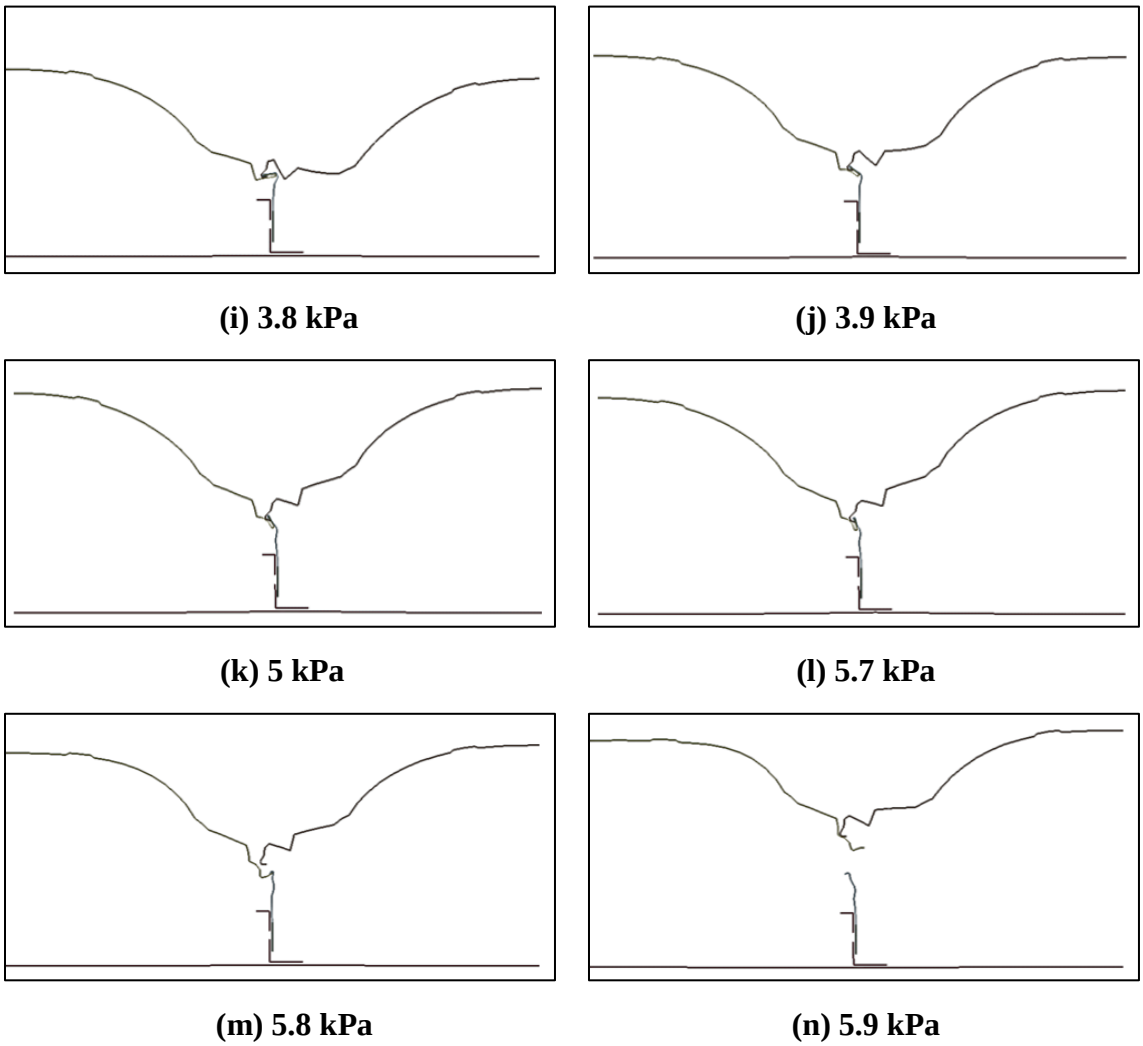

(i) 3.8 kPa **(j) 3.9 kPa**

(k) 5 kPa **(l) 5.7 kPa**

(m) 5.8 kPa **(n) 5.9 kPa**

Figure 5.11: Deformation at the seam under different wind pressure.

Figure 5.12 depicts the Von Mises stress contours of the roof system under different wind pressures. It is seen that stress concentrations occur close to the roof edge when the pressure is 2 kPa, which results in the local buckling at the roof edge. As shown in Figure 5.12 (b), when the pressure reaches 2.5 kPa, portions of the roof components inside the seam in contact with the clips are in the plastic range. As the pressure increases, stress concentrations occur between two adjacent clips and near the seam, which is shown in Figure 5.12 (c). The region of high stress expands with the increment of pressure. When the pressure reaches 3.6 kPa, the region of the roof along the seam is mostly under a state

of high stress. When the pressure rises to 3.7 kPa, the high stress near the ridge edge is released and the region of high stress concentrates in the interior of the roof, as shown in Figure 5.12 (e). The initial location of the global buckling is shown in Figure 5.13. The roof near the seam is crumpled, which results in the drastic deformation of the panel.

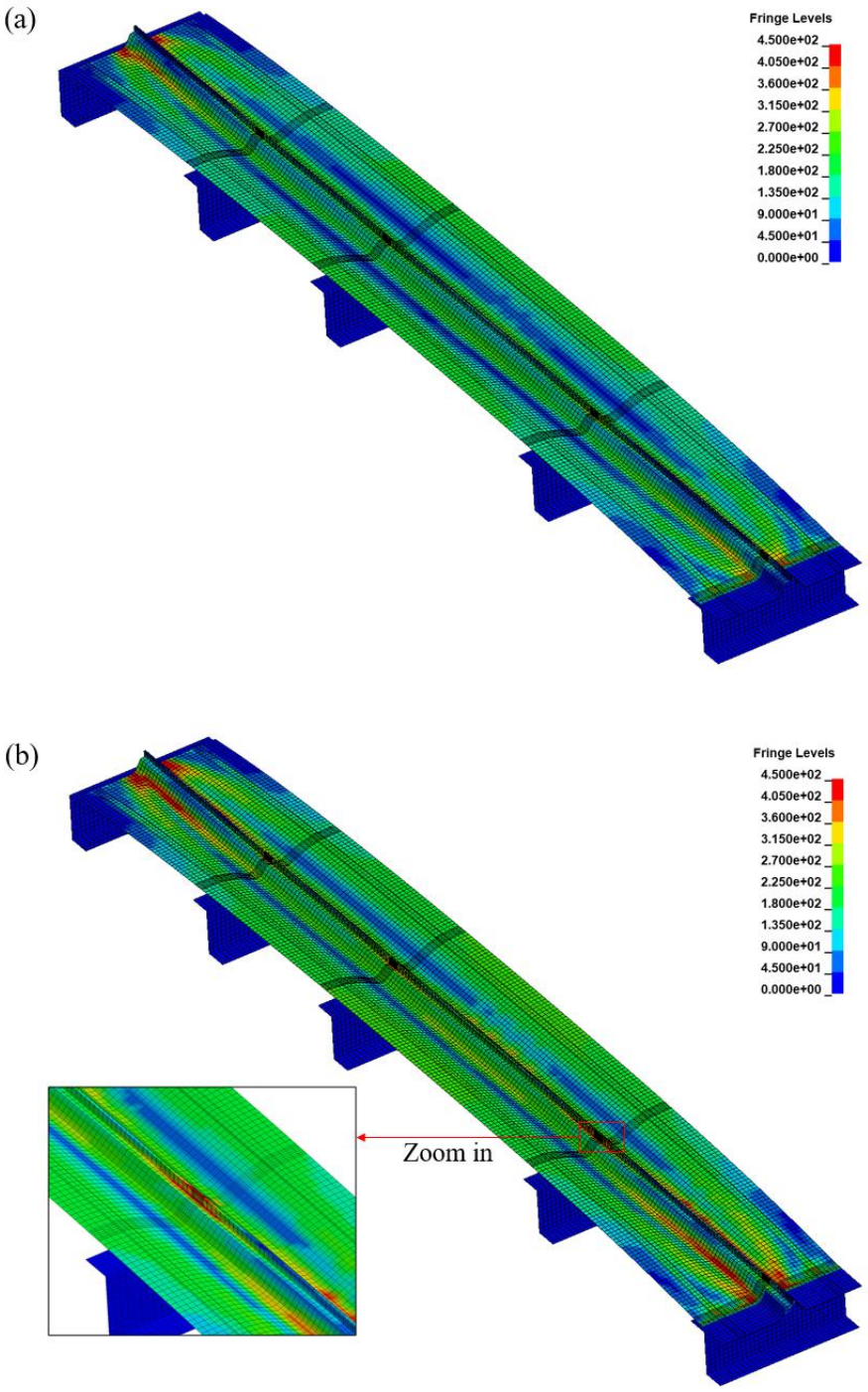

(c)

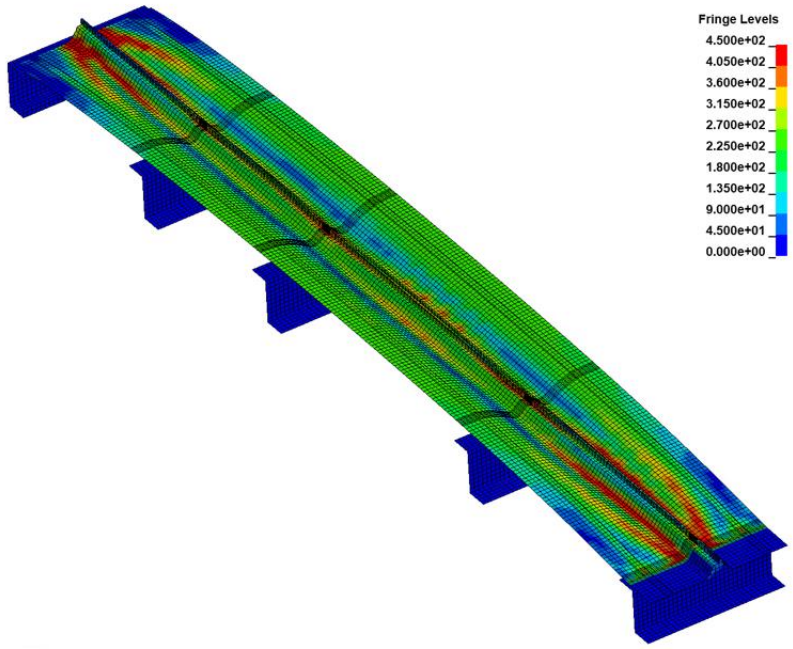
Fringe Levels
4.500e+02
4.050e+02
3.600e+02
3.150e+02
2.700e+02
2.250e+02
1.800e+02
1.350e+02
9.000e+01
4.500e+01
0.000e+00

(d)

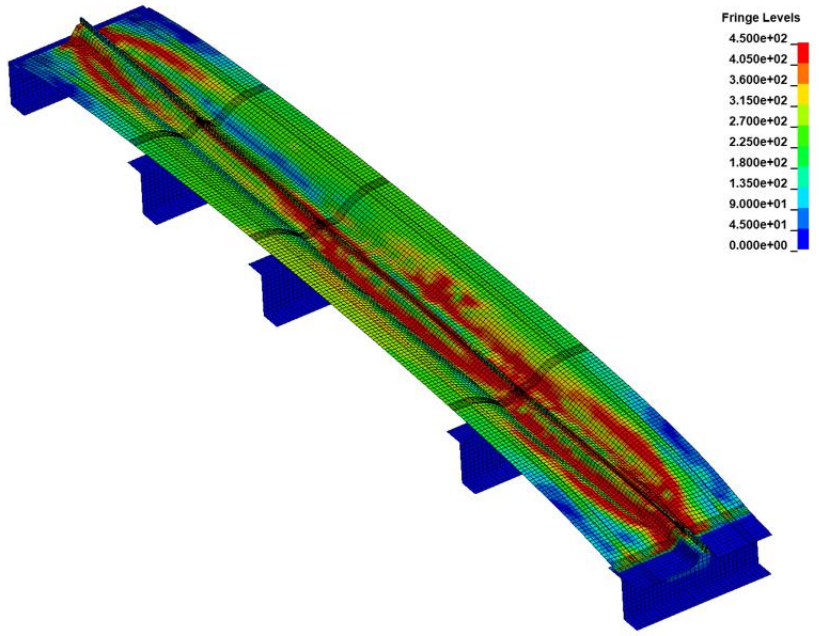
Fringe Levels
4.500e+02
4.050e+02
3.600e+02
3.150e+02
2.700e+02
2.250e+02
1.800e+02
1.350e+02
9.000e+01
4.500e+01
0.000e+00

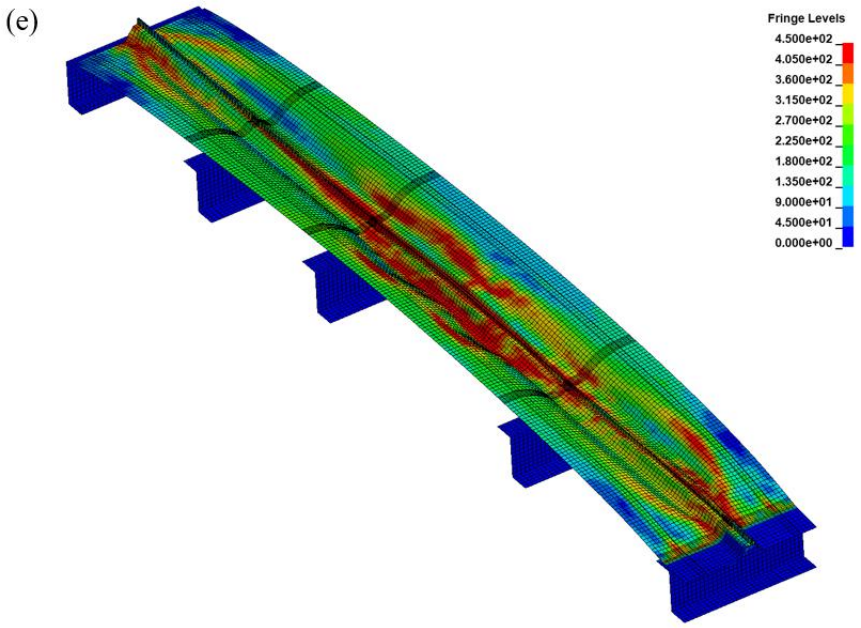

Figure 5.12: Stress contours of the roof system under wind with a magnitude of (a) 2 kPa, (b) 2.5 kPa, (c) 3 kPa, (d) 3.6 kPa, and (e) 3.7 kPa.

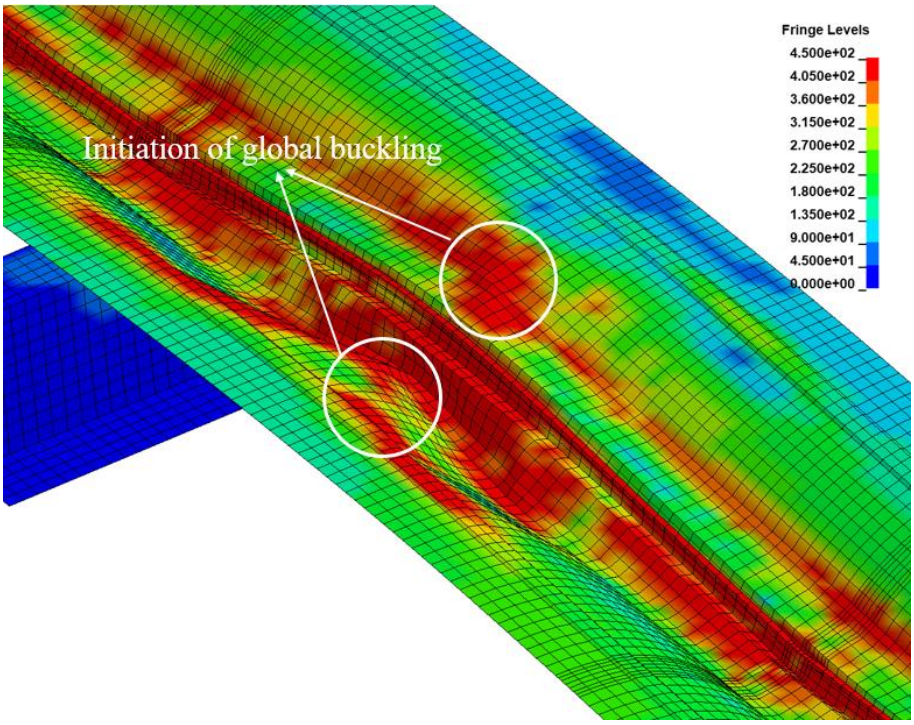

Figure 5.13: Stress contours near the location of initial global buckling.

Figure 5.14 shows the loads going to the fasteners at the eave edge. When pressure is below 3.7 kPa, the relationship between load and pressure is still nonlinear. At higher pressure, a greater amount of load transfers to the edge fasteners, which proves why the ratio of the induced load to the total applied load decreases at a higher pressure in Table 4.1. When pressure is between 3.7 kPa and 4.2 kPa, the load decreases first, then increases as pressure increases. This is due to the complicity of overall buckling and load redistribution.

When comparing the clip loads at the limit state to the geometric area loads, which is shown in Table 5.2. The geometric tributary area method overestimates the load transfer to clips, and the maximum deviation is up to 116.8% (clip 122). Since clip 122 is located near the eave edge, by comparing the data in Figure 5.14, it can be concluded that fewer load transfers to the clip near the eave edge at higher pressure due to the effects of edge fasteners. For the most highly loaded clip (clip 122), the geometric area method still overestimates the load by 8.07%.

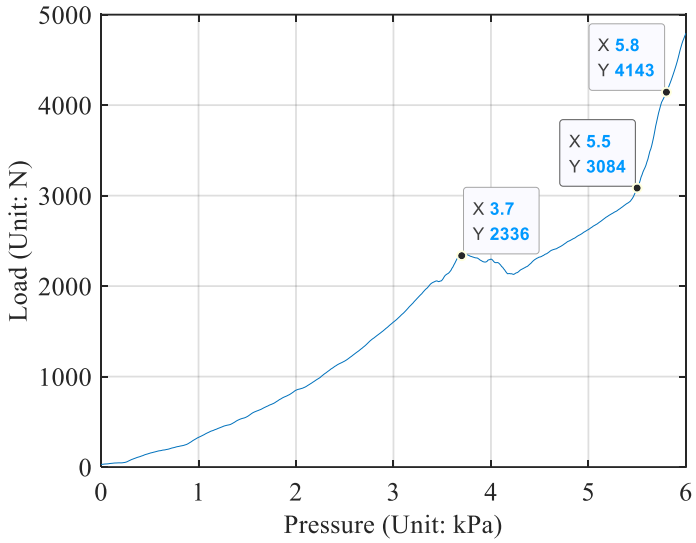

Figure 5.14: The relationship between pressure and loads going to the edge fasteners.

Table 5.2: Comparison between estimated clip reaction using different methods

Clip	FEM (N)	Geometric area load (N)
78	2468	3317
100	3440	4378
122	3570	3859
144	1338	2901

5.4 Summary

A FEM was used to study the performance of the SSMR system under uplift wind load. Clip reactions and deflections of roof panels from FEM and experiment were compared. The good agreement between the experiment and FEM indicates that FEM is suitable to simulate the response of the SSMR system.

The explicit analysis was able to reveal the progression of failure. The initial location of global buckling and the disengagement failure between panel and clip at the seam were simulated, which were consistent with the observations from the experiments. Stress concentrations occurred at the connection between clips and seams first. Later on, the area of stress concentration extended along the seam. It is found that the stress concentration causes the deformation of roof panels, which results in global buckling and load redistribution. The buckling and seam opening is connected to the most highly loaded clip. More load transfers to the edge fasteners at edge fasteners which causes the overestimation of clip load using the geometric area method. Thus, we should pay attention to these weaker parts of roof systems.

6. Numerical simulation (load sharing)

As described in chapter 5, the previous simulation is based on explicit analysis. Although it could simulate the progression of failure, it is time-consuming. The previous case of explicit analysis was run on a workstation with 8 cores and the total computational time is more than 120 hours. Therefore, a more time-saving approach is needed.

People are more concerned about load distribution, as well as the effects of boundary conditions under moderate wind loads (i.e., under normal use) since the roof systems are at the elastic stage and have no irreversible plastic failure. Thus, the implicit analysis is adopted in the following analysis and the maximum applied pressure is 2 kPa.

6.1 Description of the finite element model (implicit analysis)

The commercial software, ANSYS, was used in the implicit analysis. The difference between implicit and explicit simulation is specified in section 2.3.2.1. Experiment 1 is chosen as the basis for simulation, as shown in Figure 6.1(a). The roof panels, clips, and purlins were created based on the real dimensions, while the fasteners and screws were considered as constraints in numerical simulation. The 4-node shell element SHELL181, which has 6 degrees of freedom at each node and can consider bending stiffness for large deflections, was used to create the model. The definitions of material property and the boundary restraints are the same as that for the explicit analysis, which is given in section 5.1. The contact elements TARGE 170 and CONTA 173 were adopted to consider the face-to-face contact between the roof components inside the seam.

As shown in Figure 6.1(a), the panel were constrained at the eave edge and ridge edge, which can be regarded as fixed boundary conditions. In order to examine the influence of boundary conditions (fixed boundary conditions and free boundary conditions), the node restraints at the eave edges were released and the back-up plate at the ridge edge was

removed to simulate the free boundary condition. The symmetry boundary conditions were applied along the length of the roof panel due to the symmetry of the roof structure and applied loads. Due to the greater efficiency of implicit analysis, a 6-panel-wide roof model could be considered, which helps us to investigate the load transfer perpendicular to the seams. The finite element model with different boundary conditions is given in Figure 6.1. Uniform pressures were applied on the roof panel, which were increased linearly until 2 kPa.

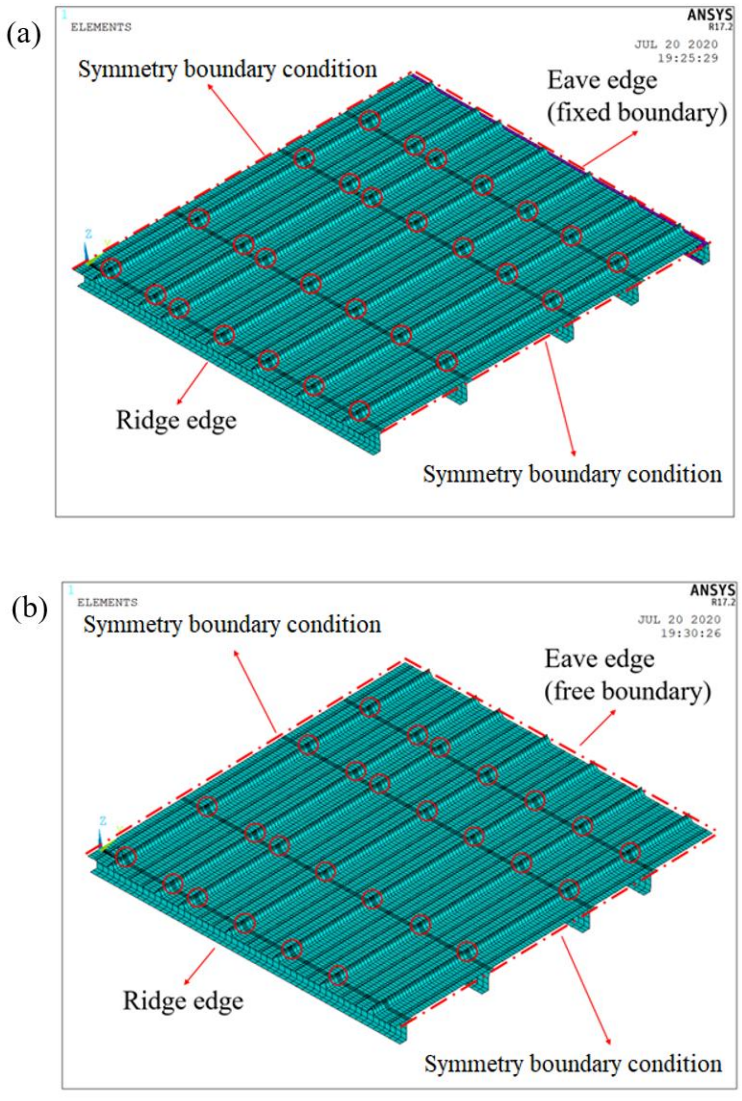

Figure 6.1: Finite element model with (a) fixed boundary condition and (b) free boundary condition.

6.2 Model validation and load sharing among clips

Figure 6.2 reveals the clip reactions of SSMR systems with the fixed boundary condition under the linearly varying pressures. The results presented were acquired from the experiment, FEM, and tributary area method. For the tributary area method, the clip reaction is obtained by multiplying its geometric tributary area with the applied pressure. By comparing the clip reactions between FEM and experiments, it can be seen that the main trends are captured well. For the data from the experiments, there are significant differences between the two clips, even though they have the same geometric tributary area. This may be due to the complexity of the real structure, which results in the load transfer perpendicular to the seam. By calculating the average value of the curves with the same geometric tributary area from the experiment, a new curve is obtained, which is shown in Figure 6.3. It can be assumed that part of the clip loads transfers to the clips at the adjacent seams. By averaging the clips loads on the adjacent seams, there is a good agreement between the experiment and FEM. It demonstrates that FEM is an effective approach to model the SSMR system, within the variation occurring in the actual roof.

As described in the previous chapter, load redistribution among clips is noted for higher pressures. At higher pressure, a greater amount of load transferred to the clips near the ridge (clip77 and clip78), with a smaller amount of load transferred to the other clips. The most highly loaded clip (clip 99 and 100) has a reduction of 13% at 2 kPa when compare to the estimated clip load using the tributary area method. The experimental results suggest that, for the most highly loaded clip, the geometric tributary area method contains a deviation of about 13%; and up to 93% for the clips near the ridge.

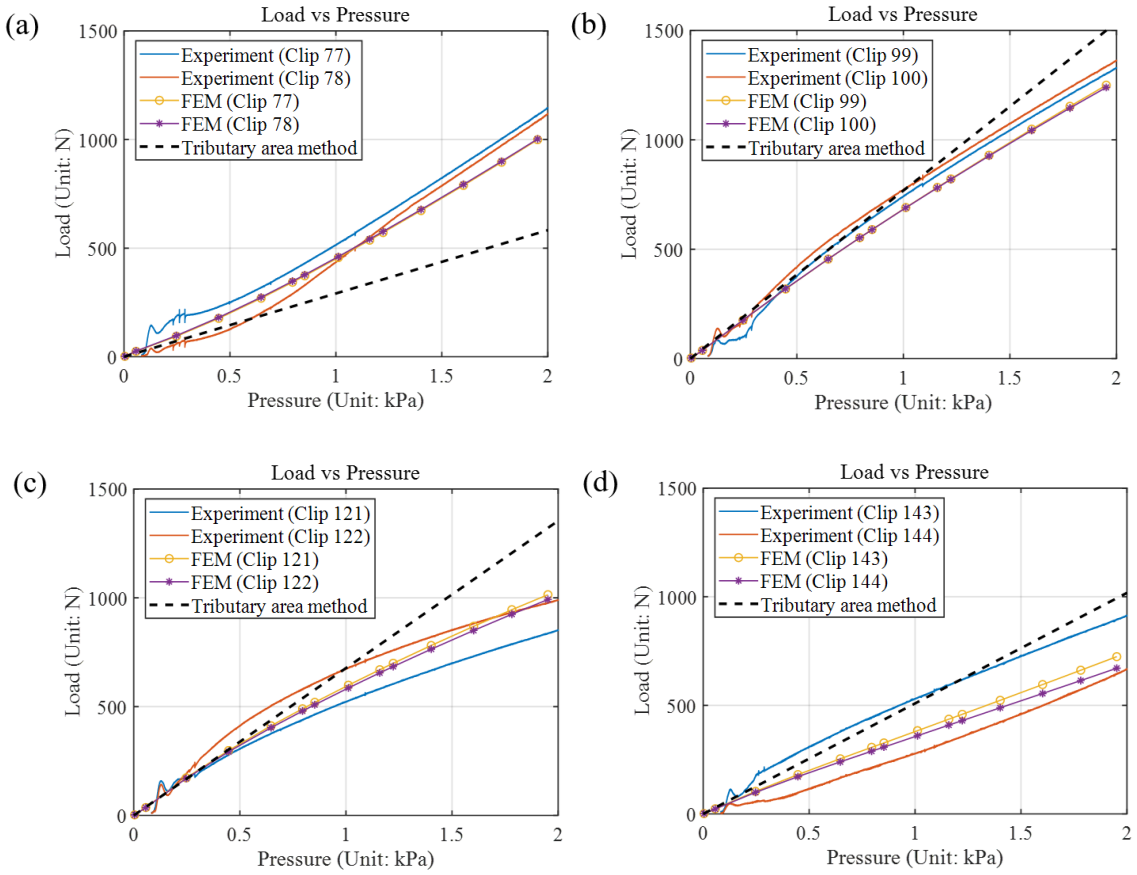

Figure 6.2: Load-pressure curves of clips with fixed boundary conditions for experiment 1 (see Figure 4.1).

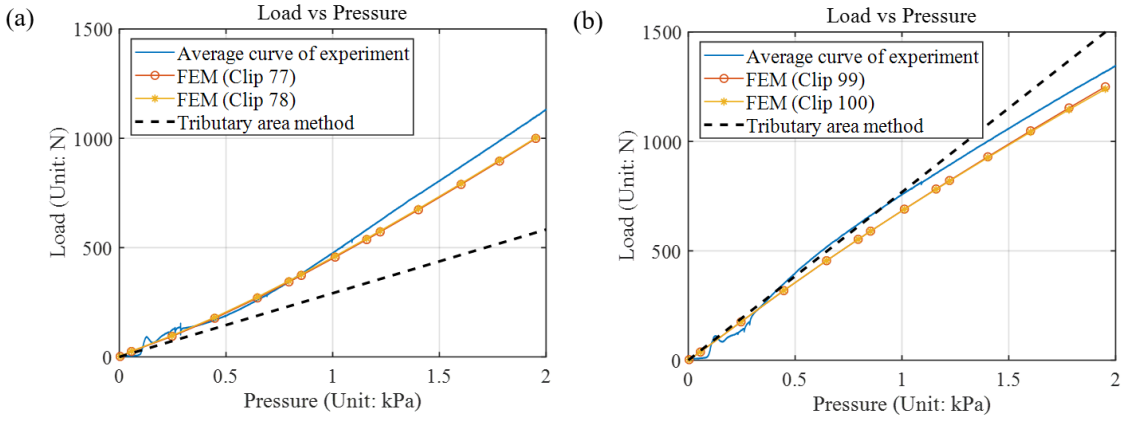

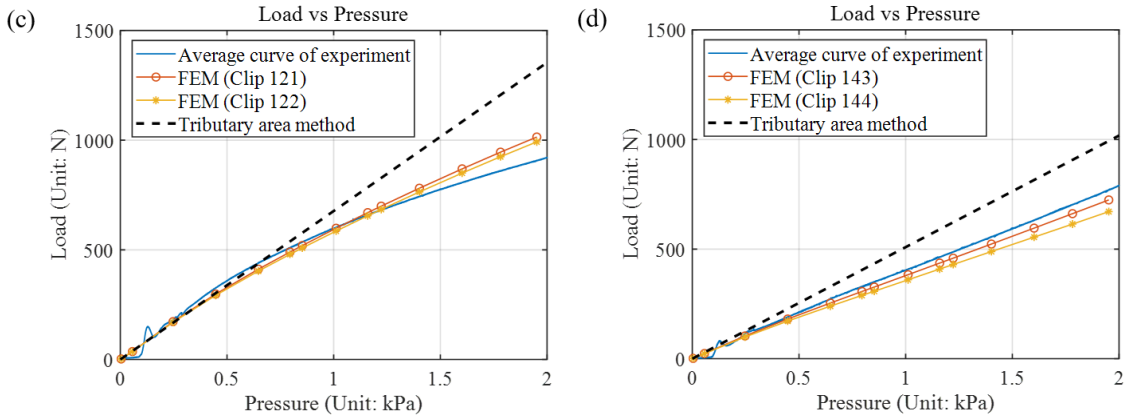

Figure 6.3: Load-pressure curves of clips with fixed boundary conditions by averaging the curves from experiment 1 (see Figure 4.1).

6.3 Effects of boundary restraints

The effects of the boundary conditions were analyzed. Figure 6.4 illustrates the deflection along the panel centerline (i.e., midway between two adjacent seams) with the two different boundary conditions using FEM. The origin of the coordinate system is set at the ridge of the roof, as shown in Figure 6.5. For the roof system with fixed boundary conditions, the displacements are small near the ridge and eave edges of the roof due to the restraints at the boundary. The largest displacement happens near the middle of the panel. In contrast, the deflection of the panel with the free boundary condition at both ends is almost constant along the length. By comparing Figures 6.8 (a) and 6.8 (b), it is noted the deformation of the roof panel with the free boundary condition is much larger than that with the fixed boundary condition under the same pressure. The deformation of the panel is greatly reduced (by over 50%) due to the restraints at the ends of the panel.

Figure 6.6 presents the clip reactions of SSMR systems with the free-end boundary conditions. The relationship between clip reactions and pressures is nearly linear, which indicates that the load redistribution among clips is insignificant when compared to the

fixed conditions. By comparing Figure 6.3 and Figure 6.6, it can be concluded that the boundary conditions have a notable effect on load sharing. For the free boundary condition, load redistribution is not obvious even though the vertical displacement of the panel is large. For the fixed boundary condition, load sharing among clips changes with the increase of the pressure, since the ridge clips take relatively more load and the other clips take relatively less load at higher pressure. As a result, the change of load is shown in Table 4.1, which is due to more load going to the ridge and eave fasteners at higher loads. What's more, the tributary area method underestimates the load of ridge clips and overestimates the load of other clips for free boundary conditions and fixed boundary conditions.

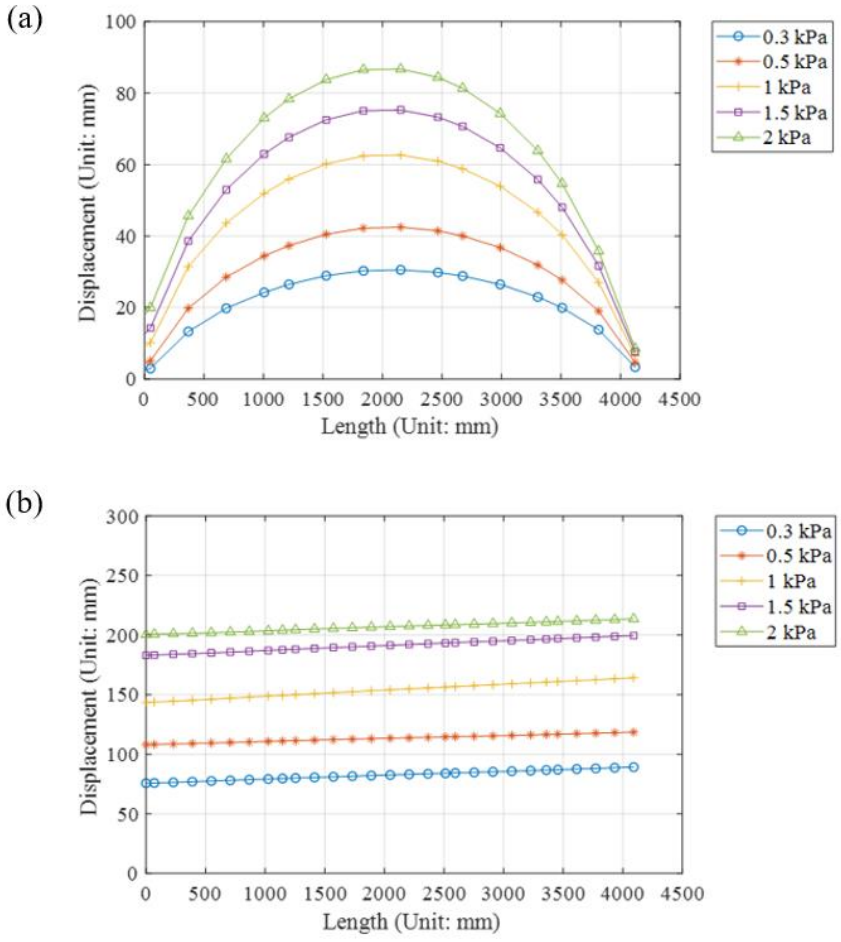

Figure 6.4: Deformation of the panel along panel centerline under different loads with (a) the fixed boundary condition and (b) the free boundary condition.

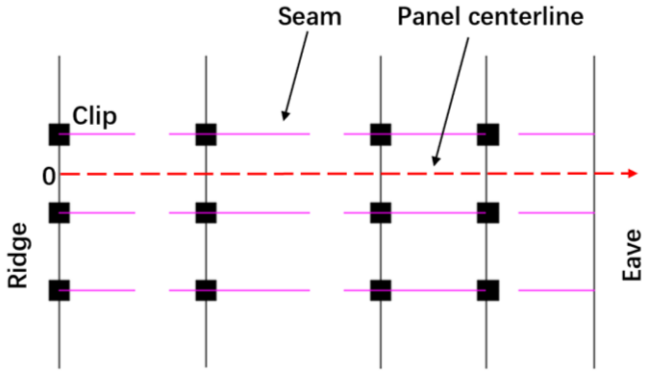

Figure 6.5: Location of panel centerline.

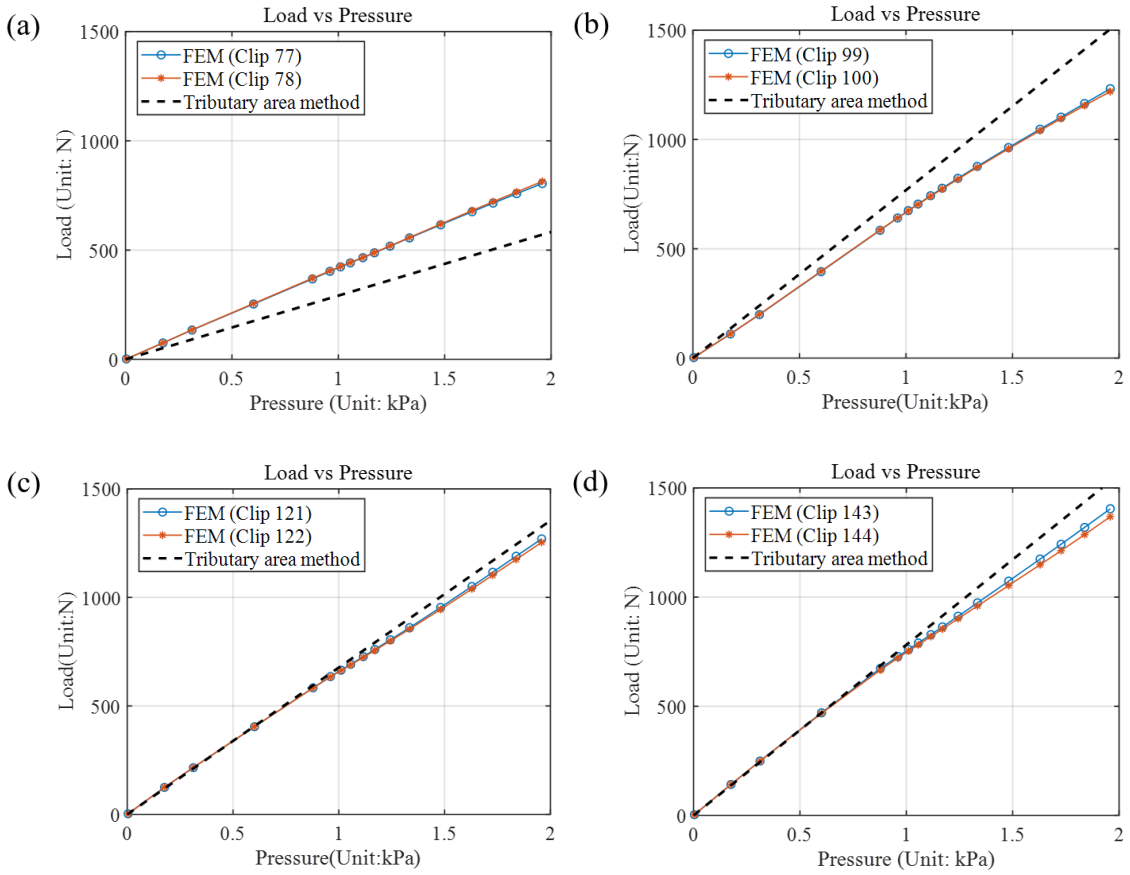

Figure 6.6: Load-pressure curves of clips (free boundary condition).

6.4 Wind load transfer to the gable end and eaves of the SSMR system

As mentioned earlier, the geometric tributary areas for design are typically defined by considering half of the distance between fasteners. Under this approach, it can be assumed that half of the applied load between the edge of the roof and the clips installed adjacent to the edges is transferred to the edge fasteners. The geometric tributary area of the roof edges and the width d_i of each geometric tributary area is shown in Figure 6.7.

There were no load cells installed at the screw fastener located at the roof edges so that the loads transfer to the edges could not be measured directly. Since the total loads applied on the roof and loads measured by load cells are already known, the loads transfer to the eave edges or gable edge can be obtained as:

$$Load_{Edge} = Load_{Total} - Load_{Clips} \tag{6.1}$$

where $Load_{Edge}$ is the load transferred to the gable edge or eave edge; $Load_{Total}$ is the total load applied on the roof; $Load_{Clips}$ is the load transferred to the clips. This equation assumes that the edge loading is uniform along the edge since fasteners were installed at equal spacing.

Knowing the transferred load at the edges and considering the same length for tributary areas, *L*, the new width, d_i, for each tributary area can be calculated as:

$$d_i = Load_{Edge}/L \tag{6.2}$$

Nasiri (2019) measured the calculated widths of tributary areas on the roof edge orderly by applying uniform pressure with a magnitude of 500 Pa on the full-scale SSMR. Figure 6.8 depicts the positions of applied uniform pressure in her study.

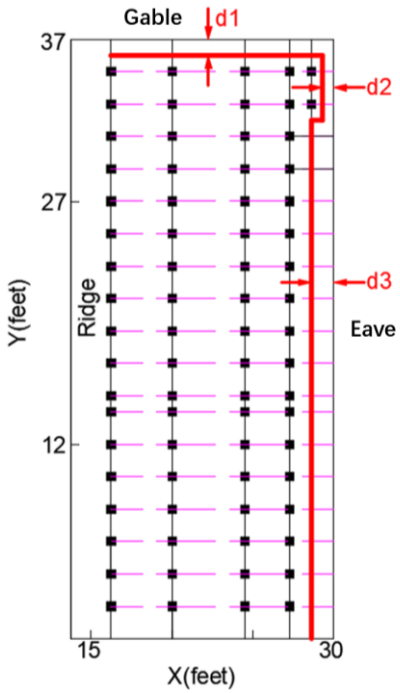

Figure 6.7: Geometric tributary areas of the edge of the roof (Nasiri, 2019).

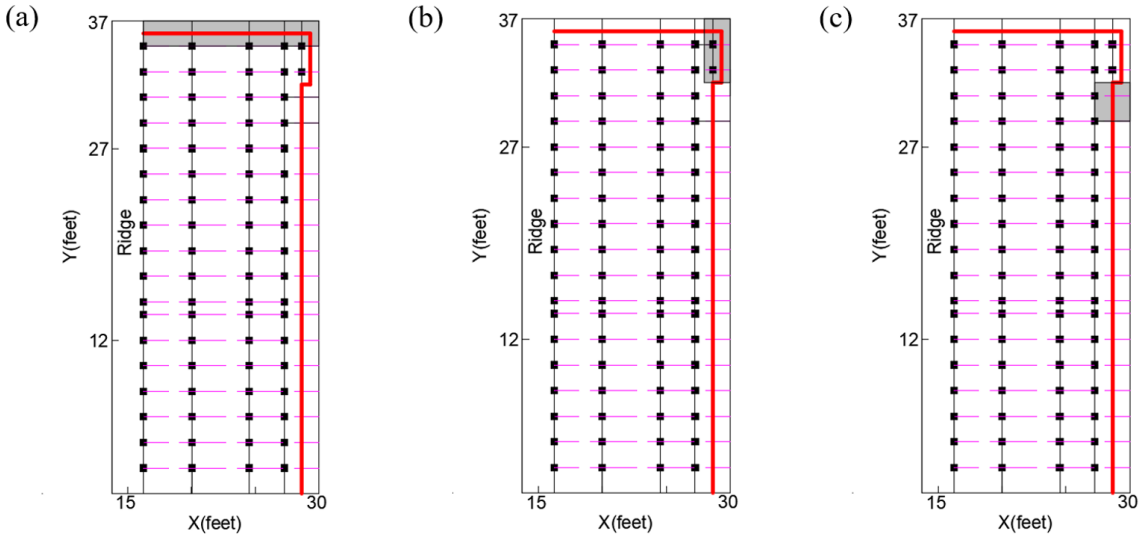

Figure 6.8: Positions of applied uniform pressure (a) along the gable edge (b) at the corner of the roof, and (c) beside the eave edge.

As described in the previous section, FEM is a reasonable method for simulating the response of SSMR subjected to wind pressure. In order to compare the data to Nasiri (2019),

the same test zone was chosen, which is given in Figure 6.9. Thus, the finite element model of SSMR near the gable end was created. Different from the full-scale experiment, loads transfer to the roof edges could be measured directly using FEM. As shown in Figure 6.10, three complete roof panels were involved. Since there was no relative movement between the rack support and the panel, the nodes at the gable end were fixed. The symmetry boundary conditions were applied along the length of the roof panel. The definitions of the material property, contact, and element type are the same as the previous model used in this chapter. Uniform pressures were applied on the corresponding roof panel as shown in Figure 6.8, which increased linearly until 2 kPa. These procedures were designed to repeat the test of Nasiri (2019).

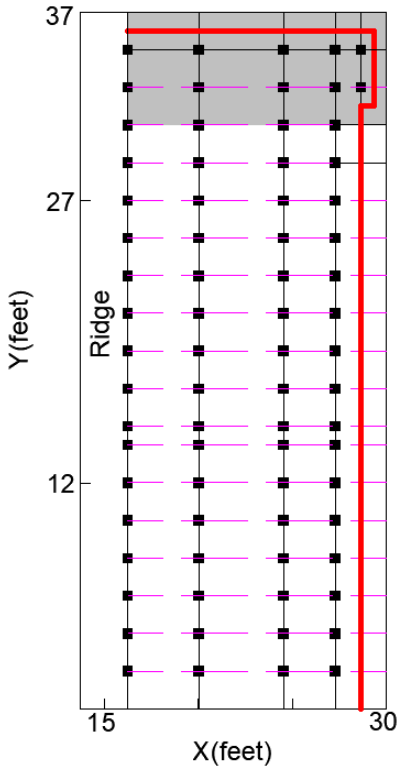

Figure 6.9: Modeling area of FEM (filled with grey).

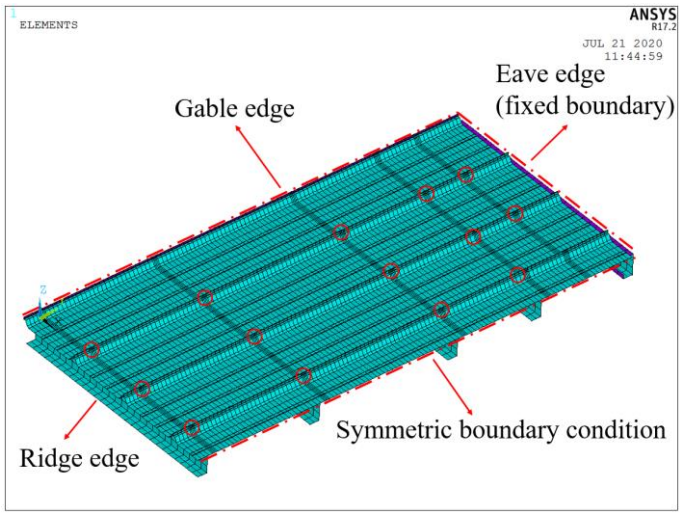

Figure 6.10: Finite element model of roof systems near the gable edge.

Although the fasteners and screws along the gable edge and eave edge were not physically modeled, their effects were simulated by constraining the nodes at the gable edge and eave edge. Since it is convenient to get the forces of nodes along the gable edge and eave edge, the loads at the gable edge and eave edge could be obtained separately. The new width, d_i, for each tributary area can also be obtained using equation (6.2), which could be compared with the result from the geometric tributary area method and full-scale experiment of Nasiri (2019). A comparison between the values of widths d_i using different methods is provided in Table 6.1. It is noted that the widths based on the geometric tributary area method are less than that based on the experiments for all three positions. The width, d_1, using full-scale experiments is 17% larger compared to using the geometric tributary area method. The width, d_3, is 20% larger. The greatest difference happens along the eave edge, at the corner of the roof. The width, d_2, from full-scale experiments is twice the one suggested by the geometric tributary area method. This indicates that the geometric tributary area method underestimates the loads transferred to the roof edge. On the other hand, the widths from FEM match well with those from the full-scale experiments. The largest difference in widths obtained from full-scale experiments and FEM is only 3.7%, which again, supports the accuracy of FEM.

Figure 6.11 depicts the relationship between applied pressure and widths of tributary areas using FEM. It is noted that the widths change with pressure. When pressure is over 0.5 kPa, the widths d_2 and d_3 increase with rising pressure, while the width d_1 decreases slightly with rising pressure. It can be concluded that the eave edge is more vulnerable under high wind pressures as a result of taking a greater portion of the load. Thus, the eave edge is more vulnerable under high wind pressure when using the geometric tributary area method to design the fasteners at the eave edges. For example, the width d_2 is 1.5 ft when pressure is 2 kPa. This is 120% larger than the geometric tributary area method suggests and even 10% larger than the value from the experiment, which was conducted at a lower load level.

Table 6.1: Comparison of calculated widths of tributary areas of roof edges

	Width from geometric tributary areas method	Width from experiment (500 Pa) (Nasiri, 2019)	Width from FEM (500 Pa)
d_1 (gable)	1.00 ft	1.17 ft	1.19 ft
d_2 (corner)	0.68 ft	1.37 ft	1.36 ft
d_3 (eave)	1.37 ft	1.64 ft	1.58 ft

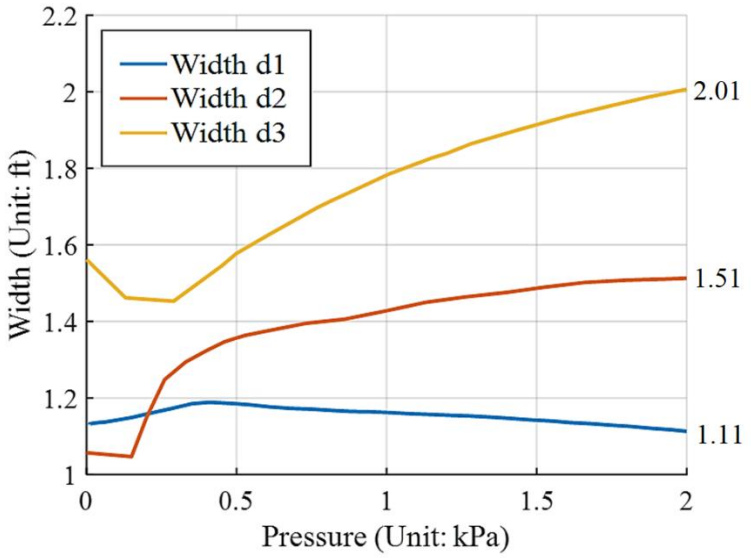

Figure 6.11: Widths of tributary areas at roof edges versus pressure.

6.5 Summary

The mechanism of load sharing, as well as the effects of boundary conditions, was investigated. The comparison of the SSMR system with fixed and free boundary conditions shows that the boundary conditions have a notable effect on load sharing. The restraints at the ridge and eave of the panel affect the load distribution and cause load redistribution when the boundaries are fixed. For the SSMR system with fixed boundary conditions, it is found that as the panel deforms, the relationship between clip reactions and pressure does not remain linear. A greater proportion of the load transfers to the ridge and eave edge of the SSMR systems at higher pressure. However, for the SSMR system with free boundary conditions, the relationship between clip reactions and pressure is nearly linear even though the roof deformation is large.

The geometric tributary area method generally underestimates the clip reactions at the ridge of the roof (about 93%) and overestimates loads for most highly loaded clips (up to 13%). However, current standards (e.g., ASCE 7) usually use the geometric tributary areas

method which eliminate the influence of boundary conditions on load distribution among clips. In comparison, the results from FEM match well with those from experiments.

The geometric tributary area method underestimates the amount of load transferred to the edges of the roof, especially at the corner of the roof, i.e., the fasteners at the gable and eave edges take up more of the load than that calculated by the geometric tributary area method. FEM provides a reliable approach for the load transfer to the edges. FEM results indicate that the tributary area of the eave edges increases with rising pressure. As a result, the eave edge will be more vulnerable under high wind loads, with more than twice the load going to the edge than expected based on purely geometric edges.

7. Influence function of clips using FEM

It can be seen the geometric tributary area method is inaccurate to calculate the clip reaction of SSMR systems since the influence of boundary conditions cannot be considered. However, the influence function method should provide a more precise estimation of clip reaction compared to the geometric tributary area method since the influence functions of the clip reactions are related to the roof structure (e.g., boundary conditions) regardless of the type of load (Nasiri, 2019). Once the influence functions of clip reactions are determined, it is possible and efficient to study the clip reactions under various wind pressure distributions.

7.1 Description of influence function using FEM

The two finite element models created in chapter 6 (see Figures 6.1(a) and 6.9) were used to obtain the influence function of clips. A series of point loads with the magnitude of 100 N was applied to the finite element models successively, and clip reactions were recorded at the same time for the locations shown in Figure 7.1. The locations of the concentrated unit load are marked with red circles and there are 625 loading cases in total. As mentioned in section 2.2.1, the influence function of clip reactions can be represented as a matrix in which each element of it is the ratio of the measured load on the clip to the applied point load.

As shown in Figure 7.1, there are two types of clip arrangement on the right side of the roof. one has four clips along the seam and the other has five. The standing seams can be assumed as 4-span and 5-span beams by considering the clips and fastener restraint at the eave edge as supports, as depicted in Figure 7.2. Clips can be categorized into six types based on the positions of the clip location, which refer to type I, type II, type III, type IV, type V, and type VI, following the notation of Nasiri (2019).

The locations of different clip types are given in Figure 7.3. Type I refer to the clips installed on the ridge of the roof. Type II and type III refer to the second and third clips on the standing seams from the ridge respectively. The fourth clip on the standing seams for 4-span beams is named as type IV. The fourth and fifth clips on the standing seams for 5-span beams are named as type V and type VI respectively.

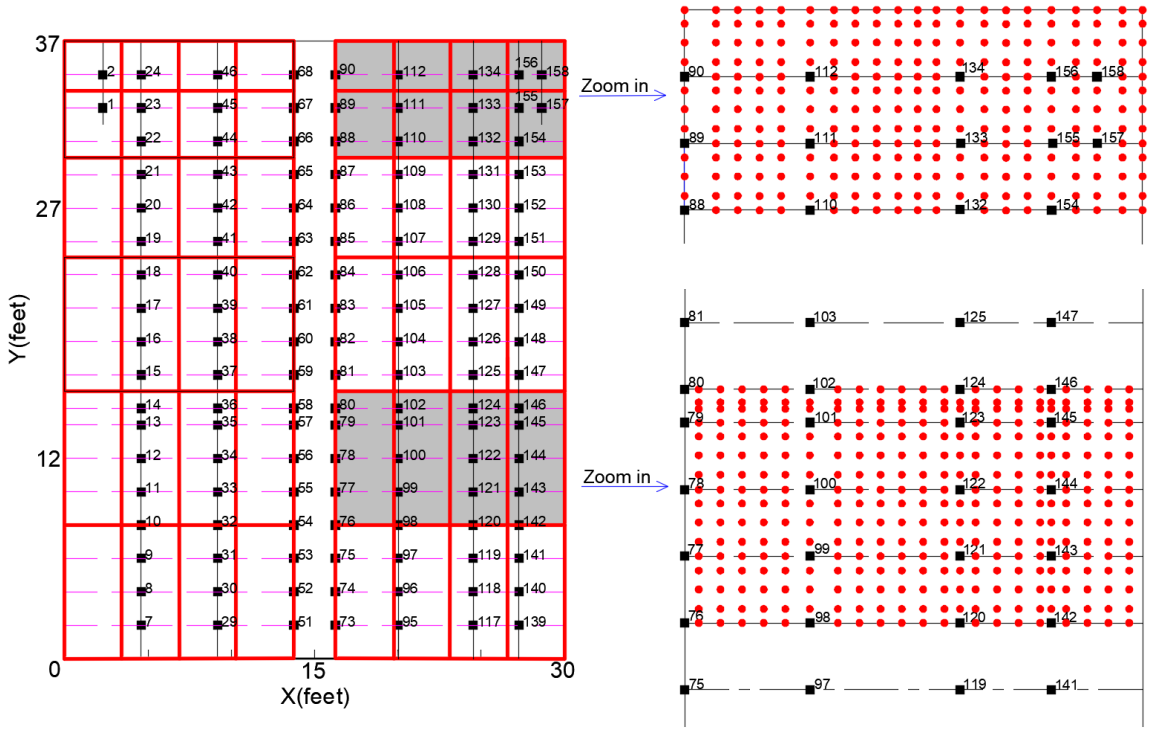

Figure 7.1: Locations of applied point load (red circle).

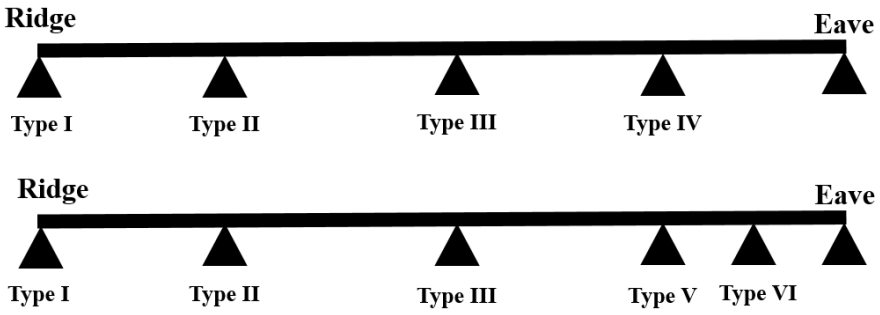

Figure 7.2: Idealized 4-span and 5-span beam models of standing seams.

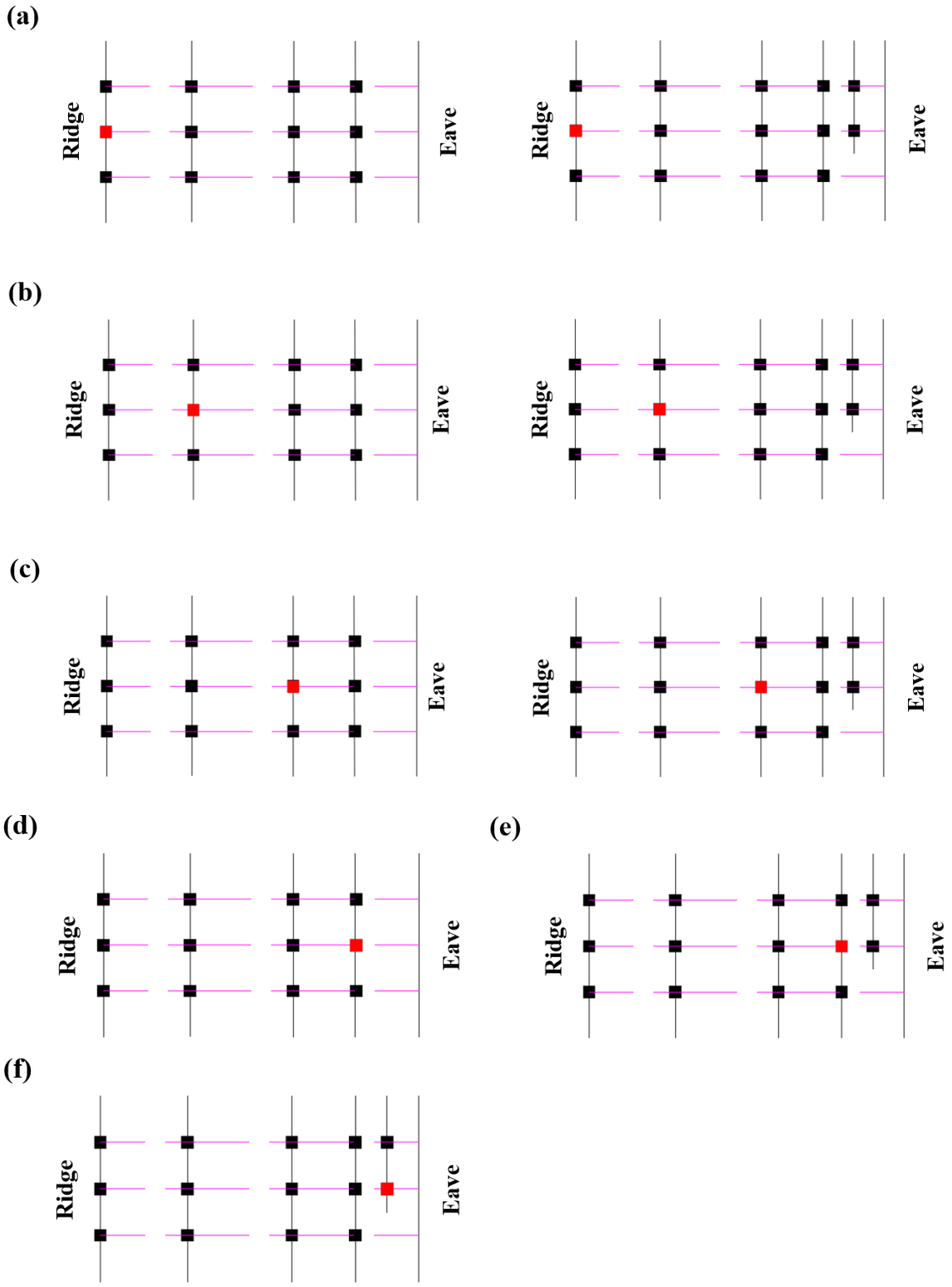

Figure 7.3: Locations of different clip types (red square): (a) type I, (b) type II, (c) type III, (d) type IV, (e) type V, and (f) type VI.

7.2 Influence function of clips using FEM

Figure 7.4 depicts the influence function of a type I clip over the area of two panels adjacent to the standing seam using FEM. The largest value of influence function is about one and it is located at the ridge clip. The influence function drops to zero on the adjacent seams. It can be observed that the influence functions drop to about zero on the adjacent seams. The changes of influence function along the seam for type I clips are shown in Figure 7.5. It can be observed that the clip reaction is influenced by applied load all along the seam.

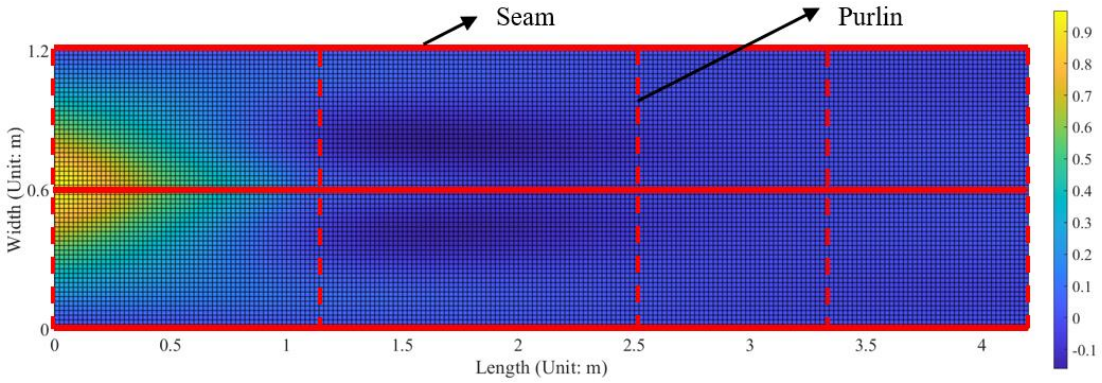

Figure 7.4: Influence function of a type I clip over the area of two panels adjacent to the standing seam using FEM.

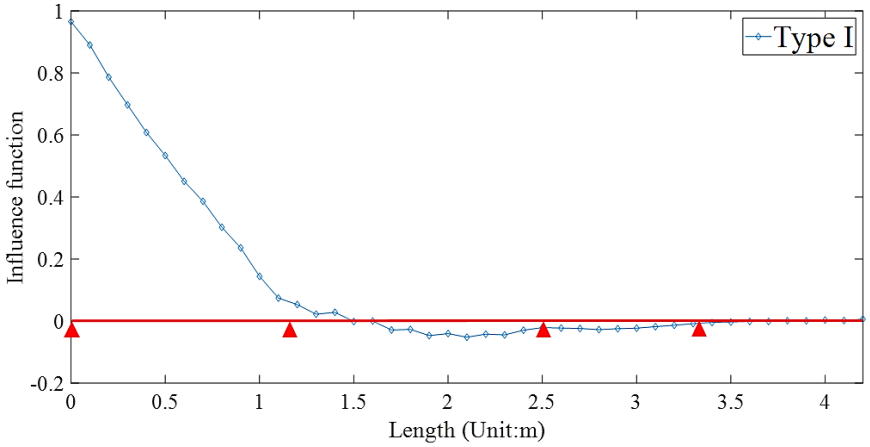

Figure 7.5: Influence function of clip reaction along the seam (Type I clip) Note: triangles represent the installed clips.

Figure 7.6 depicts the influence function of a type II clip using FEM. The influence function has a magnitude of 0.9 at the location of the clip and drops to zero at the adjacent seams. Figure 7.7 shows the changes of influence function along the seam for type II clips with installed load cells. It can be observed that the influence function at the second clip drops linearly to about zero at the adjacent clips. Note that the influence function is not equal to 1 right at the clip location because the performance of installed clips acts as vertical springs rather than simple supports (Nasiri, 2019)

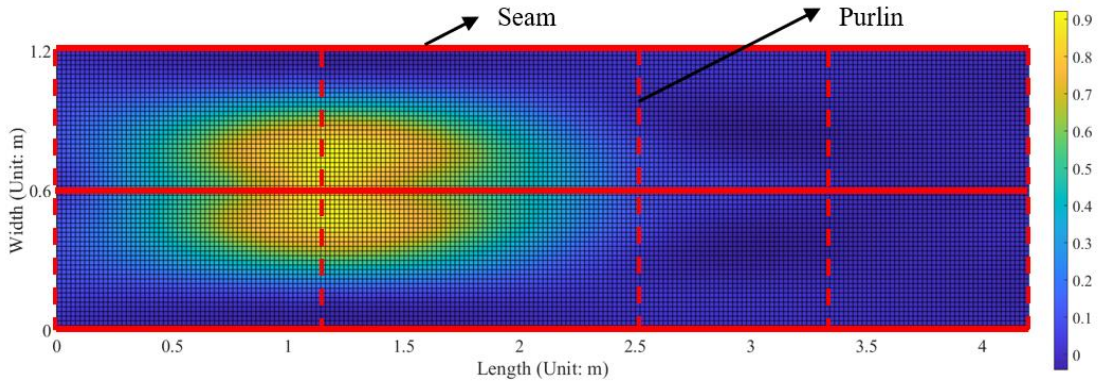

Figure 7.6: Influence function of a type II clip over the area of two panels adjacent to the standing seam using FEM.

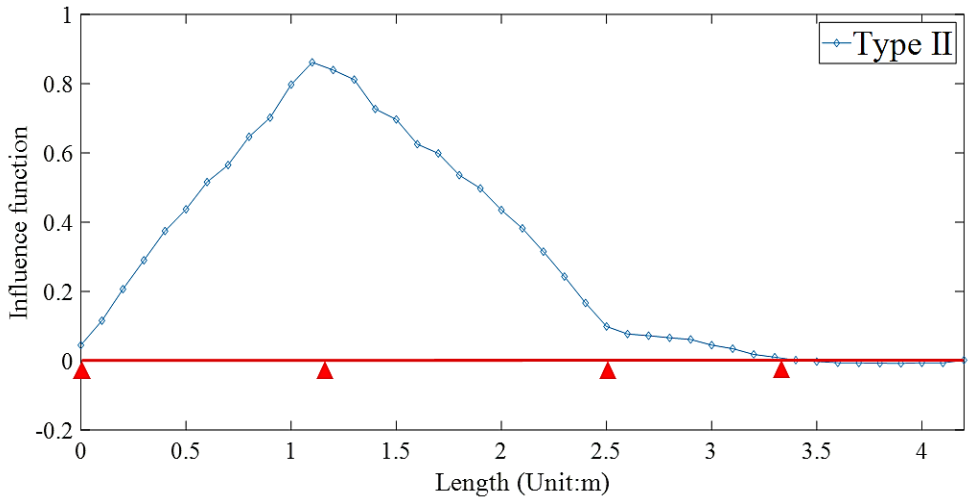

Figure 7.7: Influence function of clip reaction along the seam (Type II clip).

Figure 7.8 shows the influence function of a type III clip and the changes of influence function of the clip reaction along the seam are shown in Figure 7.9. The changes of influence function follow the same trend. However, it is noted the maximum influence function that occurs at the third clip is about 0.8, which is a little smaller than the maximum influence function of the previous clips.

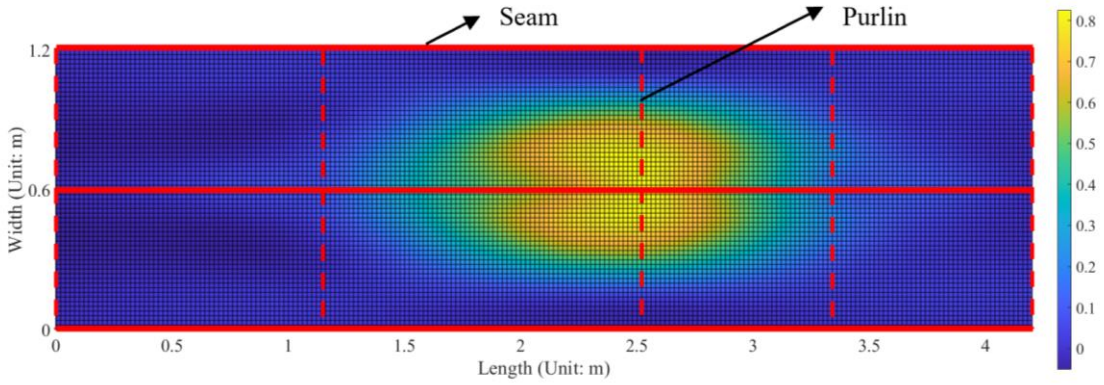

Figure 7.8: Influence function of a type III clip over the area of two panels adjacent to the standing seam using FEM.

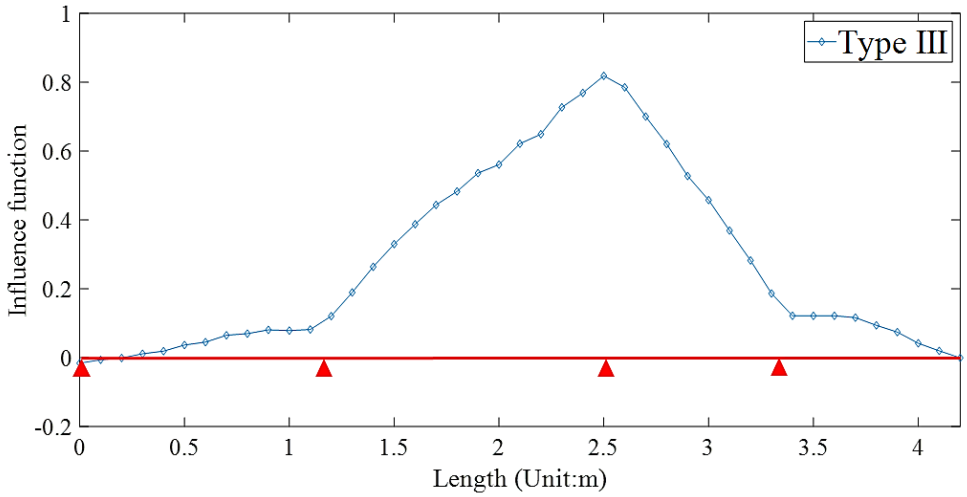

Figure 7.9: Influence function of clip reaction along the seam (Type III clip).

The type VI clip and type V clip are the fourth clip for 4-span and 5-span idealized beams respectively. On the other hand, the type VI clip and type VI clip are the closest clip to the

edge of the roof for 4-span and 5-span idealized beams respectively. The influence function of the reaction of a type IV, type V, and type VI clip is given in Figure 7.10, Figure 7.12, and Figure 7.14 successively. The changes of influence function along the seams for a type IV, type V, and type VI clip are plotted in Figure 7.11, Figure 7.13, and Figure 7.15 successively.

It can be found the influence function has the highest value at the location of the clip and reduces to zero on the adjacent seams. Along the seams, it is seen that the clip function has the highest value at the location of the clips and reduces rapidly towards the adjacent clips. By comparing Figures 7.12 and 7.14, although a type VI and type V clip are located at the same place on the standing seam, the influence functions of type VI and type V clips differ significantly due to the existence of the type VI clip. The surface with the non-zero influence function is similar for both types of clips while the magnitude of the maximum influence function for a type V clip is lower than that for a type IV clip. It can be observed in Figure 7.15 that the magnitude of the maximum influence function for a type VI clip is less than 0.5, which is much lower than the values for other types of clip. The performance of a type VI clip is strongly affected by the boundary conditions at the edges of the roof.

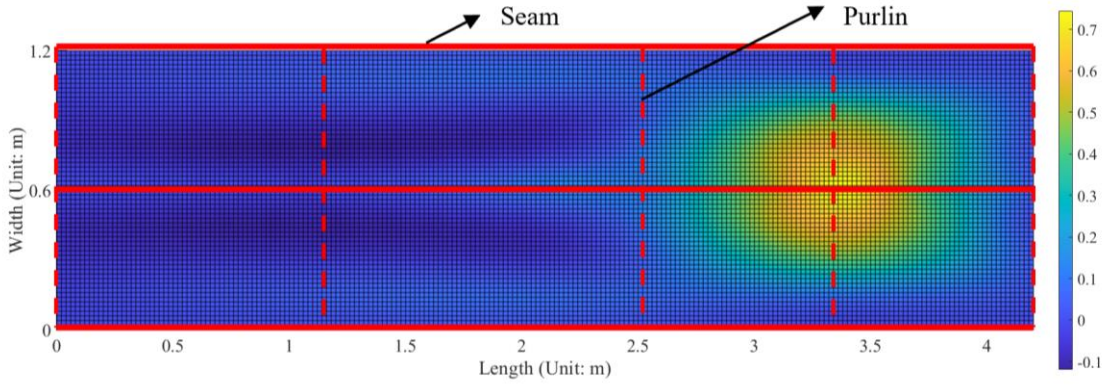

Figure 7.10: Influence function of a type IV clip over the area of two panels adjacent to the standing seam using FEM.

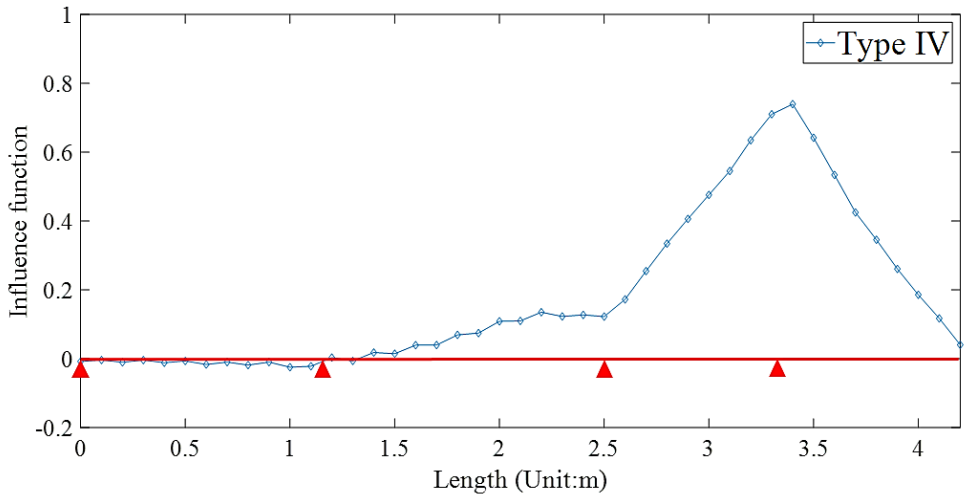

Figure 7.11: Influence function of clip reaction along the seam (Type IV clip).

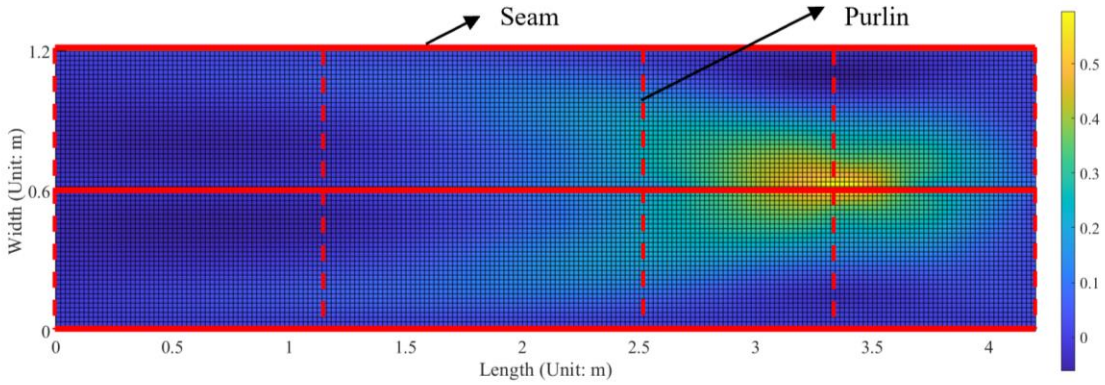

Figure 7.12: Influence function of a type V clip over the area of two panels adjacent to the standing seam using FEM.

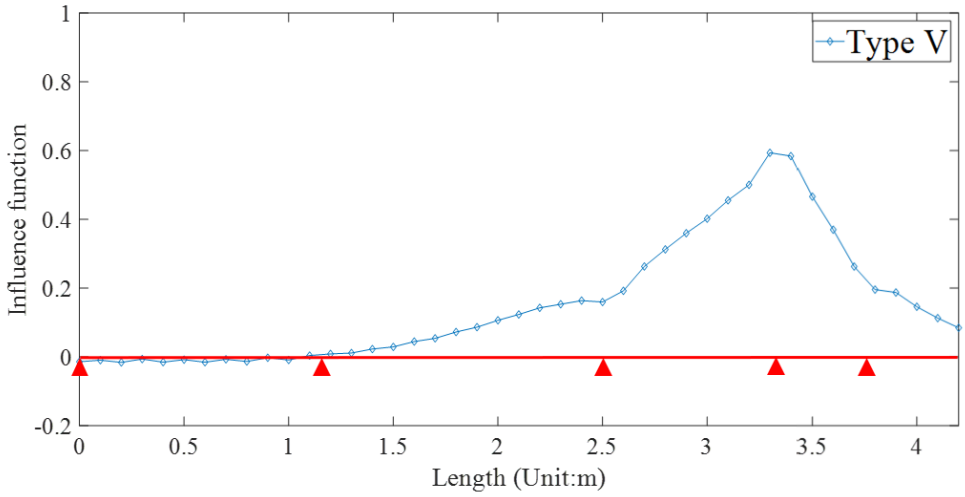

Figure 7.13: Influence function of clip reaction along the seam (Type V clip).

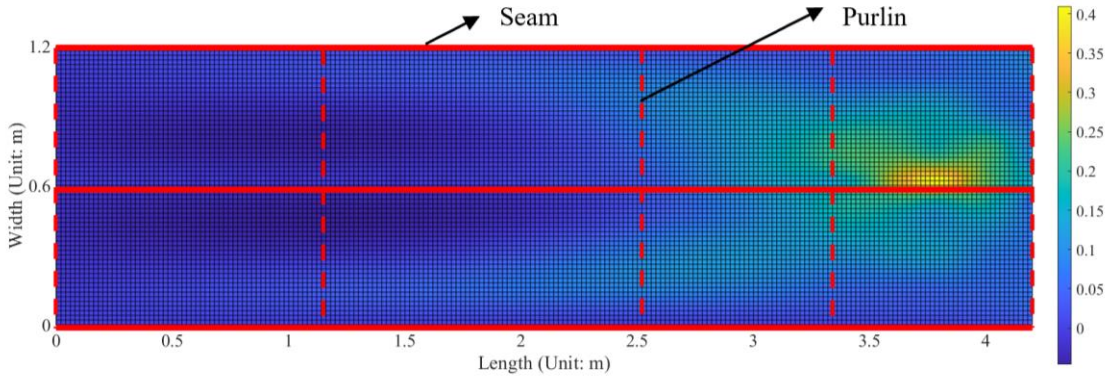

Figure 7.14: Influence function of a type VI clip over the area of two panels adjacent to the standing seam using FEM.

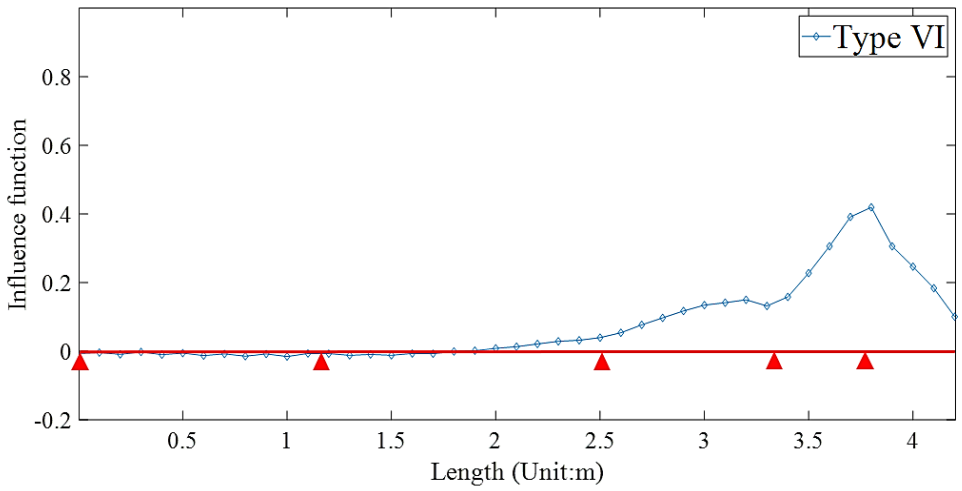

Figure 7.15: Influence function of clip reaction along the seam (Type VI clip).

From these results, the influence function method can be used to examine the influence of the boundary conditions on the reactions of clips. The surface with non-zero influence function almost covers the area of two panels adjacent to the standing seam, which is larger than the standard method suggests. The maximum influence function for different types of clips is less than one, which implies that considering clips as simple supports is not a realistic assumption. In particular, for clips close to the roof eave (type IV, type V, and type VI), the influence functions at the location of the clip are about 0.7, 0.6, and 0.5 for type IV, V, and VI of clips respectively. This implies that a large part of the applied load close to the eave transfers to the installed fasteners at the eave edge, as shown earlier.

7.3 Influence function of clips under different load levels

As mentioned earlier, Prevatt et al. (1995) investigated the measured clip reaction influence function of the tested specimen at varying pressure. The surfaces of the influence function depend on the different pressure levels. This section focuses on the changes of influence function under different load levels and boundary conditions.

Firstly, uniform pressure with varying magnitudes was applied on the SSMR systems successively and the influence function of clips under different load levels was obtained. In chapter 4.1, it can be found the deformation of the panel was obvious even under low pressure (500 Pa) and it is important to know the changes of influence function under low pressure. Figure 7.16 and Figure 7.17 give the influence function of clip reactions along the seam and perpendicular to the seam of the panel when pressure ranges from 0 kPa to 0.5 kPa. It is noted that the curves of influence function along the seam under different loads are basically unchanged. In contrast, the curves of influence function along the panel width do not coincide except for the clip at the ridge (type I clip). This may be related to the shape of the roof panel. As described in section 5.2, the deformation in the middle of the panel is obvious even under low pressure (up to 50mm when pressure is 500 Pa) while the deformation along the seam is small (only about 2mm under pressure with a magnitude of 500 Pa). Thus, the shape of the panel perpendicular to the standing seam changes significantly under low wind pressure except for the panel shape at the roof ridge since the back-up plates at the roof ridge restrict the deflection. From Figure 7.17, it is seen that the maximum influence function increases as the increment of pressure. The curve slopes of influence function become steep with the rising pressure.

(a)

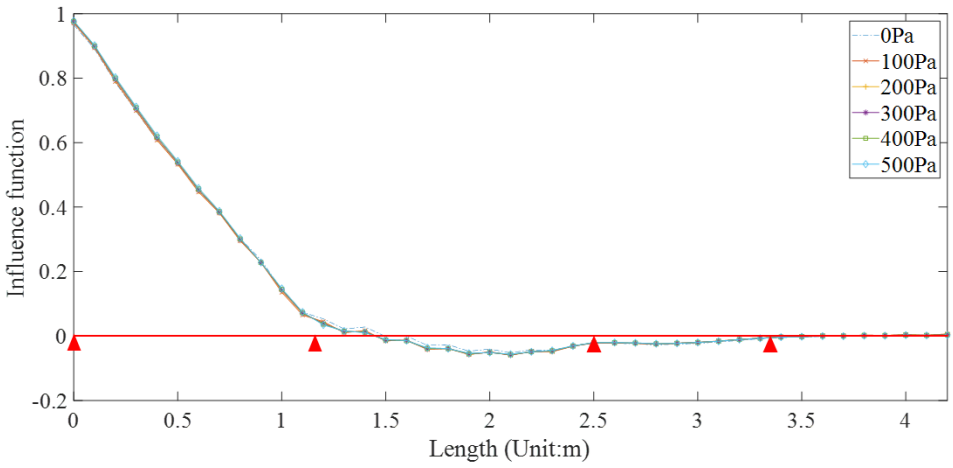

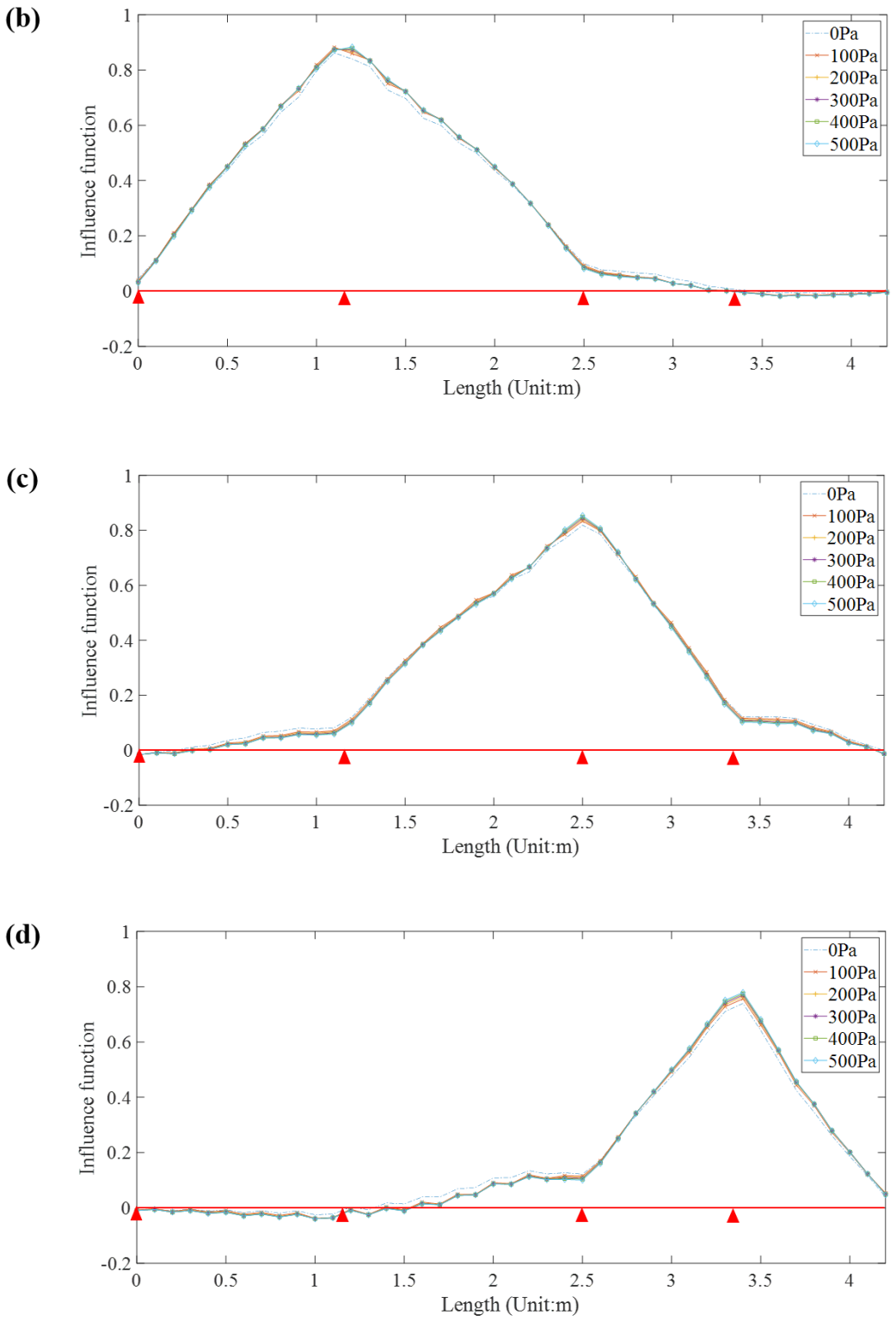

Figure 7.16: Influence function of reaction along the seam under different load levels (0 to 0.5 kPa) for clip of: (a) Type I, (b) Type II, (c) Type III, and (d) Type IV.

(a)

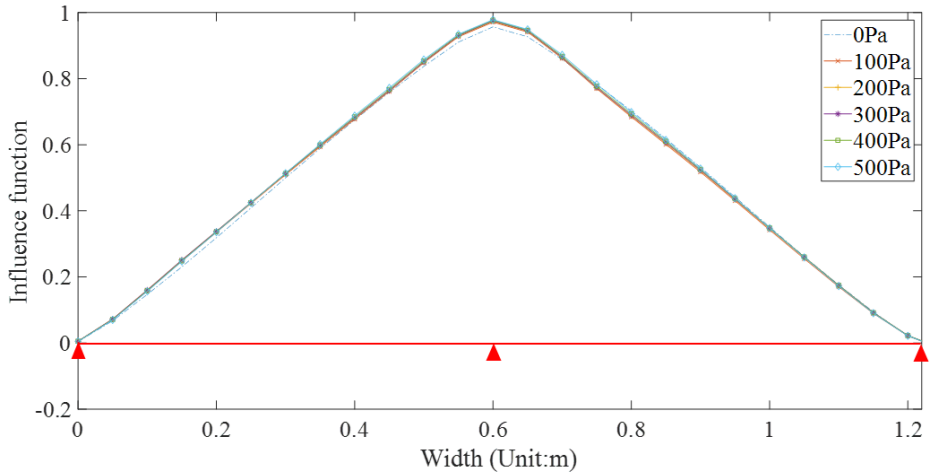
0Pa
100Pa
200Pa
300Pa
400Pa
500Pa
Influence function
Width (Unit:m)
1
0.8
0.6
0.4
0.2
0
-0.2
0
0.2
0.4
0.6
0.8
1
1.2

(b)

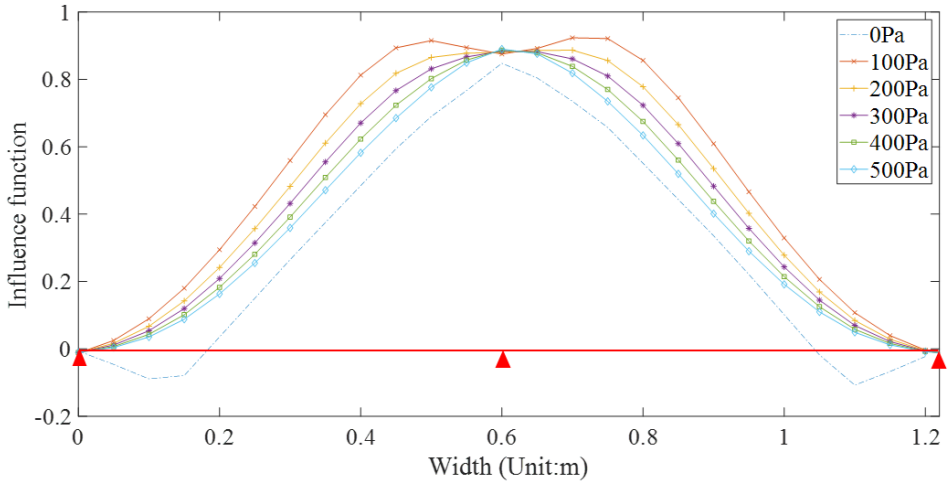
0Pa
100Pa
200Pa
300Pa
400Pa
500Pa
Influence function
Width (Unit:m)
1
0.8
0.6
0.4
0.2
0
-0.2
0
0.2
0.4
0.6
0.8
1
1.2

(c)

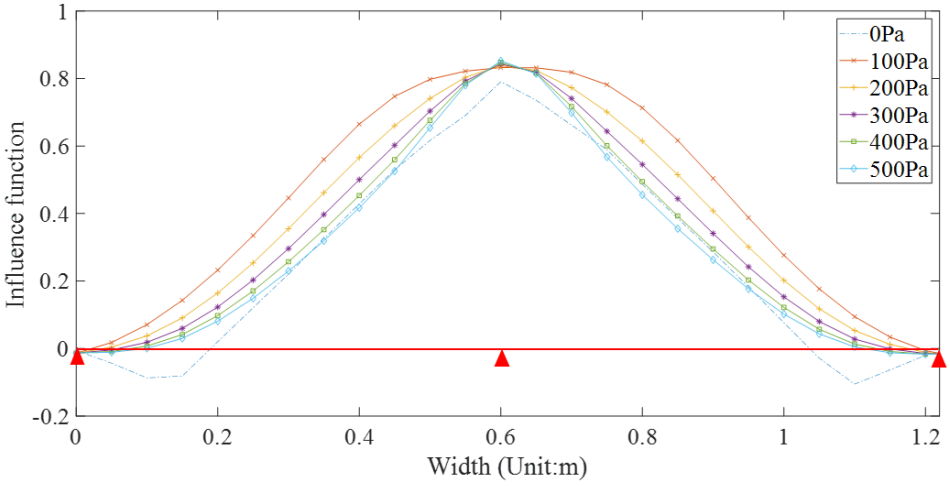
0Pa
100Pa
200Pa
300Pa
400Pa
500Pa
Influence function
Width (Unit:m)
1
0.8
0.6
0.4
0.2
0
-0.2
0
0.2
0.4
0.6
0.8
1
1.2

(d)

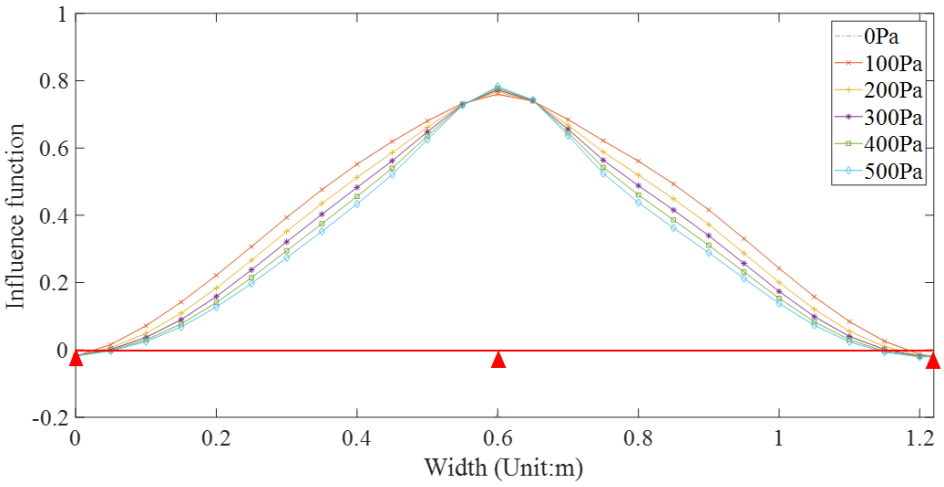

Figure 7.17: Influence function perpendicular to the seam under different load levels (0 to 0.5 kPa) for clip of: (a) Type I, (b) Type II, (c) Type III, and (d) Type IV.

Furthermore, the changes of influence function under a much broader variety of load levels (which range from 0 kPa to 2 kPa) were also investigated. Figure 7.18 and Figure 7.19 give the influence function of clip reactions along the seam and perpendicular to the seam of the panel when pressure ranges from 0 kPa to 2 kPa. It can be found from Figure 7.18 that the influence functions along the standing seam are almost the same when pressure is lower than 1000 Pa while the deviation happens when pressure is higher than 1000 Pa. From Figure 5.7, it is implied that this is due to the deformation along the standing seam. For Figure 7.19, the influence functions perpendicular to the seam under different load levels vary widely except for type I clip since the panel deformation at the roof ridge is quite small.

(a)

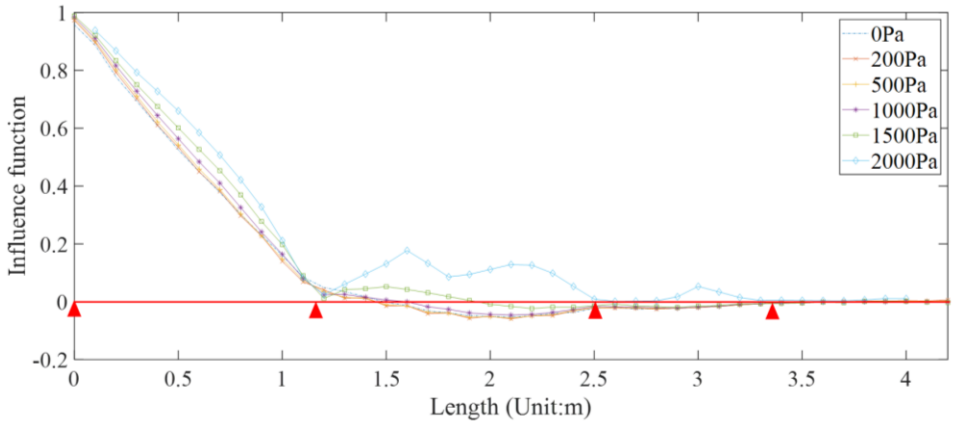
Influence function
Length (Unit:m)
0Pa
200Pa
500Pa
1000Pa
1500Pa
2000Pa

(b)

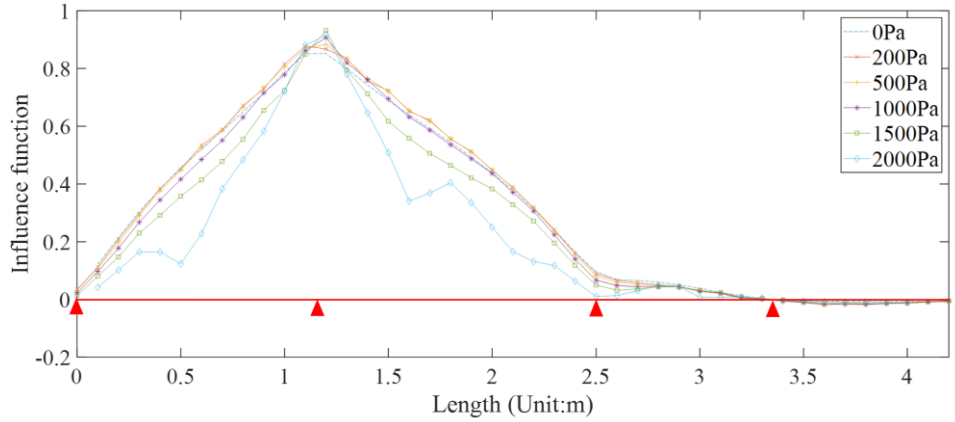
Influence function
Length (Unit:m)
0Pa
200Pa
500Pa
1000Pa
1500Pa
2000Pa

(c)

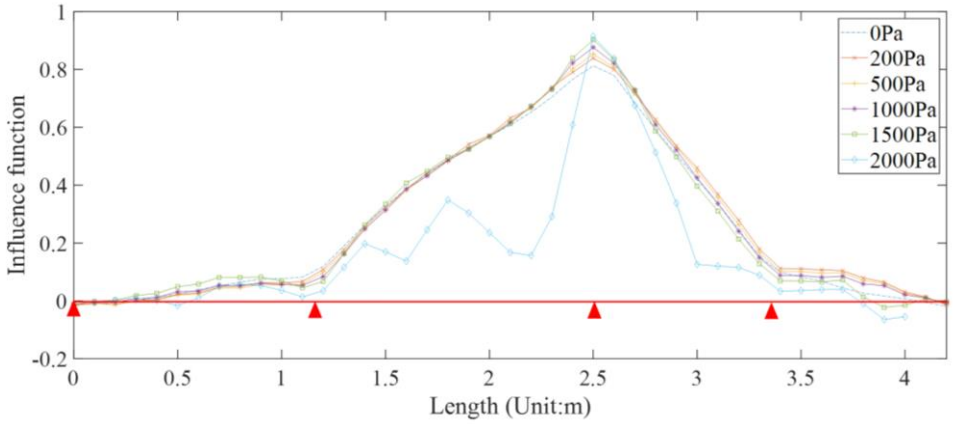
Influence function
Length (Unit:m)
0Pa
200Pa
500Pa
1000Pa
1500Pa
2000Pa

(d)

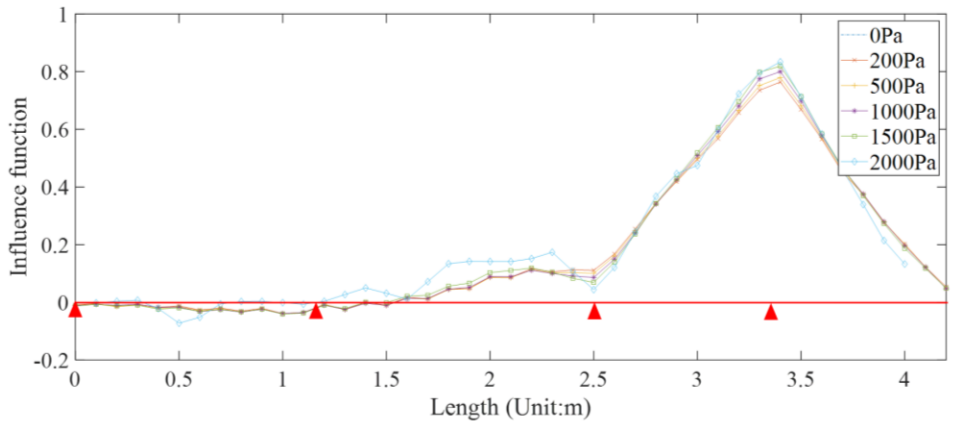

Figure 7.18: Influence function along the seam under different load levels (0 to 2 kPa): (a) Type I clip, (b) Type II clip, (c) Type III clip, and (d) Type IV clip.

(a)

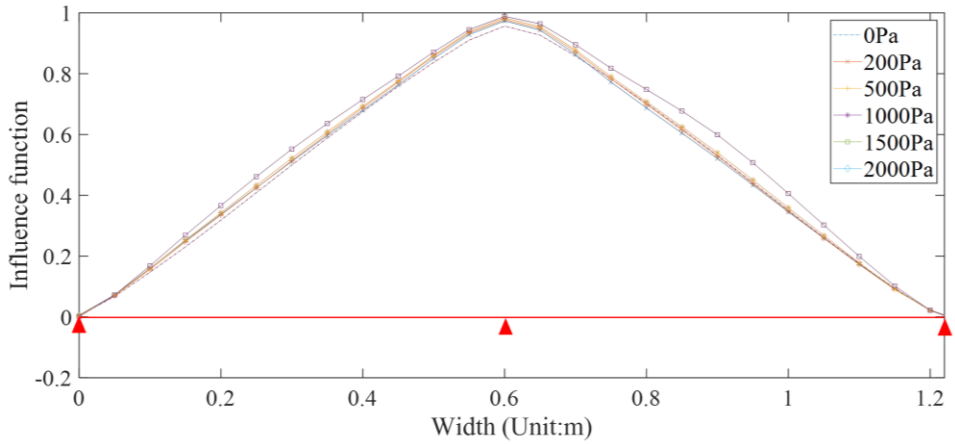

(b)

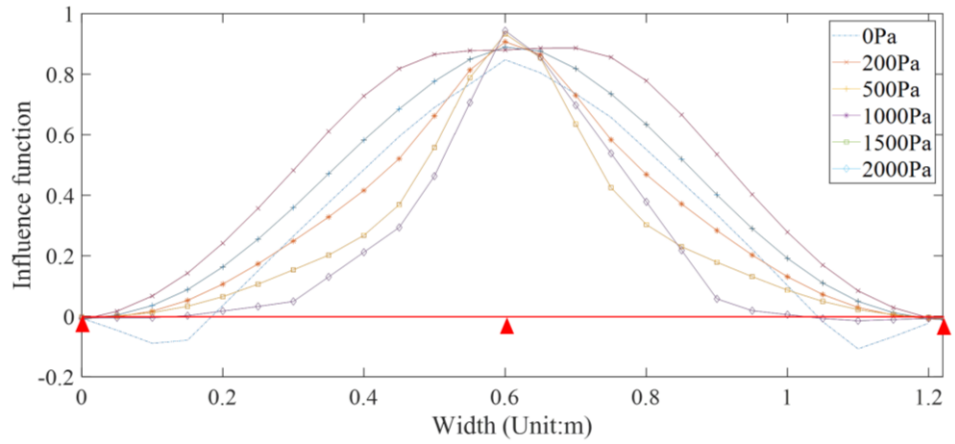

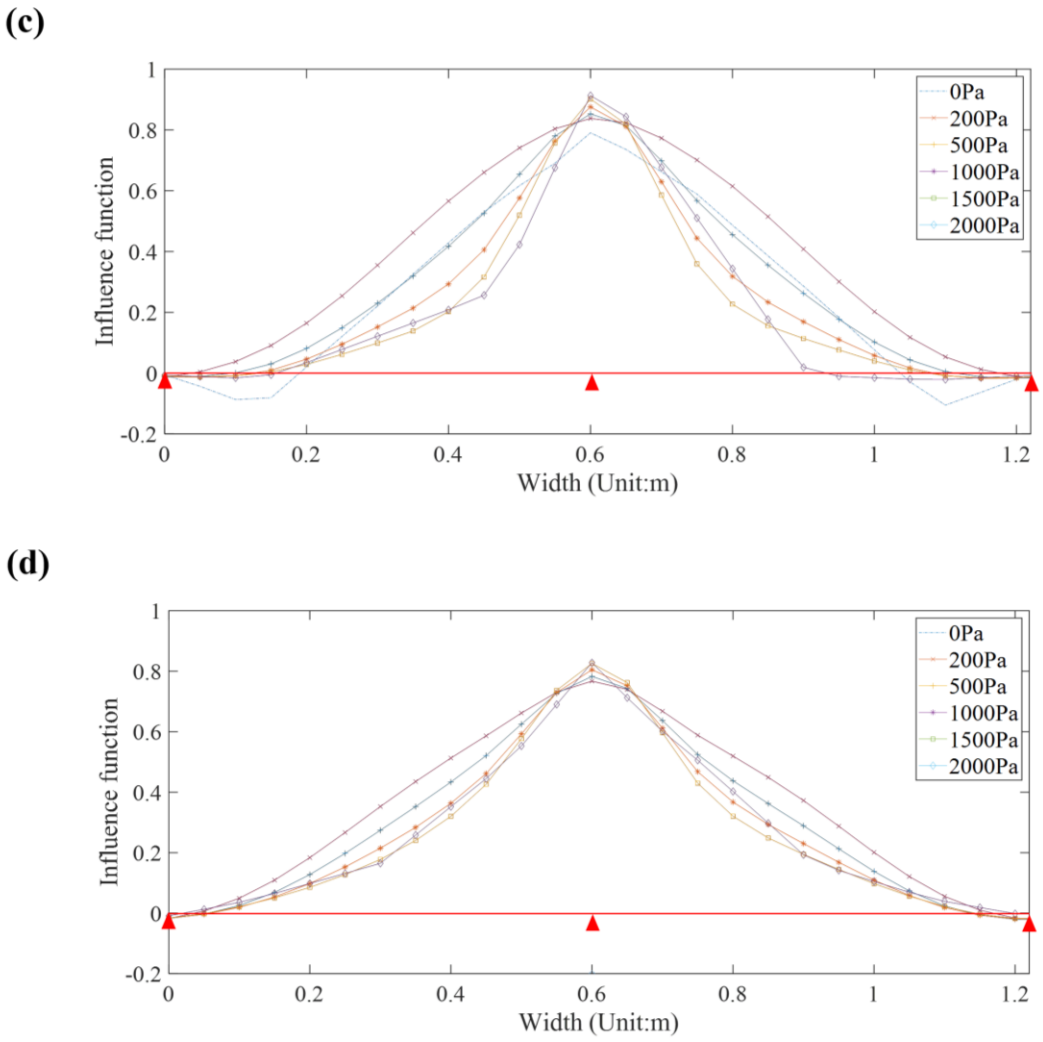

Figure 7.19: Influence function of clip reaction perpendicular to the seam under different load levels (0 to 2 kPa): (a) Type I clip, (b) Type II clip, (c) Type III clip, and (d) Type IV clip.

7.4 Influence function of clips under different boundary conditions

In section 6.3, it was shown that the calculated widths of tributary areas on the roof edge are larger than the estimation of the geometric tributary area method. The influence of the gable end on the influence function of clip reactions is investigated. As shown in Figure

7.20, the clips are divided into two parts: clips near the gable edge and clips away from the gable edge. The influence functions of clip reactions were calculated using FEM. All the calculations below were under the load level of 0 Pa.

Figure 7.21 and Figure 7.22 show the effect of boundary conditions on the influence function for different types of clips along the seam and along panel width respectively. There is not much difference for the curves of influence function for different boundary conditions. It can be concluded that gable end restraints do not have significant effects on the influence functions of clip reactions. Moreover, it can be observed that for other clips except type I clip, these clips get less load with increasing pressure. It can be implied this load should go to the eave edge, which is in constant with the previous findings.

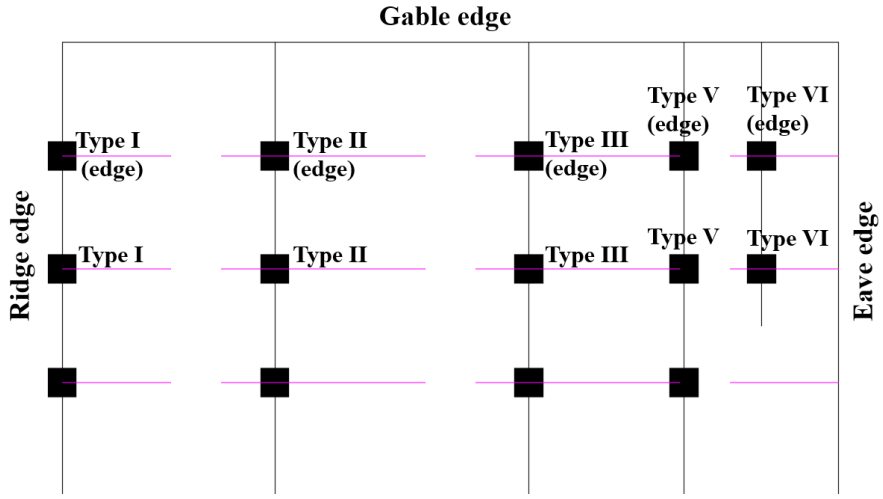

Figure 7.20: Locations of different types of clips.

(a)

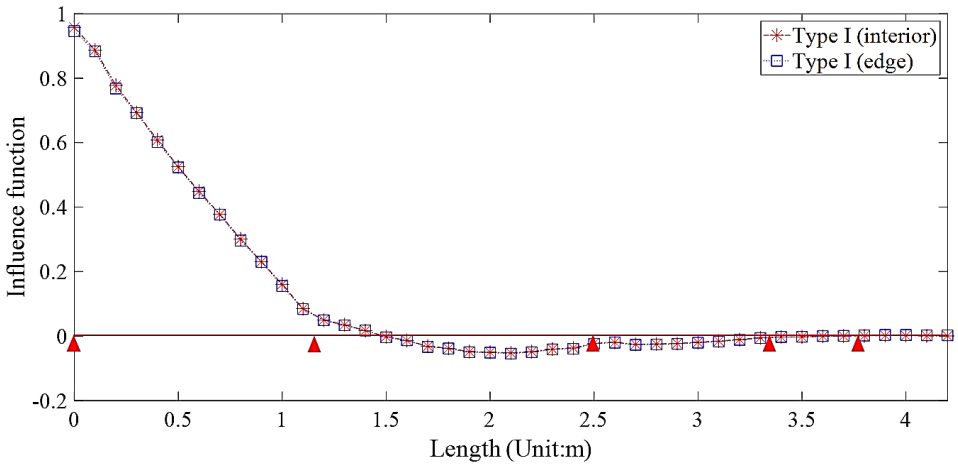
Type I (interior)
Type I (edge)
Influence function
Length (Unit:m)
1
0.8
0.6
0.4
0.2
0
-0.2
0
0.5
1
1.5
2
2.5
3
3.5
4

(b)

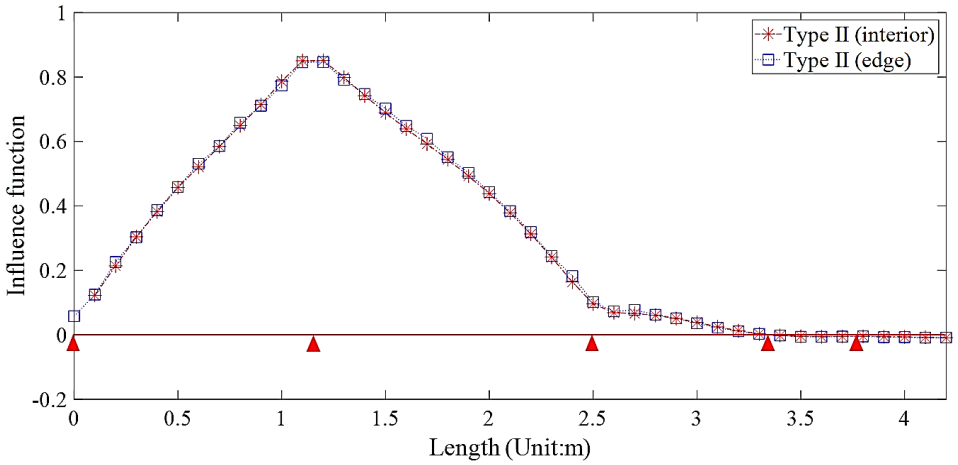
Type II (interior)
Type II (edge)
Influence function
Length (Unit:m)
1
0.8
0.6
0.4
0.2
0
-0.2
0
0.5
1
1.5
2
2.5
3
3.5
4

(c)

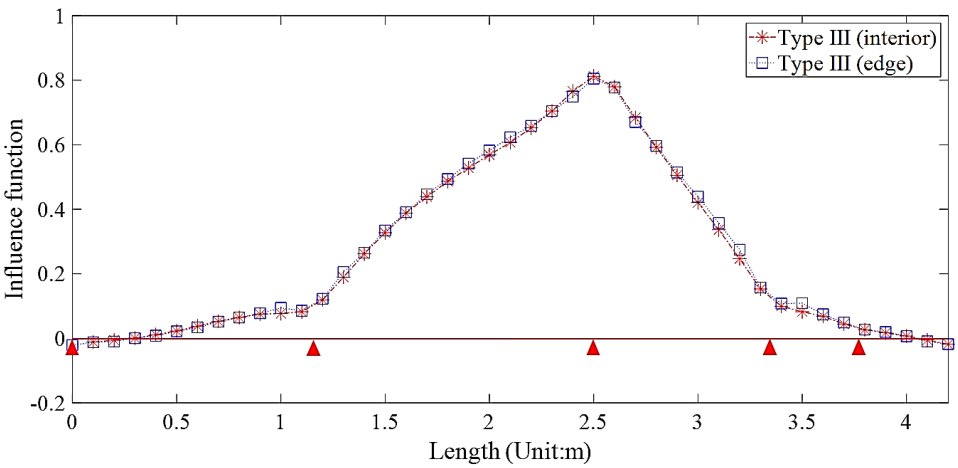
Type III (interior)
Type III (edge)
Influence function
Length (Unit:m)
1
0.8
0.6
0.4
0.2
0
-0.2
0
0.5
1
1.5
2
2.5
3
3.5
4

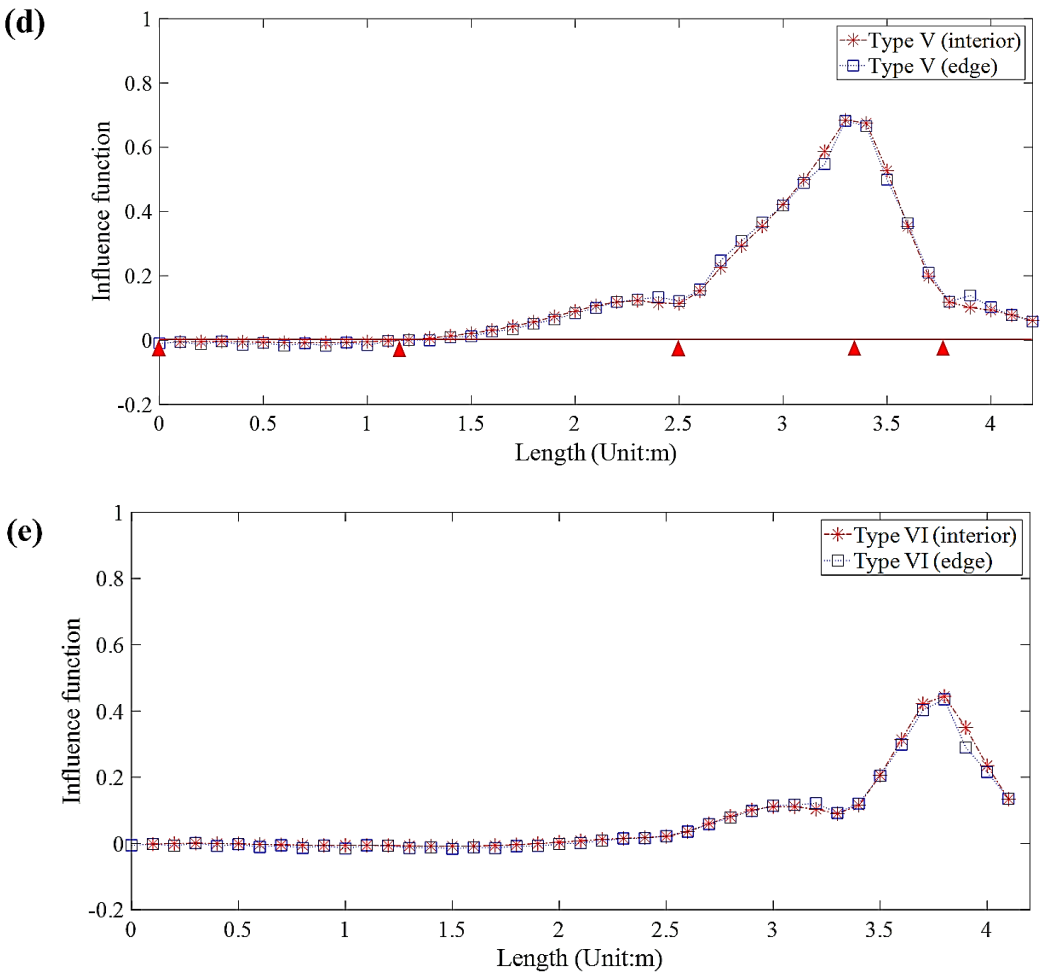

Figure 7.21: Effects of boundary conditions on clip reaction influence function along the seam (a) Type I clip, (b) Type II clip, (c) Type III clip, (d) Type V clip, and (e) Type VI clip.

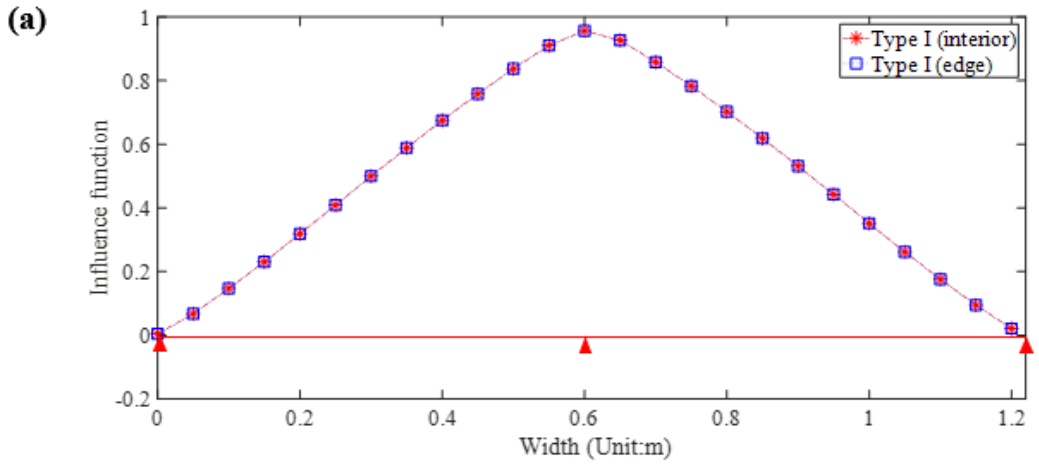

(b)

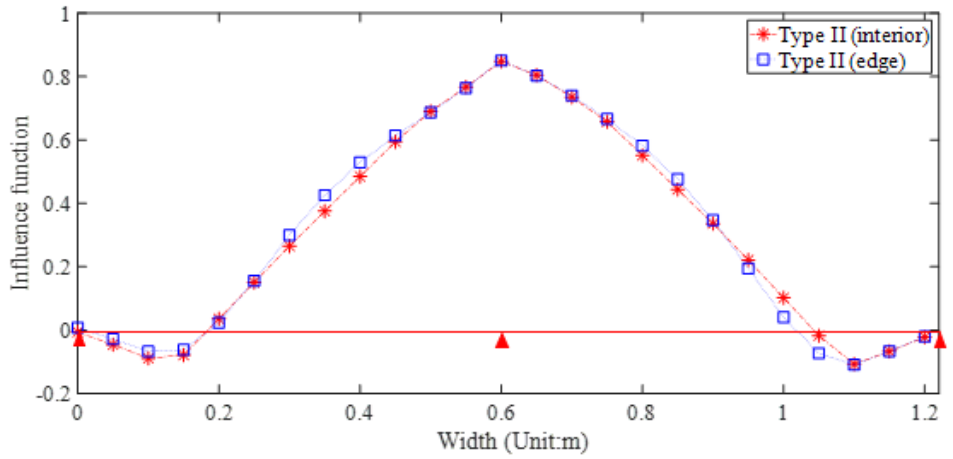
Type II (interior)
Type II (edge)
Influence function
Width (Unit:m)

(c)

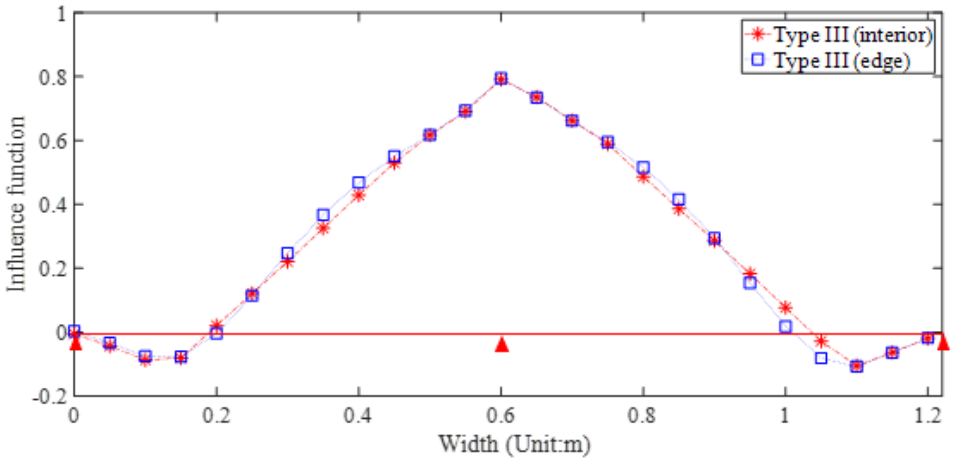
Type III (interior)
Type III (edge)
Influence function
Width (Unit:m)

(d)

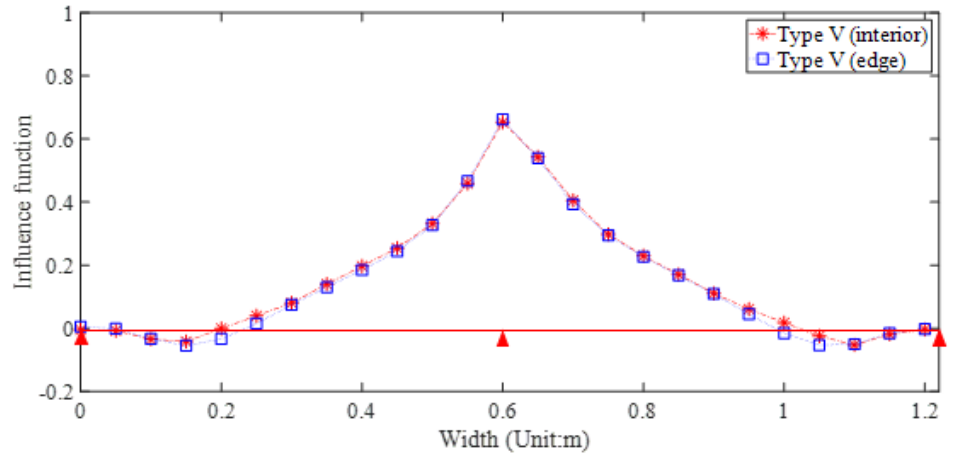
Type V (interior)
Type V (edge)
Influence function
Width (Unit:m)

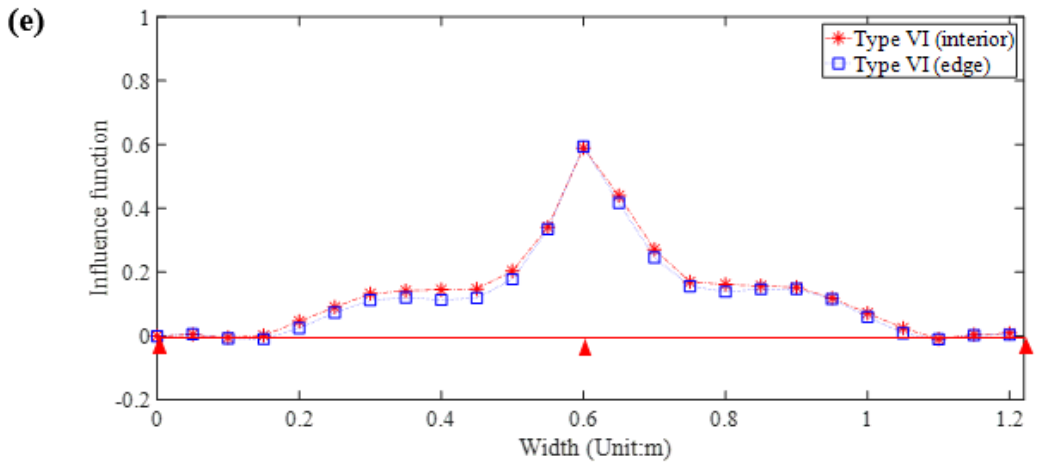

Figure 7.22: Effects of boundary conditions on clip reaction influence function along panel width (a) Type I clip, (b) Type II clip, (c) Type III clip, (d) Type V clip, and (e) Type VI clip.

7.5 Summary

The influence functions using FEM are investigated. The changes of influence coefficients along the seam and perpendicular to the seam are discussed.

The clips of the test SSMR system could be divided into six types. The surface with nonzero influence coefficients is limited within the adjacent seams. It can be found the influence function has the highest value at the location of the clip and reduces to zero on the adjacent seams.

The maximum value of influence function is affected by the clip arrangement and boundary conditions (e.g., the maximum value of influence function for clips close to the eave edge is only 0.5).

By comparing the influence functions under different load levels (between 0 to 0.5 kPa), it can be found the load level has a significant effect on the influence functions perpendicular to the seam while the influence functions along the seam under different load levels are

basically unchanged, which is due to the difference of stiffness in two directions. However, the influence functions along the seam show deviation when pressure is over 1 kPa. The influence functions vary with load levels, which results in the nonlinearity of the load versus pressure.

The boundary condition at the gable end does not have notable effects on the influence function. Thus, this effect could be ignored in future research or application.

8. An analytical model of influence function of clips

The tested SSMR system at IRLBH is a specific roof system with certain panel size, clip arrangement, and boundary conditions. The comparison between full-scale experiments and FEM has proved FEM is useful to study the structural response of the SSMR system with different panel dimensions, clip arrangement, and boundary conditions. However, it is crucial to understand the influence functions of clip reactions theoretically. Thus, an analytical model is developed to generalize the clip reactions influence functions. It should be noted that this is all done with 0 kPa pressure. Since this analytical model is not based on the limit state, the load redistribution due to buckling is not included. As a result, this method gives an un-conservative estimation of peak clip reaction.

8.1 Description of a linear analytical model

Ho et al. (1995) assumed the standing seam as a continuous beam and molded clips as simple supports. There is a discrepancy between the experimental results and the analytical model. As shown in Figure 8.1, a comparison between the analytical model of Ho et al. and measured clip reaction influence functions for the type II clip is provided by Nasiri (2019). It can be observed that the measured influence function at the location of clips is less than one and is not zero at the adjacent clips. In contrast, the model of Ho et al. (1995) shows clip reaction influence function at the location of the clip is equal to one and equal to zero at the locations of other clips, which implies that it is not appropriate to assume the clips as simple supports.

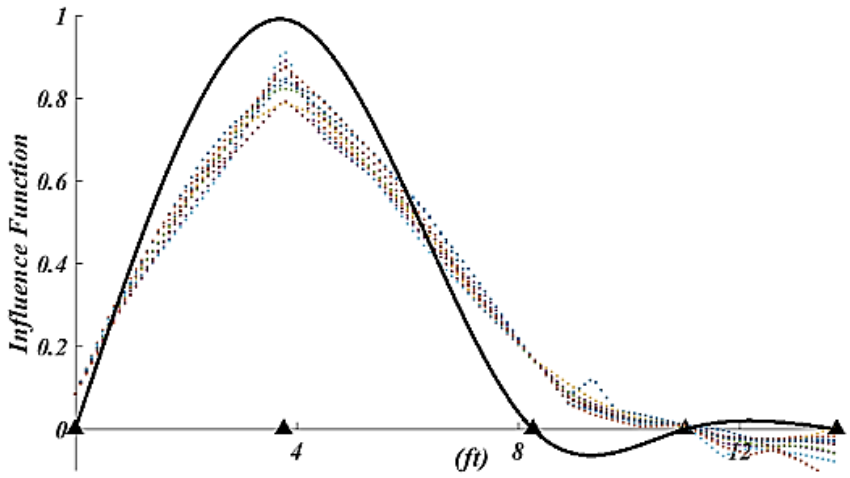

Figure 8.1: Comparison between the measured influence function along the seam for Type II clips (dotted lines) and the model suggested by Ho et al. (1995) (black solid line) (Nasiri, 2019).

Nasiri (2019) put forward an analytical model by idealizing standing seam as multi-span beams. As depicted in Figure 8.2, the clip at the ridge and fastener at the eave were considered as simple supports while other clips were assumed as vertical springs. Figure 8.3 and Figure 8.4 depict the comparison of clip reaction influence function between experiments and theoretical models. It can be observed that the model suggested by Nasiri (2019) provides a better estimation compared to the model of Ho et al. (1995). However, as shown in Figure 8.4, the influence function drops to zero at the locations of the fastener at the eave edge for both analytical models while the measured influence function is not equal to zero at this location. It can be concluded that modeling the performance of interior clips as vertical spring provides better estimation compared to considering clips as simple support while it is inappropriate to model the clip at ridge and fastener at eave as simple supports. Thus, this thesis put forward an updated analytical model which represents the influence function of clip reactions more accurately.

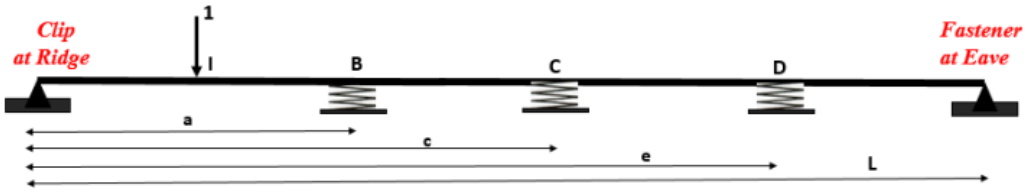

Figure 8.2: 4-span beam with simple supports at two ends and vertical springs representing the clips (Nasiri, 2019).

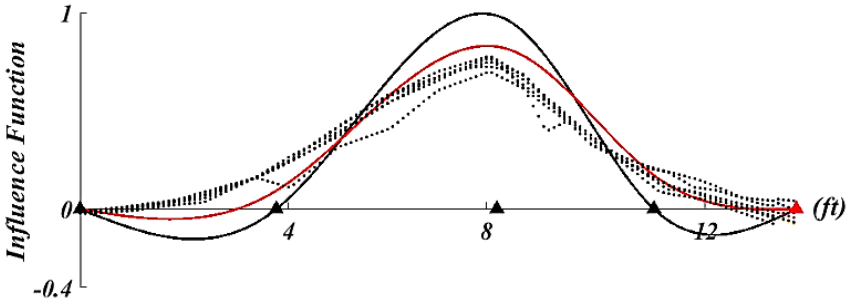

Figure 8.3: Comparison between measured influence function of clip reaction (Type III) along the seam, influence function of the clip suggested by Ho et al. (1995) (black line), and influence function of the clip suggested by Nasiri (2019) (red line) Note: triangles represent the installed clips. (Nasiri, 2019).

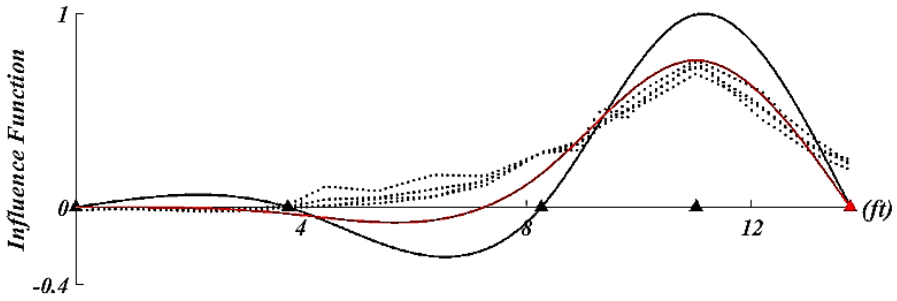

Figure 8.4: Comparison between measured influence function of clip reaction (Type IV) along the seam, influence function of the clip suggested by Ho et al. (1995) (black line), and influence function of the clip suggested by Nasiri (2019) (red line) Note: triangles represent the installed clips. (Nasiri, 2019).

Force method is used to analyze the influence function of clip reactions. Since the standing seams are modeled as multi-span beams, it is an indeterminate structure. The first step is to convert the indeterminate structure to a determinate structure by removing unknown forces and replacing them with unit forces. Then the calculated unknown forces are required to achieve compatibility with the original structure using the superposition principle. (Hourani, 2002).

As shown in Figure 8.5, a double-span beam subjected to a unit load is used to illustrate the force method. In Figure 8.6, it can be seen that the support in the middle of the beam is removed and the unknown support reaction is replaced with a unit force. The deflection of the double-span beam subjected to a unit load can be divided into two parts: the deflection of a single-span beam subjected to a unit load and the deflection of a single-span beam subjected to a unit load at the location of the removed support. Using the principle of superposition, it is known that the deflection of the double-span beam subjected to a unit load is the summation of these two parts. For the original structure, the displacement at the location of removed support is equal to zero and should be equal to the summation of the deflections of two beams as shown in Figure 8.6, which can be calculated as;

$$\delta_{BI} - R_B \delta_{BB} = 0 \tag{8.1}$$

Where;

δ_{BI}: Vertical displacement at point B due to unit load at point I

δ_{BB}: Vertical displacement at point B due to unit load at point B

δ_{IB}: Vertical displacement at point I due to unit load at point B

δ_{II}: Vertical displacement at point I due to unit load at point I

R_B: Reaction at support B

It should be noted that δ_{BI} is equal to δ_{IB} due to reciprocal theorem of displacement.

Using equation 8.1, the reaction of support B can be calculated as;

$$R_B = \frac{\delta_{BI}}{\delta_{BB}} \tag{8.2}$$

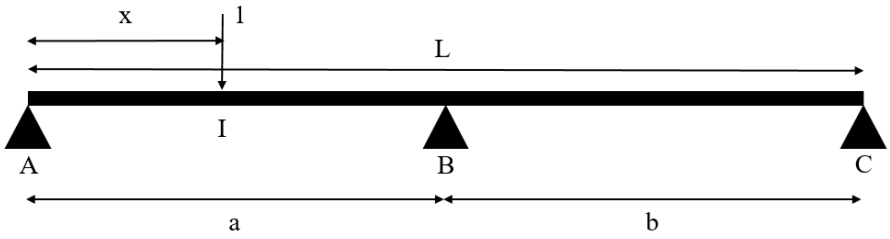

Figure 8.5: A double-span beam subjected to a unit load.

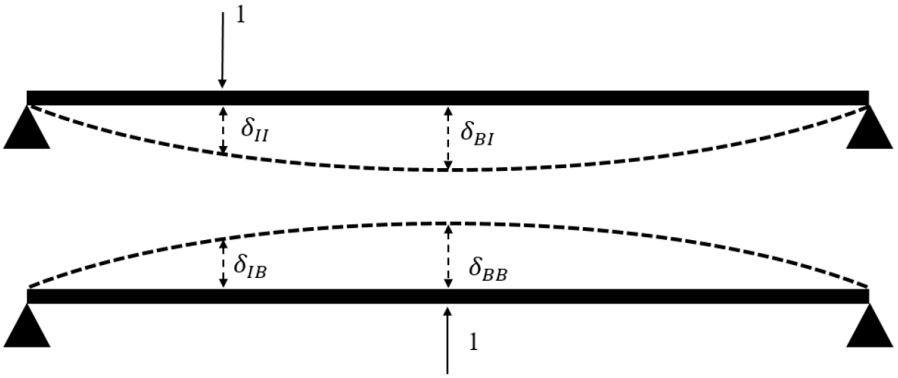

Figure 8.6: Deflection compatibility of the indeterminate double-span beam.

Hourani (2002) pointed out that the vertical deflection at any point along the beam due to a unit vertical load at B (i.e., δ_{BI}) can be written as;

$$\begin{aligned} &\left(\frac{1}{6EIL}\right)[-bx^3 + ab(a+2b)x] && 0 \le x \le a \\ &\left(\frac{1}{6EIL}\right)[a(x-L)^3 - ab(2a+b)(x-L)] && a \le x \le L \end{aligned} \tag{8.3}$$

The deflection at point B due to a unit vertical at B is;

$$\delta_{BB} = \frac{a^2 b^2}{3EIL} \tag{8.4}$$

Thus, the influence function of reaction is;

$$R_B = \frac{-x^3 + (a^2 + 2ab)x}{2a^2 b} \qquad 0 \le x \le a$$
$$R_B = \frac{(x - L)(x^2 - 2Lx + a^2)}{2ab^2} \qquad a \le x \le L \tag{8.5}$$

This method can be expanded to a continuous beam with several spans. As discussed previously, the standing seam with the specific clip arrangement in full-scale experiments can be modeled as 4-span and 5-span beams. Figure 8.7 gives a 4-span beam subjected to unit load. Different from Nasiri's model, the updated model considers all the clips and fasteners at the eaves as vertical springs, as depicted in Figure 8.8. This indeterminate beam can be converted into four determinate beams as shown in Figure 8.9.

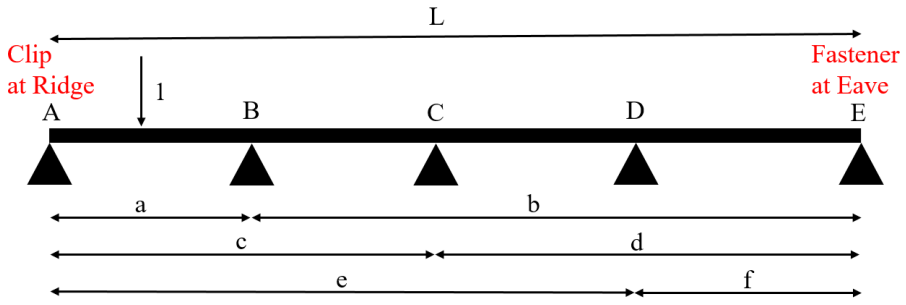

Figure 8.7: 4-span beam subjected to unit point load.

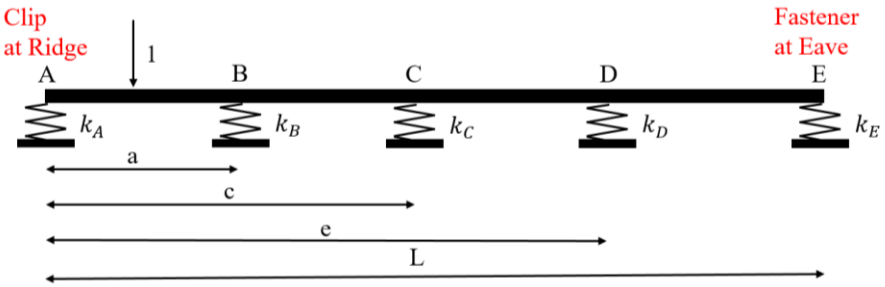

Figure 8.8: 4-span beam with vertical springs representing the restraints of clips and fastener.

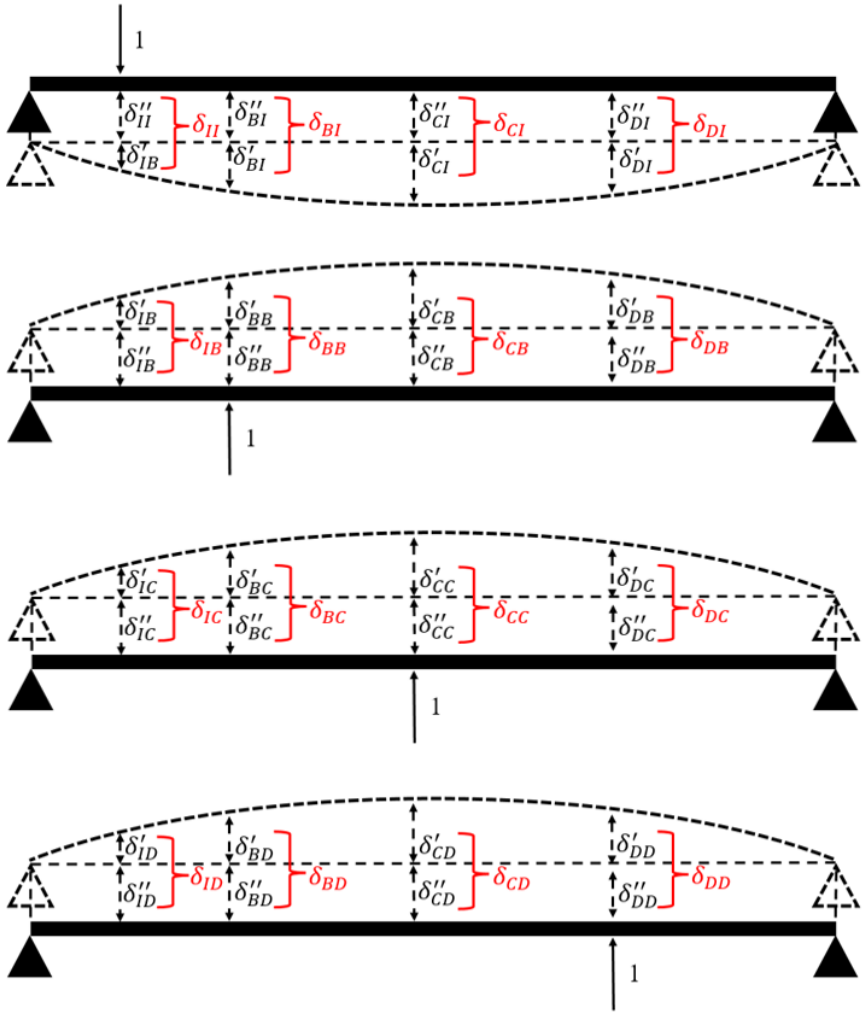

Figure 8.9: Determinate beam subjected to unit loads at locations of supports.

δ_{ij} denotes the total vertical displacement at i due to a unit vertical load at j. The total vertical displacement at any point can be divided into two parts: the vertical displacement due to support displacement and the vertical displacement due to the deformation of the beam itself. δ'_{ij} denotes the vertical displacement of beam deflection at i due to a unit vertical load at j and δ''_{ij} denotes the vertical displacement of support displacement at i due to a unit vertical load at j. Also, it is noted that $\delta_{ij}=\delta_{ji}$, $\delta'_{ij}=\delta'_{ji}$, and $\delta''_{ij}=\delta''_{ji}$.

Equations 8.3 and 8.4 could be used to calculate the displacement of beam deformation at the location of each support, which can be expressed as;

$$\delta'_{BB} = \frac{a^2 b^2}{3EIL} \qquad \delta'_{CC} = \frac{c^2 d^2}{3EIL} \qquad \delta'_{DD} = \frac{e^2 f^2}{3EIL} \tag{8.6}$$

$$\begin{aligned} \delta'_{BC} = \delta'_{CB} &= \frac{a(c-L)(c^2-2Lc+a^2)}{6EIL} \\ \delta'_{CD} = \delta'_{DC} &= \frac{c(e-L)(e^2-2Le+c^2)}{6EIL} \\ \delta'_{BC} = \delta'_{CB} &= \frac{a(e-L)(e^2-2Le+a^2)}{6EIL} \end{aligned} \tag{8.7}$$

As shown in Figure 8.10, by considering clip at ridge and fastener at eave as vertical spring and neglecting the deformation of the beam itself, the support reactions at point A and E due to the point load at point I can be calculated as;

$$\begin{aligned} R_A &= 1 - \frac{x}{L} \\ R_E &= \frac{x}{L} \end{aligned} \tag{8.8}$$

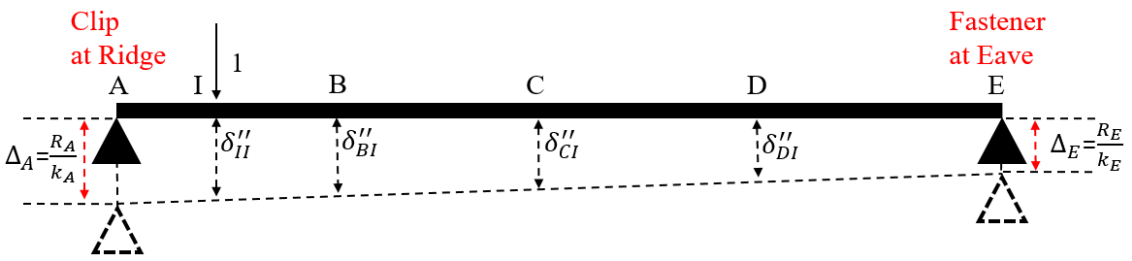

Figure 8.10: Support displacement of a determinate beam subjected to unit loads at point I.

The support displacement of the beam at locations of support can be calculated as;

$$\Delta = -\frac{R}{k} \tag{8.9}$$

where R is the clip reaction and k is the clip stiffness. Using equation 8.9, the support displacement at point A and E can be calculated as;

$$\begin{aligned} \Delta_A &= -\frac{R_A}{k_A} \\ \Delta_E &= -\frac{R_E}{k_E} \end{aligned} \tag{8.10}$$

Since the deformation of the beam itself is ignored, the vertical displacement along the beam changes linearly. The displacement at point B, C, D due to support displacement can be expressed as;

$$\begin{aligned} \delta''_{BI} &= \frac{ax}{k_E L^2} + \frac{b(L-x)}{k_A L^2} \\ \delta''_{CI} &= \frac{cx}{k_E L^2} + \frac{d(L-x)}{k_A L^2} \\ \delta''_{DI} &= \frac{ex}{k_E L^2} + \frac{f(L-x)}{k_A L^2} \end{aligned} \tag{8.11}$$

Similarly, as shown in Figure 8.11, the displacement at point B, C, and D due to support displacement when subjected to unit loads at locations of supports can be expressed as;

$$\delta''_{BB} = \frac{b^2}{k_A L^2} + \frac{a^2}{k_E L^2} \qquad \delta''_{CC} = \frac{d^2}{k_A L^2} + \frac{c^2}{k_E L^2} \qquad \delta''_{DD} = \frac{f^2}{k_A L^2} + \frac{e^2}{k_E L^2} \tag{8.12}$$

$$\delta''_{BC} = \delta''_{CB} = \frac{bd}{k_A L^2} + \frac{ac}{k_E L^2}$$

$$\delta''_{CD} = \delta''_{DC} = \frac{df}{k_A L^2} + \frac{ce}{k_E L^2} \tag{8.13}$$

$$\delta''_{BD} = \delta''_{DB} = \frac{bf}{k_A L^2} + \frac{ae}{k_E L^2}$$

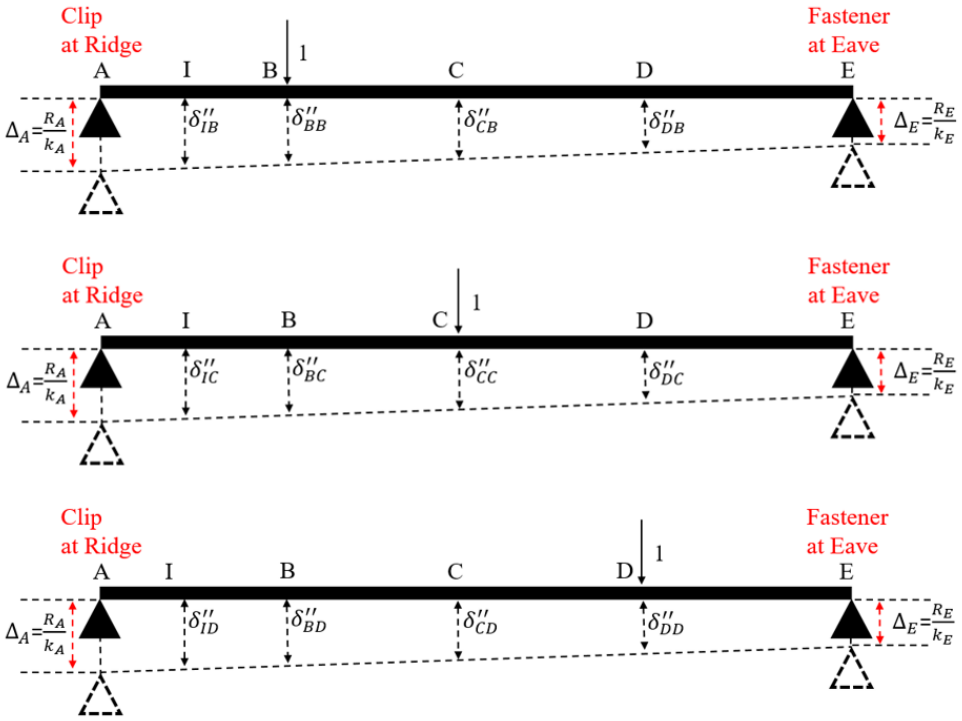

Figure 8.11: Support displacement of a determinate beam subjected to unit loads at supports B, C, and D.

By calculating the results through equations 8.6, 8.7, 8.12, and 8.13, the total vertical displacement at supports due to a unit load can be expressed as;

$$\delta_{BB} = \delta'_{BB} + \delta''_{BB} \qquad \delta_{CC} = \delta'_{CC} + \delta''_{CC} \qquad \delta_{DD} = \delta'_{DD} + \delta''_{DD} \tag{8.14}$$

$$\begin{aligned} \delta_{BC} = \delta_{CB} = \delta'_{BC} + \delta''_{BC} = \delta'_{CB} + \delta''_{CB} \\ \delta_{CD} = \delta_{DC} = \delta'_{CD} + \delta''_{CD} = \delta'_{DC} + \delta''_{DC} \\ \delta_{BD} = \delta_{DB} = \delta'_{BD} + \delta''_{BD} = \delta'_{DB} + \delta''_{DB} \end{aligned} \tag{8.15}$$

δ'_{BI}, δ'_{CI}, and δ'_{DI} represent the deflection of the beam itself at each support as the point load is applied at point I, which can be calculated using equation 6.4;

$$\delta'_{BI} = \begin{cases} \delta'_{BI,1} = \left(\frac{1}{6EIL}\right)[-bx^3 + ab(a+2b)x] & 0 \le I \le a \\ \delta'_{BI,2} = \left(\frac{1}{6EIL}\right)[a(x-L)^3 - ab(2a+b)(x-L)] & a \le I \le L \end{cases} \tag{8.16}$$

$$\delta'_{CI} = \begin{cases} \delta'_{CI,1} = \left(\frac{1}{6EIL}\right)[-dx^3 + cd(c+2d)x] & 0 \le I \le c \\ \delta'_{CI,2} = \left(\frac{1}{6EIL}\right)[c(x-L)^3 - cd(2c+d)(x-L)] & c \le I \le L \end{cases} \tag{8.17}$$

$$\delta'_{DI} = \begin{cases} \delta'_{DI,1} = \left(\frac{1}{6EIL}\right)[-fx^3 + ef(e+2f)x] & 0 \le I \le e \\ \delta'_{DI,2} = \left(\frac{1}{6EIL}\right)[e(x-L)^3 - ef(2e+f)(x-L)] & e \le I \le L \end{cases} \tag{8.18}$$

Considering the superposition principle, the deformation at locations of supports will be;

$$R_B\delta_{BB} + R_C\delta_{BC} + R_D\delta_{BD} = \delta'_{BI} + \delta''_{BI} + \Delta_B = \delta_{BI} - \frac{R_B}{k_B}$$

$$R_B\delta_{CB} + R_C\delta_{CC} + R_D\delta_{CD} = \delta'_{CI} + \delta''_{CI} + \Delta_C = \delta_{CI} - \frac{R_C}{k_C} \quad (8.19)$$

$$R_B\delta_{DB} + R_C\delta_{DC} + R_D\delta_{DD} = \delta'_{DI} + \delta''_{DI} + \Delta_D = \delta_{DI} - \frac{R_D}{k_D}$$

These equations can be represented as;

$$\begin{bmatrix} \delta_{BB} + \frac{1}{k_B} & \delta_{BC} & \delta_{BD} \\ \delta_{CB} & \delta_{CC} + \frac{1}{k_C} & \delta_{CB} \\ \delta_{DB} & \delta_{DC} & \delta_{DD} + \frac{1}{k_D} \end{bmatrix} \begin{bmatrix} R_B \\ R_C \\ R_D \end{bmatrix} = \begin{bmatrix} \delta_{BI} \\ \delta_{CI} \\ \delta_{DI} \end{bmatrix} \quad (8.20)$$

It should be noted that different expressions of δ'_{BI} δ'_{CI}, and δ'_{DI} will be used for each span, which is listed in Table 8.1. Span #1 represents the span between support A and B. The spans located on the right side of span #1 are named as span #2, span #3, and span #4, respectively.

Table 8.1: Deflection equations used for calculation of clip reaction

	Span #1	Span #2	Span #3	Span #4
R_B	$\delta'_{BI,1},\ \delta'_{CI,1},\ \delta'_{DI,1}$	$\delta'_{BI,2},\ \delta'_{CI,1},\ \delta'_{DI,1}$	$\delta'_{BI,2},\ \delta'_{CI,2},\ \delta'_{DI,1}$	$\delta'_{BI,2},\ \delta'_{CI,2},\ \delta'_{DI,2}$
R_C	$\delta'_{BI,1},\ \delta'_{CI,1},\ \delta'_{DI,1}$	$\delta'_{BI,2},\ \delta'_{CI,1},\ \delta'_{DI,1}$	$\delta'_{BI,2},\ \delta'_{CI,2},\ \delta'_{DI,1}$	$\delta'_{BI,2},\ \delta'_{CI,2},\ \delta'_{DI,2}$
R_D	$\delta'_{BI,1},\ \delta'_{CI,1},\ \delta'_{DI,1}$	$\delta'_{BI,2},\ \delta'_{CI,1},\ \delta'_{DI,1}$	$\delta'_{BI,2},\ \delta'_{CI,2},\ \delta'_{DI,1}$	$\delta'_{BI,2},\ \delta'_{CI,2},\ \delta'_{DI,2}$

By solving equation 8.20, the clip reaction influence functions along the seam can be calculated. The clip stiffness is still questionable. As mentioned earlier, the current roof system is similar to the ones investigated by El Damatty et al. (2003) and Farquhar et al. (2003). El Damatty et al. (2003) used FEM to study the response of SSMR systems and considered the clips as vertical springs. The vertical stiffness of clips was measured by

component tests and was estimated to be 1721.3 N/mm. Farquhar et al. (2003) calculated the stiffness of the clip based on the MSU full-scale experiments (Sinno et al., 2001), which is 2553.9 N/mm. The difference between estimated values of clip stiffness cannot be only measurement errors. Component tests might underestimate the clip stiffness since the clips were tested separately. However, it is noted that clips were part of roof components and the interaction between clips and standing seams was complex. The stiffness might be higher than that estimated by the component test because roof components work together to resist wind load rather than the separate clip. Thus, 2553.9 N/mm is chosen for the magnitude of clip stiffness. The stiffness at the ridge and eave edge is 7916.3 N/mm and 5071.8 N/mm respectively, which is based on the results of FEM. The changes of influence function of clips perpendicular to the seam are assumed linear from the calculated influence coefficient on the standing seam to zero on the adjacent seam.

8.2 Comparing influence function with previous models

Figures 8.12 to 8.17 depict the comparison between measured influence functions and estimated influence functions using different methods for each type of clip. It can be observed that for the type I clip, as shown in Figure 8.12, the magnitude of clip reaction influence function at the location of the ridge clip and the adjacent clip is about one and 0.15 respectively, while all the estimated influence functions at these locations are around 1 and zero respectively. All the estimated influence functions match well for the type I clip. The comparison of influence functions for the type II clip is given in Figure 8.13. It is seen that considering the installed clips as vertical springs provides better estimation compared to considering clips as simple supports. The difference is evident for type III, IV, V, and VI clips as shown in Figures 8.14, 8.15, 8.16, and 8.17 respectively.

Also, it should be noted that the model of Nasiri and the current updated model match well for clips of type I, type II, and type III while the model of Nasiri is not consistent with the updated model for clips of type IV, V, and VI and the updated model provides a better

estimation of the influence function. Since the updated analytical model considers the ridge clip and fasteners at the eave as vertical springs while the analytical models of Nasiri consider the ridge clip and fasteners at the eave as a simple support. As described previously, the stiffness of the ridge clip used in the updated analytical model is much larger than the stiffness of other clips while the stiffness of fasteners at the roof eave used in the updated analytical model lies between the stiffness of the ridge clip and other clips. Thus, it can be concluded that it is reasonable to consider the ridge clip as a simple support, while it is not appropriate to consider the fasteners at the eave as simple supports. Also, it is supposed that considering the fastener at the eave as a vertical spring has a notable effect on the influence functions of type III, IV, V, and VI clips. In other words, the different assumptions for the fasteners at the eave affect the influence function of clips located near the roof eave, which is about 5.48 ft (1.67 m) away from the roof eave. On the other hand, FEM provides a better estimation of influence functions compared to other methods for all types of clips.

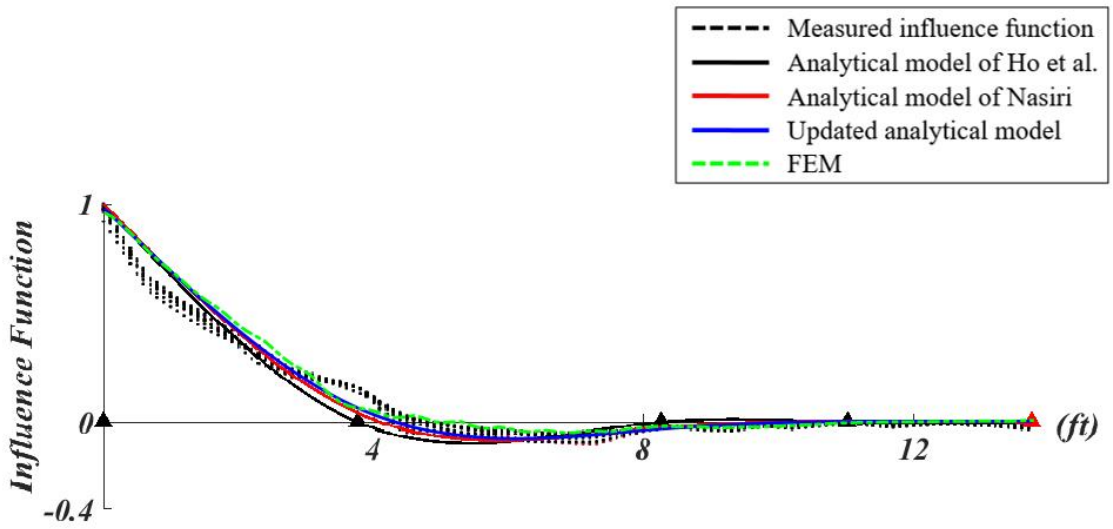

Figure 8.12: Comparison between measured influence function of clip reaction (Type I) along the seam and estimated influence functions using different models

Note: Supports with installed clips (▲) and Eave end with installed fasteners (▲).

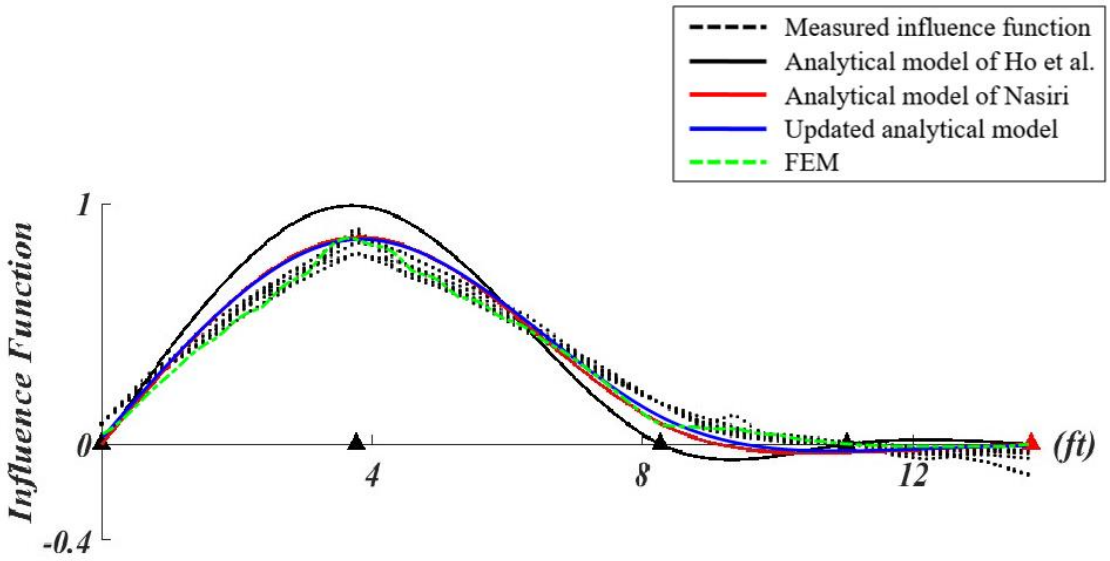

Figure 8.13: Comparison between measured influence function of clip reaction (Type II) along the seam and estimated influence functions using different models

Note: Supports with installed clips (▲) and Eave end with installed fasteners (▲).

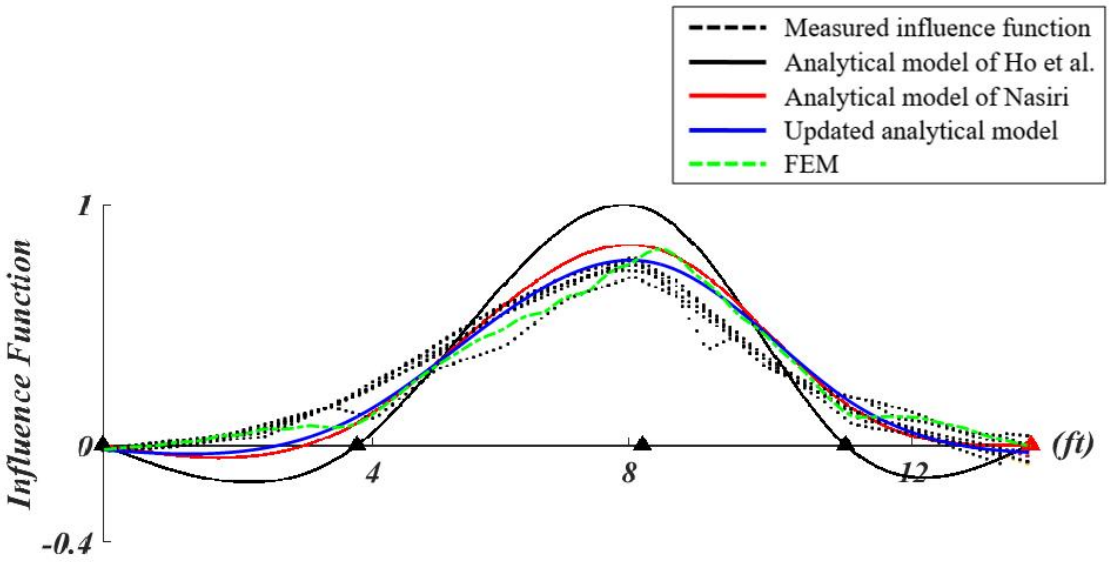

Figure 8.14: Comparison between measured influence function of clip reaction (Type III) along the seam and estimated influence functions using different models

Note: Supports with installed clips (▲) and Eave end with installed fasteners (▲).

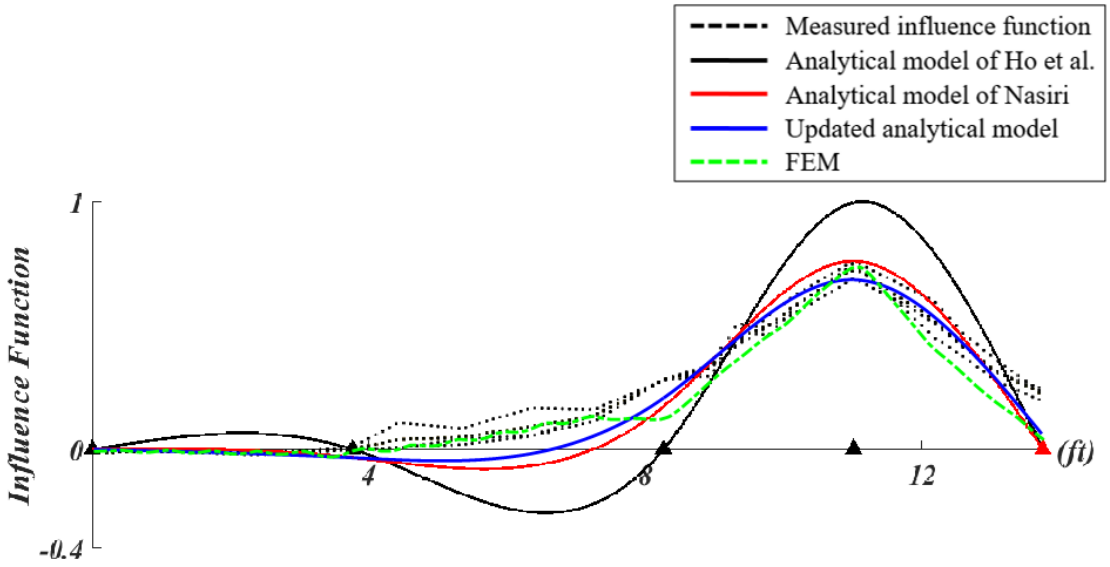

Figure 8.15: Comparison between measured influence function of clip reaction (Type IV) along the seam and estimated influence functions using different models

Note: Supports with installed clips (▲) and Eave end with installed fasteners (▲).

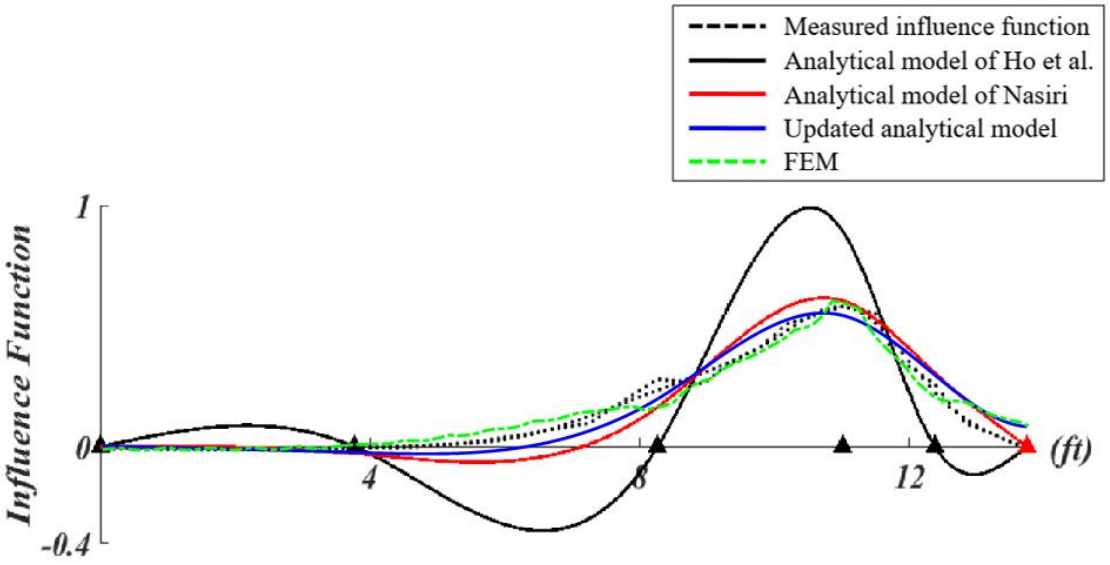

Figure 8.16: Comparison between measured influence function of clip reaction (Type V) along the seam and estimated influence functions using different models

Note: Supports with installed clips (▲) and Eave end with installed fasteners (▲).

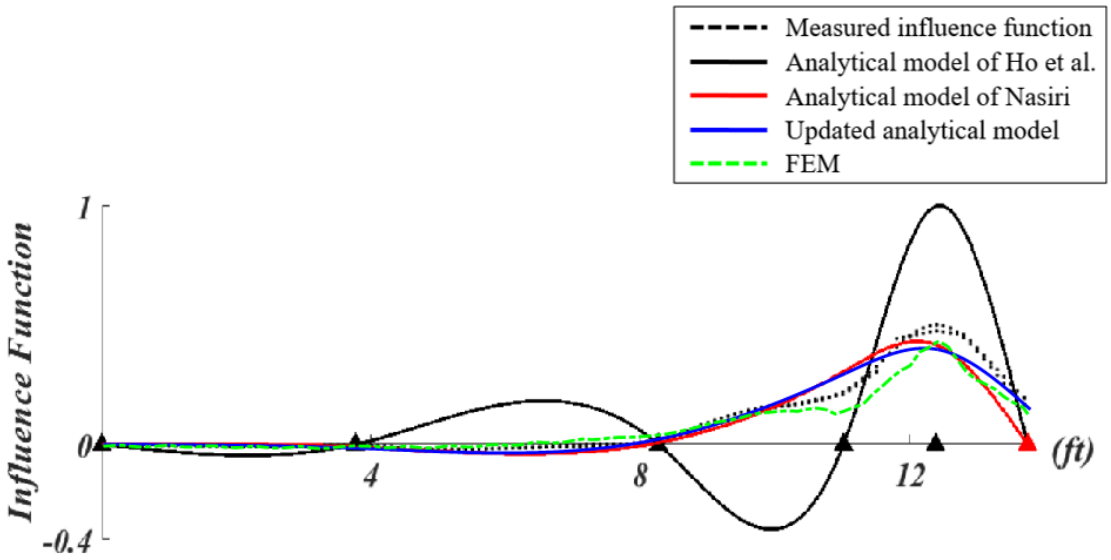

Figure 8.17: Comparison between measured influence function of clip reaction (Type VI) along the seam and estimated influence functions using different models

Note: Supports with installed clips (▲) and Eave end with installed fasteners (▲).

As mentioned before, the changes of clip reactions influence functions perpendicular to the seam are assumed to be linear from the calculated influence coefficient on the standing seam to zero on the adjacent seam. The comparison between the measured influence functions and estimated influence functions along the panel width for all types of clips is given in Figure 8.18. It can be observed that for the type I clips, the changes of influence functions can be considered linear. Both the analytical model and FEM match well with the measured influence functions for type I clip. However, for other types of clips, the changes of influence functions of clips along panel width are nonlinear from the calculated influence coefficient on the standing seam to the adjacent seam. This difference may due to the back-up plate at the roof ridge which reduces the influence of panel deformation on these clips. Using the linear analytical model, it overestimates induced load on clips for all types of clips except the type I clip. It should be noted that the analytical model is only used for the seam behavior, not the panel behavior. On the other hand, FEM provides a good estimation of influence functions for all types of clips except type VI clip. The

mismatch may due to the complex structure at the roof eave. The roof panel at the eave were connected to the purlin through fasteners. However, FEM only simulated the constraining effects rather than the physical model of fasteners. The simplification of FEM at the eave results in the deviation of the influence function for type VI clip.

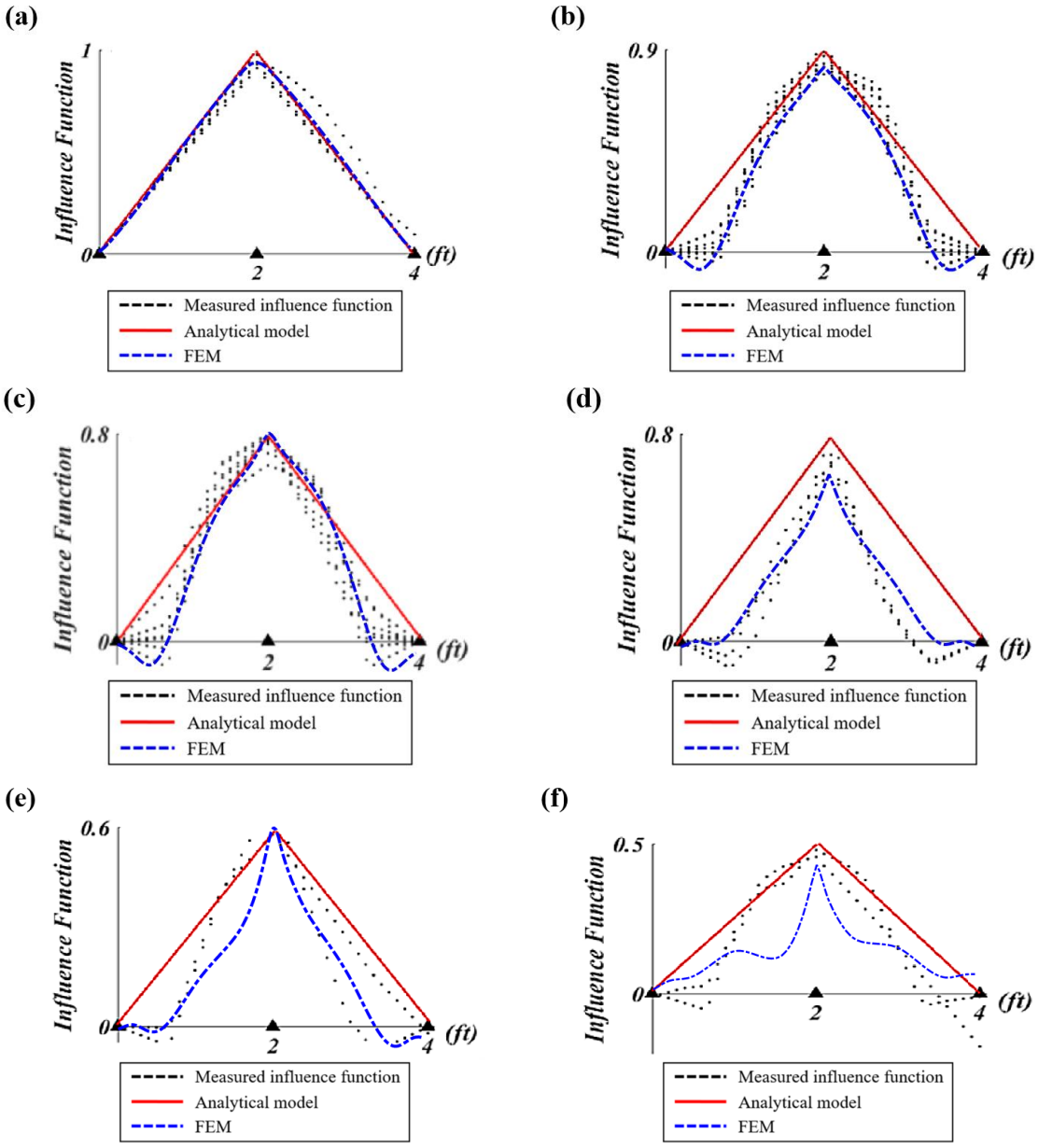

Figure 8.18: Comparison between measured influence function of clip reaction along the panel width and estimated influence functions for: (a) Type I clip, (b) Type II clip, (c) Type III clip, (d) Type V clip, and (e) Type VI clip.

8.3 Application of clip reaction influence function

As described earlier, the DAD method can calculate the structural reaction under the spatio-temporal varying wind loads by integrating aerodynamic information and structural information. Aerodynamic information was obtained from NIST aerodynamic database to give an example of this. The building is located in open terrain with a plan dimension of 30ft (9.1 m) × 45 ft (13.7 m), an eaves height of 13 ft (3.9 m), and a roof slope of 1/4 on 12. Figure 8.19 shows the definition of wind directions in NIST database, which includes 22 wind directions. The 3-second wind speed is 25.8 m/s at 10 m above the ground, which is consistent with the wind speed in IBHS. The updated analytical model was used to provide the clip reaction influence function. It should be noted that since limited load cells were used in the IBHS test, only the clips within the red rectangle were chosen.

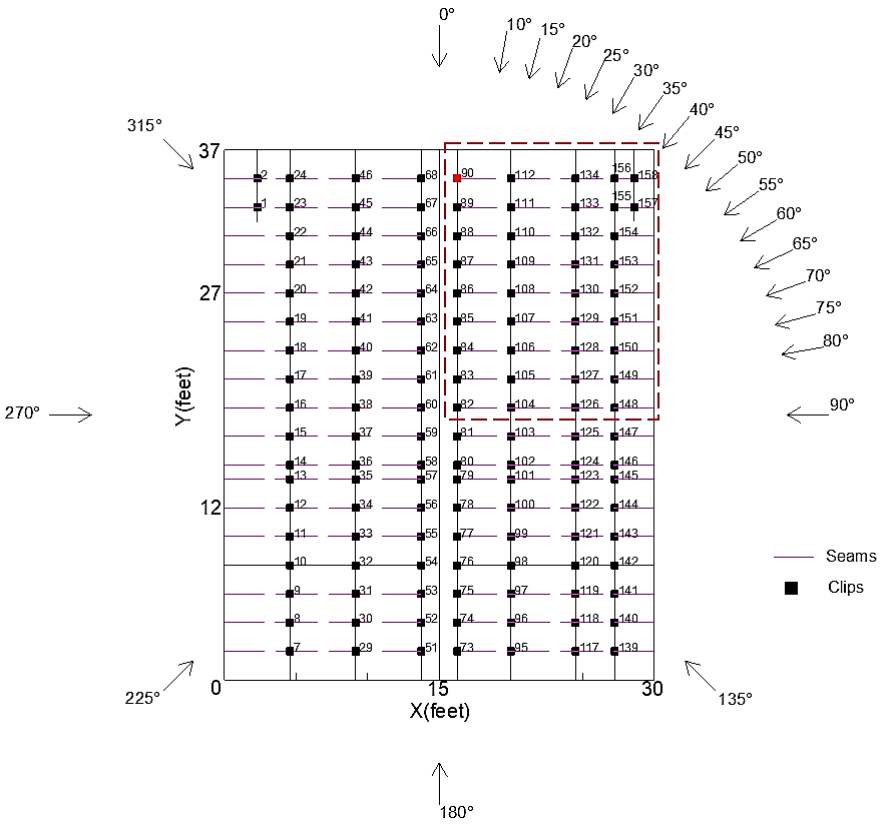

Figure 8.19: Definition of wind directions in NIST database.

The current study uses statistical peak clip reactions rather than the absolute highest clip reactions. These statistical peaks could be obtained through the following steps:

1. The time histories were divided into 10 segments;

2. The peaks from each segment were extracted and fit with a Gumbel distribution;

3. Using the Lieblein BLUE (1974) method, the statistical peaks were obtained, which were 78^{th} percentile values from the Gumbel distribution extrapolated to 1 h using the method of Cook and Mayne (1979);

Figure 8.20 gives the time series of clip reaction under different wind directions for clip 90. The peaks using Lieblein BLUE method are also plotted in Figure 8.20. Repeating steps 1 to 3 and using an enveloping approach, the peak clip reactions over all wind directions could be obtained. The peak induced load on clip 90 is listed in Table 8.2. It can be found that the peak load on clip 90 over all wind directions is -221.5 N when the wind direction is 20°. Table 8.3 lists the peak load over all wind directions for all clips.

In general, load codes defined the pressure distribution on the roof which could be used to calculate the induced load on clips. To verify the rationality of load codes, the pressure distribution on the roof was adopted according to American and Chinese codes respectively. The pressure distribution on the roof defined in ASCE7-16 and GB 50009 (2012) are shown in Figures 8.21 and 8.22, respectively. The updated analytical model was used to obtain the clip reaction influence function, and then to calculate the effective tributary area used for estimating the induced load on clips.

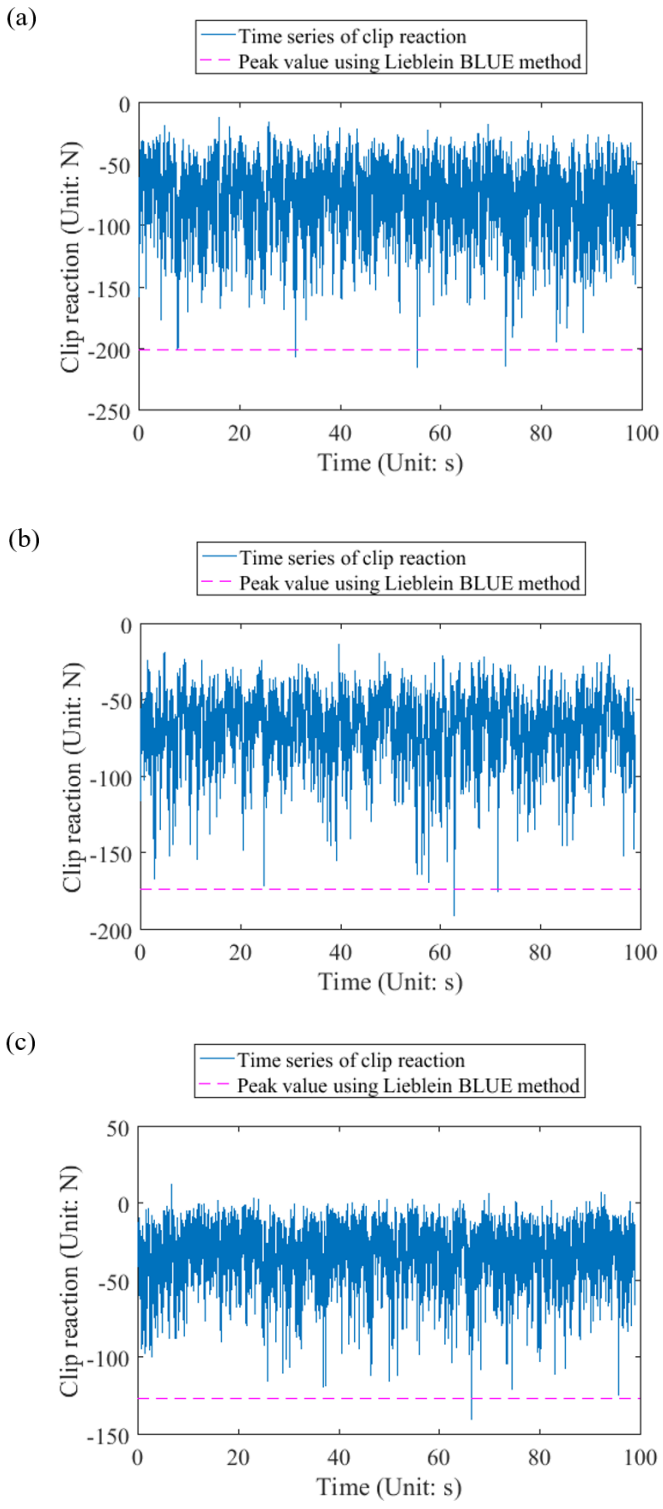

Figure 8.20: Time series of clip reaction under different wind directions (Clip 90): (a) 0°, (b) 45°, and (c) 90°.

Table 8.2: Peak induced load on clip 90 under different wind directions

Wind Direction	Peak Load (N)	Wind Direction	Peak Load (N)
0°	-200.6	60°	-120.6
10°	-223.8	65°	-118.3
15°	-212.3	70°	-106.4
20°	-221.5	75°	-96.4
25°	-215.4	80°	-92.8
30°	-202.6	90°	-126.3
35°	-194.6	135°	-87.4
40°	-172.3	180°	-35.2
45°	-173.0	225°	-82.1
50°	-161.3	270°	-105.3
55°	-148.0	315°	-209.7

Table 8.3: Peak induced load on clips under all wind directions

Clip	Peak Load (N)	Clip	Peak Load (N)	Clip	Peak Load (N)	Clip	Peak Load (N)
82	-139.7	105	-432.3	128	-439.4	151	-368.7
83	-133.1	106	-421.0	129	-425.3	152	-386.8
84	-129.5	107	-412.9	130	-440.2	153	-391.8
85	-132.1	108	-408.4	131	-422.7	154	-408.3
86	-159.9	109	-412.8	132	-420.8	155	-293.1
87	-166.9	110	-502.4	133	-500.9	156	-437.5
88	-198.4	111	-572.6	134	-603.5	157	-203.9
89	-244.0	112	-569.4	148	-365.7	158	-287.4
90	-221.5	126	-453.0	149	-367.2		
104	-444.7	127	-441.9	150	-370.3		

As mentioned previously, the basic wind speed in different codes varies. The basic wind speed in ASCE 7-16 and NIST is defined as 3-second gust wind speed at 10 m above the ground, while the basic wind speed in GB 50009 (2012) is defined as 10-minute wind speed at 10 m above the ground. Therefore, the Durst gust duration curve (Durst 1960) is used for converting the basic wind speed between these standards and experiments.

Two representative regions were chosen to calculate the clip reaction. As shown in Figures 8.21 and 8.22, two selected regions were marked with blue dash lines, which are located near the gable end and in the middle of the roof, respectively. Using equations (1.1) and (1,2), the design load for clips can be calculated. In particular, the values of K_e, K_{zt}, K_d, and K_z in ASCE 7-16 are 1.0, 1.0, 1.0, and 0.85, respectively. The values of β_{gz}, μ_z in GB 50009 (2012) are 1.7 and 1.0, respectively. The Comparison between estimated clip reactions using different methods is shown in Table 8.4.

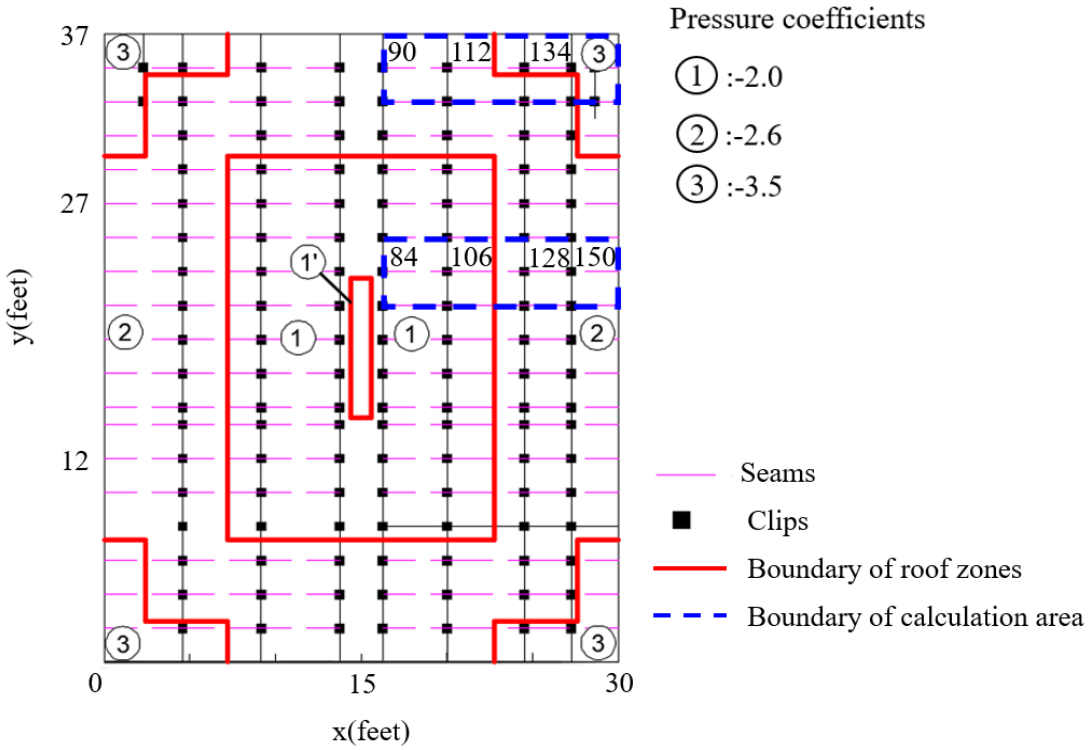

Figure 8.21: Defined zones of pressure coefficients on the tested standing seam metal roof according to ASCE 7-16 (ASCE7, 2016).

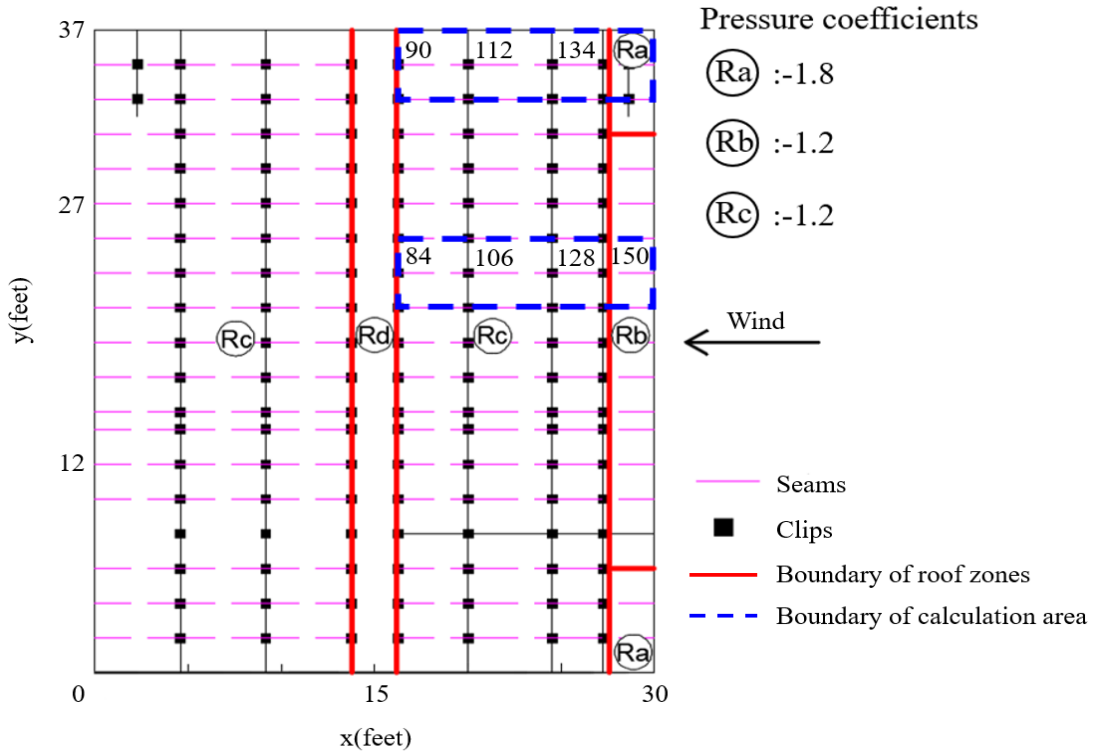

Figure 8.22: Defined zones of pressure coefficients on the tested standing seam metal roof according to GB 50009 (2012) (GB 50009, 2012).

Table 8.4: Comparison between estimated clip reaction using different methods

Clip	ASCE7-16 (N)	GB 50009 (2012) (N)	DAD method (N)
90	-325.4	-128.9	-223.8
112	-894.0	-339.5	-569.4
134	-878.2	-293.7	-603.5
156	-504.1	-175.6	-437.5
158	-315.8	-123.5	-287.4
84	-249.4	-128.9	-129.5
106	-691.2	-339.5	-421.0
128	-694.6	-293.7	-439.4
150	-513.6	-236.7	-370.3

DAD method provides the actual load on clips, and the standardized test gives the load capacity of the clip, so code design is safe when the DAD method is less than the code value. From Table 8.4, it can be found that the results from ASCE 7-16 are closer to those from the DAD method. ASCE 7-16 gives conservative estimates for clip reaction. The maximum deviation is 48.1%. On the other side, the results from GB 50009 (2012) underestimate the clip reaction, and the maximum deviation is up to 149.1%.

8.4 Summary

To calculate the clip reaction of SSMR systems, an updated analytical model was proposed. The performance of a standing seam can be idealized as a continuous beam with clips and fasteners as vertical springs. The vertical stiffness of clips was calculated based on FEM. The changes of clip reaction influence functions perpendicular to the seam are assumed linear from the calculated influence coefficient on the standing seam to zero on the adjacent seam. The changes of influence functions along the seams and perpendicular to the seams are investigated and compared with the results from the experiment and FEM. Compared to the previous analytical models, this updated analytical model gives a better estimation for different types of clips.

DAD method provides the clip reaction under spatio-temporal varying pressure. Structural information was provided using the updated analytical model. The NIST database could provide the time histories of wind pressure while standards consider the spatial variation of wind pressure by defining zones with uniform pressure coefficients. It is observed that the estimated clip reactions using GB 50009 (2012) are much smaller than the peaks using the DAD method, which makes the clips more vulnerable under severe wind suction. ASCE 7-16 gives a conservative estimation of clip reaction.

9. Conclusions and future research recommendations

9.1 Summary and conclusions of the dissertation

Standing seam metal roof systems are widely used due to its easy installation, good waterproof performance, and thermal expansion resistance. However, since it is lightweight and flexible, it is sensitive to wind loads. Previous experiments could not consider all the details of the structures which play a critical role in the performance of the cladding systems. Thus, the wind-induced response and wind-resistance performance of standing seam metal roof system, as well as the internal interaction mechanism between the clip reaction and wind load should be fully understood, in order to calculate and analyze the wind-resistance performance of similar structures, provide a more sufficient theoretical basis for code revisions and practical engineering application. This paper focuses on the structural response of the standing seam metal roof system under wind suction, especially the load paths and structural failure modes. Through the full-scale test, finite element method, and theoretical method, the mechanical behavior of the standing seam metal roof system under the wind suction is systematically studied.

(1) Wind-induced response of roof system based on the full-scale test. The full-scale test was carried out on a standing seam metal roof system, which was designed and installed according to the real roof structure. By measuring the displacement on the roof panel and the clip reactions, the deformation and the load paths of the roof system under wind loads were obtained, as well as the ultimate bearing load and corresponding failure modes. The results show that the deformation begins in the middle of the roof panel. Under low wind pressures (less than 500 Pa), there is a linear relationship between the wind pressure and clip reaction. When the wind loads continue to increase, the load distribution between clips changes, and the linear relationship between the wind pressure and the clip reaction is no longer maintained. More loads transfer to the clips and fasteners at the roof edge. For the

roof near the corner, between 27 to 47% of the applied loads were transferred to the edges of the eave and gable end. For the roof away from the corner, between 17 to 23% of the applied loads were transferred to the eave edge. The failure pressure is 5.8 kPa, 5.3 kPa, and 5.5 kPa for Experiments 1, 2, and 3, respectively. Before the roof system reaches the ultimate bearing capacity, the roof panel undergoes overall buckling. The initial position of overall buckling is in the middle of the two clips near the seam. The clip loads near the buckling position increase sharply at the same time. Two failure modes, clip separation, and fastener failure were observed in the tests. Different failure modes are relevant to the variation of clip arrangement and boundary conditions. The failure load during the dynamic wind load experiment was found to be slightly higher than that obtained from the ramp load experiment. This indicates that the ramp load experiment is slightly conservative compared to the dynamic wind load test.

(2) Entire process tracking of wind-induced roof failure based on finite element method (FEM). FEM considers the geometry, material, and contact non-linearities, and the whole failure process of the roof system is simulated accurately. It also reproduced the typical stages of roof systems, including overall buckling, seam opening, and clip separation. The results show that as the wind load increases, the linear relationship between clip reaction and wind pressure is no longer maintained. The results also reveal that boundary conditions have notable effects on load distribution and the boundary constraint at roof ridge and eaves is the main reason for load redistribution. Since the geometric tributary method does not consider the influence of boundary conditions when calculating the peak clip loads at the limit state, it overestimates the load transfer to clips with a maximum deviation up to 116.8% (clip 122).

(3) Study on clip reaction influence functions using the finite element method. The wind load is related to the clip reaction through the concept of the clip reaction influence function. By calculating the influence functions of 6 kinds of clips, it is found that the influence

range is in the adjacent roof panel and the value of the clip reaction influence function drops to zero at the adjacent seam. For the clip reaction influence function along the seam, it can be seen that the value of the influence function is less than 1 at the position of the corresponding support, while it is not equal to 0 at the adjacent support. The maximum value of the clip reaction influence function is affected by the support arrangement and roof edge constraints. The maximum value is only 0.5 for the support near the eaves. It is inferred that a fair proportion of loads transfer to the fasteners at the roof eave. It is found that the magnitude of the wind pressure has little influence on the influence function along the seam direction and obvious impact on the influence along the width direction, which is mainly caused by the difference in stiffness of the roof in the two directions.

(4) Study on clip reaction influence functions using the theoretical method. The proposed theoretical model considers the standing seam as a continuous beam with equivalent spring supports, which is more suitable for the load transfer mechanism of different types of clips. Compared to the previous theoretical models, this model could describe the influence function for different kinds of clips more accurately. It is shown that considering the clips at the roof ridge as a rigid constraint or equivalent springs has little difference while treating the fastener connection at the roof eave as a ridge constraint causes a relatively large error. This is due to the large difference in stiffness of these two connections.

(5) The clip reaction analysis using the database-assisted design (DAD) method and current standards. By combining with the aerodynamics database and clip reaction influence function through the DAD method, the clip reaction of roof system under real wind load could be calculated, which could be regarded as the actual loads on clips. Since the standards provide the load capacity of the clips, it is safe only when code values are over the realistic clip reactions. After calculating the load capacity of clips using the Chinese and American standards, it is found that the values given by the Chinese standard are

unconservative, and the maximum deviation is up to 149.1%. In contrast, the values given by the American standard are generally conservative, and the maximum deviation is 48.1%.

The key contribution of this research is improving the understanding of load paths and structural behavior of SSMR systems with realistic boundary conditions when subjected to wind uplift load up to the limit state using full-scale test and finite element method.

9.2 Recommendations for future research

The limitations of the current study, and the recommendations for future work, can be summarized as follows:

It is not an easy task to simulate the fastener failure since there were no load cells installed on the fasteners and the failure loads at fasteners are hard to obtain. Component tests are needed in further study to have a better understanding of fastener failure. Future research can be carried out to incorporate the fasteners into the FE model.

This dissertation was focused on simple rectangular buildings with gable roofs and single-ply metal roofs. It is not sure whether the results are similar for other building shapes and more complicated structural systems. Additional research should be carried out to verify the findings.

In this research, the DAD analysis has been carried out for the linear case. However, it would be of great interest to build upon and expand the DAD methodology based on non-linear analysis.

References

Allen, J. (2016). “Understanding Wind Uplift Testing for Standing Seam Roof Systems.” http://blog.mbci.com/understanding-wind-uplift-testing-standing-seam-roof-systems/ (September 2, 2017).

Ali, H. M., & Senseny, P. E. (2003). Models for standing seam roofs. Journal of wind engineering and industrial aerodynamics, 91(12-15), 1689-1702.

An, L., Guan, Y., Zhu, Z., Wu, J., & Zhang, R. (2019). Structural failure analysis of a river-crossing transmission line impacted by the super typhoon Rammasun. Engineering Failure Analysis, 104, 911-931.

ANSI/FM Approvals. ANSI/FM Approvals 4474. American National Standard for Evaluating the Simulated Wind Uplift Resistance of Roof Assemblies Using Static Positive and/or Negative Differential Pressures. ANSI. March 2014.

American Society of Civil Engineers (ASCE). (2016). Minimum design loads and associated criteria for buildings and other structures. ASCE/SEI 7, Reston, VA.

Asbridge, E., Lucas, R., Rogers, K., & Accad, A. (2018). The extent of mangrove change and potential for recovery following severe Tropical Cyclone Yasi, Hinchinbrook Island, Queensland, Australia. Ecology and evolution, 8(21), 10416-10434.

Asghari Mooneghi, M. (2014). Experimental and analytical methodologies for predicting peak loads on building envelopes and roofing systems.

ASTM. (2005). Standard test method for structural performance of sheet metal roof and siding systems by uniform static air pressure difference. E1592, Conshohoken, PA.

ASTM E1592. (2017). Standard Test Method for Structural Performance of Sheet Metal Roof and Siding Systems by Uniform Static Air Pressure Difference. West Conshohocken, PA: ASTM International.

Baskaran, A., Chen, Y., & Vilaipornsawai, U. (1999). A new dynamic wind load cycle to evaluate mechanically attached flexible membrane roofs. Journal of testing and evaluation, 27(4), 249-265.

Baskaran, A., Liu, K., Lei, W., & Delgado, A. (2003). A new facility to simulate simultaneous wind and thermal effects on roofing systems. Journal of testing and evaluation, 31(4), 311-320.

Baskaran, A., Molleti, S., Ko, S., & Shoemaker, L. (2011). Wind uplift performance of composite metal roof assemblies. Journal of Architectural Engineering, 18(1), 2-15.

Belytschko, T., Liu, W. K., Moran, B., & Elkhodary, K. (2013). Nonlinear finite elements for continua and structures. John wiley & sons.

CAN/CSA. (2020). CAN/CSA-A123.21-20. Standard Test Method for the Dynamic Wind Uplift Resistance of Membrane Roofing Systems.

Cauffman, S. A. (2006). Performance of physical structures in Hurricane Katrina & Hurricane Rita: A reconnaissance report. DIANE Publishing.

Cermak, J. E. (1975). Applications of fluid mechanics to wind engineering—a Freeman Scholar lecture.

Coburn, B. H., Wu, Z., & Weaver, P. (2014). Local buckling of blade stiffened variable angle tow panels. In 55th AIAA/ASMe/ASCE/AHS/SC Structures, Structural Dynamics, and Materials Conference (p. 0167).

Collins, M., Kasal, B., Paevere, P., & Foliente, G. C. (2005a). Three-dimensional model of light frame wood buildings. I: Model description. Journal of Structural Engineering, 131(4), 676-683.

Collins, M., Kasal, B., Paevere, P., & Foliente, G. C. (2005b). Three-dimensional model of light frame wood buildings. II: Experimental investigation and validation of analytical model. Journal of Structural Engineering, 131(4), 684-692.

Construction Magazine Network. (2010). "Manufacturer testing." http://www.constructionmagnet.com/metal-roofing-magazine/manufacturer_testing (December 24, 2017).

Cook, N. J., & Mayne, J. R. (1979). A novel working approach to the assessment of wind loads for equivalent static design. Journal of Wind Engineering and Industrial Aerodynamics, 4(2), 149-164.

Cook, N. J., Keevil, A. P., & Stobart, R. K. (1988). Brerwulf-the big bad wolf: I'll huff and I'll puff and I'll blow your house down!. Journal of Wind Engineering and Industrial Aerodynamics, 29(1-3), 99-107.

Corbel, G., Allen, J. T., Woolf, D. K., & Gibb, S. (2007, January). Wind trends in the Highlands and Islands of Scotland 1960–2004 and their relation to the North Atlantic Oscillation. In 19th Conference on Climate Variability and Change, San Antonio, Texas.

Cramer, S. M., Drozdek, J. M., & Wolfe, R. W. (2000). Load sharing effects in light-frame wood-truss assemblies. Journal of Structural Engineering, 126(12), 1388-1394.

Crandell, J. H., Nowak, M., Laatsch, E. M., van Overeem, A., Barbour, C. E., Dewey, R., ... & Angleton, H. (1993). Assessment of damage to single-family homes caused by Hurricanes Andrew and Iniki. US Department of Housing and Urban Development, Washington, DC.

Datin, P. L. (2010). Structural load paths in low-rise, wood-framed structures. University of Florida

Davenport, A. G. (1961). The application of statistical concepts to the wind loading of structures. Proceedings of the Institution of Civil Engineers, 19(4), 449-472.

Davenport, A. G. (1995). How can we simplify and generalize wind loads?. Journal of Wind Engineering and Industrial Aerodynamics, 54, 657-669.

Dixon, C. R., & Prevatt, D. O. (2010). What Do We Learn from Wind Uplift Tests of Roof Systems?. In Structures Congress 2010 (pp. 2405-2416).

Dixon, C., Prevatt, D., & Datin, P. (2011). Influence of edge restraint on clip fastener loads of standing seam metal roof panels. In Roofing Research and Standards Development: 7th Volume. ASTM International.

Durst, C. S. (1960). Wind speeds over short periods of time. Meteor. Mag, 89(1056), 181-187.

El Damatty, A. A., Rahman, M., & Ragheb, O. (2003). Component testing and finite element modeling of standing seam roofs. Thin-walled structures, 41(11), 1053-1072.

Farquhar, S., Kopp, G. A., & Surry, D. (2005). Wind tunnel and uniform pressure tests of a standing seam metal roof model. Journal of Structural Engineering, 131(4), 650-659.

FEMA. (1999). Building Performance Assessment Report: Oklahoma and Kansas Midwest Tornadoes of May 3, 1999: Observations, Recommendations, and Technical Guidance. FEMA 342, Federal Emergency Management Agency.

FEMA. (2009). FEMA P-757: Hurricane Ike in Texas and Louisiana-Building Performance Observations, Recommendations and Technical Guidance, FEMA, Washington, DC.

GB50009, M. O. H. U. R. D. (2012). Load code for the design of building structures. Ministry of Housing and Urban-Rural Construction of the People's Republic of China, Haidian District, Beijing, China.

Griffin, C. W., & Fricklas, R. (2006). Manual of low-slope roof systems. McGraw Hill Professional.

Gulavani, O. V. (2011). Non-linear finite element analysis led design of a novel aircraft seat against certification specifications (CS 25.561).

Gupta, R., & Limkatanyoo, P. (2008). Practical approach to designing wood roof truss assemblies. Practice Periodical on Structural Design and Construction, 13(3), 135-146.

Gurley, K., Davis, Jr, R. H., Ferrera, S. P., Burton, J., Masters, F., Reinhold, T., & Abdullah, M. (2006). Post 2004 hurricane field survey--an evaluation of the relative performance of the standard building code and the Florida building code. In Structures Congress 2006: Structural Engineering and Public Safety (pp. 1-10).

Habte, F., Mooneghi, M. A., Chowdhury, A. G., & Irwin, P. (2015). Full-scale testing to evaluate the performance of standing seam metal roofs under simulated wind loading. Engineering Structures, 105, 231-248.

Henderson, D., & Ginger, J. (2008). Role of building codes and construction standards in windstorm disaster mitigation. Australian Journal of Emergency Management, The, 23(2), 40-46.

Hibbeler, R. C., & Kiang, T. (2015). Structural analysis. Upper Saddle River: Pearson Prentice Hall.

Ho, T. C. E., Surry, D., & Morrish, D. (2003a). NIST/TTU cooperative agreement–windstorm mitigation initiative: Wind tunnel experiments on generic low buildings. The Boundary Layer Wind Tunnel Laboratory, University of Western Ontario.

Ho, T. C. E., Surry, D., & Morrish, D. (2003b). NIST/TTU cooperative agreement–windstorm mitigation initiative: Wind tunnel experiments on generic low buildings. The Boundary Layer Wind Tunnel Laboratory, University of Western Ontario.

Ho, T. C. E., Surry, D., Morrish, D., & Kopp, G. A. (2005). The UWO contribution to the NIST aerodynamic database for wind loads on low buildings: Part 1. Archiving format and basic aerodynamic data. Journal of Wind Engineering and Industrial Aerodynamics, 93(1), 1-30.

Holmes, J. D., & Bekele, S. (2018). Wind loading of structures (Vol. 11). London: SPON press.

Hourani, M., (2002). Mathematical model of influence lines for indeterminate beams, presented at Annual Conference, Montreal, Canada. https://peer.asee.org/11191

Ishihara, T., Yamaguchi, A., Takahara, K., Mekaru, T., & Matsuura, S. (2005, September). An analysis of damaged wind turbines by Typhoon Maemi in 2003. In Proceedings of the 6th Asia-Pacific Conference on Wind Engineering. Seoul, Republic of Korea2005 (pp. 1413-28).

Jungmann, M. D. (2007). Finite element analysis and field observation of a residential roof subjected to hurricane winds

Kind, R. J. (1986). Worst suctions near edges of flat rooftops on low-rise buildings. Journal of Wind Engineering and Industrial Aerodynamics, 25(1), 31-47.

Kind, R. J., & Wardlaw, R. L. (1982). Failure mechanisms of loose-laid roof-insulation systems. Journal of wind engineering and industrial aerodynamics, 9(3), 325-341.

Kirby, J. R., and Sockalingam, B. (2003). NRCA analyzes and tests metals. Professional Roofing, 28–36.

Kopp, G. A., Morrison, M. J., & Henderson, D. J. (2012). Full-scale testing of low-rise, residential buildings with realistic wind loads. Journal of Wind Engineering and Industrial Aerodynamics, 104, 25-39.

Kopp, G. A., Morrison, M. J., Gavanski, E., Henderson, D., and Hong, H. P. (2010). The 'three little pigs' project: hurricane risk mitigation by integrated wind tunnel and full-scale laboratory tests. Nat. Hazards Rev. 11, 151–161.

Kumar, A. S., Himabindu, G., Raman, M. S., & Reddy, K. V. K. (2013). Experimental investigations with crush box simulations for different segment cars using LS-DYNA. International Journal of Current Engineering and Technology, Special Issue-2 (Feb 2014).

Kunz, M., Mühr, B., Kunz-Plapp, T., Daniell, J. E., Khazai, B., Wenzel, F., ... & Zschau, J. (2013). Investigation of superstorm Sandy 2012 in a multi-disciplinary approach. Natural Hazards and Earth System Sciences, 13(10), 2579-2598.

Lieblein, B. J. . (1976). Efficient methods of extreme-value methodology. National Bureau of Standards.

Liu, Y. X., Tong, G. S., Du, H. L., & Zhang, L. (2014). Test and finite element analysis on torsional restrain of corrugated steel sheet to purlin through clips. Journal of Building Structures, 35, 116-124.

Mahaarachchi, D., & Mahendran, M. (2009). Wind uplift strength of trapezoidal steel cladding with closely spaced ribs. Journal of Wind Engineering and Industrial Aerodynamics, 97(3-4), 140-150.

Main, J. A., & Fritz, W. P. (2006). Database-assisted design for wind: concepts, software, and examples for rigid and flexible buildings. National Institute of Standards and Technology, Technology Administration, US Department of Commerce.

Morrison, M. J., & Reinhold, T. A. (2015). Performance of metal roofing to realistic wind loads and evaluation of current test standards. In Proceeding of the 14th International Conference on Wind Engineering.

Morrison, M. J., & Kopp, G. A. (2010). Analysis of wind-induced clip loads on standing seam metal roofs. Journal of structural engineering, 136(3), 334-337.

Nasiri, M. (2019). Full-scale measurements to evaluate single-ply metal roof performance under extreme wind loads.

Ortiz, M., & Nour-Omid, B. (1986). Unconditionally stable concurrent procedures for transient finite element analysis. Computer Methods in Applied Mechanics and Engineering, 58(2), 151-174.

Paevere, P. J., Foliente, G. C., & Kasal, B. (2003). Load-sharing and redistribution in a one-story woodframe building. Journal of Structural Engineering, 129(9), 1275-1284.

Perry, D. C., ASCE, M., McDonald, J. R., Saffir, H. S., & ASCE, F. (1990). Performance of metal buildings in high winds. Journal of Wind Engineering and Industrial Aerodynamics, 36, 985-999.

Pierre, L. S., Kopp, G. A., Surry, D., & Ho, T. C. E. (2005). The UWO contribution to the NIST aerodynamic database for wind loads on low buildings: Part 2. Comparison of data

with wind load provisions. Journal of Wind Engineering and Industrial Aerodynamics, 93(1), 31-59.

Prathap, G. (2013). The finite element method in structural mechanics: principles and practice of design of field-consistent elements for structural and solid mechanics (Vol. 24). Springer Science

Prevatt, D. O., Schiff, S. D., & Sparks, P. R. (1995). A technique to assess wind uplift performance of standing seam metal roofs. In Proceedings of the 11th Conference on Roofing Technology (pp. 31-38).

Resource center, 2021, accessed April 2021, <https://www.mbci.com/ >.

Rigato, A., Chang, P., & Simiu, E. (2001). Database-assisted design, standardization, and wind direction effects. Journal of Structural Engineering, 127(8), 855-860.

Simiu, E., Sadek, F., Whalen, T. M., Jang, S., Lu, L. W., Diniz, S. M., ... & Riley, M. A. (2003). Achieving safer and more economical buildings through database-assisted, reliability-based design for wind. Journal of wind engineering and industrial aerodynamics, 91(12-15), 1587-1611.Rosenfield, M. J., Rose, W., & Dillner, W. (1986). Investigation of Standing Seam Metal Roofing (No. CERL-TR-M-

Roylance, D. (2001). Stress-strain curves. Massachusetts Institute of Technology study, Cambridge.

Rust, W., & Schweizerhof, K. (2003). Finite element limit load analysis of thin-walled structures by ANSYS (implicit), LS-DYNA (explicit) and in combination. Thin-walled structures, 41(2-3), 227-244.

Schroter, R. C. (1985). Air pressure testing of sheet metal roofing. NRCA Second International journal of Roofing Technology, 254-260.

Serrette, R., & Peköz, T. (1997). Bending strength of standing seam roof panels. Thin-walled structures, 27(1), 55-64.

Sika. (2015). SIKACOAT RF400D. Product Data Sheet, < https://usa.sika.com >. (August 16, 2018).

Simiu, E. (2011). Design of buildings for wind. Wiley, Hoboken, NJ.

Somiu, E., & Stathopoulos, T. (1997). Codification of wind loads on buildings using bluff body aerodynamics and climatological data bases. Journal of wind engineering and industrial aerodynamics, 69, 497-506.

Simiu, E., Sadek, F., Whalen, T. M., Jang, S., Lu, L. W., Diniz, S. M., ... & Riley, M. A. (2003). Achieving safer and more economical buildings through database-assisted, reliability-based design for wind. Journal of wind engineering and industrial aerodynamics, 91(12-15), 1587-1611.

Sinno, R. R. (2008). Response of metal roofs to uniform static and true hurricane wind loads.

Sinno, R. R., Surry, D., Fowler, S., & Ho, T. C. E. (2003). Testing of metal roofing systems under simulated realistic wind loads. In Proceedings of the Eleventh International Conference on Wind Engineering.

Sinno, R.R., (2008). Response of metal roofs to uniform static and true hurricane wind loads, 19th International Specialty Conference on Cold-Formed steel structures St. Louis, Missouri, USA

Smith, T. L. (1995). Insights in metal roof performance in high-wind regions. Prof. Roof. Mag, 25(2), 12-16.

Song, X., Zhang, Y., & Zhang, Q. (2017). Failure modes and loading bearing capacity of corrugated steel roofs connected by standing seam clips. International Journal of Steel Structures, 17(4), 1341-1352.

Sparks, P. R., Schiff, S. D., & Reinhold, T. A. (1994). Wind damage to envelopes of houses and consequent insurance losses. Journal of wind engineering and industrial aerodynamics, 53(1-2), 145-155.

Stathopoulos, T. (1979). Turbulent wind action on low rise Structures. London, Canada: The University of Western Ontario.

Surry, D., Sinno, R. R., Nail, B., Ho, T. C., Farquhar, S., & Kopp, G. A. (2007). Structurally effective static wind loads for roof panels. Journal of Structural Engineering, 133(6), 871-885.

Tamura, Y. (2009). Wind-induced damage to buildings and disaster risk reduction. Proceedings of the APCWE-VII, Taipei, Taiwan.

Tieleman, H. W. (2003). Wind tunnel simulation of wind loading on low-rise structures: a review. Journal of wind engineering and industrial aerodynamics, 91(12-15), 1627-1649.

Underwriters Laboratories, Cames, WA. Underwriters Laboratories. (2019). Standard for tests for uplift resistance of roof assemblies. UL 580, 5th Ed., Underwriters Laboratories, Cames, WA.

Underwriters Laboratories. (2020). Standard for uplift tests for roof covering systems. UL 1897, 7th Ed.,

van de Lindt, J. W., Graettinger, A., Gupta, R., Skaggs, T., Pryor, S., & Fridley, K. J. (2007). Performance of wood-frame structures during Hurricane Katrina. Journal of Performance of Constructed Facilities, 21(2), 108-116.

Van der Hoven, I. (1957). Power spectrum of wind velocities fluctuations in the frequency range from 0.0007 to 900 Cycles per hour. Journal of Meteorology, 14, 160- 164.

Vigdor, J. (2008). The economic aftermath of Hurricane Katrina. Journal of Economic Perspectives, 22(4), 135-54.

Walker, G. R. (1975). Report on Cyclone" Tracy': Effect on Buildings, December 1974. Department of Housing and Construction.

Whalen, T. M., Sadek, F., & Simiu, E. (2002). Database-assisted design for wind: basic concepts and software development. Journal of Wind Engineering and Industrial Aerodynamics, 90(11), 1349-1368.

Whalen, T., Simiu, E., Harris, G., Lin, J., & Surry, D. (1998). The use of aerodynamic databases for the effective estimation of wind effects in main wind-force resisting systems:: application to low buildings. Journal of Wind Engineering and Industrial Aerodynamics, 77, 685-693.

Wolfe, R. W. (1991). Structural performance of light-frame roof assemblies: II. Conventional truss assemblies (Vol. 499). US Department of Agriculture, Forest Service, Forest Products Laboratory.

Wu, R., Wu, S., Chen, T., Yang, Q., Han, B., & Zhang, H. (2021). Effects of Wave–Current Interaction on the Eastern China Coastal Waters during Super Typhoon Lekima (2019). Journal of Physical Oceanography, 51(5), 1611-1636.

Xiangting, Z. (1988). The current Chinese code on wind loading and comparative study of wind loading codes. Journal of wind engineering and industrial aerodynamics, 30(1-3), 133-142.

Yang, Q., Gao, R., Bai, F., Li, T., & Tamura, Y. (2018). Damage to buildings and structures due to recent devastating wind hazards in East Asia. Natural hazards, 92(3), 1321-1353.

Zisis, I. (2011). Wind load paths on wood buildings (Doctoral dissertation, Concordia University).

Appendices

Appendix A: Standing Seam Metal Roof (SSMR) system

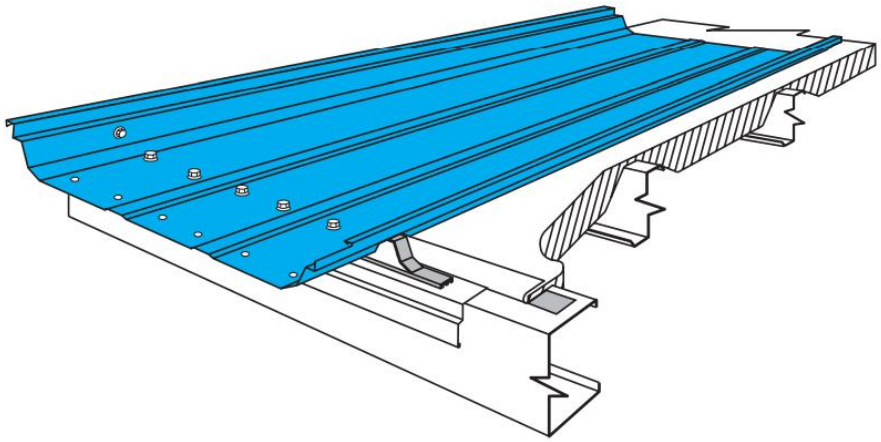

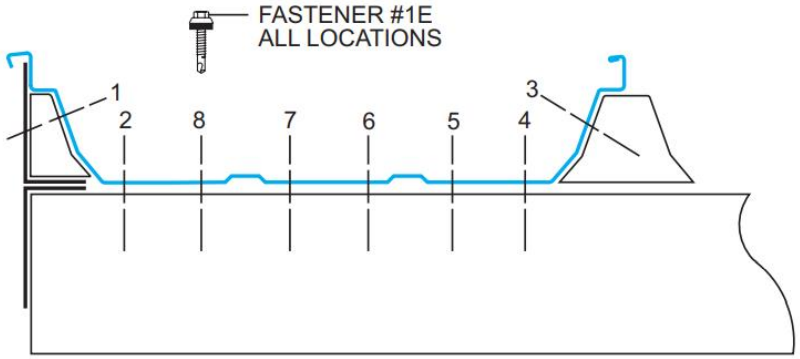

Figure A-1: Panel attachments at the eave edge of the roof.

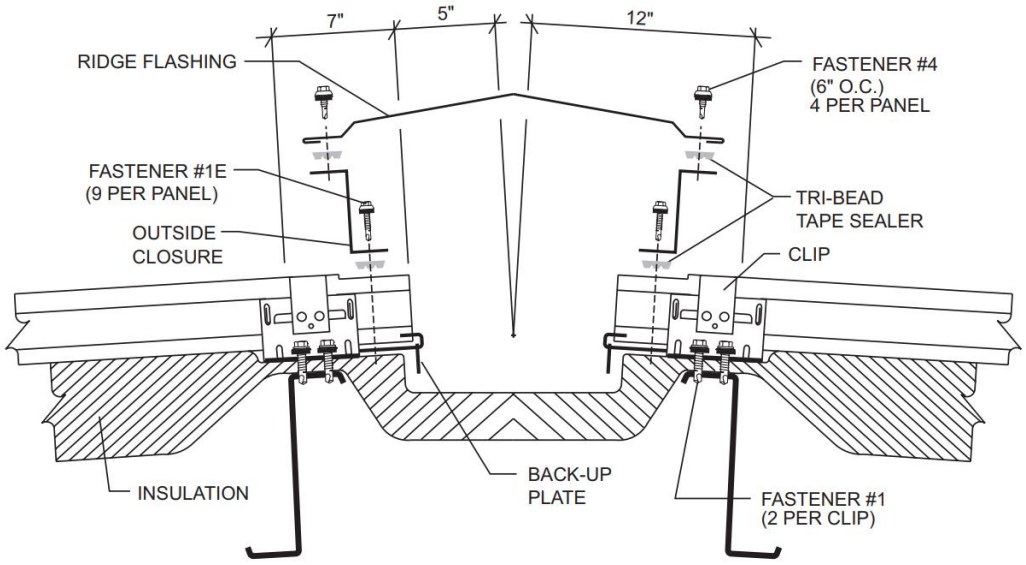

Figure A-2: Trim details at the ridge.

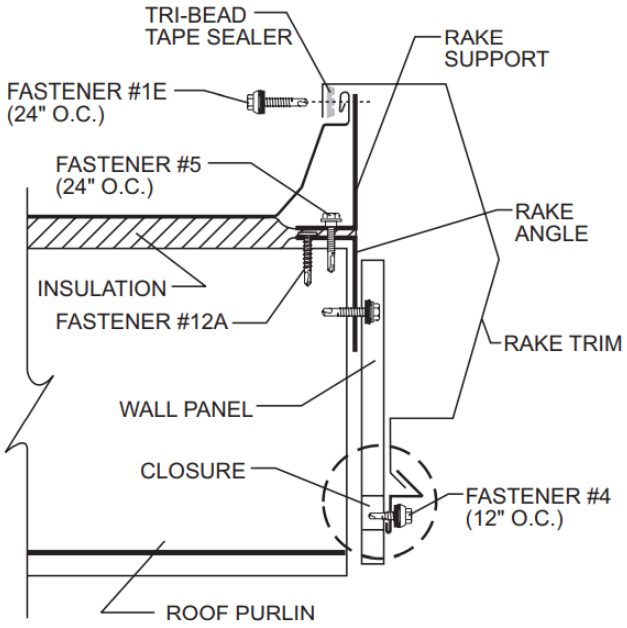

Figure A-3: Trim details of rake at the gable end.

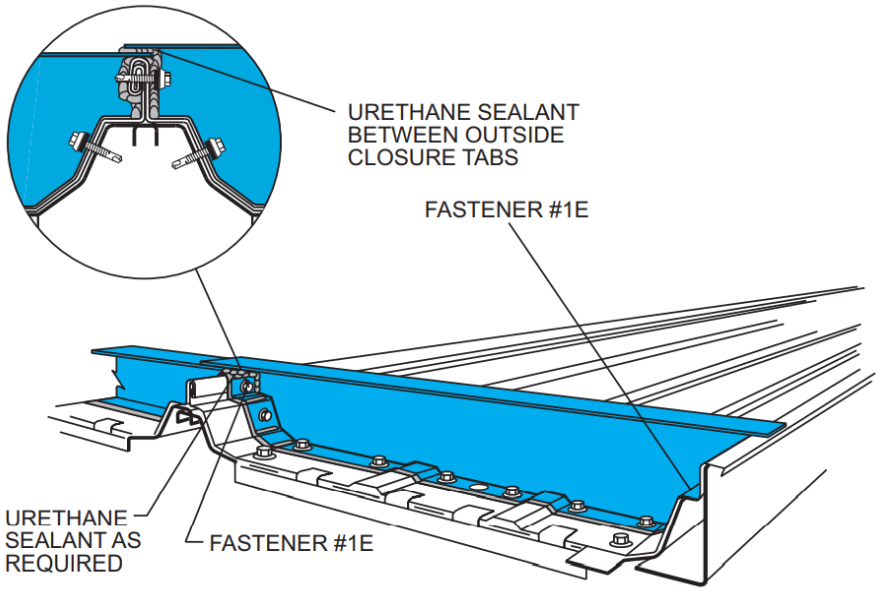

Figure A-4: Installation of outside closure at the ridge of the roof.

Curriculum Vitae

Name: Yuchao Xia

Post-secondary Education and Degrees:

Wuhan University of Technology, Wuhan, China
2010-2014 B.A.

Zhejiang University, Hangzhou, China
2014-2021 Ph.D.

The University of Western Ontario, London, Ontario, Canada
2017-2022 Ph.D. (Dual Ph.D. Program)

Related Work Experience

Teaching Assistant, Zhejiang University, 2014-2017
Teaching Assistant, The University of Western Ontario, 2018-2019